2017

Quantum Electronic Interference In Nano Amorphous Silicon And Other Thin Film Resistance Memory

Yang Lu
University of Pennsylvania, edward.yanglu@gmail.com

Quantum Electronic Interference In Nano Amorphous Silicon And Other Thin Film Resistance Memory

Abstract
This thesis describes conductivity in amorphous semiconductors and insulators—some doped with metals, in which elastic electrons can random walk across a transport length of ~10 nm. At low temperatures, back diffusion of coherent electrons causes constructive quantum interference that leads to reduced diffusivity/conductivity. Rich physics also arises in this so-called weak-localization (WL) regime from electron-phase mutilation by spin-orbit interaction (weak-antilocalization or WAL) and magnetic modulation, and from Friedel-oscillation-enhanced backscattering and Zeeman splitting (electron-electron-interaction or EEI). Conductivity is analyzed by a new tool to eliminate contact resistance without using the four-point-probe method.

The Aharonov-Bohm oscillation in magnetoresistance affords the cleanest evidence of interference, seen in amorphous HfO2 and Al2O3, each containing a single 6-7 nm conductive loop. The loop is atomically thin and has no in-loop path dispersion, which allows the oscillation to persist with uncharacteristically low attenuation. In amorphous Si, quantum conductivity correction and magnetoresistance are universally exhibited in multiple states and multiple samples. But doping amorphous Si3N4 with Pt creates a novel feature: a sharp resistance maximum at Tmax below which the WAL-mediated spin-orbit interaction completely dominates over the spin-insensitive WL. This interaction can further quench the coherent length to keep it commensurate with the magnetic length, thus permitting the EEI-directed magnetoresistance to develop to unprecedented strength. Reduced HfO2 and Al2O3 also feature the same characteristics, albeit in one-dimension conduction.

Ubiquitous to amorphous nano conductors is their strong electron-phonon interaction. It imparts electrons with up to 100x heavier mass, which is translated into up to 100x reduction in diffusivity. Yet at low enough temperatures, electron diffusion can fully saturate the 10 nm transport length in all our samples. This prevents weak localization from crossover to strong localization, so the nano amorphous devices remain conductive down to 0K. Yet under a critical voltage ~ 1 V, they can trap injected electrons at locally soft spots and stabilize them by bond relaxation; in doing so they promptly switch to the insulator state. Thanks to these attributes, which are reversible, our devices are all excellent resistance-switching non-volatile memory.

Degree Type
Dissertation

Degree Name
Doctor of Philosophy (PhD)

Graduate Group
Materials Science & Engineering

First Advisor
I-Wei Chen

Keywords
Electron-phonon interaction, Metal-insulator transition, Quantum electoronic interference, ReRAM, Resistance memory, Weak localization

Subject Categories
Mechanics of Materials | Physics

QUANTUM ELECTRONIC INTERFERENCE IN NANO AMORPHOUS SILICON AND OTHER THIN FILM RESISTANCE MEMORY

Yang Lu

A DISSERTATION

in

Materials Science and Engineering

Presented to the Faculties of the University of Pennsylvania

in

Partial Fulfillment of the Requirements for the

Degree of Doctor of Philosophy

2017

Supervisor of Dissertation

I-Wei Chen, Professor of Materials Science and Engineering

Graduate Group Chairperson

David J. Srolovitz, Professor of Materials Science and Engineering

Dissertation Committee

Ritesh Agarwal, Professor of Materials Science and Engineering

James M. Kikkawa, Professor of Physics and Astronomy

Eugene J. Mele, Professor of Physics and Astronomy

ABSTRACT

QUANTUM ELECTRONIC INTERFERENCE IN NANO AMORPHOUS SILICON AND OTHER THIN FILM RESISTANCE MEMORY

Yang Lu

I-Wei Chen

This thesis describes conductivity in amorphous semiconductors and insulators—some doped with metals, in which elastic electrons can random walk across a transport length of ∼10 nm. At low temperatures, back diffusion of coherent electrons causes constructive quantum interference that leads to reduced diffusivity/conductivity. Rich physics also arises in this so-called weak-localization (WL) regime from electron-phase mutilation by spin-orbit interaction (weak-antilocalization or WAL) and magnetic modulation, and from Friedel-oscillation-enhanced backscattering and Zeeman splitting (electron-electron-interaction or EEI). Conductivity is analyzed by a new tool to eliminate contact resistance without using the four-point-probe method.

The Aharonov-Bohm oscillation in magnetoresistance affords the cleanest evidence of interference, seen in amorphous HfO_2 and Al_2O_3, each containing a single 6-7 nm conductive loop. The loop is atomically thin and has no in-loop path dispersion, which allows the oscillation to persist with uncharacteristically low attenuation. In amorphous Si, quantum conductivity correction and magnetoresistance are universally exhibited in multiple states and multiple samples. But doping amorphous Si_3N_4 with Pt creates a novel feature: a sharp resistance maximum at T_{max} below which the WAL-mediated spin-orbit interaction completely dominates over the spin-insensitive WL. This interaction can further quench the coherent length to keep it commensurate with the magnetic length, thus permitting the EEI-directed magnetoresistance to develop to unprecedented strength. Reduced HfO_2 and Al_2O_3 also feature the same characteristics, albeit in one-dimension conduction.

Ubiquitous to amorphous nano conductors is their strong electron-phonon interaction. It imparts electrons with up to 100× heavier mass, which is translated into up to 100× reduction in diffusivity. Yet at low enough temperatures, electron diffusion can fully saturate the 10 nm transport length in all our samples. This prevents weak localization from crossover to strong localization, so the nano amorphous devices remain conductive down to 0K. Yet under a critical voltage ∼1 V, they can trap injected electrons at locally soft spots and stabilize them by bond relaxation; in doing so they promptly switch to the insulator state. Thanks to these attributes, which are reversible, our devices are all excellent resistance-switching non-volatile memory.

TABLE OF CONTENTS

LIST OF TABLES

LIST OF ILLUSTRATIONS

FIGURE 4.7 : Magnetoresistance of voltage-metallized HfO_2 cells, (2), (4), and (5) in Table 4.3, shown in (a-b), (c-d), and (e-f), respectively. In (a), (c), and (e), their positive MR cusp at low field is fitted by the 3D WAL/WL theory (Eq. (1.26)) in two ways, shown as red curves and black curves, respectively. These curves indicate WAL becomes weaker in the order of (2) to (4) to (5), consistent with Table 4.3. When the red curve fitting is used, there is a remaining contribution of nature of Aharonov-Bohm oscillations, which are shown in (b), (d), and (f), and fitted by the WAL/WL theory (Eq. (1.31), black curves) for atomically thin loops, with $W = 0.1$ nm, $L_\phi = 10$ nm, radius $r \sim 6.5$ ($\theta = 2°$), 3.8, and 3.5 nm, respectively. No θ values can be obtained for the latter two oscillations that the field is not high enough to examine possible attenuations. Oscillation in (b) starts with a local minimum at small field; such positive MR indicates WAL dominance. Oscillations in (d) and (f) start with a local maximum at small field; such negative MR indicates WL dominance. These trends are consistent with the finding in Table 4.3.115

Table 1: List of main symbols in this thesis.

Symbol	Physical Meaning	Relations
L	Sample size	N.A.
δ	Sample (film) thickness	N.A.
W	Shortest dimension of quasi-1D and 2D samples	N.A.
A	Sample (wire) cross-section area	$A = W^2$
d	Spatial conduction dimensionality	N.A.
a_0	Atomic spacing of the material	N.A.
ζ	Localization length	N.A.
l	Mean free path	$l = v_F\tau$
λ_F	Fermi wave length	$\lambda_F = 2\pi k_F$
k_F	Fermi wave number	$k_F = 2\pi/\lambda_F$
v_F	Fermi velocity	$m^* v_F = \hbar k_F$
D	Electron diffusivity	$D = v_F l/d$
n	Electron density	$n = k_F^3/3\pi^2$ (3D)
m^*	Electron effective mass	$m^* = \hbar/2D$
σ_D	Drude conductivity	$\sigma_D = ne^2\tau/m^*$
$\sigma_{\min}$	Minimum metallic conductivity	$\sigma_{\min} = e^2/3\hbar a_0$
ϕ	Phase of electron wave function	N.A.
τ	Electron momentum relaxation time	$\tau = l/v_F$
τ_ϕ	Phase relaxation time (zero-spin, singlet)	$1/\tau_\phi = 1/\tau_i + 1/\tau_s$
τ_ϕ^*	Phase relaxation time (triplet)	$1/\tau_\phi^* = 1/\tau_i + 4/3\tau_{so} + 2/3\tau_s$
τ_i	Inelastic scattering relaxation time	$\tau_i \approx T^{-p}$
τ_s	Spin-flip scattering time due to spin-spin coupling	N.A.
τ_{so}	Spin-flip scattering time due to spin-orbit coupling	N.A.
τ_T	Thermal dephasing time	$\hbar/k_B T$
L_ϕ	Dephasing length (spinless, singlet)	$L_\phi = \sqrt{D\tau_\phi}$
L_ϕ^*	Dephasing length (triplet)	$L_\phi^* = \sqrt{D\tau_\phi^*}$
L_T	Thouless/Thermal dephasing length	$L_T = \sqrt{\hbar D/k_B T}$
L_B	Magnetic length	$L_B = \sqrt{\hbar/eB}$
Φ	Magnetic field flux	N.A.
Φ_0	Quantum of magnetic flux for a charge of $2e$	$\Phi_0 = h/2e$

CHAPTER 1 : Introduction

1.1. Electron Scattering and Localization in Disordered Electron Systems

1.1.1. An Overview

The subjects of this thesis are quantum interference phenomena of coherent electrons in nanoscale disordered electron systems. In such systems, an electron can random walk as if diffusing in a non-periodic network, and after each step of random walk its momentum has changed but not necessarily its energy or phase. Disordered electron systems may include amorphous materials, which lack long-range order but maintain short-range order at the local, atomic level. But they also include single crystals or polycrystals of metals or semiconductors, which are doped with impurities that cause repeated electron scattering, hence random walk. Quantum interference phenomena of these two types of disordered electron systems have been extensively studied in bulk or mesoscopic samples since 1970s [1, 2, 3, 4]. However, as it will become clear in this thesis, the disordered electron systems may further include amorphous solid solutions of an insulator and a metal or an insulator and a semiconductor, or even an amorphous insulator itself without alloying; surprisingly, they all allow transport of coherent electrons when their physical sizes fall into the nanometer scale. They may be called *nano metals*, and two new families of nano metals are discovered here for the first time. Quantum interference of coherent electrons in nanoscale amorphous electron systems, or nano metals, has never been studied before. This thesis will report such observations in three prototypical nano metals to elucidate those features unknown to previous studies of bulk or mesoscopic disordered electron systems.

Amorphous materials allow electron states to distribute continuously within the band gap, so the sharp edges of the density of state, $N(E)$, are smeared out into band tails [5, 6]. This makes it difficult to determine whether an electron is localized or not, which led Mott to propose the concept of mobility edge: Electrons beyond the mobility edge are localized [7]. However, whether an electron is localized or not can also be determined

in the real space using the Anderson's concept of localization length [8], which predates Mott's mobility edge. Treating electrons as quantum waves, Anderson found their wave functions will exponentially decay, taking the form of $\psi = e^{-r/\zeta} \sum_n c_n e^{i\phi_n} \psi_n(r - a_n)$, if a strong random potential V is added to the periodic potential $V_o(x, y, z)$ in a periodic lattice $r = a_n$. In the above, ζ is the localization length. But in a macroscopic sample it is also the "diffusion length" of an electron that random walks by repeated scattering by V_o: A diffusing electron can only reach this distance in the landscape of disordered potential. Clearly, for a macroscopic sample, any finite ζ implies absence of long range diffusion, or conductivity, hence the material is an insulator. Although one can still define the Fermi wavelength $\lambda_F = 2\pi/k_F = 2\pi\hbar/p_F$, frequency ω, and phase ϕ for localized electrons, they do not allow conduction.

The transition that relies on tuning the random potential to form an insulator is called the *Anderson localization* or *Anderson transition*, and any insulator that derives its insulating character from the above transition is called an Anderson insulator. Because random potential that renders Anderson transition is typically rather strong, the insulating property of Anderson insulators are usually temperature independent. Therefore, Anderson's theory, derived for 0K, is mostly applicable even at higher temperatures. This concept of random-wave localization is rather general and has been applied to phonons [9] and photons [10].

Localization is inherently a concept that entails a size effect. If the sample size is less than ζ, random waves can communicate from one boundary to the other. So a nanosized sample may behave like a conductor even though it is made of a material that in the bulk form would have been called a strong insulator. This is the idea of *nano* metal that our group has explored in the last few years [11, 12, 13]. Before this thesis, nano metals were already discovered in a large family of metal-doped amorphous oxides and nitrides: Oxides include those of Si, Al, Mg, Y, Hf and Ta, nitrides include those of Si and Al, and metals include Pt and, if oxidation is prevented, Al, Cr, Cu, Ta and Ti [14, 15]. In this thesis, we shall

see that amorphous Si and Ge, even amorphous HfO_2 and Al_2O_3, also form nano metals. Remarkably, the latter two are one-dimensional nano metals.

The realization that electron localization is sensitive to dimensionality d began in mid 1970. According to the scaling theory of Abrahams, Anderson, Licciardello, and Ramakrishnan [16], localized and extended states do not always coexist in all dimensions: Localization-induced metal-insulator transitions (MIT) only occurs in 3D systems, whereas electron states in disordered 2D and 1D systems are always localized at 0K. This even applies to materials that are nominally metals at higher temperatures. Because of disorder, electrons in metals also undergo random walk: Electron's momentum eigenstate sustains a travel distance l (the distance of one random-walk step) before it changes direction due to elastic scattering; but its energy eigenstate may actually sustain a longer travel distance L_ϕ before dephasing—which requires energy change, such as one due to inelastic scattering. In the above, the so called 2D and 1D samples are actually quasi-two-dimensional or quasi-one-dimensional, in that they are three-dimensional samples made of three-dimensional materials. But because their short dimensions (thickness δ or cross-section A) are much less than L_ϕ, electrons traveling down the long dimension—across which the electrodes are located and along which electron wave propagation is detected—must be bounced back and forth so many times in the short dimensions that they have lost any memory of the short dimensions. Therefore, the conduction is as if in one-dimension, or in two-dimensions.

In the literature, the mesoscopic or macroscopic metallic films studied in the past were mostly treated as 2D systems with a thickness well below the characteristic transport length. Here, the transport length is usually the probe distance, e.g., four-probe technique may be used to measure the planar current. Since the typical probe distance exceeds the film thickness by many orders of magnitude, these are essentially mesoscopic or macroscopic experiments. In this thesis, however, we shall measure the resistance of nanometallic thin films by passing a vertical, out-of-plane current across the film thickness, so the transport length is the same as the film thickness: It is indeed nanoscale. Nevertheless, because of the

amorphous nature of the nano metals that are disordered at the atomic scale, electrons must still random walk across the film thickness, which is typically 10 nm. This may involve 3D diffusion, or sometimes 1D diffusion if a tortuous 1D pathway can be found. (It is unlikely to realize 2D diffusion in our measurement set up.) These different dimensionalities will manifest themselves in the quantum transport phenomena presented in this thesis.

1.1.2. Drude Conductivity

Impurity and phonon scattering of electrons gives rise to residual electrical resistance at zero temperature. This, too, involves a random walk process, in which the random walk step is the mean free path l an electron travels between two consecutive (elastic) scattering events. Here, $l = v_F\tau$, where v_F is the Fermi velocity and τ is the relaxation time of electron momentum. A good metal with a sample size L satisfies $\lambda_F \ll l \ll L$ (Fig. 1.1), i.e., electrons undergo moderate scattering along their transport pathway. It can be shown by the Boltzmann formulation [17] that conductivity σ in a spherical Fermi surface is

$$\sigma = \frac{S_F e^2 l}{12\pi^3\hbar} \tag{1.1}$$

Applying surface area $S_F = 4\pi k_F^2$, mean free path $l = v_F\tau$, and 3D electron density $n = k_F^3/3\pi^2$ [18] to Eq. (1.1), one obtains Drude conductivity

$$\sigma_D = \frac{ne^2\tau}{m^*} = \frac{ne^2 l}{m^* v_F} = \frac{e^2}{\hbar}\frac{n}{k_F^2}k_F l \tag{1.2}$$

where m^* is the effective mass. The 3D conductivity σ_D in Eq. (1.2) has the unit of $(\Omega\cdot\mathrm{m})^{-1}$. More generally, practical conductivity may be expressed in the unit of $(e^2/h)L^{2-d}$, which becomes Ω^{-1} in 2D and $\Omega^{-1}\cdot\mathrm{m}$ in 1D.

In the Drude regime, l is much longer than λ_F ($l \gg \lambda_F$, or $p_F l \gg \hbar$). Moreover, wavefunctions have already dephased before each new collision occurs, i.e., $l > L_\phi$. Therefore, there is very little quantum effect in this regime, and considering electrons as classical particles one can also obtain the Drude conductivity from the classical collision model. The quan-

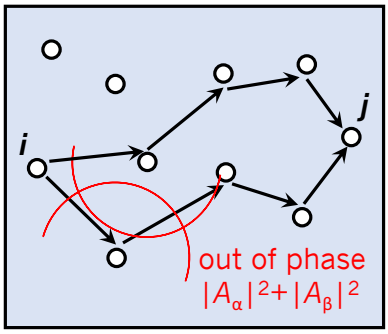

Figure 1.1: Schematic electron trajectory in Drude transport regime when $\lambda < L_\phi \ll l \ll L$. Spherical scattered waves have random phase, their interference is unimportant.

tum interference between scattered electron waves is unimportant in this case because the spherical waves scattered by different centers have random phases as depicted in Fig. 1.1 [4]. The probability p of an electron starting at point i to reach point j can be calculated using the amplitude A_α of each path α connecting i and j

$$p = |\sum_\alpha A_\alpha|^2 = \sum_\alpha |A_\alpha|^2 + \sum_{\alpha,\beta} A_\alpha A_\beta^* \tag{1.3}$$

Because of the random phase between α and β, the second term in Eq. (1.3) can be ignored and the total intensity is the simple sum of the intensities of the two paths: $|A_\alpha|^2 + |A_\beta|^2$ [19]. This is the classical picture of electron transport before the 1979 papers of Abrahams, Anderson, Licciardello, and Ramakrishnan [16], and of Altshuler and Aronov [20, 21].

1.1.3. Coherent Backscattering of Diffusive Electrons: Weak Localization

As the lattice becomes more disordered with stronger and stronger random potential, l decreases and eventually approaches λ_F. In this limit, Anderson localization emerges and electron diffusion vanishes. This is also the limit of minimum metallic conductivity, since it is not possible to maintain a wave-like electron with $k_F l < 1$ as pointed out by Ioffe and Regel [22]. This Ioffe-Regel criterion can be alternatively stated as: It is not possible for a wave-like electron to have more than one elastic scattering within one atomic spacing a_0, i.e., $l \geq a_0$. Applying $k_F l = \pi$ and $l = a_0$ into Eq. (1.2), Mott found the minimum metallic

conductivity $\sigma_{\min} = e^2/3\hbar a_0$. For $a_0 = 3$Å, $\sigma_{\min} \sim 2800$ $(\Omega\text{cm})^{-1}$ [7].

While the Anderson transition to strongly localized insulator and the breakdown of a conductor at the minimum metallic conductivity were well understand, it came as a surprise in late 1970s (20 years after Anderson's localization theory) that electrons in metals are also weakly localized [1, 23, 21]. What is remarkable in this case is that even though l is still well beyond the regime of strong localization ($l \sim \lambda_F$), enhanced quantum interference [2] can already cause a monotonic resistance increase as the temperature lowers. This is called *weak localization* (WL), because it may be regarded as a precursor to strong localization (Fig. 1.2). In this regime, which may be termed the (quantum) diffusive transport regime, electrons again random walk as a result of multiple scattering, but unlike in the Drude regime they now satisfy $l < L_\phi$, i.e., the random walk distance is short compared to the dephasing length. Therefore, diffusive electrons may preserve their phase coherence over a long distance. This may even be the case under inelastic scattering, because if inelastic collision can only cause a very small energy change, then over a sufficiently short time and within the uncertainty principle the initial and the final states are still indistinguishable and may be regarded as having the same phase. Interference phenomena can then take place, and one of them has the effect of causing the conductivity to decrease.

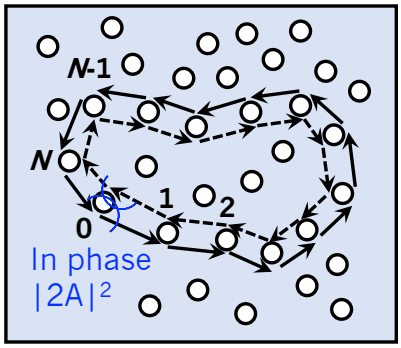

Figure 1.2: Schematic self-crossing electron trajectory of diffusive electrons when $\lambda < l < L_\phi \ll L$. Phase coherence is preserved in the backscattering direction between time-reversed loops, which interfere constructively.

This is clear from considering the loops with a self-crossing trajectory such as the one in Fig. 1.2. Two waves propagating in the opposite directions will accumulate the same phase difference, so the wave traveling in the direction $0 \to 1 \to 2 \to 3$, ..., $\to N-1 \to N$ returns to 0 in phase with its conjugate time-reversal wave that travels in the opposite direction $0 \to N \to N-1 \to ... \to 2 \to 1 \to 0$. Together, they give rise to an intensity of $|2A|^2$ in Eq. (1.3), which is twice the incoherent intensity, $2|A|^2$. Since such constructive interference enhances the probability of backscattering and favors electron return, it may be regarded as a form of electron localization. Figuratively, it is as if the more coherent medium can "pull" the electron back, thus decreasing the conductivity.

The effect of weak localization (WL) on diffusion and conductivity is dependent on spatial dimensionality d: When random walk takes place along a line ($d = 1$) or on a surface ($d = 2$), path crossing is much more likely than in a body ($d = 3$) in which path crossing may be evaded by going under or going over. This picture is supported by solving the diffusion equation, which gives the density function of a diffusing electron, released at time $t = 0$ from $r = 0$ to be found at distance r at time t [4]

$$P(r,t) = (4\pi Dt)^{-d/2} \exp(-r^2/4\pi Dt) \tag{1.4}$$

Since path crossing is equivalent to finding the electron diffusing back to the origin at any time after its release, over all the trials of random walk, from first trial (at time τ) to the last trial (at time τ_ϕ) before dephasing, one can write its cumulative probability, i.e., the number of times of path crossing, as

$$\int_\tau^{\tau_\phi} P(0,t) l^d \frac{dt}{\tau} = \int_\tau^{\tau_\phi} \frac{l^d}{(4\pi Dt)^{d/2}} \frac{dt}{\tau} \propto \begin{cases} 1 - \sqrt{\dfrac{\tau}{\tau_\phi}} & d = 3 \\ \ln \dfrac{\tau_\phi}{\tau} & d = 2 \\ \sqrt{\dfrac{\tau_\phi}{\tau}} - 1 & d = 1 \end{cases} \tag{1.5}$$

(In analogy to the distinction between l and L_ϕ mentioned above, we can distinguish τ and

time τ_ϕ as follows: τ is the lifetime of the momentum eigenstate, and τ_ϕ is the lifetime of the energy eigenstate [2].) In the above, the diffusivity is given by $D = l^2/\tau d$. Eq. (1.5) predicts much stronger WL in 1D and 2D than in 3D: For $\tau_\phi \to \infty$, the integral is bounded in 3D but unbounded in 1D and 2D. Since τ_ϕ/τ is just the number of jumps in the random walk, it is clear that after the particle will not return to the origin in a 3D discrete lattice unless there are infinite jumps while it will return infinite times in lower dimensions (i.e., the return probability tends to be 1 in 2D and 1D for infinite jumps).

1.2. WL-Dominated Quantum Correction to Conductivity (QCC)

1.2.1. Temperature Dependence of QCC

Quantum correction to conductivity (QCC), $\Delta\sigma^T/\sigma$, may be estimated form the back diffusion probability [4]. To do so, we need to modify Eq. (1.5) in three ways. First, we will replace l by λ_F. This is because Eq. (1.5) is strictly applicable to random walk on a discrete (though not necessarily periodic) lattice, so when the random walker returns to the origin within a distance l, the lattice point must coincide with the origin. For wavelike particles, however, interference between them requires the two particles within one wavelength of each other, which can be much less than l. Second, we will replace l^{d-1} by λ_F^2, or equivalently l^d/τ by $v_F\lambda_F^2$ since $v_F = l/\tau$. This is because experimentally only quai-1D and quasi-2D samples are used. So the actual interference always occurs in 3D within a cross section of λ_F^2 from the returning particle. Third, since the conductivity (or interference probability) across the short dimension (W) of the quasi-1D and quasi-2D samples is the same, we introduce a factor W^{3-d} in the denominator to complete the modification. Therefore, we write the probability of self-crossing path as

$$\int_\tau^{\tau_\phi} P(0,t)\frac{l\lambda_F^2}{W^{3-d}}\frac{dt}{\tau} = \int_\tau^{\tau_\phi} \frac{l\lambda_F^2}{(4\pi Dt)^{d/2}W^{3-d}}\frac{dt}{\tau} \tag{1.6}$$

This gives the following correction to the diffusivity and conductivity

$$\Delta\sigma^T/\sigma \propto -\int_\tau^{\tau_\phi} \frac{l\lambda_F^2}{(4\pi Dt)^{d/2}W^{3-d}}\frac{dt}{\tau} \propto \begin{cases} -\dfrac{\lambda_F^2}{l^2}(1-\sqrt{\dfrac{\tau}{\tau_\phi}}) & d=3 \\ -\dfrac{\lambda_F^2}{lW}\ln\dfrac{\tau_\phi}{\tau} & d=2 \\ -\dfrac{\lambda_F^2}{W^2}(\sqrt{\dfrac{\tau_\phi}{\tau}}-1) & d=1 \end{cases} \tag{1.7}$$

It is common to introduce $\Delta\sigma_2^T = \Delta\sigma^T W$ for 2D conduction, and $\Delta\sigma_1^T = \Delta\sigma^T W^2$ for 1D conduction, and along with $\Delta\sigma^T$ in 3D, they are all subject to quantum corrections in the following way

$$\begin{cases} \Delta\sigma^T \propto -\sigma_o\dfrac{\lambda_F^2}{l^2}(1-\sqrt{\dfrac{\tau}{\tau_\phi}}) & d=3 \\ \Delta\sigma_2^T \propto -\sigma_o\dfrac{\lambda_F^2}{l}\ln\dfrac{\tau_\phi}{\tau} & d=2 \\ \Delta\sigma_1^T \propto -\sigma_o\lambda_F^2(\sqrt{\dfrac{\tau_\phi}{\tau}}-1) & d=1 \end{cases} \tag{1.8}$$

In the above, σ_o is the Drude conductivity, σ_D. This correction is always negative, indicating a decreased conductivity relative to Drude conductivity, hence a precursor to strong localization.

Substituting $\sigma_o = \sigma_D = ne^2\tau/m^* = ne^2 l/m^* v_F$ into the above expressions, and noting $n \sim 1/\lambda_F^3$, $m^* v_F = p$, and $p\lambda_F = h$, we obtain

$$\begin{cases} \Delta\sigma^T \propto -\dfrac{e^2}{h}\dfrac{1}{l}(1-\sqrt{\dfrac{\tau}{\tau_\phi}}) & d=3 \\ \Delta\sigma_2^T \propto -\dfrac{e^2}{h}\ln\dfrac{\tau_\phi}{\tau} & d=2 \\ \Delta\sigma_1^T \propto -\dfrac{e^2}{h}l(\sqrt{\dfrac{\tau_\phi}{\tau}}-1) & d=1 \end{cases} \tag{1.9}$$

Therefore, it is the number of jumps in the random walk that determines the QCC. Note that these corrections have different units in different dimensions, related to l. Also note that such l is correlated to τ in the bracket in the form of $l/\sqrt{\tau}$, which is $\sqrt{D}$. So we can appreciate that when τ_ϕ changes, for example, due to a temperature perturbation, a large

τ or a small l will make a more rapid change in $\Delta\sigma$ in 3D, and vice versa in 1D. Since these changes are relative to the Drude conductivity, it is common to evaluate normalized changes relative to some reference conductivity at low temperatures, which is usually close to the Drude conductivity if the QCC is small.

As mentioned before, the effective dimensionality is determined by comparing the shortest dimension δ with the dephasing length $L_\phi = \sqrt{D\tau_\phi}$, which measures the average distance an electron maintains its phase coherence. For a film whose thickness satisfies $\delta \ll L_\phi$, it supports 2D transport parallel to the film plane; for a wire whose radius satisfies $r \ll L_\phi$, it supports 1D transport along the wire direction. Since L_ϕ is a function of temperature, one sample may cross over from 3D to 2D, or from 3D to 1D, as the temperature lowers.

To quantify the temperature-dependence of QCC, we need to specify τ_ϕ in Eq. (1.9). The phase relaxation time or dephasing time τ_ϕ is primarily determined by various inelastic interactions (with scattering time τ_i) that cause the loss of coherency. Generally, the relaxation time increases with decreasing temperature following a power law, $\tau_i \propto T^{-p}$. For example, $p = 3$ for electron-phonon scattering, and $p = 2/3$ (3D) or $p = 1$ (2D) for electron-electron scattering.

Until now, we have regarded electron as a spinless particle. If its spin is taken into account, the electron wave may acquire an additional phase of π that breaks the time reversal invariance of the wave function when it spin-flips during the spin-spin scattering off a magnetic impurity; this may occur at a frequency $1/\tau_s$. Likewise, it may also suffer spin-orbit scattering off heavy impurity atoms at a frequency of $1/\tau_{so}$. These additional time scales have been incorporated into τ_ϕ by Hikami, Larkin and Nagaoka (known as the HLN theory) [24] as follows.

Electrons in collisions, scattering, or self-crossing conjugate waves all involve a two-electron state. For such states, one can distinguish the singlet state ($J = 0$) that has one antisymmetric spin wave function from the triplet state ($J = 1$) that has three symmetric spin wave

functions. For the singlet spin state, HLN theory found

$$\frac{1}{\tau_\phi} = \frac{1}{\tau_i} + \frac{2}{\tau_s} \tag{1.10}$$

and for *triplet* spin state

$$\frac{1}{\tau_\phi^*} = \frac{1}{\tau_i} + \frac{4}{3\tau_{so}} + \frac{2}{3\tau_s} \tag{1.11}$$

Eq. (1.10)-(1.11) were originally derived by HLN for 2D systems, but they are also valid in other dimensions as demonstrated in other theoretical studies [25, 26, 27] and summarized in the review by Altshuler, Aronov, Gershenson and Sharvin [4]. These results predict that when spin-orbit interaction becomes important, it will cause rapid decay of triplet state's energy eigenstate, but it has no effect on the singlet state. On the other hand, the antisymmetric singlet state has an opposite effect on conjugate-wave interference to that of the symmetric triplet state. These aspects need to be considered quantitatively to assess the overall effect of spin orbit interaction (or magnetic scattering) on quantum correction of conductivity (QCC).

Taking into consideration of singlet and triplet states and summarizing their combined effect on QCC, evaluated by comparing conductivity corrections at two reference temperatures, T_1 and T_2 (typically T_2 taken as 0K), we write the following two equivalent sets results [4]

$$\Delta\sigma^T|_{T_1}^{T_2} = \begin{cases} \dfrac{e^2}{2\pi^2\hbar}\left\{\dfrac{3}{2}\Delta\left[L_\phi^{*-1}\right]|_{T_1}^{T_2} - \dfrac{1}{2}\Delta\left[L_\phi^{-1}\right]|_{T_1}^{T_2}\right\} & d=3 \\ -\dfrac{e^2}{2\pi^2\hbar}\left\{\dfrac{3}{2}\Delta\left[\ln L_\phi^*\right]|_{T_1}^{T_2} - \dfrac{1}{2}\Delta\left[\ln L_\phi\right]|_{T_1}^{T_2}\right\} & d=2 \\ -\dfrac{e^2}{\pi\hbar}\left\{\dfrac{3}{2}\Delta\left[L_\phi^*\right]|_{T_1}^{T_2} - \dfrac{1}{2}\Delta\left[L_\phi\right]|_{T_1}^{T_2}\right\} & d=1 \end{cases} \tag{1.12}$$

$$\Delta\sigma^T|_{T_1}^{T_2} = \begin{cases} \dfrac{e^2}{2\pi^2\hbar\sqrt{D}}\left\{\dfrac{3}{2}\Delta\left[\tau_\phi^{*-1/2}\right]|_{T_1}^{T_2} - \dfrac{1}{2}\Delta\left[\tau_\phi^{-1/2}\right]|_{T_1}^{T_2}\right\} & d=3 \\ -\dfrac{e^2}{2\pi^2\hbar}\left\{\dfrac{3}{2}\Delta\left[\ln\tau_\phi^*\right]|_{T_1}^{T_2} - \dfrac{1}{2}\Delta\left[\ln\tau_\phi\right]|_{T_1}^{T_2}\right\} & d=2 \\ -\dfrac{e^2\sqrt{D}}{\pi\hbar}\left\{\dfrac{3}{2}\Delta\left[\tau_\phi^{*1/2}\right]|_{T_1}^{T_2} - \dfrac{1}{2}\Delta\left[\tau_\phi^{1/2}\right]|_{T_1}^{T_2}\right\} & d=1 \end{cases} \tag{1.13}$$

In the above, the difference (Δ) is taken between T_1 and T_2, the dephasing length of the singlet state is denoted as $L_\phi = D\tau_\phi$ and that of the triplet state as $L_\phi^* = D\tau_\phi^*$. Derivations of Eq. (1.12)-(1.13) can be found in [28, 29] for 1D, [30, 31] for 2D, and [21] for 3D, and 3D, and it directly follows Eq. (1.9) including the connection between l, τ and D established there. Here, following the common notation, we let the conductivity change have units of $(\Omega\cdot\mathrm{m})^{-1}$, Ω^{-1}, and $\Omega^{-1}\cdot\mathrm{m}$ for 3D, 2D, and 1D, respectively. It is now clear that the interference of the singlet term (that contains $L_\phi = \sqrt{D\tau_\phi}$ with a factor of 1/2) has an opposite sign to that of the triplet state (that contains $L_\phi^* = \sqrt{D\tau_\phi^*}$ with a factor of 3/2). As already mentioned above, this opposite sign comes from the opposite symmetries of single and triplet. Its consequence is that the singlet term results in a decrease of resistance (increase of conductivity) as the temperature decreases, which is opposite to what results from the triplet term. Note that if the singlet and triplet states have the same relaxation time, which is possible in the absence of spin-orbit and magnetic scattering, then their combined QCC is still a negative one, with a factor of 1, which is from 3/2—1/2. So, it is just like the WL contribution of spinless electrons. On the other hand, when spin-orbit interaction dominates, the rapid decay of the triplet states makes the triplet term unimportant, leaving only the singlet term, which gives a positive QCC. This is opposite to that of the WL contribution, and for this reason, the singlet contribution is called the *weak antilocalization* contribution or WAL. Note that WAL has only one half the magnitude of WL, which is an important feature when comparing the two.

The two limiting cases of WL and WAL are further discussed below.

(i) Weak Localization (WL): As mentioned before, inelastic scattering time τ_i increases

with decreasing temperature, and follows the power law of T^{-p}. On the other hand, being composition dependent only, neither spin-orbit scattering time τ_{so} nor magnetic scattering (spin-flip) time τ_s is sensitive to temperature. Therefore, in the absence of magnetic impurities and spin-orbit interaction when $\tau_s,\ \tau_{so} \gg \tau_i,\ \tau_\phi^* \approx \tau_\phi \approx \tau_i,\ \Delta\tau_\phi^* = \Delta\tau_\phi = \Delta\tau_i$, Eq. (1.12) becomes

$$\Delta\sigma^{\mathrm{WL,T}} = \begin{cases} \dfrac{e^2}{2\pi^2\hbar}\Delta\left(L_\phi^{-1}\right) = \dfrac{e^2}{2\pi^2\hbar\sqrt{D}}\Delta\left(\tau_i^{-1/2}\right) & d=3 \\ -\dfrac{e^2}{2\pi^2\hbar}\Delta\left(\ln L_\phi\right) = -\dfrac{e^2}{2\pi^2\hbar}\Delta\left(\ln\tau_i\right) & d=2 \\ -\dfrac{e^2}{\pi\hbar}\Delta\left(L_\phi\right) = -\dfrac{e^2\sqrt{D}}{\pi\hbar}\Delta\left(\tau_i^{1/2}\right) & d=1 \end{cases} \tag{1.14}$$

Writing L_ϕ as $aT^{-p/2}$, Eq. (1.14) reduces to the same form of the equations derived by Lee and Ramakrishnan for the spin-zero state [3].

$$\Delta\sigma^{\mathrm{WL,T}} = \begin{cases} \dfrac{e^2}{\hbar\pi^3}\dfrac{1}{a}T^{p/2} & d=3 \\ \dfrac{p}{2}\dfrac{e^2}{\hbar\pi^2}\ln T & d=2 \\ -\dfrac{ae^2}{\hbar\pi}T^{-p/2} & d=1 \end{cases} \tag{1.15}$$

A few important points of WL-induced QCC in Eq. (1.15) should be noted. (a) Except when $d = 3$, $\Delta\sigma^T$ diverges as $T \to 0$. This comes directly from the previous observation that in lower dimensions, a diffusing electron is bound to return to the origin at some point. Therefore, weak localization is much stronger in 1D and 2D than in 3D. (To avoid mathematical difficulty, the reference σ_0 may be chosen at a temperature above 0K.) (b) For all dimensions, $\sigma - \sigma_0$ decreases as T decreases, which justifies the name of weak localization as it implies an increase of resistance. This is expected from the enhanced backscattering probability at lower temperatures. Moreover, since at higher temperatures the metallic resistance has a positive temperature coefficient due to phonon scattering, a resistance minimum $R_{\min}$ must appear at some intermediate temperature $T_{\min}$, which

signals the onset of quantum interference of coherent electrons. This is the case unless the disordered electron system contains magnetic impurities, which may cause the Kondo effect that can also increase the resistance at below the Kondo temperature [32]. (c) For metallic thin films with $d = 2$, Eq. (1.15) predicts $\ln T$ regardless of p, which was taken as the first experimental evidence of WL [33] that was later confirmed in numerous other metallic thin films [34].

(ii) Weak Anti-Localization (WAL): If the spin-orbit interaction is strong, $\tau_{so} \ll \tau_i$, $\tau_\phi^* \approx \tau_{so}$, $\Delta\tau_\phi^* = 0$, Eq. (1.12) becomes

$$\Delta\sigma^{\mathrm{WAL,T}} = \begin{cases} -\dfrac{e^2}{4\pi^2\hbar}\Delta\left(L_\phi^{-1}\right) = -\dfrac{e^2}{4\pi^2\hbar\sqrt{D}}\Delta\left(\tau_i^{-1/2}\right) & d = 3 \\ \dfrac{e^2}{4\pi^2\hbar}\Delta\left(\ln L_\phi\right) = \dfrac{e^2}{4\pi^2\hbar}\Delta\left(\ln \tau_i\right) & d = 2 \\ \dfrac{e^2}{2\pi\hbar}\Delta\left(L_\phi\right) = \dfrac{e^2\sqrt{D}}{2\pi\hbar}\Delta\left(\tau_i^{1/2}\right) & d = 1 \end{cases} \tag{1.16}$$

These results have an identical temperature dependence to that of Eq. (1.15), but they differ by sign. Therefore, the resistance decreases with decreasing temperature, which is opposite to weak localization and thus this contribution may be termed weak anti-localization (WAL) [35]: It negates the effect of weak localization, and causes anti-localization. As mentioned before, the physical origin of the opposite QCC of WAL lies in the antisymmetric nature of the singlet state spin wave function. This is also manifested in another property of quantum particles of spin 0 and spin 1/2: While the former returns to the same state after a rotation of 2π, the latter requires a rotation of 4π to return to the same state—a rotation of 2π will change its sign. Therefore, their interference effects are just the opposite, resulting in oppositely signed QCC.

Starting at a higher temperature when $\tau_i < \tau_{so}$, we see WL initially dominates following Eq. (1.14) but it later yields to WAL in Eq. (1.16) at lower temperatures when $\tau_i > \tau_{so}$. (Recall that τ_{so} is temperature independent.) Because of the opposite signs of their QCC, this crossover is expected to result in a resistance maximum $R_{\max}$, at a temperature $T_{\max} <$

$T_{\min}$. This adds a new feature to QCC, which may be exploited. In a way, the inclusion of spin-orbit interaction is like introducing a "contrast agent" to enhance the features of quantum interference of coherent electrons, which stems from the interference of conjugate waves depicted in Fig. 1.2 regardless of the spin of electrons (both WL and WAL effect comes from interference of conjugate paths.) Such use of contrast agent will be exploited in Chapter 3 to help unravel the QCC mechanisms in nano metals. (See Chapter 3 for details).

1.2.2. Magnetic Dependence of QCC

We next consider WL/WAL QCC under a magnetic field, i.e., the *magnetoresistance* (MR) caused by interference of conjugate waves. The magnetic field destroys the time-reversal symmetry of the self-crossing trajectories by introducing an additional *Aharonov-Bohm phase*

$$\Delta\phi = 2\pi\frac{\Phi}{\Phi_0} \tag{1.17}$$

between the two conjugate loops. Here, Φ is the enclosed magnetic flux and $\Phi_0 = h/2e$ is the magnetic flux quantum, which is a fundamental constant. As first pointed out by Altshuler and Aronov [36], the Φ_0 above is only half of the original value derived by Aharonov and Bohm [37], and this is as if the electron has a charge $2e$. That an electron has a charge $2e$ is well-known in superconductors because of Cooper pairs [38]. But it is also true in WL because one must consider the conjugate path, which is like a time-reversed path, thus forming a pair of charge $2e$ that effectively encircles $2\Phi_0$ [39]. So the interfering electron waves will cross the paths at least twice, although more, like 4 times and 6 times, are also theoretically possible.

Alternatively, the above concept can be understood from the solution of the diffusion equation for a particle-particle pair or a particle-hole pair, the latter obtained by allowing time reversal for one of the particles in the particle-particle pair. The effective mass and charge in diffusion can be seen as follows. In the solutions of particle-particle diffusion or particle-hole diffusion, there is a pole at $D\boldsymbol{q}^2 = i\omega$, where ω is the frequency and the right hand

side can be further generalized to include scattering due to impurities, spins, or spin-orbit interaction by letting $1/\omega$ to include additional relaxation times τ_i, τ_s and τ_{so}. Equating $(\hbar \boldsymbol{q})^2/2m^* = \boldsymbol{p}^2/2m^*$ to $\hbar\omega$, where p is the momentum, we find $m^* = \hbar/2D$. If we further introduce the vector potential in the diffusion limit

$$\hbar \left\{ D \left[\boldsymbol{q} - (2e/c)\boldsymbol{A} \right]^2 - i\omega + 1/\tau_\phi \right\} C_w(\boldsymbol{r}, \boldsymbol{r'}) = \delta(\boldsymbol{r} - \boldsymbol{r'}) \tag{1.18}$$

where $\boldsymbol{q}$ is the momentum operator, we can see that the effective charge is $2e$ for both the particle-particle channel and the particle-hole channel. Therefore, the effective charge is $2e$ when considering quantum interference of coherent diffusive electrons, and their effective mass can be directly obtained from the random-walk diffusivity D! (As a quick check of the above result, we use $D = v_F^2\tau$, then $m^* = \hbar/2D = (\hbar/\tau)/2v_F^2 = 2\Delta E/2v_F^2$. So, if $\Delta E = mv_F^2$, we recover $m^* = m$.)

In principle, the interference originated from the phase difference should oscillate as the magnetic field is varied. However, since the magnetic fluxes of different electron pathways (loops) are all different, the overall interference effect is randomized and comes to zero. (We shall see, in a later section, that magnetoresistance will indeed oscillate when there is only one loop, which was first predicted by Altshuler, Aronov and Spivak [36], and experimentally realized by Sharvin and Sharvin [40]. In this thesis, we will report such experiment in Chapter 4 using a nano loop of a size of ~ 7 nm.) Such self-cancellation is essentially complete when the average loop of conjugate waves allows $\Phi/\Phi_0 \cong 1$. Setting the critical loop radius as L_B, called the magnetic length, we have

$$L_B = \sqrt{\frac{\Phi_0}{\pi B}} = \sqrt{\frac{\hbar}{eB}} \tag{1.19}$$

which is $L_B \approx 25.6/\sqrt{B}$ nm for B in Tesla. Therefore, if L_B falls below the dephasing length L_ϕ, we expect the external magnetic field to suppress the WL/WAL QCC effect, and a significant MR will arise. It follows that under a constant field, the MR becomes more prominent as the temperature decreases. Likewise, at a constant temperature, the

MR becomes more prominent as the field increases. It also follows that if the QCC is dominated by WL, then the MR is *negative*. Conversely, if the QCC effect is dominated by WAL, then the MR is positive. The contrasting WL/WAL MR was first demonstrated by Bergmann in the study of Mg thin film with and without a thin layer of surface-coated Au [2]. As more spin-orbit scattering is caused by surface Au, the negative WL-MR turns into a positive WAL-MR. It was also found that as magnetic field increases further, the WAL-MR eventually gives way to WL-MR. This is understandable from the following argument: (i) The essential magnetic effect is to suppress WAL's and WL's QCC, so at high field, both QCC are completely suppressed; (ii) the WAL's QCC is only half the magnitude of WL's QCC, so on the way to high field and full suppression, it is WAL-MR that is gone first leaving some residual WL-MR. More on this will be given later following the presentation of theoretical predictions.

One remarkable feature of WL-MR is that it occurs at classically weak fields. This is because the crossover of L_B and L_ϕ occurs at

$$B_\phi = \frac{\hbar}{4eD\tau_\phi} \tag{1.20}$$

For $\sqrt{D\tau_\phi} = L_\phi = 0.1$ μm in a typical mesoscopic sample, $B_\phi \approx 2000$ G $= 0.2$ T, which is classically week. However, since the sample size of nano metals is orders of magnitude smaller, one need to reexamine this aspect when designing experiments to probe their MR.

We now examine the quantitative theory of WL/WAL-MR, $\Delta\sigma^{\mathrm{B}}$, defined as $\sigma(B,T) - \sigma(0,T)$. This was given by Hikami, Larkin and Nagaoka [24] and by Altshuler, Larkin, Aronov, Khmelnitskii, and Lee [41].

For $\boldsymbol{d = 1}$ (thickness δ and wire width $W \ll L_\phi, L_\phi^*, L_B$) [42]

$$\Delta\sigma^{\mathrm{B}}_{1\mathrm{D}} = \frac{e^2}{\pi\hbar}\left[\frac{3}{2}\Delta L_\phi^*(B) - \frac{1}{2}\Delta L_\phi(B)\right] \tag{1.21}$$

The above result has the unit of $\Omega^{-1}\cdot$m. In the above, the difference (Δ) is taken between

finite field and zero field, and the field-dependent diffusion length can be calculated from

$$\frac{1}{L_\phi(B)^2} = \frac{1}{D\tau_\phi} + \frac{1}{3}(\frac{W}{L_B^2})^2 \tag{1.22}$$

$$\frac{1}{L_\phi^*(B)^2} = \frac{1}{D\tau_\phi^*} + \frac{1}{3}(\frac{W}{L_B^2})^2 \tag{1.23}$$

For quasi-1D wires, $W \ll L_B$, so the second term in Eq. (1.22) that contains magnetic field B vanishes, which renders L_ϕ and L_ϕ^* field-independent thus $\Delta L_\phi = \Delta L_\phi^* = 0$. Therefore, $\Delta\sigma_{\rm 1D}^{\rm WL,B} = 0$ in Eq. (1.21). The zero-MR of quasi-1D samples can be explained by self-cancellation: In a quasi-1D sample, electrons will bounce back and forth from the wall many times before completing a dephasing length, and the self-crossing paths will form many loops of different orientations—defined by the right-handed rule. Therefore, the magnetic fluxes received by these loops are of many signs and magnitude, which sum to almost nothing.

For $\boldsymbol{d = 2}$ (thickness $\delta \ll L_\phi, L_\phi^*, L_B$), $\Delta\sigma_{\rm 2D}^{\rm B}$ is orientation-dependent, so we define $B_\perp$, the B component perpendicular to the motion of electrons, and $B_\parallel$, the B component parallel to the motion of electrons [2, 42].

$$\begin{aligned}\Delta\sigma_{\rm 2D}^{\rm B_\perp} &= \frac{e^2}{2\pi^2\hbar}\left\{\frac{3}{2}f_2(4\frac{L_\phi^{*2}}{L_{B_\perp}^2}) - \frac{1}{2}f_2(4\frac{L_\phi^2}{L_{B_\perp}^2})\right\} \\ &= \frac{e^2}{2\pi^2\hbar}\left\{\frac{3}{2}f_2(\frac{4De\tau_\phi^*}{\hbar}|B_\perp|) - \frac{1}{2}f_2(\frac{4De\tau_\phi}{\hbar}|B_\perp|)\right\}\end{aligned} \tag{1.24}$$

$$\begin{aligned}\Delta\sigma_{\rm 2D}^{\rm B_\parallel} &= \frac{e^2}{2\pi^2\hbar}\left\{\frac{3}{2}\ln(1+\frac{\delta^2 L_\phi^{*2}}{3L_{B_\parallel}^4}) - \frac{1}{2}\ln(1+\frac{\delta^2 L_\phi^2}{3L_{B_\parallel}^4})\right\} \\ &= \frac{e^2}{2\pi^2\hbar}\left\{\frac{3}{2}\ln(1+\frac{\delta^2 De^2\tau_\phi^*}{3\hbar^2}{B_\parallel}^2) - \frac{1}{2}\ln(1+\frac{\delta^2 De^2\tau_\phi}{3\hbar^2}{B_\parallel}^2)\right\}\end{aligned} \tag{1.25}$$

The above results have the unit of Ω^{-1}. In the above, $f_2(x) = \ln x + \psi(1/2 + 1/x)$, and ψ is the digamma function. When H has an inclined angle θ with respect to the plane of

film (current direction), both Eq. (1.24) and Eq. (1.25) must be used with $H_{\|} = H\cos\theta$, $H_{\perp} = H\sin\theta$, and τ_{ϕ}^{-1} replaced by $\tau_{\phi}^{-1} + \tau_{H}^{-1}$, where $\tau_H = 3L_{B_{\|}}^4/DW^2$.

For $\boldsymbol{d = 3}$, MR is orientation-independent [25].

$$\begin{aligned}\Delta\sigma_{3\mathrm{D}}^{\mathrm{B}} &= \frac{e^2}{2\pi^2\hbar L_B}\left\{\frac{3}{2}f_3(4\frac{L_\phi^{*2}}{L_B^2}) - \frac{1}{2}f_3(4\frac{L_\phi^2}{L_B^2})\right\} \\ &= \frac{e^2}{2\pi^2\hbar}\sqrt{\frac{e|B|}{\hbar}}\left\{\frac{3}{2}f_3(\frac{4De\tau_\phi^*}{\hbar}|B|) - \frac{1}{2}f_3(\frac{4De\tau_\phi}{\hbar}|B|)\right\} \end{aligned} \tag{1.26}$$

This result has the unit of $(\Omega\cdot\mathrm{m})^{-1}$. In the above, $f_3(x) = \sum_{n=0}^{\infty}\{2(\sqrt{n+1+1/x} - \sqrt{n+1/x}) - 1/\sqrt{n+1/x+1/2}\}$. (Model fitting in the whole x range can be done using the algebraic approximation $f_3(x) \approx 2[(2+1/x)^{1/2} - (1/x)^{1/2}] - [(1/2+1/x)^{-1/2} + (3/2 + 1/x)^{-1/2}] + 1/48(2.03+1/x)^{-3/2}$ [27].)

Eq. (1.24) (Here, $B = B_{\perp}$ for the perpendicular field only) and Eq. (1.26) can be approximated in the following limits.

(i) WL-MR: Here τ_{so}, $\tau_s \gg \tau_i$, $\tau_\phi^* \approx \tau_\phi \approx \tau_i \propto T^{-p}$. Thus, Eq. (1.24) becomes

$$\Delta\sigma_{2\mathrm{D}}^{\mathrm{WL,B}} = \frac{e^2}{2\pi^2\hbar}f_2(\frac{4De\tau_\phi}{\hbar}|B|) \tag{1.27}$$

and Eq. (1.26) becomes

$$\Delta\sigma_{3\mathrm{D}}^{\mathrm{WL,B}} = \frac{e^2}{2\pi^2\hbar L_H}f_3(4\frac{L_\phi^2}{L_B^2}) = \frac{e^2}{2\pi^2\hbar}\sqrt{\frac{e|B|}{\hbar}}f_3(\frac{4De\tau_i}{\hbar}|B|) \tag{1.28}$$

Since the conductivity increases, this WL-MR is negative. It can be understood as follows: As time reversal symmetry is destroyed by a magnetic field, so is the WL QCC, which amounts to an increase in conductivity and a negative MR.

(ii) WAL-MR: When $\tau_{so} \ll \tau_i$,

$$\Delta\sigma_{2\mathrm{D}}^{\mathrm{WAL,B}} = -\frac{e^2}{4\pi^2\hbar}f_2(\frac{4De\tau_\phi}{\hbar}|B|) \tag{1.29}$$

$$\Delta\sigma_{3D}^{WAL,B} = -\frac{e^2}{4\pi^2\hbar L_B} f_3(4\frac{L_\phi^2}{L_B^2}) = -\frac{e^2}{4\pi^2\hbar}\sqrt{\frac{e|B|}{\hbar}} f_3(\frac{4De\tau_i}{\hbar}|B|) \tag{1.30}$$

Since the conductivity change is negative, this WAL-MR is positive. It can be understood as follows: As time reversal symmetry is destroyed by a magnetic field, so is the WAL QCC, which amounts to a decrease in conductivity and a positive MR.

While the negative WL-MR or positive WAL-MR may dominate at low field, it turns out the MR is always negative in the large field limit [2]. Therefore, when WAL is present, the MR features a characteristic crossover at a magnetic field that related to the relative magnitude of τ_{so}, τ_ϕ and τ_ϕ^*. Mathematically, this is best understood by returning to Eq. (1.24) and (1.26), where we see that at large field both f_2 and f_3 approach their respective saturating asymptotes (being $\ln x$ for f_2 and a constant for f_3, see below for details). So the first term in Eq. (1.24) and (1.26) with a larger prefactor of 3/2 always dominate, giving a positive magnetoconductance and a negative magnetoresistance at large field.

Lastly, the WL/WAL MR takes characteristic asymptotic forms at low field and high field, summarized below.

(i) Low field approximation: when $x, x^* \ll 1$, $f_2(x) \approx x^2/24 \propto \tau_\phi^2 B^2$ and $f_2(x^*) \approx (x^*)^2/24 \propto (\tau_\phi^*)^2 B^2$ in 2D; meanwhile $f_3(x) \approx x^{3/2}/48 \propto (\tau_\phi)^{3/2} B^{3/2}$ and $f_3(x^*) \approx (x^*)^{3/2}/48 \propto (\tau_\phi^*)^{3/2} B^{3/2}$ in 3D. Applying these asymptotic forms into Eq. (1.24) and Eq. (1.26), we find $\Delta\sigma_{2D}^{B} \propto \left(3(\tau_\phi^*)^2 - \tau_\phi^2\right) B^2$ and $\sigma_{3D}^{B} \propto \left[3(\tau_\phi^*)^{3/2} - \tau_\phi^{3/2}\right] B^2$. Therefore, the low field MR should be of a parabolic shape and its magnitude is temperature-dependent because τ_ϕ and τ_ϕ^* are.

(ii) High field approximation: when $x, x^* \gg 1$, $f_2(x) \approx \ln x$, $f_2(x^*) \approx \ln x^*$, and they are $\propto \ln(|B|)$ in 2D; meanwhile $f_3(x) \approx f_3(x^*) \approx 0.605$ in 3D. Referring to Eq. (1.24) and Eq. (1.26), we find $\Delta\sigma_{2D}^{B} \propto \ln(|B|)$ and $\Delta\sigma_{3D}^{B} \propto B^{1/2}$, both independent of temperature.

1.3. Altshuler-Aronov-Spivak Oscillation in Disordered Conductors

A vivid manifestation of quantum interference between electron waves is given by the Altshuler-Aronov-Spivak (AAS) oscillation originated from the Aharonov-Bohm effect for a pair of electrons in the weak localization regime. As discussed in the preceding section, the phase difference between the two conjugate trajectories generated by a magnetic field B is given by $\Delta\phi = 2\pi\Phi/\Phi_0$, where $\Phi_0 = h/2e = 2.07 \times 10^{-7}$ G·cm^2 and Φ is the magnetic flux. As Φ varies by H, $\Delta\phi$ will oscillate with a period of $h/2e$. Since phase difference can influence electrical conductivity through backscattering interference, conductivity oscillation in a magnetic field is observed when a single loop is provided. Having more than one loop, however, will generally cause cancellation, making the oscillation much weaker as shown in Eq. (1.21).

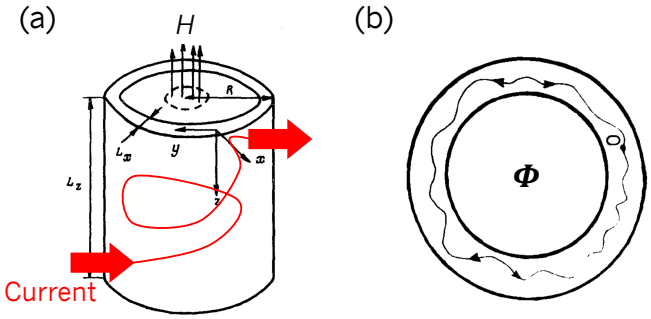

Figure 1.3: Aharonov-Bohm effect in the metallic film cylinder. (a) Schematic of the cylindrical sample; (b) Constant magnetic flux Φ for all conjugate waves returning to point 0.

Remarkable MR oscillation with a period of $h/2e$ was first predicted by Altshuler, Aronov and Spivak [36] for doubly connected metallic structures such as rings and cylinders (Fig. 1.3a) under a magnetic field parallel to its axis. As depicted in Fig. 1.3b, in the thin-walled hollow cylinder all pairs of conjugate electron waves return to the initial point 0 from different paths will have the same phase of $2\pi\Phi/\Phi_0$. Indeed, $\Phi = N\Phi_0 = Nh/2e$, $\Delta\phi = N2\pi$, for any N that is an integer, after N revolutions of electrons. At small field, $B \cong 0$ and $\Delta\phi \cong 0$, the constructive interference between waves will increase the probability of finding electrons at

the starting point and decease the conductivity. Correspondingly, magnetoresistance should start at zero and become negative as a field is imposed. The opposite holds if there is strong spin-orbit interaction: It will shift the oscillation phase by π [43].

As derived in [36], if both the thickness W and height b of the cylinder are small compared with the phase relaxation length L_ϕ, i.e., for a ring with radius r, the change of conductance of a unit length $G_1 = \sigma A$ (in the unit of $\Omega^{-1}\cdot$m) is given by

$$\Delta G_1 = -\frac{e^2 L_\phi}{\pi\hbar} \frac{\sinh(\frac{2\pi r}{L_\phi})}{\cosh(\frac{2\pi r}{L_\phi}) - \cos(2\pi\frac{\Phi}{\Phi_0})} \tag{1.31}$$

For a cylinder of a radius r and height b, the conductance change in the unit of Ω^{-1} is

$$\Delta G = -\frac{e^2}{\pi^2\hbar}\frac{2\pi r}{b}\left\{\ln\frac{L_\phi(H)}{L_\phi(0)} + 2\sum_{n=1}^{\infty}\left[K_0\left(n\frac{2\pi r}{L_\phi(H)}\right)\cos\left(2\pi n\frac{\Phi}{\Phi_0}\right) - K_0\left(n\frac{2\pi r}{L_\phi(0)}\right)\right]\right\} \tag{1.32}$$

where $K_0(x)$ is the Macdonald function ($K_0(x) \sim \exp(-x)$ when $x > 1$). In practice, often only $n = 1$ is used to calculate Eq. (1.32). Note that Eq. (1.32) considers non-zero field inside the cylinder with a wall thickness W, which results in the field dependence of $L_\phi(H)$ that is given by

$$\frac{1}{L_\phi(H)^2} = \frac{1}{D\tau_\phi} + \frac{1}{3}(\frac{W}{L_H^2})^2 \tag{1.33}$$

Moreover, Eq. (1.32) is derived when the magnetic field direction is parallel to the axis of the cylindrical samples. If there is a small angle θ between the two axes, W in Eq. (1.33) should be replaced by [44]

$$W^{*2} = W^2\cos^2\theta + 6r^2\sin^2\theta \tag{1.34}$$

Both Eq. (1.33) and Eq. (1.34) predict a monotonic decrease of resistance as the field increases in addition to the oscillatory MR.

Several months after the theoretical prediction of the AAS oscillation, the first experimental

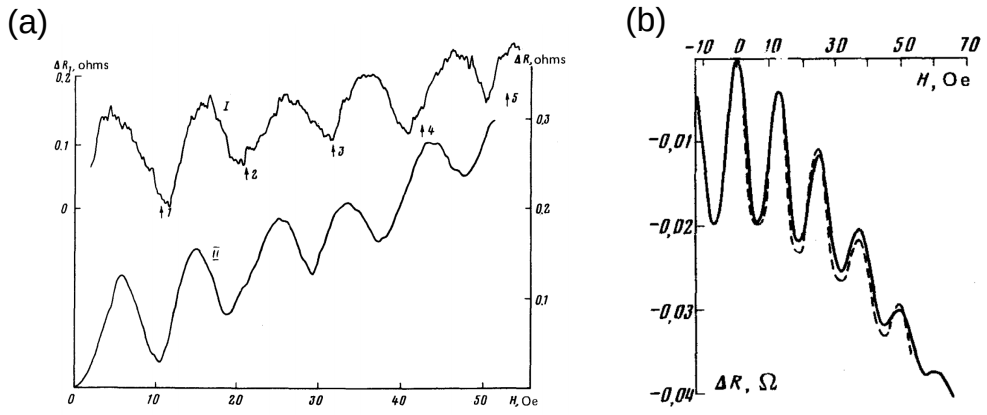

Figure 1.4: Experimental results of Aharonov-Bohm oscillation of magnetoresistance in cylinders made of and (a) magnesium with spin-orbit interaction ($\tau_\phi \gg \tau_{so}$) and (b) lithium without spin-orbit interaction. Note oscillation in (b) has the opposite phase to (a).

demonstration was published by Sharvin and Sharvin [40], who performed experiment on Mg cylinder, which has spin-orbit interaction (Fig. 1.4a). This study confirmed the predicted oscillation of $h/2e$ instead of h/e as in the standard Aharonov-Bohm oscillation. It was followed by a more direct confirmation obtained by Altshuler et al [45] on Li samples, which has no spin-orbit interaction (Fig. 1.4b, showing experimental data in excellent agreement with prediction of Eq. (1.32) given as the dashed curve). Confirmation of Eq. (1.31) and Eq. (1.32) was also found in later experiment of single- and multi-walled carbon nanotubes [46, 47], among others.

1.4. Electron-Electron-Interaction-Dominated QCC

In a periodic system, electrons in a Fermi liquid are plane waves (Bloch waves). Their collisions are occurring at the Fermi surface, and they involve a large momentum change (which must be a lattice momentum) but a small energy change ($\sim k_BT$ because it is limited by Fermi-Dirac statistics, in that final states at energy more than k_BT away from the Fermi surface are not available.) These electrons do not see each other very much and they spend little time together during the collision. Their quasi-particles are stable for a long time, because the probability for inelastic collision is small in the phase space, as the

collision must satisfy momentum conservation as well as staying on the Fermi surface. If the excitation energy of a quasi-particle is ϵ ($\epsilon \sim k_B T$ at the maximum), then the energy spread (uncertainty or decay rate) of the quasi-particle is of the order of $\epsilon(\epsilon/E_F)$, which is small. This is why quasi-particles are rather stable in a Fermi liquid despite strong interactions.

In a disordered system, diffusing electrons must take a much longer time before they can leave each other after each collision (encounter.) That is, two colliding electrons after each encounter are effectively "stuck together" until they find a way out by tortuous random-walking. (See Fig. 1.5a.) This is especially true in 3D. Since the two electrons that come into each other (encounter) are physically close in space, momentum and energy, and they will stay so for a long duration, their interaction is much enhanced and is qualitatively different from that of Bloch-wave electrons in a periodic system. The phase space allowed for electron-electron scattering is also much larger, because the scattering allows small momentum transfer now that the restriction of lattice momentum is no longer relevant. It further includes both large energy transfer ($\epsilon \sim k_B T$) and small energy transfer ($\epsilon \ll k_B T$). This gives rise to a much larger energy spread than $\epsilon(\epsilon/E_F)$, possibly reaching $k_B T$. Such larger energy spread (decay rate) implies a much shorter lifetime of quasi-particles.

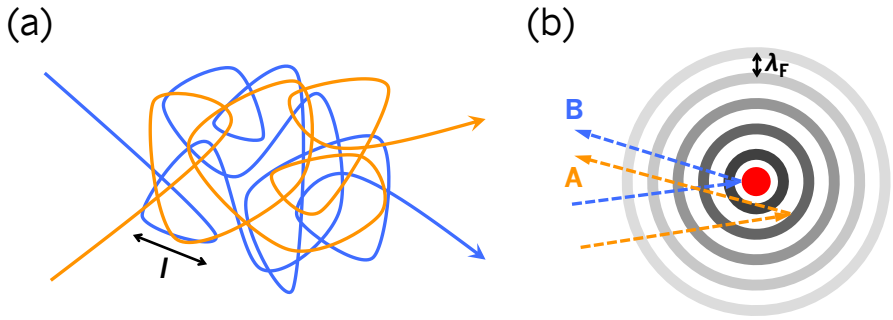

Figure 1.5: Electron-electron interaction in disordered metals. (a) Trajectories of two coherent electrons trapped in their random walks with small mean free path l experiencing enhanced interaction. (b) Scattering of a given electron by the Friedel oscillation of the rest of electrons. Interference between path A and path B coherently contribute to the enhanced backscattering, thus reducing the conductivity.

The electron-electron interaction (EEI) involving small energy transfer is equivalent to the interaction of an electron with the fluctuating EM fields produced by all other electrons in the disordered system. As shown by Zala, Narozhny, and Aleiner for 2D systems [48], the quantum corrections due to EEI amount to the effect of elastic scattering by the Friedel oscillation of the rest of the electrons, which produces a static self-consistent potential and result in back scattering. The physical picture of Friedel oscillation in Fig. 1.5b resembles a diffraction grating, in which Bragg-scattered electrons interfere with each other. More specifically, as shown in Fig. 1.5b, path A corresponds to the scattering by the Friedel oscillation and path B is the scattering off the impurity itself. Since the extra phase accumulated along path A, e^{i2kR} (R being the length of the extra path interval relative to B), is canceled by the phase of the Friedel oscillation $e^{-i2k_F R}$, the two paths A and B are coherent, and the probability of backscattering is enhanced in exactly the same way as that of conjugate waves in WL. This effect decreases with temperature because the Friedel oscillation is smeared at higher temperature. Interestingly, Zala, Narozhny and Aleiner found that the above picture works not only in the diffusive regime ($L_T = \sqrt{D\tau_T} = \sqrt{\hbar D/k_B T} \gg l$) but also in the ballistic regime ($L_T = \sqrt{D\tau_T} = \sqrt{\hbar D/k_B T} \ll l$). So the EEI of a Fermi liquid in the entire disordered system can be understood on a unified footing.

1.4.1. Temperature Dependence of QCC

Like in the case of WL/WAL, there are two spin-dependent terms from EEI contributing to the QCC; they both involve a thermal diffusion length $L_T = \sqrt{D\tau_T} = \sqrt{\hbar D/k_B T}$. The triplet term is the Hartree term, or direct term, which has a negative sign in its conductivity correction, and the singlet term is the Fock term, or exchange term, which has a positive sign in the conductivity correction [3]. Therefore, the electrical resistance may either increase or decrease with decreasing temperature depending on the strength of EEI, which is characterized by the Fermi-liquid parameter $\tilde{F}_\sigma$. Calculation by Altshuler,

Khmelnitskii, Larkin, and Lee [3, 41] gives the following temperature-dependent QCC,

$$\Delta\sigma^{\mathrm{EEI,T}} = \begin{cases} \dfrac{e^2}{\hbar}\dfrac{1}{4\pi^2}\dfrac{1.3}{\sqrt{2}}\left(\dfrac{4}{3}-\dfrac{3}{2}\tilde{F}_\sigma\right)\dfrac{1}{L_T} = \dfrac{e^2}{\hbar}\dfrac{1}{4\pi^2}\dfrac{1.3}{\sqrt{2}}\left(\dfrac{4}{3}-\dfrac{3}{2}\tilde{F}_\sigma\right)\sqrt{\dfrac{k_BT}{\hbar D}} & d=3 \\ -\dfrac{e^2}{\hbar}\dfrac{1}{4\pi^2}\left(2-\dfrac{3}{2}\tilde{F}_\sigma\right)\ln L_T = -\dfrac{e^2}{\hbar}\dfrac{1}{4\pi^2}\left(2-\dfrac{3}{2}\tilde{F}_\sigma\right)\ln\dfrac{\hbar D}{k_BT} & d=2 \\ -\dfrac{e^2}{\hbar}\dfrac{1}{2\sqrt{2}\pi}\left(4-\dfrac{3}{2}\tilde{F}_\sigma\right)L_T = -\dfrac{e^2}{\hbar}\dfrac{1}{2\sqrt{2}\pi}\left(4-\dfrac{3}{2}\tilde{F}_\sigma\right)\sqrt{\dfrac{\hbar D}{k_BT}} & d=1 \end{cases} \quad (1.35)$$

The results have the units of $(\Omega\mathrm{m})^{-1}$, Ω^{-1}, and $\Omega^{-1}\cdot\mathrm{m}$, respectively. Here, $\tilde{F}_\sigma = 8(1+F/2)\ln(1+F/2)/F - 4$ when $d=2$, $\tilde{F}_\sigma = -[32/d(d-2)][1+dF/4) - (1+F/2)^{d/2}]$ when $d \neq 2$, F being the average of interaction on the Fermi surface from the Hartree term. While Eq. (1.35) predicts different temperature dependence of $T^{1/2}$, $\ln T$, and $T^{-1/2}$ for QCC in 3D, 2D, and 1D, respectively, they all contain an identical set of material parameters: D and $\tilde{F}_\sigma$. For simplicity, it can be rewritten as

$$\Delta\sigma^{\mathrm{EEI,T}} = \begin{cases} \alpha_3\left(\dfrac{4}{3}-\dfrac{3}{2}\tilde{F}_\sigma\right)T^{1/2} & d=3 \\ -\alpha_2\left(2-\dfrac{3}{2}\tilde{F}_\sigma\right)\ln T & d=2 \\ -\alpha_1\left(4-\dfrac{3}{2}\tilde{F}_\sigma\right)T^{-1/2} & d=1 \end{cases} \quad (1.36)$$

where $\alpha_3 = (e^2/\hbar)(1.3/4\pi^2)(k_B/2\hbar D)^{1/2}$, $\alpha_2 = (e^2/\hbar)(1/4\pi^2)$, and $\alpha_1 = (e^2/\hbar)(1/2\pi)$ $(\hbar D/2k_B)^{1/2}$. The formal similarity of Eq. (1.36) with the QCC derived from WL (Eq. (1.15)) is explained by Altshuler and Arnov using a quasiparticle picture: The more diffusion and sticky the electrons are, the more the correction to the effective coupling constant of electron quasiparticles, which leads to their corrections to the kinetic quantities including the conductivity. Therefore, the same integral for back diffusion applies with the appropriate substitution of dephasing time ($\tau_T = \sqrt{\hbar/k_BT}$) or dephasing length ($L_T$). Lastly, spin-orbit interaction, which is not considered in Eq. (1.36), will affect the spin-nonzero triplet (Hartree) term in EEI below a temperature T_0 when $\tau_{so} \ll \hbar/k_BT_0$. This point is not made explicit in the literature, but it follows directly from the time scale argument, and

it affects how different time scales go into different terms: Below T_0, the dephasing time of the triplet is frozen at τ_{so}, so the diffusion length of $J_z = \pm 1$ triplet states is capped by $\sqrt{D\hbar/k_B T_0}$ below T_0, thus giving no further increment of QCC as temperature lowers. Therefore, the pre-factors in Eq. (1.36) should be rewritten as 4/3, 2, and 4 for 3D, 2D, and 1D, respectively. In Chapter 3, we will demonstrate such interplay in 3D EEI in several systems that exhibit strong spin-orbit interaction due to Pt dopants.

1.4.2. Magnetic Dependence of QCC

We next consider the effect of magnetic field and quantify EEI-induced magnetoresistance in $d = 2$ and $d = 3$. (Similar to 1D WL/WAL MR, the effect is much weaker in thin wires than it is in bulk samples [49].) As mentioned already, when two electrons collide, both the initial state and the final state are two-electron states, each having a combined spin state J that may either be the singlet state or the triplet state. When a magnetic field is imposed, the $J_z = \pm 1$ terms in the triplet state are split by the Zeeman effect into two energy levels. This splitting changes the effective density of states, which decreases the final state population that is available for the transition from the initial state, hence the electron conductivity in the Kubo formula. This effect gives rise to a positive MR. Since the interaction and the transition are between electrons that are close in energy within $k_B T$, we should normalize $g\mu_B B$ by $k_B T$, and use $\tilde{h} = g\mu_B B/k_B T$ as a new field parameter.

More specifically, the triplet term, which is the one proportional to $\frac{3}{2}\tilde{F}_\sigma$ in Eq. (1.36), is divided under a magnetic field into a spin-zero state, $J_z = 0$ and two spin-one states, $J_z = \pm 1$. The $J_z = 0$ state in the triplet and the singlet term are unaffected by B while there is an effect of $g\mu_B B$ over $k_B T$ for $J_z = \pm 1$. So we can write $\Delta\sigma(B,T) = \Delta\sigma'(T) + \Delta\sigma''(H,T)$: The first term is the field-independent singlet contribution plus $J_z = 0$ triplet contribution (i.e., the Friedel oscillation part) given by

$$\Delta\sigma'(T) = \begin{cases} \alpha_3(\frac{4}{3} - \frac{1}{2}\tilde{F}_\sigma)T^{1/2} & d = 3 \\ \alpha_2(2 - \frac{1}{2}\tilde{F}_\sigma)\ln T & d = 2 \end{cases} \tag{1.37}$$

and the second field-dependent $J_z = \pm 1$ triplet term (i.e., the Zeeman splitting part) can be written as

$$\Delta\sigma''(H,T) = \begin{cases} -0.77\alpha_3\tilde{F}_\sigma T^{1/2} g_3(\tilde{h}) - \alpha_3\tilde{F}_\sigma T^{1/2} & d=3 \\ -\alpha_2\tilde{F}_\sigma g_2(\tilde{h}) - \alpha_2\tilde{F}_\sigma \ln T & d=2 \end{cases} \tag{1.38}$$

Experimentally, we often measure magnetoconductance (or magnetoresistance with an opposite sign) $\Delta\sigma^{\mathrm{B}} = \sigma(B,T) - \sigma(0,T)$, the change of conductivity from zero field at fixed temperature T . From Eq. (1.37) and Eq. (1.38), we get

$$\Delta\sigma^{\mathrm{EEI,B}} = \begin{cases} -0.77\alpha_3\tilde{F}_\sigma T^{1/2} g_3(\tilde{h}) = -\dfrac{e^2}{\hbar}\dfrac{1}{4\sqrt{2}\pi^2}\tilde{F}_\sigma\dfrac{1}{L_T}g_3(\tilde{h}) & d=3 \\ -\alpha_2\tilde{F}_\sigma g_2(\tilde{h}) = -\dfrac{e^2}{\hbar}\dfrac{1}{4\pi^2}\tilde{F}_\sigma g_2(\tilde{h}) & d=2 \end{cases} \tag{1.39}$$

where $g_3(\tilde{h}) = \int_0^\infty d\Omega \frac{d^2}{d\Omega^2}[\Omega N(\Omega)](\sqrt{\Omega+\tilde{h}} + \sqrt{|\Omega-\tilde{h}|} - 2\sqrt{\Omega})$ and $g_2(\tilde{h}) = \int_0^\infty d\Omega \frac{d^2}{d\Omega^2}[\Omega N(\Omega)]$ $\ln|1-\frac{\tilde{h}^2}{\Omega^2}|$. The expressions g_2 and g_3 take two limits:

(i) The low field approximation: When $\tilde{h} \ll 1$ ($g\mu_B B \ll k_B T$), $g_3(\tilde{h}) \approx 0.053\tilde{h}^2$, $\Delta\sigma_{\mathrm{3D}}^{\mathrm{EEI,B}} \propto -T^{-3/2}B^2$; meanwhile, $g_2(\tilde{h}) \approx 0.084\tilde{h}^2$, and $\Delta\sigma_{\mathrm{2D}}^{\mathrm{EEI,B}} \propto -T^{-2}B^2$. This form can be easily justified because g_2 and g_3 are even functions.

(ii) The high field approximation: When $\tilde{h} \gg 1$ ($g\mu_B B \gg k_B T$), $g_3(\tilde{h}) \approx \sqrt{\tilde{h}} - 1.3$, and $\Delta\sigma_{\mathrm{3D}}^{\mathrm{EEI,B}} \propto -\sqrt{|B|} - \alpha_3\tilde{F}_\sigma T^{1/2}$; meanwhile $g_2(\tilde{h}) \approx \ln(\tilde{h}/1.3)$, and $\Delta\sigma_{\mathrm{2D}}^{\mathrm{EEI,B}} \propto -\ln(|B|)$. This form can be justified by having the diffusion distance limited by the magnetic length.

Lastly, the presence of spin-orbit interaction will influence the MR of the 3D EEI origin in the following way. This comes from the fact that such interaction caps the dephasing time of the triplet state at τ_{so} below a crossover temperature T_0 where $\tau_{so} = \hbar/k_B T_0$ (similar to $\tau_{so} = \tau_i \sim T^{-p}$ in WL). Since it is the $J_z = \pm 1$ states in the triplet that are subject to the Zeeman splitting and contribute to the MR, once their characteristic time is capped, their MR contribution changes. This amounts to fixing the temperature prefactor, $T^{1/2}$ in

the $g_3(\tilde{h})$ terms above, to $T_0^{1/2}$. In general, it has an effect of enhancing MR below T_0 by a factor of $(T_0/T)^{1/2}$ in 3D conduction. It has no effect on 2D MR.

Model fitting in the whole field range can be done using the analytical approximation of $g_3(x)$ and $g_2(x)$. For $d = 3$, $g_3(x)$ is given by [50]

$$g_3(x) \approx \begin{cases} 5.6464 \times 10^{-2}x^2 - 1.4759 \times 10^{-3}x^4 + 4.2747 \times 10^{-5}x^6 & \\ -1.5351 \times 10^{-6}x^8 + 6 \times 10^{-8}x^{10} & x \leq 3 \\ 0.64548 + 0.235\delta - 7.45 \times 10^{-4}\delta^2 - 2.94 \times 10^{-3}\delta^3 & \\ +6.32 \times 10^{-4}\delta^4 - 5.22 \times 10^{-5}\delta^5 & 3 \leq x \leq 8 \\ x^{1/2} - 1.2942 - \pi^2 x^{-3/2}/12 - \pi^4 x^{-7/2}/16 & \\ -5\pi^6 x^{-11/2}/32 & x \geq 8 \end{cases} \tag{1.40}$$

where $\delta = x - 4$.

Table 1.1: Comparison of QCC induced by weak localization (WL), weak anti-localization (WAL) and electron-electron interaction (EEI). Only the T and B difference is listed for simplicity. Check Eq. (1.12), (1.24), (1.25), (1.26), (1.35), and (1.39) for details. $\Delta\sigma^{\mathrm{B}}$ that has an angular dependence is marked by ✓.

QQC	1D dependence	2D dependence	3D dependence
$\Delta\sigma^{\mathrm{WL,T}}$	$-T^{-p/2}$	$\ln T$	$T^{p/2}$
$\Delta\sigma^{\mathrm{WAL,T}}$	$T^{-p/2}/2$	$-\ln T/2$	$-T^{-p/2}/2$
$\Delta\sigma^{\mathrm{EEI,T}}$	$-(4 - 3\tilde{F}_\sigma/2)/\sqrt{T}$	$(2 - 3\tilde{F}_\sigma/2)\ln T$	$(4/3 - 3\tilde{F}_\sigma/2)\sqrt{T}$
$\Delta\sigma^{\mathrm{WL,B}}$ (low field)	$T^{-p}B^2$ ✓	$T^{-2p}B^2$ ✓	$T^{-3p/2}B^2$
$\Delta\sigma^{\mathrm{WAL,B}}$ (low field)	$\frac{1}{2}T^{-p}B^2$ ✓	$-\frac{1}{2}T^{-2p}B^2$ ✓	$-\frac{1}{2}T^{-3p/2}B^2$
$\Delta\sigma^{\mathrm{WL,B}}$ (high field)	B^{-1} ✓	$\ln B$ ✓	$B^{1/2}$
$\Delta\sigma^{\mathrm{WAL,B}}$ (high field)	$-\frac{1}{2}B^{-1}$ ✓	$-\frac{1}{2}\ln B$ ✓	$-\frac{1}{2}B^{1/2}$
$\Delta\sigma^{\mathrm{EEI,B}}$ (low field)	N.A.	$-T^{-2}B^2$	$-T^{-3/2}B^2$
$\Delta\sigma^{\mathrm{EEI,B}}$ (high field)	N.A.	$-\ln B$	$-B^{1/2}$

Table 1.1 provides a quick reference to compare QCC induced by different mechanisms

(WL, WAL, and EEI) in different dimensions. Clearly, they may have different signs, temperature dependence, and orientational sensitivity, which may be used to help determine the dominant mechanism.

1.5. Size Effect

The interference phenomena of coherent electrons are obviously sensitive to the length scale, and much research has been devoted to the dimensionality crossover when one or two of the sample dimensions are reduced. However, quantum transport phenomena were rarely studied in nanomaterials because of the difficulty of measurement: 4-point probe is not practical. With the exception of tunneling junctions [51, 52] and some single-molecule junctions [53], there is little known in this area. Our subtraction technique described in Appendix C and [54] allows a definitive measurement of the relative resistance of the nanofilms by out-of-plane current, which opens the possibility of studying these phenomena under perturbations of temperature and magnetic field for the first time.

In nano metals, made of nanosized amorphous insulators that become conducting when their sizes (e.g., the film thickness δ) fall below the localization length ζ, it is possible to achieve very small electron diffusivity because of structural disorders at the atomic level. Yet they achieve metallic conduction because their transport length is less or on the order of ζ. Therefore, they may allow the unthinkable opportunity of studying coherent electrons of insulators, at the nanoscale. Since their structural networks are completely amorphous, the random walk step distance l is of the order of bond length, typically less than 0.5 nm, much shorter than δ. So, 3D random walk of coherent electrons is entirely possible even within a very small transport length of, say 10 nm. (Transport along an essentially 1D path between the two electrodes is also possible.) In nano metals, one may thus anticipate a new size effect that the coherent diffusion distance may be limited by the sample size. Such capping will prevents the crossover from weak localization to strong localization, which happens when L_ϕ exceeds ζ, as has been reported for quasi-1D Si δ-doped GaAs structures at low temperature [55].With this suppressed in nano metals, quantum interference phenomena

should be observable down to 0K.

Suppressed diffusion of electrons is beneficial to observing stronger QCC induced by both EEI and WL. In 3D, as seen from Eq. (1.41) and Eq. (1.42)

$$\Delta\sigma_{3\mathrm{D}}^{\mathrm{EEI,T}} = \frac{1.3}{4\sqrt{2}\pi^2}\left(\frac{4}{3} - \frac{3}{2}\tilde{F}_\sigma\right)\frac{e^2}{\hbar}\frac{1}{L_T} \tag{1.41}$$

$$\Delta\sigma_{3\mathrm{D}}^{\mathrm{WL,T}} = \frac{1}{2\pi^2}\frac{e^2}{\hbar}\frac{1}{L_\phi} \tag{1.42}$$

a larger QCC at shorter diffusion length is predicted. But reduced diffusion is less favorable for observing quantum interference under a magnetic field that involves a magnetic length L_B. This is because

$$\Delta\sigma_{3D}^{\mathrm{WL,B}} = \frac{1}{2\pi^2}\frac{e^2}{\hbar}\frac{1}{L_B}f_3(4\frac{L_\phi^2}{L_B^2}) \tag{1.43}$$

where f_3 being a monotonically increasing function of $L_\phi/L_B \ll 1$ will decrease if L_ϕ decreases. So, weaker MR of the WL (and WAL) origin is expected. This is less a problem for EEI-induced MR, which is mostly unaffected by small D because, as shown before, it originates from the Zeeman splitting characterized by a k_BT-normalized field $\tilde{h} = g\mu_B B/k_BT$

$$\Delta\sigma_{3D}^{\mathrm{EEI,B}} = -\frac{\tilde{F}_\sigma}{4\sqrt{2}\pi^2}\frac{e^2}{\hbar}\frac{1}{L_T}g_3(\frac{g\mu_B B}{k_BT}) \tag{1.44}$$

and the function g_3 that is the counterpart of f_3 depends on $\tilde{h}$ but is independent of diffusion distance. Indeed, the EEI-MR should not saturate even if the diffusion length is capped by sample dimensions because such capping will only cause L_T in the prefactor of the expression above to be replaced by the sample thickness. That is, while the maximal QCC (usually achieved by lowering the temperature) may be capped because the diffusion length is capped, the EEI MR powered by the k_BT-normalized Zeeman splitting will continue to increase as the temperature is lowered towards 0K. This distinction between the size effects on QCC and on EEI MR may be advantageously exploited to detect the presence of EEI in nano metals.

Dimensionality is of essential importance to quantum interference because diffusion scaling is dependent on dimensionality and path crossing is greatly enhanced in lower dimensions. In 1D, QCC by WL and EEI are described by

$$\Delta\sigma_{1\mathrm{D}}^{\mathrm{WL,T}} = -\frac{1}{\pi}\frac{e^2}{\hbar}\frac{L_\phi}{A} \tag{1.45}$$

$$\Delta\sigma_{1\mathrm{D}}^{\mathrm{EEI,T}} = -\frac{1}{2\sqrt{2}\pi}(4-\frac{3}{2}\tilde{F}_\sigma)\frac{e^2}{\hbar}\frac{L_T}{A} \tag{1.46}$$

where A is the cross-section area of conducting path, introduced to the equations to make the 1D conductivity have the same unit as the 3D conductance. So short diffusion lengths that are expected for nano metals will weaken both WL/WAL and EEI contributions to 1D QCC, which is opposite to the case of 3d QCC. Nevertheless, 1D QCC in nano metals has the inherent advantage of a much smaller wire cross section: It is possible to have wires of the atomic dimension, $A \sim 0.3$ nm $\times$ 0.3 nm. This is much less than what was used in previous studies, of lithographically defined wires (tens of nm to microns) or naturally grown wires such as carbon nanotubes or nanowires (tens of nm), so a larger QCC is expected in nano metals. However, in atomically thin 1D transport, electrons having few encounters and possibly easier random walk may experience weaker EEI (through $\tilde{F}_\sigma$), if so, they may not be able to take advantage of the smaller A.

Conventionally, 1D MR is thought to not exist: No equation of EEI-induced MR can be found in the literature [49]. This is understandable for conventional 1D MR experiments: They are only quasi-1D in nature, in that the lateral dimensions of the sample are much shorter than the diffusion length, and their electrons will bounce back and forth from the wall many times before completing a diffusion distance, or coherent distance. Naturally, the multiply intersected areas traced out by the electron will give self-cancelling magnetic area, so the integral of the vector potential is zero, and the integral of magnetic flux is zero. This is why it has no "longitudinal" (the term used by Altshuler, Aronov, Spivak, and Shavin-Sharvin) MR in conventional 1D studies. However, 1D WL MR of the Aharonov-Bohm

oscillation nature is possible if one uses a multiply connected structure, as in the case of hollow cylinder. In this case, the MR oscillates as described below, and its amplitude is again increased by the small A

$$\Delta\sigma_{1D}^{WL,H} = -\frac{1}{\pi}\frac{e^2}{\hbar}\frac{L_\phi}{A}\frac{\sinh(\frac{2\pi r}{L_\phi})}{\cosh(\frac{2\pi r}{L_\phi}) - \cos(2\pi\frac{\Phi}{\Phi_0})} \tag{1.47}$$

Therefore, nano metals with 1D wires of atomic sized wire cross-section may have enhanced Aharonov Bohm oscillations, and with the highest field available (18-40 T), it is theoretically possible to measure loops as small as a few nm in diameter.

1.5.1. Plan of the Thesis

Since nano metals are known as conductors that realize metallic conductivity at low temperatures, they potentially can provide a novel platform to explore quantum interference phenomena of coherent electrons, at small dimensions and across dimensionalities. Nano metals are known for many thin films, including both *nanometallic* [11, 12, 13] and *filamentary* resistance memory [56, 57, 58] (see Appendix A-B for a brief introduction of resistance memories, known as ReRAM, made from these two types of thin films.) But it is not known whether quantum phenomena for coherent electrons exist in them or not. This is an intriguing question because nano metals are made of materials that are strong insulators when in the bulk form, and such strong insulators have never been thought to be possible candidates for observing coherent electrons. This question will be settled in this thesis, which seeks to establish quantum electronic interference phenomena in thin-film nano matals that are of particular interest to resistance-switching memory.

To provide the simplest ReRAM for a comprehensive study of these quantum electronic phenomena, I have developed an amorphous Si device that exhibits non-volatile resistance switching. It switches in the same way as the so-called nanometallic RRAM, which are metal-doped amorphous nitrides and oxides. This developmental effort is documented in Appendix A, which also explains why O and N doping can enable switching. Experimental

results in Chapter 2 unequivocally confirm that 3D EEI dominates the QCC in Si nano metals, causing a positive MR that is not saturated even though the diffusion length is cutoff by sample thickness. The result also allows the determination of diffusivity, which at 3×10^{-2} cm^2/sec is about one to two orders smaller than conventionally seen in mesoscopic metals. Such lower diffusivity can be directly equated to a large effective mass for electrons, which is indicative of strong electron phonon interaction. The subject of electron-phonon interaction is of central importance to resistance switching and the stabilization of the insulator state in nanometallic ReRAM, and it is a subject that has been much explored in the past in our group. But further experimental evidence in the form of effective mass is provided here for the first time, through QCC and MR measurements, as will become clear throughout Chapter 2-4.

Amorphous Si has generally rather weak MR because of the small dimensions of the materials, which prevent large loops to form to allow a large WL/WAL-MR effect. However, as shown in Eq. (1.14)-(1.16), low diffusivity can enhance QCC of both the WL and WAL origin in 3D, and this is used advantageously in Chapter 3 that studies three nanometallic oxide/nitride glasses, doped with Pt atoms. This is because doping allows tunable diffusivity (the lower the Pt concentration, the lower the D), reaching as low as 10^{-4} cm^2/sec suggesting an effective mass as large as 100 m_e. It also exhibits WAL because of the strong spin orbit interaction of Pt. As mentioned previously, WAL and WL have opposite signs, and the spin-orbit interaction can play the role of imparting a "contrast" agent that will flip the sign of the QCC at a certain crossover temperature when scattering by Pt takes over other inelastic scattering. This adds new features to the QCC and with them it is possible to fully unravel all the interactions (WL, WAL, and EEI) in the Si_3N_4:Pt thin films.

Unlike the case of Si and nanometallic Si_3N_4:Pt in which quantum interference and conductivity are distinctly 3D, in filamentary ReRAM made of amorphous HfO_2 and Al_2O_3, the conducting path is 1D [59, 60, 61], some part of it made of loops tilted at a certain angle relative to the film normal. Evidence of such loops is presented in Chapter 4 in the

form of remarkable Aharonov-Bohm oscillations under a magnetic field, originating from the quantum interference of coherent electrons in a single loop. The development of these filamentary ReRAM also takes advantage of electron-phonon interaction, as evidenced by the pressure-induced insulator to metal transition documented in Appendix B. But filaments in these ReRAM can be made by another method that is well known in the ReRAM field: applying a voltage to cause dielectric breakdown. Chapter 4 compares the QCC and Aharonov-Bohm oscillations from filaments and loops formed by both hydrostatic pressure and electrical voltage, and found different forming methods have remarkable effects on altering the dimensionality of and imparting spin-orbit interactions to QCC. In particular, voltage creates more random field due to the reduction of cations, distributed in the loop or in a 3D mesh, which impart strong spin-orbit interaction and cusp-like MR at small magnetic fields. Using these methods, we are able to measure loops of a size of 6.5 nm in both HfO_2 and Al_2O_3, which is the smallest loop ever detected inside a solid.

This research has generated unprecedentedly detailed insight to the operation of ReRAM. It also for the first time demonstrates QCC and coherent electron interference in a nanoscale volume $\sim(10\text{ nm})^3$. Remarkably, such observations were made in materials that are usually known, in their bulk form, as random insulators, whose conducting electrons have never been exposed so clearly before. A further outcome of this research is the development of a new metrology tool that enables resistance probing at the length scale of 10 nm, where standard four-point probe is so far impractical. These results are important for ReRAM technology and for understanding electron transport in nanodevices.

CHAPTER 2 : Electron Interference and Metal-Insulator Transitions Mediated by Local Structures in Amorphous Si Nanofilms

2.1. Introduction

Although Anderson first predicted a metal-insulator transition triggered by random potential that causes strong localization and absence of diffusion for electrons [8], it took another twenty years before it was realized that electrons in metals are also weakly localized (WL) [1, 23]. This manifests in the quantum correction to conductivity (QCC), which partially negates the Drude conductivity. The correction arises from interference and interaction of coherent electrons [3, 62], which becomes pronounced when their diffusion distance L_{T} diverges at temperature $T \rightarrow 0$K. WL has been extensively studied in metals at the mesoscopic length scale [2, 4], and it grows into strong localization at the metal-insulator transition [63]. The crossover was also observed at low temperature when L_{T} exceeds the localization length ζ [55]. We will demonstrate in this chapter, however, that random insulators despite their strong random potentials can also manifest metal-like WL phenomena all the way down to 0K. The unexpected findings are made possible by probing a nanoscopic sample: Below a critical dimension $\delta < \zeta$, the insulator sample actually behaves like a (nano) metal.

To frame the study on nano metals made of strongly localized insulators in this thesis in a broader context, we now enumerate all the relevant length scales earlier introduced in Chapter 1. In addition to ζ (typically a few nm here) and $\delta \sim \zeta$, there is the mean free path l of electrons, taken to be 0.27 nm for Si, which is the Si-Si (bond) distance of Si's random network on which electrons diffuse. Since $l \ll \zeta \sim \delta$, one may contemplate the possibility of three-dimensional (3D) coherent electron diffusion in a δ^3 volume, which is a remarkable departure from past mesoscopic conduction studies of 2D metallic films. Of course, to realize this, electrons must be wave-like; thus l sets the upper limit for the Fermi wavelength $\lambda_{\mathrm{F}} < 2\pi l$. Meanwhile, coherent diffusion, during which WL prevails, can only last for the duration of the dephasing time τ_T of electrons, which sets L_{T} to $\sqrt{D\tau_T}$. In

nano metals, $L_{\rm T}$, which varies as $\sqrt{\hbar D/k_B T}$, may approach δ at millikelvin temperature. So one can examine the nanoscale size effect in the regime of $L_{\rm T} > \delta$: QCC is completely saturated in this regime. On the other hand, while dephasing can also be caused by a magnetic field B over a magnetic length $L_{\rm B} = \sqrt{\hbar/2eB}$ [64], it is irrelevant in nano metals because $\delta \ll L_{\rm B}$ for all practical fields, thus rendering magnetic decoherency ineffective. (It takes $B = 20$ T to get $L_{\rm B} = 10$ nm.) This leaves the Zeeman splitting that affects the diffusion channels in electron-electron interaction (EEI) [3] as the only magnetic effect. Lastly, the size limitation of $\delta \lesssim \zeta$ prevents the crossover from WL to strong localization from taking place even when $L_{\rm T} > \zeta$ as $T \to 0$K. Therefore, unlike disordered metals of large dimensions, disordered insulators of small dimensions will remain nanometallic, rich in coherent electrons, at $T \to 0$K!

In this chapter, our study was conducted in amorphous silicon and germanium, some doped with B or P. At low temperatures, they are known as insulators with a band gap of 0.7-2 eV [65]. In recent years, our group discovered that random insulators can exhibit robust *nano* metallicity at $\delta < \zeta$ [14]. Importantly, one can tune ζ by electron doping, or by injection/removal of trapped charge, which increases random potential by erecting a Coulomb repulsion barrier [66]. In the Appendix A and this chapter, we will demonstrate that this is also the case for amorphous Si and Ge, although to trap electrons, they need additional dopants of N or O. Even with a small amount of B, P, N or O, these pure and doped Si have no magnetic impurity and little spin-orbit interaction, which greatly simplifies the description for QCC. On the other hand, random nano metals share a ubiquitous feature of negative U centers, in which trapped charge are stabilized by locally strong electron-phonon interaction [15]. (Apparently, N and O in Si and Ge are instrumental for introducing these centers.) We shall see that such interaction has also left a mark on QCC by affecting electron's effective mass m^* and diffusivity D.

2.2. Experiment

2.2.1. Sample Fabrication and Materials Characterization

Amorphous Si/Ge thin films were RF-sputtered using undoped or n/p-doped Si/Ge targets onto an unheated substrate−either a 100 p-type silicon single crystal or a two-side-polished fused silica−pre-coated by DC sputtering to form a continuous 30 nm thick Mo bottom electrode. To incorporate O/N into Si/Ge during sputtering, either O_2/N_2 was co-injected with Ar, or an additional oxide/nitride target (Si_3N_4, AlN, SiO_2, Al_2O_3 and HfO_2) was co-sputtered. A final 40 nm thick Pt top electrode was RF sputtered through a shadow mask to define cells of 50-250 μm in radius. The fabricated heterostructures contain x-ray-amorphous (Rigaku GiegerFlex D/Max-B diffractometer) Si/Ge films (grown on either bare or Mo-coated substrates), which have a RMS roughness of 0.28 nm over an area of 10×10 μm^2 according to topographical mapping by Asylum MFP-3D AFM. The relative composition of O:N:Si was determined by XPS using a RBD-upgraded PHI-5000C ESCA system (Perkin Elmer) with Mg Kα radiation (hν = 1253.6 eV). Direct metallic contact between the top and bottom electrodes was not found even in the largest cells when the Si/Ge films were at least 2 nm thick; this was verified by other data described below. (Also see Discussion.)

2.2.2. Electrical Measurement of Transport Properties

Temperature dependent electrical properties of films with and without a magnetic field were measured in Quantum Design Physical Property Measurement System (PPMS, 2-300K, −9-9 T) at Penn's Shared Experimental Facilities and two superconducting magnets at National High Magnetic Field Laboratory (SCM2, 0.3-2K, −18-18 T; and SCM1, 0.018-2K, −18-18 T). Si or Ge films of different thickness or preset in different resistance states by voltage/pressure were mounted on sample holders, either a sample puck for PPMS or a set of 16-pin dip sockets for SCM1 and SCM2. With one end soldered to the pins on the sample holder, a gold wire was silver-paste-bonded to the top Pt electrode of a Si/Ge cell

of a radius of 250 μm (t1). Another wire was similarly bonded to one edge of the bottom Mo electrode (t2) to form a two-terminal connection to the cell (t1-t2). A three-terminal connection was formed by further bonding a third gold wire to the opposite edge of the Mo electrode (t3); these three-terminal connections (t1-t2-t3) used samples deposited on a fused silica substrate, which is insulating.

During measurements, the following setups were used. (a) Two-point DC resistance (defined as $V_{2\mathrm{pt}}/I$) was obtained using a Keithley 237 High Voltage Source Measure Unit to apply a constant voltage of 0.01 V ($V_{2\mathrm{pt}}$) across t1 and t2, while measuring the current (I) passing through the films. (b) Three-point DC resistance (defined as $V_{3\mathrm{pt,DC}}/I$) was measured using a Keithley 237 to apply a constant current of 10 μA (I) between t1 and t2, while measuring the voltage using a Keithley 2182A nanovoltmeter between t1 and t3. This configuration removes the spreading resistance but still include the resistance (as well as the interface resistance) of the top and bottom electrodes within the cell area. (c) Three-point AC resistance (defined as $V_{3\mathrm{pt,AC}}/I$) was measured using an SR 830 lock-in amplifier and a standard resistor of 100 kΩ. The amplifier sent a sine wave of 1 V amplitude at 31 Hz to the standard resistor and the cell, in serial connection. Since the resistance of our cell in the metallic state is typically much less than 100 kΩ, the above is equivalent to applying a constant current of 10 μA (I) across t1 and t2. Meanwhile, using the lock-in amplifier, the voltage ($A - B$ voltage or $V_{3\mathrm{pt,AC}}$) between t1 (A) and t3 (B) was measured when locked to the same frequency of 31 Hz at a time constant of 1 s. An auto offset and 10$\times$ signal expansion were used to improve the voltage resolution to enable measuring small resistance changes. (a)-(b) were used in PPMS runs, and (b)-(c) were used in SCM1 and SCM2 runs. All the measurements were performed in the Ohmic regime and yielded almost identical results when fitted by the same set of parameters.

Electrical measurements were mainly conducted under two temperature/field-sweep conditions: cooling/heating at a fixed magnetic field, and ramping magnetic field at fixed temperature. During these measurements, synchronized voltage, current, temperature and field

data were recorded while the heating/cooling rate was set at an appropriate value. Sweeping of the magnetic field was typically at 0.5 T/min in PPMS and 0.3 T/min in SCM1 and SCM2. The field/sample-orientation dependence of magnetoresistance was determined in SCM1 and SCM2 by rotating the sample at 3 degrees/min in a fixed magnetic field, or by rotating the sample to a new orientation, then sweeping the field to ±18 T. Precaution against temperature/magnetic-field/orientation/voltage hysteresis was taken by repeating all the temperature/magnetic-field/orientation/voltage sweeps in two directions to ascertain their ramping curves overlap exactly. For the same temperature/field range, data collected in PPMS, SCM1 and SCM2 were in excellent agreement with each other despite the fact that they were measured several months apart. Excellent sample-to-sample reproducibility was observed, as evidenced by the overlapping $R(T)$ curves of different insulator states and different metal states. In addition, the Weibull statistics of resistance values and threshold switching voltages of metal and insulator states are very narrow at both 300K and 2K (see Results section). Thus, our materials and sample cells are apparently highly uniform, stable and reproducible.

2.2.3. Data Analysis

Despite different film thickness, resistance and composition, all our PPMS, SCM1 and SCM2 measurements used sample cells of the same size and configuration, which are likely to have the same parasitic load resistance due to leads, electrodes, spreading resistance and electrode/film interfaces. Moreover, although the measured resistance necessarily contains some parasitic load resistance, we found it possible to precisely determine the resistance change of the films in our sample cells as illustrated by the following example. Consider two cells that contain two different films that are self-similar in the following sense: Both films have a magnetoresistance at 10 T that is 1% of its 0 T resistance. (Note that their total cell magnetoresistance, which includes the magnetoresistance of both the film and the parasitic resistance, is not self-similar even if film's magnetoresistance is.) If so, then the difference of the two cell-resistances will also show a magnetoresistance of 1% of its

0 T value, because unlike the cell-resistance the difference does not include the parasitic resistance. This example suggests that, instead of analyzing the two-terminal cell resistance individually, we can analyze a set of them, and compare their pair differences, which will carry the same information of the relative resistance change of the film. (There is an analogous case in diffraction of matter: The diffraction intensity is the Fourier transform of the vectors of atom-pairs; it is not the Fourier transform of the position vectors of atoms. Nevertheless, the diffraction intensity still informs the structure of matter satisfactorily.) We have formalized this analysis and reported it elsewhere (See Appendix C and [54]). Below is a summary of the procedure used for data analysis here.

Let the resistances of two self-similar cells, 1 and 2, increase from $R(1)$ and $R(2)$ at $(T, B) = (0, 0)$ to $R'(1)$ to $R'(2)$ at (T, B), respectively. Then the relative conductivity change $\Delta\sigma/\sigma_o$ can be obtained from the relative change of the resistance difference of the cell pair, $-\Delta R/R_0$. Here, $R_0 = R'(1) - R'(2) \approx R(1) - R(2)$ and $\Delta R = [R'(1) - R'(2)] - [R(1) - R(2)] = [R'(1) - R(1)] - [R'(2) - R(2)]$ is the change of the resistance difference due to the change of (T, B). The above result is exact. This method can be used to accurately determine $\Delta\sigma/\sigma_o = \Delta R/R_0$ down to 0.1%.

In our data analysis, for each composition we first selected a set of metallic cells that differ in either Si/Ge thickness or the resistance value. These cells will be named cell 1, 2, etc. Assuming they are self-similar, we followed the resistance difference method to calculate $-\Delta R$. (The resistance difference between two cells used for the following analysis was in the Ohmic regime.) The self-similarity assumption is considered validated if (i) the resultant $-\Delta R$ obeys a scaling law; for example, $-\Delta R$ of various (T,0) follows a temperature scaling law, and (ii) $\Delta\sigma/\sigma = -\Delta R/R$ of all the pairs falls on a universal curve/line consistent with the scaling law. Model fitting thus obtained $\Delta\sigma/\sigma_o = -\Delta R/R_0$ data then allows determination of the parameters for each composition. Since there are only two materials parameters, one related to diffusion, the other to interaction, two independent sets of data, e.g., temperature dependence and magnetoresistance, will suffice for solving the parameters

(see Results for details).

2.2.4. Insulator-to-Metal Transition Triggered by Mechanical Stress

A hydraulic pressure was found to be able to trigger insulator-to-metal transition in amorphous Si and Ge. Before the pressure treatment, the two-point resistance of each Si/Ge cell in an array on the same chip was read at 0.1 V or pre-switched to certain resistance state using Keithley 237. Next, the chip was disconnected from the voltage source, wrapped in an aluminum foil, vacuum-sealed in an elastomer bag, and suspended in a liquid-filled pressure vessel (Autoclave Engineers, Erie, US) that was charged to a pre-set hydraulic pressure of 2-350 MPa at room temperature and held for <5 min before sample removal. The resistance of each cell was read again at 0.1 V and compared with its pre-pressure-treatment value, and switched back to the insulator state again by electrical voltage for the pressure-switched metallic state. No difference was found between the transition of pressure-induced state and that of the voltage-induced state. Some higher pressure (up to 1 GPa) experiments were also similarly performed in a hydraulic pressure vessel (Dr. CHEF) at Takasago Works, Kobe Steel, at Takasago, Japan.

A magnetic pressure burst was also used to trigger insulator-to-metal transition in amorphous Si/Ge. In principle, a magnetic pressure may be generated by passing a burst magnetic flux between the Si/Ge-filled gap of the two electrodes, which form a metallic "container" that confines the burst magnetic field. (At high frequency, the gap resistance at the edges of the electrodes is very small so the two electrodes form a continuous circuit.) Assuming Si has a relative permeability of unity, the magnetic pressure $P_B = (B/0.501)^2$ with P_B expressed in bar (1 bar = 0.1 MPa) and B in T. The burst magnetic flux was received from an electron bunch, which is a spatially localized bundle of 20 GeV electrons generated at Stanford Linear Accelerator Center (SLAC) using the FACET facility. Each bunch contained $\sim 10^9$ electrons (>1 nC) that are narrowly collimated ($\sim$25 μm). It had a short duration, passing in $\sim$0.1 ps, which is the time for the bunch to travel 25 μm at near the speed of light, and was available on a bunch-by-bunch basis. We only allowed

each cell to see one bunch during the experiment; after each shot the sample was moved to a new position before the second shot was fired. The electron bunch hit the sample chip in the normal direction. Since the maximum magnetic field around the bunch is $\sim$ 70 T at the edge of the bunch, i.e., $\sim$ 40 μm from the flight path [67], and it decays with the radial distance r from the bunch roughly according to $1/r$, we can estimate the magnetic pressure in each cell from the cell location relative to the flight path. (To maximize the induced magnetic pressure inside the cell, we chose the cell size to be 20 μm, comparable to the bunch size.) So, the estimated maximum magnetic pressure is $\sim$1,950 MPa, and at 500 μm away it decays to $\sim$12.5 MPa. (The above estimates are lower bounds since they do not consider the pressure caused by the induced current in the electrodes.) Because of symmetry, however, there is no magnetic field at the center of the bunch. This was verified by the observation in some experiments one or two center cell that that suffered neither physical damage nor resistance change. (It also provided direct evidence that the impact damage due to momentum transfer was minimum, which is expected because the collision cross-section of a relativistic electron at 20 GeV is very small. See further discussion in [13]) The electric field is radial and follows the same radial variation as the magnetic field, but it is unimportant for this experiment as previously established in [15].

Similar to the hydraulic pressure experiment, before the magnetic-pressure treatment, cells were pre-transitioned by a voltage to certain resistance states, with their two-point resistance values recorded at 0.1 V by a Keithley 237. Their resistance was again read in the same way after the magnetic-pressure treatment and compared with the pre-treatment value. In a typical representation of the data, each cell is colored to indicate its resistance value before and after the treatment, and the colored maps are presented to aid comparison. In some experiments, the chip was covered by a photoresist, which is not a conductor and has no effect on the magnetic field. But because it can be blown away by a large magnetic field, it serves as a marker to help identify the flight path of the electron bunch. Since the cell size is about the same as the bunch size, maps that have hundreds of cells each appearing as a "dot" with changed colors provide direct evidence for the far-field effect of an electron

bunch. Lastly, the magnetic-pressure-induced metallic state was tested by electrical voltage to check if it can transition back to insulator state. Its subsequent electrical switching curve was compared with the curves before the shot by electron bunch.

2.3. Results

2.3.1. Nanometallic Transition in Amorphous Si

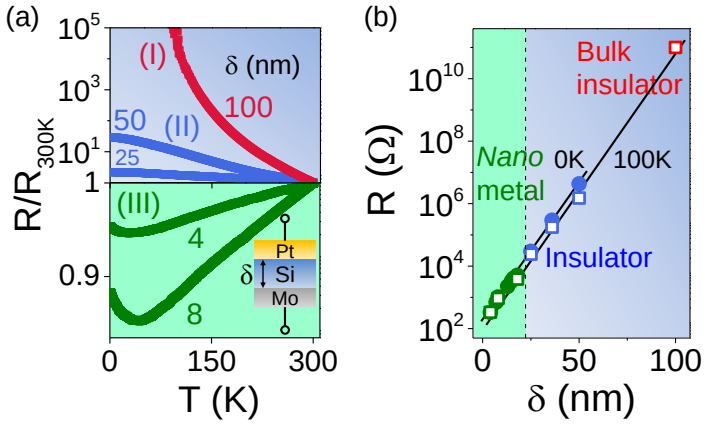

Figure 2.1: Thickness-controlled nanometallic transition in amorphous Si. (a) Pure Si films exhibit three distinctive types of $R(T)$ as thickness δ, labeled in nm, varies. Inset: Schematic of sample configuration. (b) 0K and 100K resistance ($R_{0K/100K}$) follows same $\exp(\delta/\zeta)$ dependence (solid line) across nanometallic metal-insulator boundary.

We collected the resistance-temperature $R(T)$ curves within the small-signal Ohmic regime identified by the two-point current-voltage curves as shown in Fig. 2.1. The $R(T)$ curves of pure Si in Fig. 2.1a fall into three types: The $R(T)$ in thicker films diverges as $T \to 0$K like in bulk amorphous Si [68, 69], the $R(T)$ in intermediate thickness films is capped by the tunneling resistance, and $R(T)$ in thinner films is metal-like but with a resistance minimum reminiscent of slightly disordered metals [70]. The contrasting $R(T)$ curves of different types suggest a nanometallic metal-insulator boundary at ~25 nm. But this is not a traditional metal-insulator transition boundary, and it is not associated with any property discontinuity (see Discussion). Indeed, the 0K and 100K resistance of different types of $R(T)$ curves follows the same $R_{0K/100K} \sim \exp(\delta/\zeta)$ dependence, shown in Fig. 2.1b, supporting the continuous nature of the transition. (The 0K resistance of 100 nm films is not shown,

because it exceeded the instrumental limit, ∼100 GΩ at 0.1 V.) Interpreting Fig. 2.1b using Anderson's picture of localized wave function, we obtain a surprisingly long ζ of 4.8 nm, $\sim 18l$, at both temperatures, in all the films. Apparently, metal-like behavior can be seen up to $\delta \sim 5\zeta$, which may be regarded as the practical upper limit of nano metals, beyond which the sample resistance becomes bulk-like (e.g., seen in the 100 nm-thick sample). Note that while the metal-insulator boundary was easily located in our experiment by two-point measurements (the schematic inset of Fig. 2.1a), any standard four-point measurement would have missed it because its probe distance most likely exceeds 25 nm.

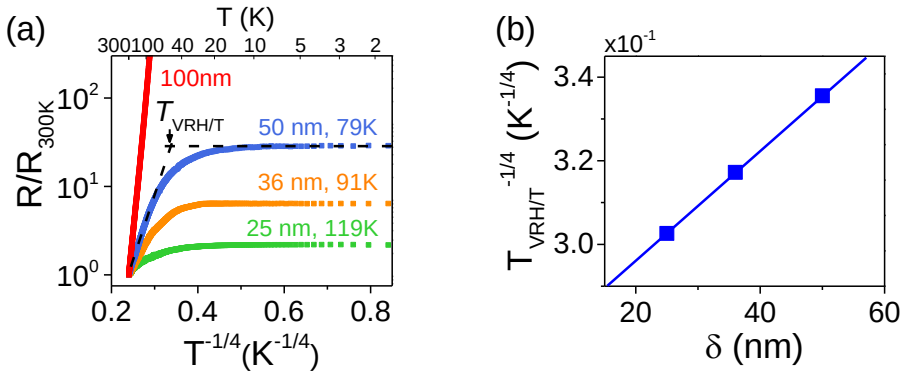

Figure 2.2: Variable range hopping (VRH) in insulating films of amorphous Si. (a) $T^{-1/4}$ VRH plot for different thickness (δ) films; linear relation holds only in thickest (100 nm) film. In thicker films, VRH is capped by tunneling at $T_{\mathrm{VRH/T}}$, as marked, when hopping distance crossovers to δ. (b) $T_{\mathrm{VRH/T}}^{-1/4}$ is proportional to δ as predicted by Mott's VRH law.

We found the type I and type II curves at high temperature obeys Mott's $\exp((T_o/T)^{1/4})$ law (Fig. 2.2a), which was explained by Mott by electron hopping between localized states separated by various longer-than-ζ distances that overall scale with $T^{-1/4}$ [7]. (T_o scales with ζ^{-3}.) In this respect, our films behave the same as in bulk amorphous Si and Ge in the strong localization regime. As the prevailing hopping distance scaling with $T^{-1/4}$ reaches the film thickness at lower temperature, which we shall call $T_{\mathrm{VRH/T}}$, the variable range hopping will crossover to flat tunneling. Thus, $\delta \sim T_{\mathrm{VRH/T}}^{-1/4}$, which is verified in Fig. 2.2b and further confirms Mott's law. Therefore, despite the novel discovery of nanometallicity at $\delta \lesssim \zeta$, nothing is changed when the transport distance is long, i.e., when $\delta \gg \zeta$. This

again supports our claim that the metal-insulator transition in the thickness space is a continuous transition.

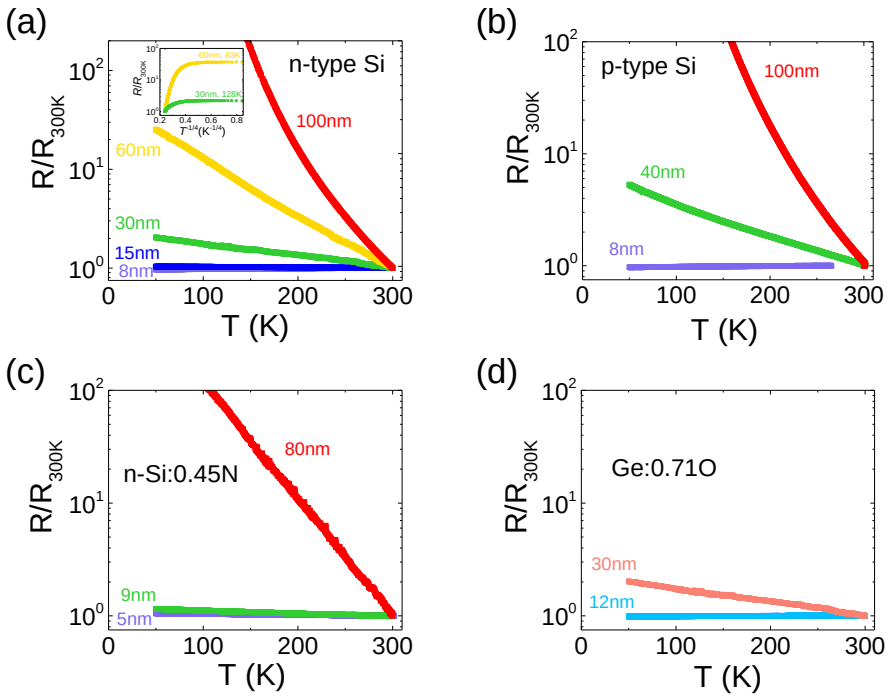

Figure 2.3: Temperature dependence of R normalized by R_{300K} shows thickness-triggered insulator-metal transition similar to the one in Fig. 2.1 in amorphous films of n-type Si (a); p-type Si (b); n-Si:0.45N (c); and Ge:0.71O (d). Insulator's resistance changes by orders of magnitude while metal's is nearly constant. Inset of (c): Normalized resistance vs. $T^{-1/4}$ for insulating films obeys "1/4" law at high temperature but saturates at low temperature.

Similar thickness-dependent behaviors were found in other nano metals, which are also thin films of bulk insulators made of doped and undoped Si/Ge as shown in Fig. 2.3, in which resistance of insulators changes by orders of magnitude while metal's is nearly constant as temperature decreases from 300K to 50K.

Just like nanometallic electron-doped nitride and oxide glasses [14, 66, 15], nanometallic N- or O-doped Si and Ge can be electrically and reversibly stimulated at 2K and 300K (Fig. 2.4a) to transition from an insulator state to a metallic state at a set of constant threshold voltages, about ±1 V. Indeed, a multitude of metallic states of various resistances are obtained in Fig. 2.4a by controlling the current compliance (similar results and more

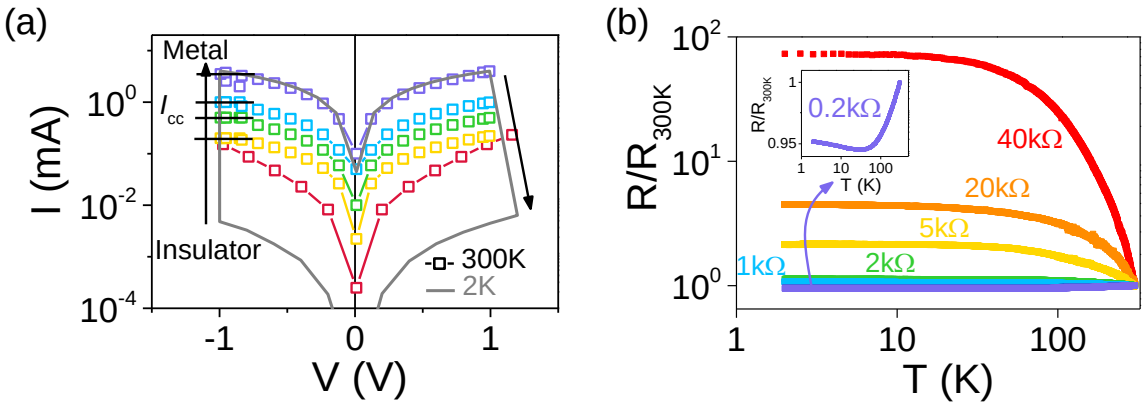

Figure 2.4: Reversible metal-insulator transition stimulated by electrical voltage in amorphous n-type Si film doped with N (n-Si:0.45N). (a) Reversible transitions at 2K (grey curve) and 300K (symbols) shown in hysteric $I-V$ curves, triggered by same electrical voltage of ± 1 V. Multiple intermediate metal/insulator states at 300K achieved by controlling current compliance (I_{cc}). Arrows indicate transition direction. (See Appendix A for details.) (b) $R(T)$ dependence of same cell in different resistance states (room-temperature resistance labeled next to curve) validates metal and insulator states marked in (a). Inset: Enlarged $R(T)$ of least resistive, hence most metallic state.

transition characteristics can be found in Appendix A). Unlike the transition in the thickness space, this one is a genuine metal-insulator transition, as verified by inspecting the $R(T)$ curves (Fig. 2.4b) of the same cell placed in different states by electrical stimulation. Moreover, the hysteric nature of Fig. 2.4a further indicates that it is a first order transition. In the next section, we will compare the various *metallic* states of Si/Ge films with and without additional O/N, obtained either from similar cells of different thickness or from the same-thickness cell(s) but conditioned by different electrical stimulations, to explore their common quantum phenomena that may be attributed to coherent metallic electrons. It will reveal a universal QCC shared by all such states, at $\delta \lesssim \zeta$.

2.3.2. Quantum Interference Dominated by Electron-Electron Interaction

As we introduced in Chapter 1, enhanced EEI is generally expected in amorphous networks for a simple reason: Two "colliding" electrons after each encounter are effectively "stuck together" until they can find a way out by tortuous random walk. At 0K and in the zero-energy limit, a coherent electron may be Bragg-scattered off the Friedel oscillations of

other diffusive electrons, which amounts to singular backscattering [48]. (Non-interacting electrons can also have singular backscattering by diffusion back to the origin, which is equivalent to two electrons crossing paths twice. This happens very often in 1D and 2D and is commonly cited as the dominant QCC mechanism in WL, but it is relatively rare in 3D, where QCC is dominated by EEI [62].) In our samples, within a volume of $\sim(10\text{ nm})^3$ between the electrodes, we have found metallic conductivity bearing two signatures of EEI-dominated WL despite the small transport length: resistance (R) minimum in Fig. 2.5a-b and positive magnetoresistance (MR) in Fig. 2.5c and Fig. 2.6. This is unexpected because, previously, these phenomena were always studied (a) in metal samples and (b) at a macroscopic or mesoscopic transport distance [33, 71, 72, 73, 74]. Another new feature is that, in Fig. 2.7, the QCC has reached the L_T-δ crossover thus experiencing resistance saturation, which is impossible in mesoscopic samples that have δ orders of magnitude longer. Lastly, whereas mesoscopic samples may support a long diffusion distance that allows magnetic decoherence to come into play, such effect is prohibited in nano metals because $\delta \ll L_B$ at all practical fields. So we are left with the Zeeman splitting in EEI as the only magnetic effect responsible for MR.

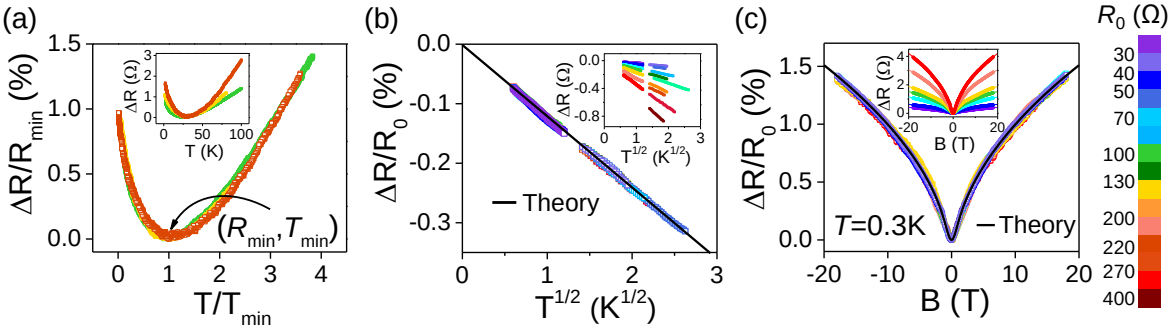

Figure 2.5: Universal QCC shared by multiple metallic states of 11 nm n-Si:0.45N films as demonstrated by overlapped relative resistance change ΔR against (a) $T/T_{\min}$, (b) $T^{1/2}$ below $T_{\min}$, and (c) magnetic field B at 0.3K. Insets: plot of ΔR of individual metallic states before normalization. Solid line/curve in (b) and (c): prediction by Eq. (2.1). Various resistance states with R_0 indicated by color spectrum on right.

As seen from Eq. (1.36) and Eq. (1.39) in Chapter 1, the EEI-dominated weak localization

theory predicts a QCC to 3D conductivity [3],

$$\Delta\sigma(T,B) = \quad \sigma(T,B) - \sigma_o = \\ \alpha(4/3 - 3\tilde{F}_\sigma/2)\sqrt{T} - 0.77\alpha\tilde{F}_\sigma\sqrt{T}g_3(\tilde{h}) \tag{2.1}$$

Here, $\sigma_o = \sigma(0,0)$ is 0K conductivity, B is magnetic field causing normalized Zeeman splitting $\tilde{h} = g\mu_B B/k_B T$ (we shall set $g = 2$), and g_3 is an even function of $\tilde{h}$ with asymptotes $\tilde{h}^2$ at $\tilde{h} \ll 1$ and $\tilde{h}^{1/2}$ at $\tilde{h} \gg 1$ [1]. There are three material parameters in Eq. (2.1): (i) $\alpha = (e^2/\hbar)(1.3/4\pi^2)\sqrt{k_B/2\hbar D}$, which is set by electron diffusivity D, (ii) Fermi-liquid constant $\tilde{F}_\sigma$, which specifies the strength and sign of EEI, and (iii) σ_o, which is the uncorrected Drude conductivity at 0K. Since $\Delta\sigma/\sigma_o$ depends only on α/σ_o and $\tilde{F}_\sigma$, we can uniquely determine them using the two independent datum sets of Fig. 2.5-2.6, which give the temperature and field dependence of $\Delta\sigma/\sigma_o$ that equals $-\Delta R/R_0$, the normalized resistance correction from $R_{0\mathrm{K}}$. Next, from the resistance saturation in Fig. 2.7, we can further determine D, hence α, and hence σ_o, thus completing the analysis. This is outlined below for n-Si:0.45N nanofilms: for films of various thickness from 8 nm to 16 nm, and for the 11 nm films, set in various metallic states from 28 Ω to 393 Ω per Fig. 2.4a. Specifically, we will demonstrate that they all share a universal $\Delta\sigma/\sigma_o$, thus they must have the same α/σ_o and $\tilde{F}_\sigma$.

Figures 2.5-2.7 display the temperature/field responses of $\Delta R/R_0$. To demonstrate universal $\Delta\sigma/\sigma_o$, we have normalized them as overlapping data plots. In each panel, the overlapping plot contains multiple data sets covering several metallic states (Fig. 2.5), or at several temperatures for a single state (Fig. 2.6), or several thicknesses (Fig. 2.7). In fact, there are many more data sets shown in Fig. 2.8 at the end of the analysis, which also follow the exactly same $\Delta R/R_0$ plot if under the same (T,B) perturbation. So, without doubt, $\Delta\sigma/\sigma_o$ of this material is state and thickness independent. (The universality provides the basis to

[1] An analytic expression of the function $g_3(x)$ is given in [50], $g_3(x) = 5.6464 \times 10^{-2}x^2 - 1.4759 \times 10^{-3}x^4 + 4.2747 \times 10^{-5}x^6 - 1.5351 \times 10^{-6}x^8 + 6 \times 10^{-8}x^{10}$ when $x \le 3$, $g_3(x) = 0.64548 + 0.235\delta - 7.45 \times 10^{-4}\delta^2 - 2.94 \times 10^{-3}\delta^3 + 6.32 \times 10^{-4}\delta^4 - 5.22 \times 10^{-5}\delta^5$ when $3 \le x \le 8$ ($\delta = x - 4$), and $g_3(x) = x^{1/2} - 1.2942 - \pi^2 x^{-3/2}/12 - \pi^4 x^{-7/2}/16 - 5\pi^6 x^{-11/2}/32$ when $x > 8$.

rigorously extract $\Delta R/R_0 = -\Delta\sigma/\sigma_o$ from multiple two-point-resistance measurements with different states/thicknesses. This is because if their "intrinsic" $\Delta R/R_0 = -\Delta\sigma/\sigma_o$ is the same despite the fact that their two-point resistance may contain an additional parasitic electrode/load/interface resistance, then after subtracting one measurement from another, the parasitic resistance can be removed and the resistance differences will all be related to $\Delta R/R_0 = -\Delta\sigma/\sigma_o$. See Appendix C and [54] for more details.) Physically, this suggests that films of different thicknesses and states merely contain different amounts of the *same* conducting elements; the more there are, the lower the R_0.

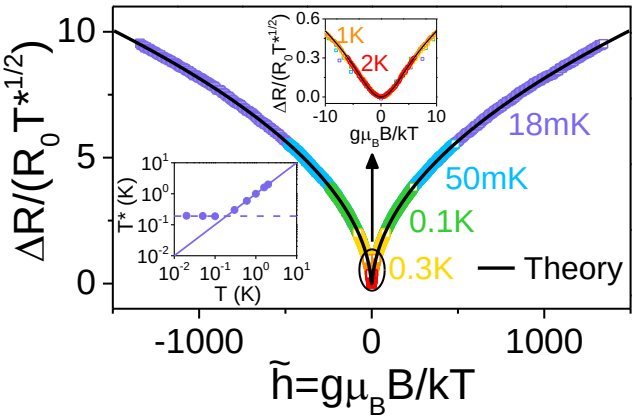

Figure 2.6: Normalized magnetoresistance vs. $\tilde{h} = g\mu_B B/k_B T$ in 11 nm n-Si:0.45N film at different temperatures. Relative MR divided by $T^{*1/2}$ (see lower inset) has overlapping $g\mu_B B/k_B T$ dependence, varying with $B^{1/2}$ at high field and with B^2 at low field (upper inset), consistent with prediction by Eq. (2.1) shown as solid curves.

In the same Fig. 2.5-2.6 and Fig. 2.8, we have also plotted the theoretical predictions as solid curves for $\tilde{F_\sigma} = 0.75$ and $\alpha/\sigma_o = 5.76 \times 10^{-3}$. They are in excellent agreement with the experimental data including: (i) from the first term of Eq. (2.1), the $T^{1/2}$ dependence at low temperature (Fig. 2.5b), (ii) from the second term with $g_3(\tilde{h})$, the $B^{1/2}$ dependence at high field (Fig. 2.5c and Fig. 2.6) and the B^2 dependence at low field (inset of Fig. 2.6), and (iii) from the 3D nature of electron conduction, the orientation independence of magnetoresistance (Fig. 2.8d-e). Indeed, 3D diffusion is also confirmed by (i), because while 1D/2D diffusion too predicts more interference at lower T, it gives very different scaling laws that are unsupported by our data (Fig. 2.8f). Altogether, the predictions with the same values

of ($\tilde{F}_\sigma$, α/σ_o) agree with more than 45 sets of data plots in Fig. 2.5-2.8, collected over 0.018K-2K, under −18T-18 T and from 0°-180° orientation for films of 8 nm-16 nm and 20 metallic states in the same 11 nm film alone.

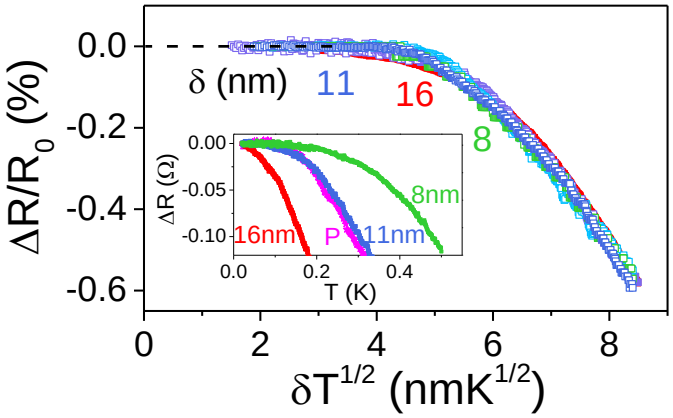

Figure 2.7: Thickness dependent resistance saturation of n-Si:0.45N films. Relative resistance changes of 3 films (in different thickness δ, filled symbols)−one (11 nm) in 3 metallic states (open symbols)−have overlapping $\delta T^{1/2}$ dependence saturating below 4.8 nm·K$^{1/2}$. Inset: Thickness-dependent saturation. Same behavior seen in pressure-transitioned metallic state in 11 nm film (pink stars marked by "P".)

We next examine the size effect when physical dimensions saturates diffusion as $L_{\rm T}$ approaches δ, which is a unique opportunity available to nanofilms because $L_{\rm T} = \sqrt{\hbar D/k_B T}$ can reach δ at a relatively modest temperature of several hundred mK. This causes saturation of QCC, which is illustrated in Fig. 2.7 by plotting normalized coherent diffusion distance, $L_{\rm T}/\delta \sim 1/\delta T^{1/2}$. Taking the bend-over at $\delta T^{1/2} = 4.8$ (nm·K$^{1/2}$), we obtain $D = 3.00 \times 10^{-6}$ m^2/s, which also applies for other metallic states (open symbols in Fig. 2.7), i.e., it is again universal within the above set of n-Si:0.45N samples. (Strictly speaking, in 3D, there should be $x^2 + y^2 + z^2 = 6D\tau$. In the z direction, we get $2D\tau \sim \delta^2$. Therefore, D should be half of the above value, which equals to 1.50 $\times 10^{-6}$ m^2/s.) This D values falls well below the lower limit $D = 10^{-4}$ m^2/s of past studies [75]. Interestingly, although the zero-field resistance saturates below the saturation temperature $T_{\rm s} \sim 0.2$K, the positive magnetoresistance in Fig. 2.6 continues to follow the (T, B) scaling and $g_3(\tilde{h})$ in Eq. (2.1) at 50mK and 18mK. This provides another confirmation of EEI, because if

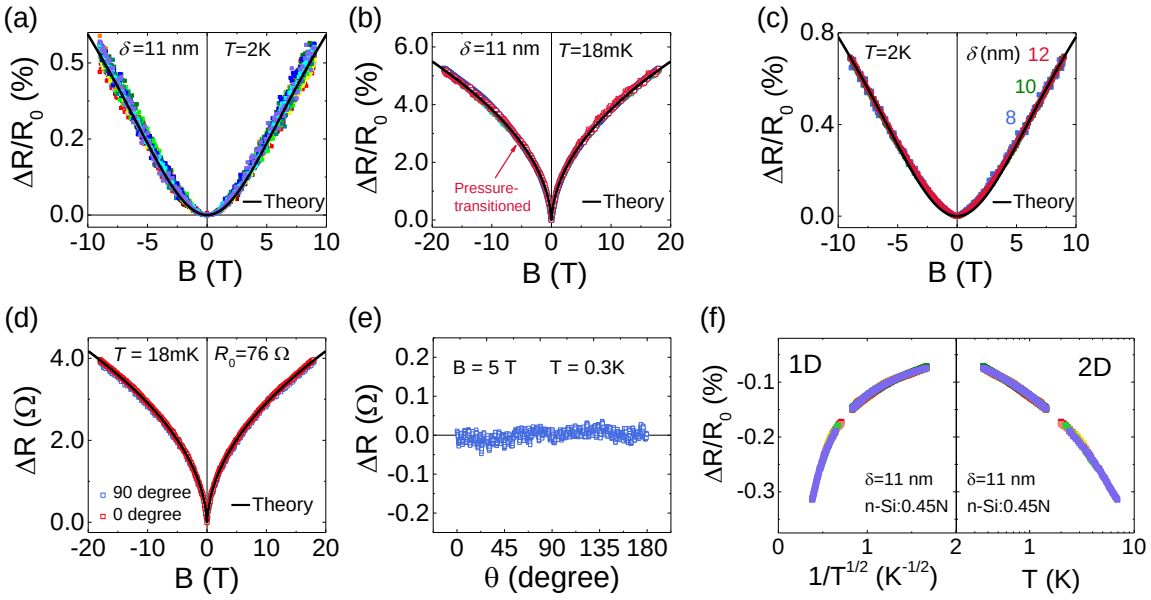

Figure 2.8: Universal QCC $\Delta\sigma/\sigma_o = \Delta R/R_0$ of n-Si:0.45N films, independent of metallic states (a-b), thickness (c), and orientations (d-e, 0 degree: field parallel to film surface; 90 degree: field normal to film surface) at various temperatures (at 2K, 300mK and 18mK) prepared by both electrical and mechanical stimuli, all in excellent agreement with the EEI-dominated 3D theory (solid lines) described by Eq. (2.1) calculated using $\tilde{F}_\sigma = 0.75$ and $\alpha/\sigma_o = 5.76 \times 10^{-3}$ the same as in Fig. 2.5-2.6. Different colors in (a) represent different resistance R_0 whose value is not labeled for simplicity. (f) QCC data represented in 1D/2D scaling form, reproduced from the linear $R-T^{1/2}$ plot in Fig. 2.5b; non-linearity is indicative of lack of agreement.

there were no EEI which allows MR to arise from the Zeeman splitting, then capping the diffusion distance ought to have also capped singular backscattering, hence saturating MR. But the curve below T_s can no longer be fit if one uses g_3's $T^{1/2}$ prefactor. Instead, when L_T is capped by δ, the prefactor $T^{1/2}$ should be replaced by $T_s^{1/2}$. So we have divided the data in Fig. 2.6 by a suitably chosen, $T_s^{1/2}$-like, $T^{*1/2}$ to bring the result to conformity with the $g_3(g\mu_B B/k_B T)$ scaling of Eq. (2.1), and plotted thus chosen T^* in the lower inset of Fig. 2.6. The T^* plot indeed flattens below $T_s \sim 0.2$K, which provides an independent check for the validity of T_s. Lastly, because 0K electrons are always localized in 1D and 2D, crossover from WL to strong localization should have set in when the phase coherent length exceeds δ if conduction in our samples were 1D- or 2D-like [55]. Therefore, seeing resistance saturation instead of divergence at $L_T \sim \delta$ again rules out 1D and 2D conduction.

In fact, since the size constraint of nano metals causes the diffusion to saturate well before L_T reaching/exceeding ζ, there cannot be any crossover to strong localization.

While the above analysis was conducted for EEI-dominated QCC of n-Si doped with N that contains multiple metallic states within the same film obtained by voltage/pressure, pure Si films (e.g., the one studied in Fig. 2.1) also exhibit the same QCC predicted by Eq. (2.1), independent of thickness. Fig. 2.9 shows such similar analysis for other compositions of nanometallic Si, p-Si, n-Si, and Si:0.48O films, which again established the state/thickness independence of QCC in agreement with theoretical predictions from Eq. (2.1) shown as solid lines. Following the same procedure for n-Si:0.45N, two complete sets of three param-

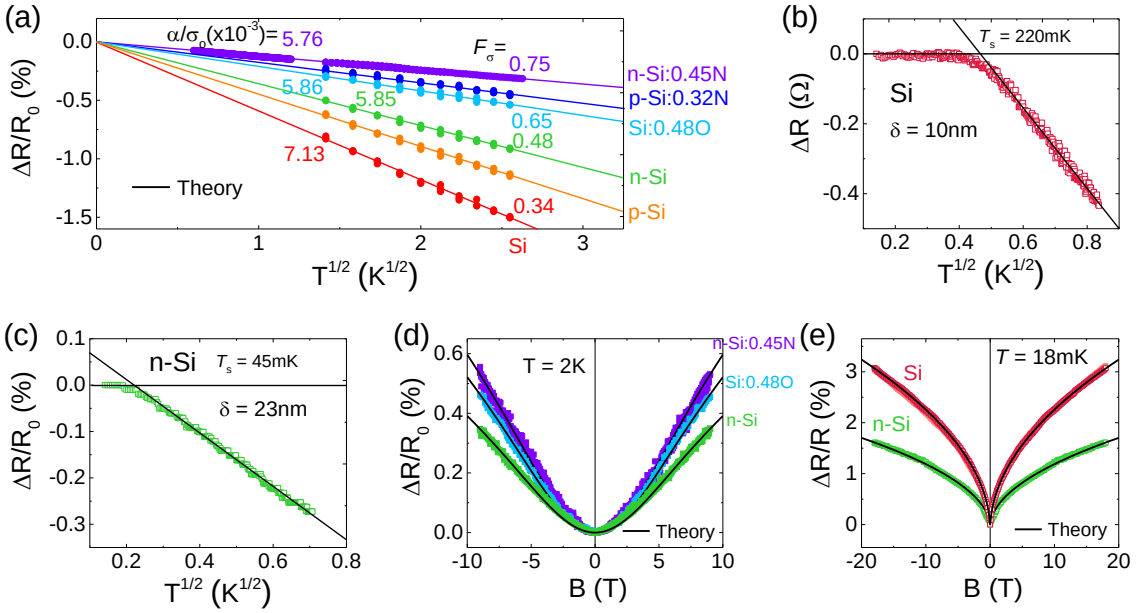

Figure 2.9: State- and thickness-independent relative resistance change and saturation of metallic Si films caused by (T, B) perturbation in various compositions. (a) Relative resistance changes $\Delta R/R_0$ of metallic Si, p-Si, n-Si, Si:0.48O, p-Si:0.32N and n-Si:45N have different slopes against $T^{1/2}$. Each plot of first three compositions includes data of different film thickness, while each plot of the last three compositions includes data of different metallic states. Solid lines are Eq. (2.1) predictions with material parameters (α/σ_o and $\tilde{F}_\sigma$) listed next to lines. (b-c), Resistance saturates at low temperature in 10 nm Si film (b) and 20 nm n-Si film (c), from which diffusivity D can be calculated. (d-e), Relative magnetoresistance of n-Si, Si:0.48O and n-Si:0.45N at 2K (d) and n-Si and Si films at 18mK (e) follows Eq. (2.1) predictions (solid curves) with the same material parameters listed in (a). Each plot contains data from several different states/thickness.

eters ($\tilde{F_\sigma}$, D, σ_o) of Si and n-Si were extracted using three experimental datasets: (i) slope against $T^{1/2}$ in $R-T$ curve below $T_{\min}$, (ii) magnetoresistance at any temperature, and (iii) resistance saturation. Given (i) and (ii) only, partial extraction of $\tilde{F_\sigma}$ and α/σ_o were also done for Si:0.48O. These parameters in various compositions are summarized in Table 2.1-2.2. Furthermore, D and σ_o obtained from model fitting can next be used to calculate other coherent electron properties if we assume $l = 0.27$ nm and a spherical Fermi surface, and identify σ_o with σ_D as follows. First, $v_{\rm F}$ and τ can be calculated using $v_{\rm F} = 3D/l$ and $\tau = l/v_{\rm F}$. Next, with a Fermi sphere and $\sigma_o = \sigma_D$ (which can be written as $\sigma_D = ne^2\tau/m^*$), we can replace n by

$$n = \frac{k_{\rm F}^3}{3\pi^2} = \frac{(m^* v_{\rm F})^3}{3\pi^2\hbar^3} \tag{2.2}$$

Therefore,

$$\sigma_o = \frac{(m^* v_{\rm F})^2 e^2 l}{3\pi^2\hbar^3} = \frac{e^2 m_e^2}{3\pi^2\hbar^3}(\frac{m^*}{m_e})^2 v_{\rm F}^2 l \tag{2.3}$$

Thus the effective mass m^*, relative to the rest mass of electron (m_e), can be calculated by

$$\frac{m^*}{m_e} = (\frac{3\pi^2\hbar^3}{e^2 m_e^2}\frac{\sigma_o}{v_{\rm F}^2 l})^{1/2} = 0.013\frac{\sqrt{\sigma_o l}}{D} \tag{2.4}$$

Finally,

$$k_{\rm F} = \frac{m_e}{\hbar}\frac{m^*}{m_e} v_{\rm F} = 8635\frac{m^*}{m_e}\frac{l}{\tau} \tag{2.5}$$

All quantities in Eq. (2.4) and Eq. (2.5) are in SI units. Based on the QCC data in Fig. 2.5-2.7 and Fig 2.8 for n-Si:0.45N nanofilms and in Fig 2.9 for other Si-based compositions, these calculated properties were calculated and also listed in Table 2.1 for comparison.

In fact, similar calculations can be done without setting $l = 0.27$ nm. According to Aronov and Sharvin [43], the effective electron mass m^* is related to the ratio of $\hbar/2D$. Therefore, we can directly obtain $m^*/m_e = \hbar/2Dm_e$ using extracted D, and then l can be calculated from Eq. (2.4) in which it is the only unknown. Once l is known, τ, $k_{\rm F}$ and n can be easily obtained from $\tau = l^2/3D$, Eq. (2.5), and $n = k_{\rm F}^3/3\pi^2$, respectively. These extracted coherent electron properties are listed in Table 2.2 and they are all close to the numbers in

Table 2.1.

Table 2.1: Properties of coherent conducting electrons in amorphous silicon nanofilms. Values of $\tilde{F}_\sigma$, σ_o, and D were obtained from data fitting to $T^{1/2}$ resistance dependence (Fig. 2.5b), magnetoresistance (Fig. 2.5c, 2.6, 2.8a-e), and resistance saturation (Fig. 2.7). From the above properties, values of v_F, m^*/m_e, k_F, and n were next calculated by setting $l = 0.27$ nm and σ_o to Drude conductivity. Small D and v_F are due to the heavy effective mass caused by a large local ϕ_ep. Additional values of the parameters were obtained from data fitting to the results of other compositions shown in Fig. 2.9 for comparison.

Si-type	$\tilde{F}_\sigma$	$\sigma_o D^{1/2}$ $(\Omega{\cdot}\mathrm{s}^{1/2})^{-1}$	D $(\mathrm{cm}^2/\mathrm{s})$	σ_o $(\Omega{\cdot}\mathrm{cm})^{-1}$	l (nm)	τ (fs)	m^*/m_e	k_F (nm^{-1})	$k_\mathrm{F} \cdot l$	n (cm^{-3})
Si	0.34	289	$1.45{\times}10^{-2}$	2398	0.27	16.76	72.1	10.03	2.71	$3.41{\times}10^{22}$
n-Si	0.48	352	$1.60{\times}10^{-2}$	2786	0.27	15.19	70.5	10.82	2.92	$4.28{\times}10^{22}$
n-Si:0.45N	0.75	346	$1.50{\times}10^{-2}$	2920	0.27	16.20	76.9	11.07	2.99	$4.58{\times}10^{22}$
Si:0.48O	0.65	351	-	-	-	-	-	-	-	

Table 2.2: Properties of coherent conducting electrons in amorphous silicon nanofilms obtained by the same experimental results used in Table 2.1 but starting from $m^*/m_e = \hbar/Dm_e$.

Si-type	$\tilde{F}_\sigma$	$\sigma_o D^{1/2}$ $(\Omega{\cdot}\mathrm{s}^{1/2})^{-1}$	D $(\mathrm{cm}^2/\mathrm{s})$	σ_o $(\Omega{\cdot}\mathrm{cm})^{-1}$	m^*/m_e	l (nm)	τ (fs)	k_F (nm^{-1})	$k_\mathrm{F} \cdot l$	n (cm^{-3})
Si	0.34	289	$1.45{\times}10^{-2}$	2398	40.0	0.47	25.4	6.39	3.00	$8.81{\times}10^{21}$
n-Si	0.48	352	$1.60{\times}10^{-2}$	2786	36.2	0.40	16.7	7.50	3.00	$1.42{\times}10^{22}$
n-Si:0.45N	0.75	346	$1.50{\times}10^{-2}$	2920	38.6	0.38	16.0	7.89	3.00	$2.37{\times}10^{22}$
Si:0.48O	0.65	351	-	-	-	-	-	-	-	

Because quantum correction is usually small for 3D conductivity, σ_o should not be far from the Drude conductivity, which is $\sigma_D = (e^2/\hbar)(n/k_{\rm F}^2)(k_{\rm F}l)$ for electrons of a density n and a Fermi wave number $k_{\rm F}$. For a spherical Fermi surface, $n = k_{\rm F}^3/3\pi^2$. So if we follow Mott and set $k_{\rm F} = \pi/l$, which is the lower limit of wave-like electron in random walk, we obtain Mott's minimum metallic conductivity of $\sigma_{\rm min} = 811.4\ (\Omega cm)^{-1}/l$ (nm). This is 3,005 $(\Omega{\rm cm})^{-1}$ if l=0.27 nm. Our D and α/σ_o give a comparable value for $\sigma_o \sim$ 2,000 $(\Omega$ cm$)^{-1}$ (Table 2.1-2.2), confirming the smallness of the correction, which is the assumption used in deriving Eq. (2.1). Interestingly, from $m^*/m_e = \hbar/Dm_e$, we see a very small D implies a very large m^*. (Again, we verified in Table 2.2, $k_{\rm F}l \sim 2.5$, which exceeds 1 for wave-like electrons and justifies the value of 0.27 nm for l in Table 2.1. So $m^* \sim 30-40m_e$, the rest mass of electron.) Since all the length scales extracted so far in Table 2.1-2.2: the mean free path l = 0.27 nm, the Fermi wavelength $\lambda_{\rm F} \sim$ 0.7 nm, and the coherent diffusion length (for $D = 10^{-6}$ m^2/s) $L_{\rm T} \sim 1/(k_BT)^{1/2} <$ 10 nm, at $T >$0.23K, are all well below the transport dimension (thickness)$\sim$10 nm in our sample, they naturally justify 3D conduction. Therefore, we have quite unexpectedly discovered a 3D metallic phase in a small volume of $\sim$(10 nm)^3: It has slow but robustly coherent electrons, its $\sigma_o \sim$ 3,000 $(\Omega$ cm$)^{-1}$ is $\sim 10^{14}$ times the room-temperature conductivity of undoped amorphous Si and $\sim 10^4$ times that of the most heavily (P and B) doped amorphous Si [76], and it is nested in a very small fraction of our films because the nominal film conductivity is only $\sim 5\times10^{-5}$ $(\Omega{\rm cm})^{-1}$ [2].

2.3.3. Electron-phonon Interaction and Electrical and Mechanical Transition between "Metallic" and "Insulating" states

The heavy m^* may be rationalized by a very strong electron-phonon interaction $\phi_{\rm ep}$, characterized by a coupling strength λ in the Fröhlich Hamiltonian. Usually, the global $\phi_{\rm ep}$

[2]Except for the lowest resistance at 70 Ω, other metallic states of the 11 nm n-Si:0.45N films have a resistance ranging from 100 to 450 Ω. Therefore, subtracting 70 Ω from the resistance values, we obtain a range of 30 to 380 Ω for the lower-bound resistance. For a cell of a radius 250 μm, the corresponding nominal film conductivity is calculated to be from 4.63×10^{-6} to 5.87×10^{-5} $(\Omega{\rm cm})^{-1}$, which is the range of the upper bound. Comparing these values with $\sigma_o \sim$ 2,000 $(\Omega{\rm cm})^{-1}$, we estimate the upper bound of conducting fraction to be 1.5×10^{-9} to 2.0×10^{-8}.

exists everywhere, and an electron with a "band" mass m_b will form a polaron with $m^* \sim 0.0202\lambda^4 m_b$ [77]. But if $\phi_{\rm ep}$ only exists at certain local structures such as soft spots next to an O or N in silicon/germanium, then a virtual bound state could be induced on itinerant electrons. Our m^* suggests $\lambda \sim 6.2$, which even exceeds the λ of highly polarizable crystals such as CsI and $SrTiO_3$ if $m_b = m_e$ [77]. To look for evidence of such large ϕ_{ep}, we attempted mechanically induced electronic transitions in O/N-doped films of intermediate thickness and succeeded in lowering their resistance by as much as 10^5 times. These films were first preconditioned to reach an insulator state by applying a $\sim +1$ V voltage, at 2K and 300K, to the Pt electrode, as already shown in Fig. 2.4a, for which a simplified version is reproduced as $R - V$ curve in Fig. 2.10a to guide the following discussion. Many other examples in Appendix A also verified that the insulator state can transition back to the metallic state, or to any number of metallic states of an intermediate resistance, at ~ -1 V. So the transition is reversible under electrical stimulation. However, we will find below that mechanically induced transition can only go one-way, from the insulator state to the metallic state(s).

We used two interchangeable means to trigger the transition: a hydraulic pressure $P_{\rm H}$ lasting for $\sim$ 1 minute (Fig. 2.10b), and a magnetic pressure $P_{\rm B}$ lasting for as short as 10^{-13} s (Fig. 2.10c). These pressurization experiments, during which no voltage was applied, have been described elsewhere for other nanometallics [15], so only the results are presented here. As $P_{\rm H}$ increased from 2 MPa to 1 GPa, it resulted in a higher transition yield and a lower average resistance in Fig. 2.10b, in which the statistics are represented by the cumulative probability in Weibull $\ln[\ln[1/(1-p)]]$ scale vs. resistance R obtained after various P_H treatments (each curve contains $\sim$ 50 cells from an array, each cell being one datum point on the curve). Likewise, as $P_{\rm B}$ increases with decreasing r in Fig. 2.10c, the transition yield of previously insulating cells (blue ones) increases, resulting in metallic states (red ones) with lower and lower resistance. Note that $P_{\rm B}$ lasted only 10^{-13} s, which is how long it took for an electron bunch that delivered P_B to travel past our samples [67]. In both experiments, the metallic state thus rendered can voltage-transition back to the insulator state, with the

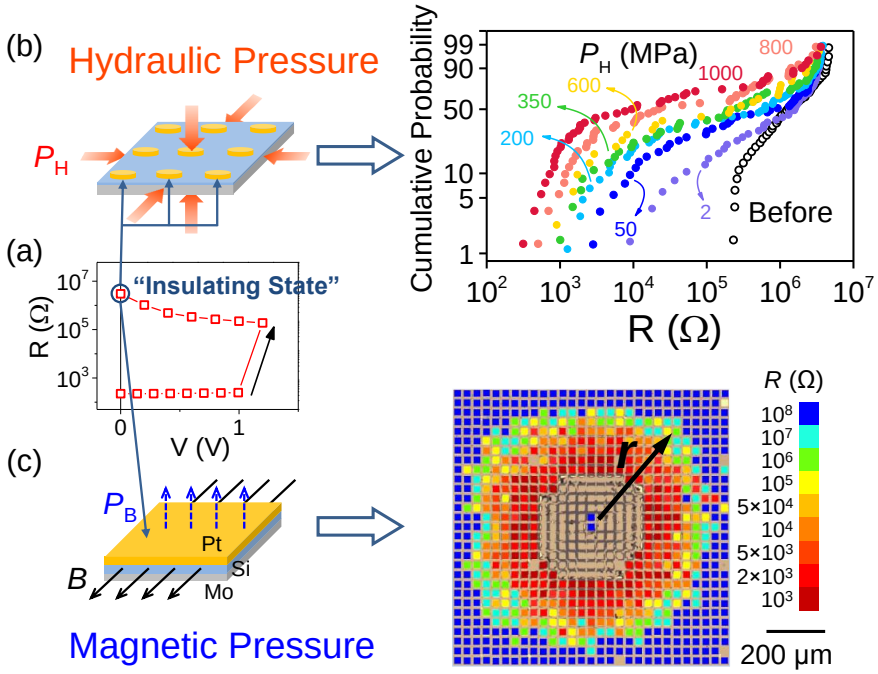

Figure 2.10: Electromechano-stimulus-triggered insulator-metal transition of amorphous Si films doped with O/N. (a) Before applying mechanical stress, all cells in device arrays were preconditioned to insulator state by applying $\sim +1$ V to Pt electrode (yellow), following $R-V$ metal-to-insulator transition curve reproduced from Fig. 2.4a. (b) Hydraulic pressure P_H (schematic on left) applied to Si:0.48O cells lowers resistance from initial distribution ("Before") to new distributions in Weibull plot (~ 50 cells in each distribution curve, each cell being one datum point on the curve), shifting left with increasing P_H. (c) One electron bunch hitting $r = 0$ generates one 10^{-13} s pulse of magnetic far field ($B \sim 1/r$) and magnetic pressure $P_B \sim 1/r^2$ inside n-Si:0.45N cells. (Each colored "dot" is a 20 μm cell.) Cell resistance (all preset to $\sim 10^8$ Ω, corresponding to dark blue at $r > 250$ μm) lowered to value color indicated according to color spectrum on right. Excessive P_B generates excessive biaxial tension in top electrode (schematic on left) and ruptures it (uncolored earth-tone cells at small r), but there is no change in two center cells because $B = 0$ there. Lower bound estimate for P_B: $r = 40$ μm (electron bunch boundary), $\sim$ 1,950 MPa; $r = 180$ μm (rupture boundary), $\sim$ 96 MPa; $r = 390$ μm (transition boundary), $\sim$ 21 MPa.

same transition curves as seen before in Fig. 2.4a (see a comparison in Appendix A). In fact, pressure-transitioned films gave the same (T, B) response as voltage-transitioned films in Fig. 2.7 and Fig. 2.8. However, while voltage can trigger two-way transitions, pressure can only induce the insulator-to-metal transition. Importantly, too, transition was not seen in films not doped by O or N, so the most stress-responsive sites are in the vicinity of Si-O/N-Si bridges.

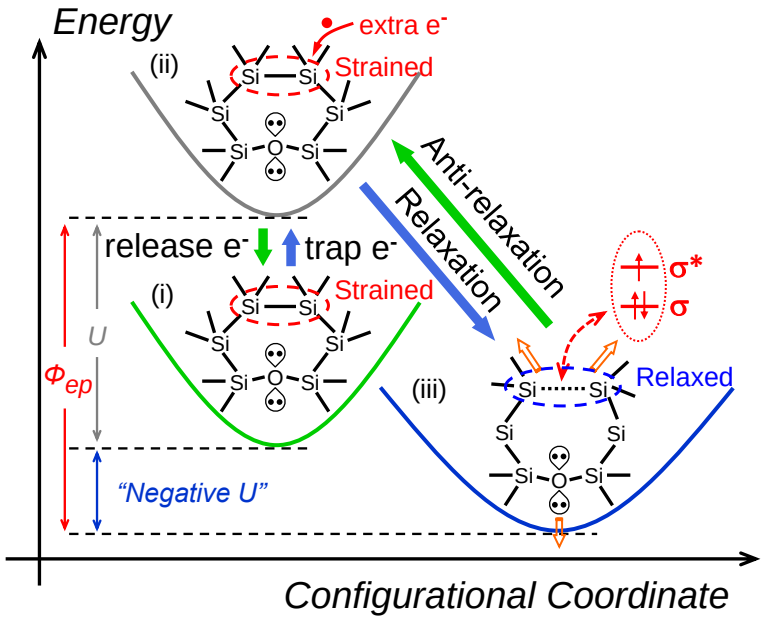

Figure 2.11: Energy-configuration coordinate diagram specialized to a strained Si-Si bond next to Si-O-Si: (i) Initial stable state (strained Si-Si bond); (ii) metastable state with positive Hubbard-U (extra electron entering strained Si-Si region); (iii) stable state (Si-Si triple bond−two bonding electrons+one anti-bonding electron); (arrowed) relaxation caused by longer bond length and electron repulsion with negative U enabled by $\phi_{\rm ep}$ due to relaxation. Interpretations: (a) Voltage delivers extra electron to trapped site; opposite voltage destabilizes trapped electron. (b) Pressure does not deliver electron but triggers detrapping by forcing (arrowed) anti-relaxation from (iii) to (ii). (c) Stably trapped electron in (iii) exerts long-range repulsion against itinerant electrons.

These results are explained by the energy-configuration diagram (Fig. 2.11) of Street and Mott [78]. The diagram was originally proposed for spin-paired bipolarons in highly polarizable chalcogenides [79]. In poorly polarizable Si and SiO_2, it only applies to some ultrasoft, thus highly polarizable Si-O/N-Si bridges. In Fig. 2.11, we depict one possible bond-electron evolution in which an ultrasoft bridge serves as a negative-U center where electron attachment (trapping) helps relieve a strained (Si-Si) bond nearby. But a new possibility also arises: One can mechanically force a relaxed bond back to the strained configuration, thereby destabilizing the trapped electron and prompting detrapping. A negative U is realized in the Si-O neighborhood if the surrounding is so soft that the newly formed bond(s) can easily adjust in length/orientation to lower electron repulsion without incurring

much elastic energy. It also helps to have an initially strained Si-Si and Si-O bonds that arise from O incorporation. This all amounts to a large local $\phi_{\rm ep}$ that overcompensates the positive Hubbard U: $\phi_{\rm ep} - U$ is the negative U that stabilizes a trapped electron.

Assuming trapped electrons can Coulomb blockade itinerant electrons to engender an insulator state, we can now explain all the observations of pressure transitions as follows. (a) It is possible to mechanically force out a trapped electron to return to the metallic state, but not vice versa. (b) The transition can be as fast as the period for one atomic vibration, i.e., 10^{-13} s. (c) Because extreme softness is statistically distributed among soft spots, the transition yield is statistical. (d) Without O/N doping, a strained Si-Si bond at a low-density soft spot can have a localized $\phi_{\rm ep}$ and cause a virtual bound state thus increasing m^*, but unlike the more severely distorted O/N heterogeneities it cannot trap electron.

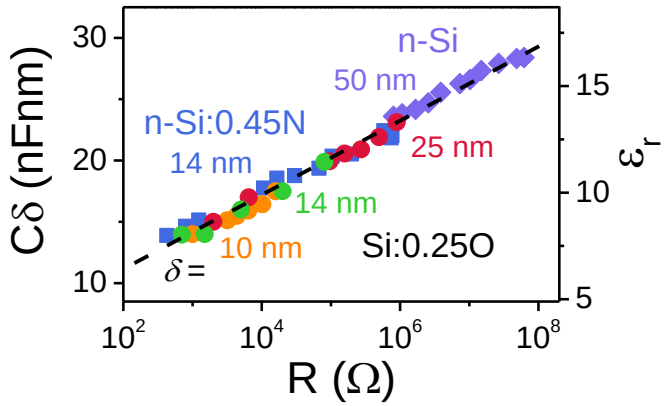

Figure 2.12: AC capacitance C correlates with resistance R; measured at 300K. Different Si nano metals in different thickness δ follow same trend when C is normalized by $1/\delta$. Right: Calculated relative dielectric constant.

Finally, anticipating a tiny fraction of soft spots, one might not have expected any anomaly in AC capacitance measurements of insulator films. Surprisingly, however, the AC capacitance C correlates with R in Fig. 2.12: When the resistance decreases from 800 MΩ to 500 Ω, the capacitance decreases by $\sim 50\%$. This may be explained by referring to their equivalent circuit, made of a parallel set of R and C. Since the higher resistance state has a larger RC constant, its AC characteristics will more readily reflect the capacitive component in

the circuit, hence an apparently larger C (more details can be found in Appendix A). This example illustrates that the nested metallic phase despite its tiny fraction can have an effect on the mean-field properties of nanometallic films. Further discussions on the resistance non-volatility and transition polarity will be omitted except to note that they hinge on the work-function difference between Pt and Mo electrodes.

2.4. Discussion

Although Si and Ge crystals can be substitutionally doped by electron donors or acceptors to induce an insulator to metal transition [80, 81, 82], similar doping of amorphous Si even at the heaviest level cannot ameliorate network's random potential. This is consistent with our expectation for strong localization in amorphous Si, which has a band gap $\sim$2 eV. Therefore, despite heaviest doping and a $10^{10}\times$ enhancement of room temperature conductivity [76], its value reaches only 0.02 $(\Omega\cdot\text{cm})^{-1}$, which is well below Mott's minimum conductivity for metals. We now see, however, that Mott's minimum conductivity does exist along a 3D conducting network in undoped amorphous Si nano metal, but its fraction is very low and it cannot be extended beyond a volume $\sim(10\text{ nm})^3$ or $\sim \zeta^3$. Doped, metallic Si and Ge single crystals of macroscopic dimensions are known to manifest QCC, mostly dominated by 3D EEI [80, 81, 82]. Remarkably, 3D EEI-dominated QCC is also demonstrated in amorphous Si nano metals here, albeit again along the same conducting network of a small volume fraction in a nano volume. While this is a totally unexpected discovery for bulk insulators since QCC has only been seen in bulk metals in the past, its physics becomes immediately transparent once we realize that the nanometallic samples, while made of bulk insulators by "nanosizing", are indeed a metal. Importantly, this remarkable transformation provides a new paradigm to view and utilize random insulators of strong localization: They can provide nano metals that share the same features of conventional metals, yet with invariably embedded negative-U centers of strong electron-phonon interaction these nano metals can be rendered "switchable"—to reliably undergo reversible metal-insulator transition under a modest electrical stimulus, thus offering on-off functionality for potential applications such

as memory devices. Such functionality is only available to nano metals and not to any conventional metal.

2.4.1. The Smooth Thickness-Triggered Transition

We described two transitions in this work, one is continuous, the other is hysteretic. (a) The voltage or stress triggered transition is a genuine metal-insulator transition with bistable states in one sample (as later shown by the hysteresis curves, which further implies first-order phase transition). (b) The smooth transition in Fig. 2.1 does not signal any change in state variable, such as carrier concentration, diffusivity, mean free path, localization length, Fermi-liquid parameter. Instead, it is a behavior transition for conductivity or resistivity, which is a function of sample size or transport length. (That is, conductivity is a non-local property, thus sensitive to the boundary condition—in this case, the transport length.) Specifically, the behavior transition occurs to reflect when the transport length (or sample size) becomes smaller or larger than the localization length, and such transition is continuous and smooth involving no discontinuity. Below we will elaborate the idea using experimental data.

The behavior transition in Fig. 2.1a is illustrated by three $R(T)$ behaviors—having three different shapes depending on the transport length or sample thickness. The transitions between different types are completely smooth, which share the same localization length as demonstrated in Fig. 2.1b, which plots the 0K resistance against δ. We first refer to the solid symbols: they follow an exponential law, $\exp(\delta/\zeta)$, which defines the localization length that seems to be the same for both type II and type III behavior. To demonstrate that this also extends to type I, for which the 0K resistance cannot be measured because it lies outside the instrumental range, we compared the 100K resistance, shown as hollow symbols in Fig. 2.1b, which again seems to follow the same exponential dependence indicating the same localization length. (In reality, there is probably a small upward off-set going from Type III (green) to Type II (blue), and again a small upward off-set going from Type II (blue) to Type I (red), reflecting the change of transport mechanisms. But since all

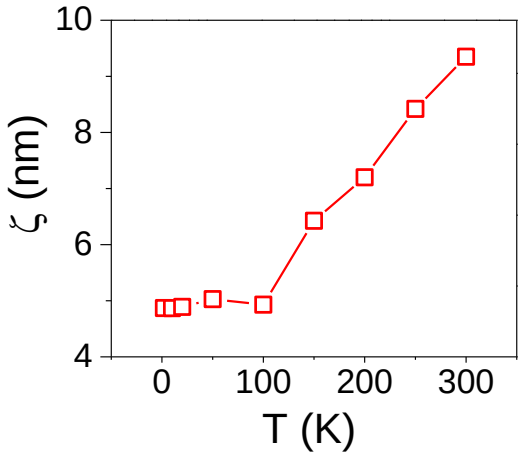

Figure 2.13: Extracted ζ from the linear fitting of $\ln R_T$ vs. δ against temperature T. Higher temperature ($\geq$ 100K) fitting includes data of thicker Si film, whose resistance exceeds measurement limit at lower T.

the transport mechanisms (including variable range hopping) involve the overlap of electron wave functions, which extend in an exponential manner, its exponential dependence mostly dominates the plot, giving apparently the same localization length ~4.9 nm despite the small off-set.) We have repeated the same analysis at other temperatures, and plotted the apparent localization length in Fig. 2.13. (Below 50K, only the thinner thickness samples were analyzed because the resistance of the thicker sample exceeds the instrumental limit.) It shows that while the apparent localization length that applies to all the samples gradually increases with temperature because of the growing contribution of (inelastic) thermal activation, there is no underlying discontinuity and all three types of behavior transition smoothly.

2.4.2. Fractional Conducting Network and Uniformity of Nanometallic Si

Naturally, the small fraction of the conducting network begs the question of uniformity in nano metals, which is best answered based on statistical empirical evidence. First, to answer whether the film is flat enough to avoid any short between the top and bottom electrodes, we point to the fact that slightly O/N doped films can all be reliably switched between the metal state and the insulator state with area-scalable resistance, which would

be impossible if they are shorted. Moreover, shorts of electrode materials, Pt or Mo, would have provided entirely different QCC. For example, Pt and Mo should feature strong spin-orbit interaction, which is known to give rise to weak antilocalization with temperature and magnetic dependences opposite to what we see in Fig. 2.5-2.6. (For example, we did not see any cusp-like MR at high temperature, which is a common signature of weak antilocalization [35].) Therefore, any possibility of Pt or Mo shortage in our ∼10 nm-thick films can be ruled out. In fact, if there were any Pt or Mo short, we could not have successfully used the subtraction method to remove the parasitic resistance of the electrodes and to demonstrate the universal $\Delta R/R$. Likewise, any Pt or Mo short would have made it impossible to observe the thickness dependence of the saturation temperature in the inset of Fig. 2.7.

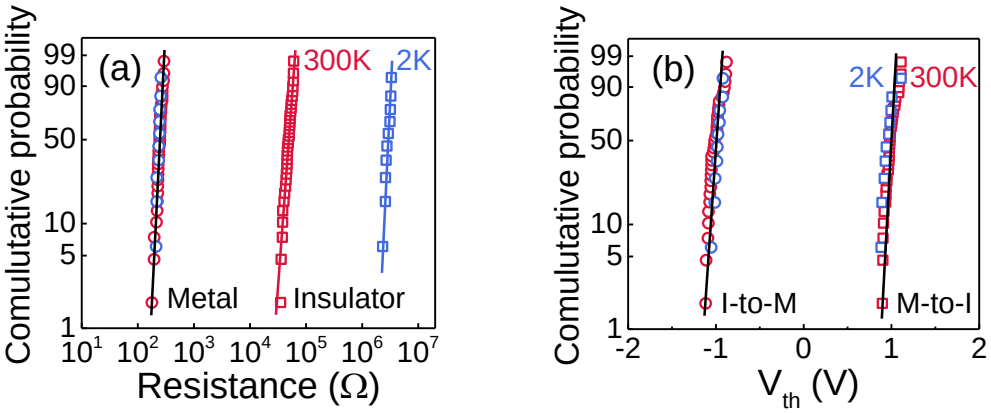

Figure 2.14: Cell-to-cell variation of n-Si:0.45N films in metal and insulator states shown in Weibull statistics plots for (a) resistance of metallic and insulating cells at 300K (35 cells each) and 2K (10 cells each), and (b) threshold voltage $V_{\rm th}$ to switch between two states at 300K (35 cells) and 2K (10 cells). Narrow distributions in (a-b) indicate film uniformity and sample-to-sample reproducibility.

Regarding spatial uniformity, we point to the excellent reproducibility of our data from sample to sample, e.g., between different films of the same thickness, or between different cells of the same film, which has already been demonstrated by the device uniformity date of two sizes in Appendix A. Here another illustration is given by the Weibull statistics at 300K and 2K of (a) the resistance of the insulator state and the metal state of different cells prepared under the same condition (Fig. 2.14a), and (b) the voltage used to switch between the two states (Fig. 2.14b). At both 300K and 2K, they are all narrowly distributed,

which is a testament of statistical uniformity. (Consistent with Fig. 2.4, only insulator resistance is strongly dependent on temperature.) Lastly, although we cannot directly probe the uniformity at the $(10\text{ nm})^3$ scale, once again the overlapping tens of $\Delta R/R$ curves of various metallic states from various samples strongly speak for the underlying uniformity at least on a statistical basis. Yet one cannot rule out the possibility that some much smaller, isolated conducting networks, such as ones that extend to the scale of, say $(1\text{ nm})^3$, exist in our films, or exclude the scenario that what it takes for a $(10\text{ nm})^3$ pathway to establish communication between the two electrodes is to provide some short-distance inter-island connections. This may explain the surprisingly long localization length of 4.8 nm, in that the actual localization length to be overcome in inter-island connections may be much shorter. Regardless, the fact that the overall properties of nano metal cells are rather uniform (including the universal $\Delta R/R$) and the robustness of the $R_{0\text{K}/100\text{K}} \sim \exp(\delta/\zeta)$ relation observed over many orders of magnitude suggest that these islands, if they do exist, are relatively uniformly distributed throughout the nano metals.

Because the conducting network only constitutes a small fraction of nano metal, we cannot directly obtain its 0K, zero-field conductivity σ_o from the film conductivity itself. This is unlike the case of other QCC studies in which σ_o can be directly measured and is not a material parameter to be extracted from model fitting. This obstacle to data analysis, however, is more than compensated by our advantage of being able to witness resistance saturation, which signals the diffusion distance reaching the sample thickness, hence allowing a direct determination of $D-$this is usually not feasible in other QCC studies on much larger samples. Another advantage of studying nano metals is that they render magnetic length irrelevant so that the only magnetic effect must come from EEI, *via* the Zeeman splitting that biases its diffusion channels. This makes our MR analysis rather definitive. On the other hand, we cannot completely rule out the possibility that interference of self-crossing non-interacting electrons can somehow contribute to the temperature dependence of QCC. (Such contribution can give rise to a $T^{p/2}$ dependence via electron's inelastic scattering time; for example, if $p = 2/3$ as from 3D electron-electron scattering, then the resulting $T^{1/3}$

dependence may not be easily distinguishable from the $T^{1/2}$ dependence seen in Fig. 2.5b.) In the next Chapter, we will purposefully introduce spin-orbit interaction to nano metals to add another set of distinct temperature and field dependence to help separate these contributions.

2.4.3. QCC as a Probe for Ultrasoft Local Structures

Lastly, our study has provided new insight into electronic transitions in amorphous insulators and their phononic connection to soft spots [83, 84, 85] in Si and Ge, where these features are made more prominent by O or N doping. But pressure-responsive nanometallic transitions have also been observed in other nano metals, which are made of random insulator-metal "alloys" such as $Si_{0.95}N_{1.33}(Pt,Cr)_{0.05}$ [15] and random Mott insulators such as HfO_2 and Al_2O_3 [86, 87] (presented in Appendix B). Therefore, although their profound effects—on coherent electron's effective mass at low temperature and on electron trapping at all temperature—are only unmasked here for the first time, ultrasoft local structures with a negative U could be ubiquitous for all amorphous inorganic insulators. Although these ultrasoft centers are very scarce in population, once electrons are trapped there they do exert a huge effect on conductivity because of the long-range Coulomb potential. This makes our electrical measurement an extraordinarily sensitive probe to these centers, which will complement any future direct structural/functional probes of high sensitivity to these local structures of extreme softness in amorphous networks to gain a better understanding of random materials.

2.5. Conclusions

1 There is a continuous transition from random insulator to metal when the sample size is reduced. The nanometallic state thus obtained contains robust electrons diffusing extensively and coherently in the random network at low temperatures.

2 In amorphous Si, 3D electron-electron interaction is responsible for the temperature and magnetic-field dependence of quantum correction to conductivity. As the diffu-

sion distance of coherent electrons reaches the dimensions of nano metals, quantum correction to conductivity saturates, but not the magnetoresistance that arises from the Zeeman splitting.

3 Controlled electron-phonon interaction can be introduced into Si and Ge by doping them with O or N, which facilitates local soft spots in the random network to trap electrons. Trapping, moreover, is tunable by a modest stress or voltage, enabling stress or voltage-induced insulator-to-metal transition.

4 The above size effect, coherent electron diffusion, quantum correction to conductivity, soft-spot-mediated electron-phonon interaction, and nanoscale insulator-metal transition, are expected to be common features of nano metals made from random insulators, making them suitable for functional electronic applications such as resistance-switching memory.

CHAPTER 3 : Weak Localization with Spin-Orbit Interaction in Nanometallic Electron-Doped Nitride Films

3.1. Introduction

Having unraveled the QCC, dominated by electron-electron interaction (EEI), in amorphous Si, we next seek for new tools to reveal more quantum interference phenomena in nano materials. In particular, we would like to have the freedom to systematically tune electron diffusivity D, which in Si nano metals remains remarkably constant regardless of dopant types/concentrations (Table 2.1-2.2). Such freedom will allow us to more directly probe the interplay between the random walk and transport length in nano scale. Outside Si, the concentration range and the type of dopants that can render nanometallicity in random insulators are much wider [12, 13]. For example, in $SiN_{4/3}$:xM, where M is an atomically dispersed metal, the metal can come from many parts of the periodic table including the main group and transition metals, and x can vary from a few percent to about 20% while the character of nano metals is maintained provided the film thickness is appropriately adjusted [14, 15]. Indeed, since a higher x is known to allow a thicker film to remain nanometallic, it is likely that it can also increase electron diffusivity. Of course, a higher x is also likely to provide more electrons thus to more efficiently screen the random fields, especially those arising from the Coulombic repulsion between trapped charges and itinerant electrons that is known to be critical for conductivity and resistance switching. In addition, metal concentration may influence EEI by altering the Fermi liquid characteristic $\tilde{F}_\sigma$. Therefore, studying $SiN_{4/3}$:xM over a range of x is likely to expose richer interference phenomena than seen already in amorphous Si.

Since the compositional universe of nanometallic $SiN_{4/3}$:xM is extremely large, more consideration on material selection is advisable before undertaking an experimental study. One important issue is the importance, or lack of weak localization (WL), in such materials. WL often coexists with EEI in disordered electron systems, as commonly seen in mesoscopic con-

ductors in 1D (Si inversion layers [88]), 2D (topological insulator thin films such as doped Bi_2Se_3 [89] and graphene [90]), and 3D (B doped Si [91]). In nano amorphous Si, however, we failed to see WL. In part, this is because it was impossible to see the WL contribution in a magnetic field anyway in a nano system. According to Eq. (1.44), quantum interference that gives rise to magnetoresistance (MR) is dictated by the magnetic length $L_B \sim 1/B^{1/2}$. For any reasonable field, however, L_B is much longer than the transport length (10 nm) or the diffusion length in such nano system, so the field cannot cause any significant dephasing to a set of conjugate waves that give rise to the MR of the WL origin. As a result, in studying nano systems, we are deprived of a powerful tool—MR—which has been commonly used to differentiate EEI and WL in mesoscopic experiments [90, 91, 92, 93, 94]. To overcome such loss, we have decided to introduce another tool to help differentiate different contributions. This is to use spin-orbit interaction (SOI), which is known to cause weak anti-localization (WAL) that in many ways—though not all—has the opposite effect of WL. As first demonstrated by Bergmann [2], WAL can results in a crossover: It dominates over longer characteristic time, only giving way to WL at shorter characteristic time. Although Bergmann's experiment was conducted with 2D films and used magnetic field to follow MR only, the same idea is applicable to 3D QCC without resort to MR if we can sample a large coherent-time scale by exploiting the temperature domain. This is the approach taken in our work. Specifically, we will let M be Pt, which as a heavy element will introduce powerful SOI that, in essence, plays the role of a "contrast agent": its WAL will shine against the WL background.

As will be demonstrated in this chapter, we have indeed observed a crossover from the WL dominance to the WAL dominance, at a characteristic temperature, in the 3D QCC of Si_3N_4:Pt nano metals. Referring to the time interval for inelastic scattering as τ_i and the time interval for SOI-controlled scattering as τ_{so}, this signals a crossover from $\tau_i \ll \tau_{so}$ (WAL much weaker than WL) at high temperature to $\tau_i \gg \tau_{so}$ (WAL much stronger than WL) at low temperature. Since WAL leads to a positive QCC, as opposed to WL that leads to a negative QCC, a novel resistance maximum is observed at the crossover temperature,

which we shall call $T_{\max}$. This feature, which is expected in all dimensions, is the signature to be looked for in our experiments. The appearance of $T_{\max}$ will ascertain both WAL and WL, and a quantitative analysis of QCC will allow further definitive assessment of the EEI, for any EEI will alter the fine balance between the positive and negative QCC at around $T_{\max}$. Additional MR experiments will provide further confirmation of the above picture and complete the quantification of all the underlying material parameters that pertain to all three contributions and the observed quantum interference phenomena.

The organization of this chapter is as follows. In the next section, we will recapitulate the major theoretical consideration that governs EEI, WL and WAL, to outline the strategy for analysis. In Section 3, we will first present QCC, then MR, and show that all the experimental features observed can be quantitatively explained by the analysis in Section 2. This will be followed by discussion in Section 4. Section 5 will conclude on this study of coherent 3D electrons in nano materials revealing all contributing mechanisms in quantum interference phenomena.

3.2. Theoretical Background

3.2.1. WL/WAL Crossover

To a good approximation, the QCC originating from WL/WAL and EEI mechanisms are additive [3, 4]. In 3D, the relative change of conductivity at zero field with reference to the 0K (and 0 T) conductivity σ_o is

$$\frac{\Delta\sigma^{\mathrm{T}}}{\sigma_0} = \frac{e^2}{\hbar}\frac{1.3}{4\pi^2}\sqrt{\frac{k_B}{2\hbar D}}\frac{1}{\sigma_0}\left(\frac{4}{3}-\frac{3}{2}\tilde{F}_\sigma\right)T^{1/2} + \frac{e^2}{\hbar}\frac{1}{2\pi^2\sqrt{D}}\frac{1}{\sigma_0}\left[\frac{3}{2}\Delta(\tau_\phi^{*-1/2}) - \Delta(\frac{1}{2}\tau_\phi^{-1/2})\right] \tag{3.1}$$

In the above, the first term is from EEI in Eq. (1.35) and the second term is from WL/WAL in Eq. (1.13), where Δ means taking the difference between the values at the current temperature and at the reference temperature, which is 0K. According to Eq. (1.10)-(1.11) [24], τ_ϕ is primarily the time τ_i between inelastic scattering—it is temperature-dependent following

the power law $\tau_i \propto T^{-p}$, and τ_ϕ^* is related to the time between spin-spin scattering—which has its own time of τ_s—and/or spin-orbit scattering time—which has its own time of τ_{so}, in addition to τ_i. These latter two times are dependent on the impurities that cause such scattering, but are otherwise independent of temperature. For simplicity, we shall let $\tau_i = a\hbar/k_BT$, where a is a fitting parameter, possibly temperature independent, so that it can be directly compared to the relaxation time of an electron quasiparticle, which is $\tau_T = \hbar/k_BT$. That is, $a > 1$ if relaxation due to impurity scattering is less important than that due to EEI, and vice versa. This assumption is justified as follows: Because p is of the order of 1, being 2/3 for 3D electron-electron scattering and 1 for 2D electron-electron scattering, and the prevailing scaling relation for 3D conduction comes in the form of $\sqrt{D\tau}$, so it is actually difficult to differentiate different p values by temperature scaling laws, especially for small relative resistance changes ($\Delta\sigma/\sigma_o$ is $\sim 1\%$) even when the data are collected over a rather wide temperature range. On the other hand, choosing $p = 1$ certainly simplifies the representation of EEI and WL because they now follow the same temperature scaling relation.

We now differentiate two cases.

(i) WL+EEI:

This is the case without spin-orbit interaction and without magnetic impurities. It satisfies $\tau_i \ll \tau_s, \tau_{so}$, $\tau_\phi \approx \tau_\phi^* \approx \tau_i$, and Eq. (3.1) reduces to

$$\frac{\Delta\sigma^{\mathrm{T}}}{\sigma_0} = \frac{e^2}{\hbar}\frac{1.3}{4\pi^2}\sqrt{\frac{k_B}{2\hbar D}}\frac{1}{\sigma_0}\left(\frac{4}{3} - \frac{3}{2}\tilde{F}_\sigma\right)T^{1/2} + \frac{e^2}{\hbar}\frac{1}{2\pi^2\sqrt{D}}\frac{1}{\sigma_0}\Delta(\tau_i^{-1/2}) \tag{3.2}$$

Therefore, the WL contribution (the second term) causes the resistance to increase with decreasing temperature, but this increase is indistinguishable from that from the EEI contribution when $4/3 - 3/2\tilde{F}_\sigma > 0$: They have the same temperature dependence of $T^{1/2}$. Therefore, if EEI is strong, it is difficult to determine whether WL plays a role or not using the QCC data alone. (This is the case in amorphous Si, in Chapter 2.)

(ii) WAL+EEI:

This is the case with strong spin-orbit interaction (SOI), which may be realized if heavy elements are introduced into the nano material, e.g., in Si_3N_4:Pt—the subject material of this chapter. It satisfies $\tau_{so} \ll \tau_i$, $\tau_\phi^* \approx \tau_{so}$, which is realized at sufficiently low temperature. So in the WL/WAL term, we have $\Delta(\tau_\phi^{*-1/2}) \approx 0$ and $\Delta(\tau_\phi^{-1/2}) \approx \Delta(\tau_i^{-1/2})$. Meanwhile, in the EEI term, a small τ_{so} also cutoffs the thermal dephasing time $\tau_T = \hbar/k_BT$ in EEI below the temperature when $\tau_{so} < \tau_T$. So it caps any further effect on QCC that from the spin-nonzero triplet state associated with $-3/2\tilde{F}_\sigma$ in the first term of Eq. (3.2). (The spin-zero term still sees inelastic scattering, though.) Therefore, after the τ_i-τ_{so} and τ_T-τ_{so} crossovers (which do not differ too much, as it turns out) below a critical temperature $T_{\max}$ (a name that will be justified soon), we have

$$\frac{\Delta\sigma^T}{\sigma_0} = \frac{e^2}{\hbar}\frac{1.3}{4\pi^2}\frac{4}{3}\sqrt{\frac{k_B}{2\hbar D}}\frac{1}{\sigma_0}T^{1/2} - \frac{e^2}{2\hbar}\frac{1}{2\pi^2\sqrt{D}}\frac{1}{\sigma_0}\Delta(\tau_i^{-1/2}) \tag{3.3}$$

Combining Eq. (3.2) and Eq. (3.3) and setting $\tau_i = a\hbar/k_BT$ as justified before, we find, with SOI, it is possible to see a slope change in QCC at the crossover temperature $T_{\max}$

$$\frac{\Delta R^{\mathrm{T}}}{R_0} = -\frac{\Delta\sigma^{\mathrm{T}}}{\sigma_0} = \begin{cases} -\dfrac{\alpha_3}{\sigma_o}\left[\left(\dfrac{4}{3} - \dfrac{3}{2}\tilde{F}_\sigma\right) + 2.176a^{-1/2}\right]T^{1/2} = S_1T^{1/2} & T > T_{\max} \\ -\dfrac{\alpha_3}{\sigma_o}\left[\dfrac{4}{3} - 1.088a^{-1/2}\right]T^{1/2} = S_2T^{1/2} & T < T_{\max} \end{cases} \tag{3.4}$$

Here

$$\alpha_3 = \frac{e^2}{\hbar}\frac{1.3}{4\pi^2}\left(\frac{k_B}{2\hbar D}\right)^{1/2} = \frac{2.05}{D^{1/2}} \tag{3.5}$$

has the unit of $(\Omega{\cdot}\mathrm{m}{\cdot}\mathrm{K}^{1/2})^{-1}$ when D is expressed in the unit of m^2/s. Meanwhile, the two slopes S_1 and S_2 (with a unit of $\mathrm{K}^{-1/2}$) are given by

$$S_1 = -\frac{\alpha_3}{\sigma_o}\left[\left(\frac{4}{3} - \frac{3}{2}\tilde{F}_\sigma\right) + 2.176a^{-1/2}\right] \quad T > T_{\max} \tag{3.6}$$

$$S_2 = -\frac{\alpha_3}{\sigma_o}\left[\frac{4}{3} - 1.088a^{-1/2}\right] \quad T < T_{\max} \tag{3.7}$$

Typically, at relatively high temperature, a resistance minimum is observed at $T_{\min}$ in nano metals (e.g., amorphous Si in Chapter 2), meaning $S_1 < 0$, which is realized unless $\tilde{F_\sigma}$ is very strong. Moreover, since $S_2 - S_1 \sim -\frac{3}{2}\tilde{F_\sigma} + 3.264a^{-1/2}$, it is possible to have $S_2 > 0$ below $T_{\max}$ and $S_1 < 0$ above $T_{\max}$ if both $\tilde{F_\sigma}$ and a are sufficiently small (i.e., weak EEI and strong scattering). A slope-sign reversal of this kind and the appearance of $T_{\max}$ will provide an unmistaken signal for the crossover from impurity-scattering dominance to SOI-scattering dominance, which may be realized by compositional control.

3.2.2. Resistance Saturation

As seen in the previous chapter, zero-field QCC of nanometallic films may saturate at sufficiently low temperature T_{sat}. This occurs when the diffusion distance of coherent electrons, $L_T = \sqrt{D\tau_T}$ (or $L_\phi = \sqrt{D\tau_\phi}$) reaches the sample thickness δ. Since the entire volume of the sample, $\sim (10\text{ nm})^3$, already fully contributes to the QCC, further lowering the temperature will not lead to any more QCC. The saturation temperature may be used to determine the diffusivity D using

$$D = \begin{cases} \delta^2 \dfrac{k_B T_{\text{sat}}}{2\hbar} & a \geq 1 \\ \delta^2 \dfrac{k_B T_{\text{sat}}}{2\hbar a} & a < 1 \end{cases} \tag{3.8}$$

3.2.3. Magnetoresistance

A magnetic field introduces additional effect on QCC, and such effect may be measured by studying magnetoresistance or QCC under the (constant) field-cool/heat condition. Under

a magnetic field, the QCC in Eq. (1.4) for 3D conduction becomes

$$\frac{\Delta R^{\mathrm{T,B}}}{R_0} = \begin{cases} -\frac{\alpha_3}{\sigma_o}\left[-0.77\tilde{F}_\sigma g_3(\tilde{h}) + \left(\frac{4}{3} - \frac{3}{2}\tilde{F}_\sigma\right) + 2.176\left(\sqrt{\frac{eB}{k_BT/D}} f_3(x) + a^{-1/2}\right)\right] T^{1/2} & T > T_{\max} \\ -\frac{\alpha_3}{\sigma_o}\left[-0.77\frac{T_{\max}}{T^{1/2}}\tilde{F}_\sigma g_3(\tilde{h}) + \frac{4}{3} - 1.088\left(\sqrt{\frac{eB}{k_BT/D}} f_3(x) + a^{-1/2}\right)\right] T^{1/2} & T < T_{\max} \end{cases} \tag{3.9}$$

where $\tilde{h} = g\mu_B B/k_B T$ and $x = 4eD\tau_i B/\hbar$. If the WL/WAL-MR contribution is omitted from the above expression, we obtain

$$\frac{\Delta R^{\mathrm{T,B}}}{R_0} = -\frac{\Delta\sigma^{\mathrm{T,B}}}{\sigma_0} = \begin{cases} -\frac{\alpha_3}{\sigma_o}\left[-0.77\tilde{F}_\sigma g_3(\tilde{h}) + \left(\frac{4}{3} - \frac{3}{2}\tilde{F}_\sigma\right) + 2.176a^{-1/2}\right] T^{1/2} & T > T_{\max} \\ -\frac{\alpha_3}{\sigma_o}\left[-0.77\frac{T_{\max}}{T^{1/2}}\tilde{F}_\sigma g_3(\tilde{h}) + \frac{4}{3} - 1.088a^{-1/2}\right] T^{1/2} & T < T_{\max} \end{cases} \tag{3.10}$$

Such omission is usually justified in nano metals. This is because their small dimensions does not allow any appreciable MR until the field is strong, which can be seen from the small ratio of B over T/D, which reduces to the ratio of L_T^2 to L_B^2 in Eq. (3.9)). In fact, even under a strong field, the 3D EEI-MR contribution tends to dominate over the 3D WL/WAL-MR, because $f_3(x)$ saturates to a constant asymptote at large x (i.e., strong field) reflecting the destructive self-cancellation of different paths when the magnetic length is much less than L_T or L_ϕ. In comparison, $g_3(\tilde{h})$ does not saturate at large $\tilde{h}$ (i.e., strong field) but instead follows $\sqrt{g\mu_B B/k_B T}$ reflecting the continued strong influence of the Zeeman splitting.

Another interesting and important feature of Eq. (3.10) is that the EEI-MR does not saturate below T_{sat} (or below $T_{\max}$). This is again because, unlike QCC, EEI-MR derives from the Zeeman splitting, and $g_3(\tilde{h})$ is a monotonically increasing even when $\tilde{h} \to \infty$. This limit is satisfied at 0K: The Zeeman splitting is even more difficult to overcome at lower temperature for electron-electron scattering, which is limited to within an energy k_BT, from either zero energy or from the Fermi energy. Therefore, below T_{sat}, the EEI-MR will increasingly dominate over the QCC terms (WL/WAL and EEI) in (constant) field-cool/heat measurements, making such measurements valuable for detecting and isolating the EEI

contribution.

The direct measurement of MR is also valuable. The relative magnetoresistance $\Delta R^B/R_0$ at fixed temperature T according to Eq. (1.39) is

$$\frac{\Delta R^{\mathrm{B}}}{R_0} = -\frac{\Delta \sigma^{\mathrm{B}}}{\sigma_0} = \begin{cases} 0.77\dfrac{\alpha_3}{\sigma_o}\tilde{F_\sigma}T^{1/2}g_3(\tilde{h}) = 0.77\alpha_3 M T^{1/2}g_3(\tilde{h}) & T > T_{\max} \\ 0.77\dfrac{\alpha_3}{\sigma_o}\tilde{F_\sigma}T_{\max}^{1/2}g_3(\tilde{h}) = 0.77\alpha_3 M T_{\max}^{1/2}g_3(\tilde{h}) & T < T_{\max} \end{cases} \tag{3.11}$$

Here the prefactor M

$$M = \tilde{F_\sigma}/\sigma_o \tag{3.12}$$

has the unit of $T^{-1/2}$ and may be directly compared with the slope S_1 and S_2 of QCC to gain a sense of the strength of the Fermi liquid characteristics $\tilde{F_\sigma}$. Note that below $T_{\max}$, Eq. (3.11) uses $T = T_{\max}$ because it is the spin-nonzero triplet state ($J_z = \pm 1$) that is vulnerable to Zeeman splitting and responsible for the positive MR, and its characteristic time $\tau_T = \hbar/k_B T$ in Eq. (3.11) is capped by τ_{so} below $T_{\max}$ as already discussed in Eq. (3.3). (QCC from the spin-zero and singlet state terms, which do not suffer the Zeeman splitting, is not affected by τ_{so}-τ_T cutoff at $T_{\max}$, and will get saturated below T_{sat}.)

3.2.4. Observables and Material Parameters

Measurements of S_1 and S_2 of QCC, $T_{\max}$ for SOI-inelastic scattering crossover, T_{sat} for saturation of diffusion distance, and M of MR are sufficient for solving five unknowns, which are the material parameters D (and thus α_3), σ_o, $\tilde{F_\sigma}$, a, and τ_{so}. Specifically, (1) τ_{so} can be estimated from $a\hbar/k_B T_{\max}$ if $a < 1$ (or $\hbar/k_B T_{\max}$ if $a > 1$), and (2) D (or α_3) can be calculated by Eq. (3.8). (3) Given α_3 and combining Eq. (3.6), Eq. (3.7), and Eq. (3.12), the solutions of σ_o, $\tilde{F_\sigma}$, and a are obtained from

$$\sigma_o = \frac{4\alpha_3}{3\alpha_3 M/2 - S_1 - 2S_2} \tag{3.13}$$

$$\tilde{F}_\sigma = M\sigma_o \tag{3.14}$$

$$a = \frac{10.654}{\left[(S_2 - S_1)\,\sigma_o/\alpha_3 + 3\tilde{F}_\sigma/2\right]^2} \tag{3.15}$$

In the above, all the quantities are expressed in the SI units. This strategy will be applied in the next section to analyze the data of several compositions of Si_3N_4:Pt.

Lastly, we note that only one equation out of the two in Eq. (3.11), for EEI-MR, is needed in the above procedure; the other one can serve as an independent consistency-check of the theory. For example, in the same manner of Fig. 2.6 in Chapter 3, one can select T^* to make the different temperature branches overlap in the $\Delta R/R_0 T^{*1/2} - \tilde{h}$ plot. (According to Eq. (3.11), $T^* = T$ when $T > T_{\max}$ and $T^* = T_{\max}$ when $T \leq T_{\max}$.) This is because all the branches overlap in the reduced MR plot regardless of whether $T > T_{\max}$ or $T \leq T_{\max}$; so there is also one plot, and it can be described by either equation.

3.3. Results

Normalized $R - T^{1/2}$ plot of nanometallic Si_3N_4:Pt films in Fig. 3.1a shows four transport regimes (I-IV) delineated by three characteristic temperatures for all three different compositions. (I) Above $T_{\min}$, nanometallic Si_3N_4:Pt behaves like a normal metal with a decreasing resistance at lower temperature. It indicates that electrons endure electron-phonon scattering in this regime. (II) Resistance minimum appears at $T_{\min} \sim$ 20—30K, which increases with $f_{\rm Pt}$. It suggests that electrons start to maintain phase coherence over a nonnegligible diffusion distance so the resistance begins to increase linearly with decreasing $T^{1/2}$ due to the quantum correction, given by Eq. (3.2). (III) Resistance maximum occurs at $T_{\max}$ ~3—5K below $T_{\min}$, with $T_{\max}$ itself also increasing with $f_{\rm Pt}$. On the normalized $R - T^{1/2}$ curve, there is a sharp change in the slope and its sign at $T_{\max}$. This is the signature that we are looking for, the crossover from WL to WAL, which causes the opposite temperature dependence according to the prediction of Eq. (3.3). (IV) Resistance saturates

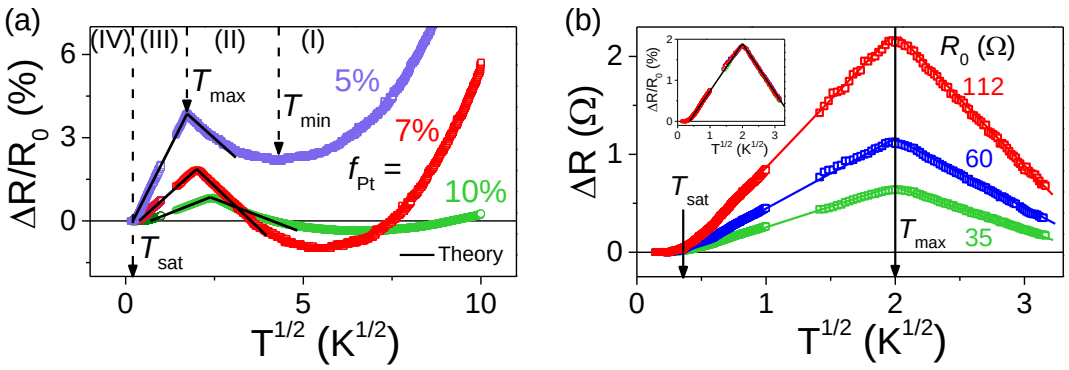

Figure 3.1: (a) Relative resistance change normalized by 0K resistance R_0 against $T^{1/2}$, for three Si_3N_4:Pt films. Four regimes (I-IV) are separated by T_{min}, T_{max}, and T_{sat}, where opposite slopes in (II) and (III) are in agreement with predictions of Eq. (3.4) shown as solid lines. Atomic Pt percentage for (1-f_{Pt})$SiN_{4/3}$:f_{Pt}Pt labeled next to curve. Film thickness $\sim$ 10 nm. (b) Resistance change for 93%$SiN_{4/3}$:7%Pt films in (a) actually contain data in three different metallic states, separately shown here without normalization by their resistance R_0, as labeled. Inset: Different states are self-similar in that their relative resistance—after being normalized by R_0—overlap with each other. These data follow the same T_{max} and T_{sat}, as in (a).

at a millikelvin temperature T_{sat}, most likely indicating that diffusion length has reached the sample dimension so that Eq. (3.8) is satisfied. Below T_{sat}, there is no further change in QCC and the resistance reaches its 0K value R_0. Behavior of the (I), (II), and (IV) type has also been observed for amorphous Si films in Chapter 2. But region (III) is seen here for the first time and we attribute it to the strong spin-orbit interaction from Pt atoms: It causes both τ_i and τ_T to be cutoff by τ_{so}, which results in an QCC of an opposite sign as outlined in the Introduction and last section. Another novel feature of Fig. 3.1a is that the saturation below T_{sat} corresponds to the resistance settling at a lower level, unlike the saturating resistance settling at a higher level as seen in amorphous Si films in Chapter 2. Again, this reflects the Si_3N_4:Pt films have crossovered to the dominance of spin-orbit interaction at low temperatures.

As in the case of nanometallic Si, these features are universal in that multiple metallic states of the same film are self-similar—curves in Fig. 3.1a actually contains overlapping data from several resistance states. This is further illustrated in Fig. 3.1b, in which ΔR of different

states are plotted to demonstrate how they share the same $T_{\max}$ and T_{sat}, and after being normalized by its resistance R_0, they collapse into a universal QCC in the inset. Again, this property suggests different states of the nano metal contain different amounts of the same conducting elements, which also explains why we can remove the parasitic resistance (from electrodes, interfaces, and external loads) by the subtraction method described in Appendix C and [54].

The good adherence to the straight-line behavior allows us to accurately determine the values of S_1 and S_2 from linear fittings (shown as solid lines in Fig. 3.1a). These extracted data are listed in Table 3.1 for later reference. Comparing these values with the theoretical predictions in Eq. (3.6)-(3.7), we note that while the qualitative temperature dependence (i.e., the opposite slope) can be mostly explained by WL and WAL above and below $T_{\max}$, respectively, a quantitative comparison indicates that there must be an additional contribution of EEI in Si_3N_4:Pt films. This is because if there were no EEI, S_2 should be precisely one half of S_1 according to Eq. (3.6)-(3.7), which is inconsistent with the values listed in Table 3.1 for all three compositions. Therefore, these slopes can provide quantitative information of the mechanism involved, specifically $\tilde{F_\sigma}$ and a, which is an integral part of the full determination of the material parameters D, σ_o, $\tilde{F_\sigma}$, a, and τ_{so}.

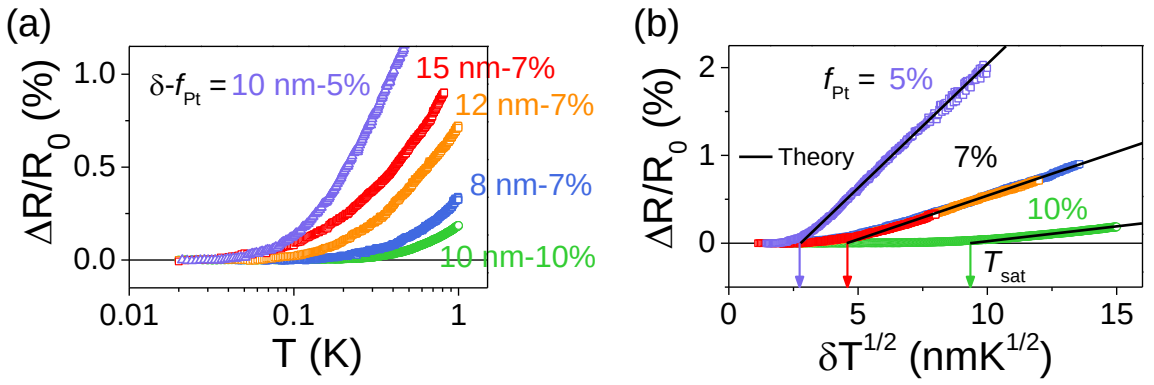

Figure 3.2: (a) Thickness (δ)- and composition (f_{Pt})-dependent resistance saturation of Si_3N_4:Pt films. δ-f_{Pt} information is labeled next to each curve. (b) Relative resistance changes of 3 films in different thickness δ have overlapping $\delta T^{1/2}$ dependence saturating at composition-dependent critical δT_{sat} as marked by the arrow.

We next check the resistance saturation at $T_{\rm sat}$ in more details. As shown in Fig. 3.2a, films of the same Pt composition ($f_{\rm Pt} = 7\%$) in different thickness $\delta = 8$, 12, 15 nm saturate at different $T_{\rm sat}$, suggesting the saturation is related to diffusion saturation, which is thickness-dependent. This is further verified by referring to Eq. (3.8) and plotting $\Delta R/R_0$ saturation in different thickness for 93%$SiN_{4/3}$:7%Pt films against $\delta T^{1/2}$ in Fig. 3.2b: Indeed, $\delta T_{\rm sat}^{1/2} \sim 2D$ is the same for different δ. Films with different compositions are found to saturate at different temperature in Fig. 3.2a. In the normalized plot, their $\delta T_{\rm sat}^{1/2}$ and the slope S_2 are dependent on $f_{\rm Pt}$, indicating different diffusivity D. Using the $\delta T_{\rm sat}^{1/2}$ as marked in the axis of Fig. 3.2a, we can calculate D by Eq. (3.8).

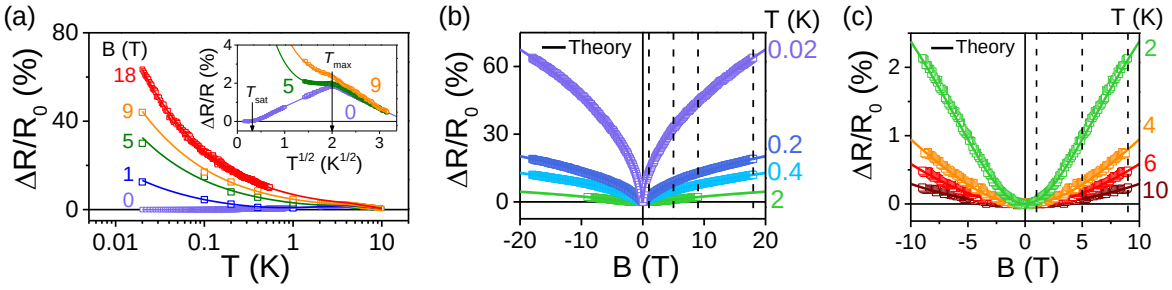

Figure 3.3: EEI-dominated QCC under magnetic field for 8 nm 93%$SiN_{4/3}$:7%Pt films. (a) "Field-cool" $R(T)$ at 18 T (red) does not saturate compared with zero-field curve (purple) reproduced from Fig. 3.2. Data points at other magnetic field extracted at dashed lines in (b) and (c) are also included. Inset: Normalized $R - T^{1/2}$ dependence around $T_{\rm max}$ at three magnetic fields (in T) as labeled. Resistance maximum persists up to 5 T, beyond which only a kink appears at $T_{\rm max}$. All the data agrees with predictions of Eq. (3.10) shown as solid curves. (b)-(c) Non-saturating positive magnetoresistance normalized by 0K resistance R_0 at various temperatures below and above $T_{\rm sat}$ (a), and below and above $T_{\rm max}$ (b). Solid curves are model fitting by Eq. (3.11).

More direct evidence of EEI comes from the field-heat/cool $R(T)$ curves, shown in Fig. 3.3a, under a constant magnetic field. According to Fig. 3.2, if WL and WAL are the only contributions, then under a fixed field we should expect full saturation of resistance below $T_{\rm sat}$. For the 8 nm-thick 93%$SiN_{4/3}$:7%Pt sample, when its diffusion length is capped by the film thickness at $T_{\rm sat} \sim 0.1$K, we found the field-cool/heat $R(T)$ at 18 T (red curve) continues to rise in Fig. 3.3a, even well below 0.1K. This is in sharp contrast to the zero-field $R(T)$ data (purple curve, reproduced from Fig. 3.2) which is completely flat below

0.1K. Therefore, the $R(T)$ curve at 18 T provides direct evidence for EEI, which continues to strengthen below $T_{\rm sat}$ because the normalized Zeeman splitting $\mu B/k_BT$ continues to increase even though the diffusion distance is already capped by the sample thickness. (The same phenomenon was seen in amorphous Si as described in Chapter 2.)

To corroborate this observation, we have also measured MR at various temperatures, shown in Fig. 3.3b-c. From these data, we can construct additional field-cool/heat $R(T)$ curves by comparing the MR under the same field but measured at different temperatures, after taking into account the temperature dependence of the zero field resistance. These reconstructed field-cool/heat $R(T)$ curves are shown in Fig. 3.3a for 1, 5, and 9 T. Again, they confirm that there is no resistance saturation under a non-zero magnetic field, the more so the stronger the field. The effect of the magnetic field, which mostly enhances the EEI, can also be seen on the field-cool/heat $R(T)$ curves at higher temperatures near $T_{\rm max}$. This is illustrated in the inset of Fig. 3.3a. We can see that, because of the increased contribution of EEI, the resistance maximum that persists up to 5 T gives away to a kink at $T_{\rm max}$ at above 5T. Lastly, the existence of EEI is further confirmed in the MR at above $T_{\rm max}$. This is because, above $T_{\rm max}$ when τ_ϕ is relatively small, WL should be the dominant mechanism if EEI were absent. If this is the case, one would expect negative MR above $T_{\rm max}$, say at about 4K. However, the MR shown in Fig. 3.3c from 4K to 10K are clearly positive, so it cannot be just due to WL; indeed, it is almost entirely due to EEI as we shall see later. This is also consistent with the field-cool/heat $R(T)$ curves at above $T_{\rm max}$ in the inset of Fig. 3.3a: A magnetic field always raises the resistance of these curves.

We finally describe two features of the "universal" MR in these films. First, similar to amorphous Si (Fig. 2.6), the non-saturating MR in Fig. 3.3b-c can be normalized by incorporating a temperature factor $T^{*1/2}$ and by plotting against $\tilde{h} = g\mu_B B/k_BT$ shown in Fig. 3.4a. Consistent with the model of 3D EEI, the universal MR varies with $B^{1/2}$ at high field and with B^2 at low field (upper inset). Model fitting shown as the solid curve also allows us to extract M in Eq. (3.12). Second, these MR are universal in that multiple states

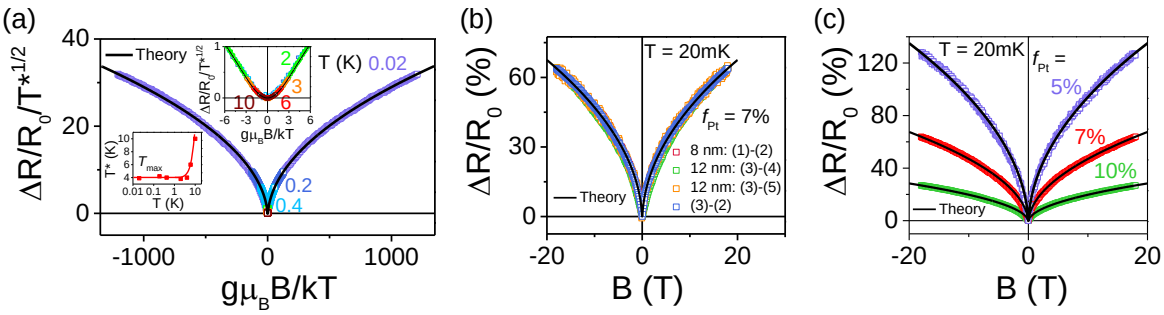

Figure 3.4: "Universal" MR of Si_3N_4:Pt films. (a) Relative resistance change under magnetic field perturbation in Fig. 3.3a-b normalized by $T^{*1/2}$ given in the lower left inset; they are in agreement with prediction of Eq. (3.11) shown as solid curves. Upper inset: Low-field data follows B^2 dependence at various temperatures labeled in K. (b-c) Relative resistance change under magnetic field perturbation at 20mK for (b) self-similar $f_{\rm Pt} = 7\%$ cells (1)-(5) in the same and different thickness and (c) dissimilar cells with different $f_{\rm Pt}$. Solid curves are best-fit predictions of Eq. (3.11), from which M can be extracted..

of the same film (cells 3-5), and films of different thickness (cells 1-5) all share the same MR, as shown in Fig. 3.4b. Not surprisingly, the universal MR is composition dependent: It increases with decreasing $f_{\rm Pt}$ as shown in Fig. 3.4c. Therefore, these universal curves allow us to obtain the values of M of different compositions by fitting them with the theoretical predictions (solid curves in Fig. 3.4c).

Table 3.1 lists the QCC parameters S_1, S_2, M, $\delta T_{\rm sat}$, and $T_{\rm max}$ determined from the above measurements. This procedure is repeated for three different Pt compositions, $f_{\rm Pt} = 5\%$, 7%, and 10%. From these data, we have calculated the WL/EEI parameters, D, α_3, σ_o, a, and τ_{so} using Eq. (3.8), Eq. (3.13)-(3.15), and $\tau_{so} = a\hbar/k_BT$ described in the Introduction. Other coherent electron properties then follow: $m^*/m_e \approx \hbar/2D$, l, k_F, and n are obtained following the same procedure outlined by Eq. (2.2)-(2.5) in Chapter 2. These results are listed in Table 3.2.

Table 3.1: Measured QCC parameters for three Pt (electron)-doped Si_3N_4 glasses.

f_{Pt}	S_1 ($K^{-1/2}$)	S_2 ($K^{-1/2}$)	M ((Ω·m·$K^{1/2}$)$^{-1}$)	$\delta T_{sat}^{1/2}$ (nm·$K^{1/2}$)	T_{max} (K)
5%	-2.50×10^{-2}	2.70×10^{-2}	1.35×10^{-5}	2.736	3
7%	-1.23×10^{-2}	1.13×10^{-2}	9.60×10^{-6}	4.587	4
10%	-6.00×10^{-3}	4.65×10^{-3}	7.99×10^{-6}	9.344	5.5

Table 3.2: Properties of coherent electrons inferred from measured QCC parameters in Table 3.1 for three Pt (electron)-doped Si_3N_4 glasses.

f_{Pt}	D (cm^2/s)	σ_o (Ω·cm)$^{-1}$	$\tilde{F}_\sigma$	a	τ_{so} (ps)	m^*/m_e	l (nm)	τ (fs)	k_F (nm^{-1})	$k_F \cdot l$	n (cm^{-3})
5%	4.9×10^{-3}	3866	5.22	0.05	0.45	118	0.39	51.7	7.69	3.00	1.54 ×10^{22}
7%	1.4×10^{-2}	4731	4.54	0.06	0.38	42.2	0.31	11.4	9.70	3.01	3.08×10^{22}
10%	5.5×10^{-2}	4872	3.90	0.08	0.35	10.2	0.29	2.55	10.4	3.02	3.81×10^{22}

3.4. Discussion

3.4.1. Quantum Interference Phenomena Related to WL and EEI in Nano Metals

Accurate probing of coherent electrons in nano materials as summarized in Table 3.2 is possible only if one can successfully differentiate WL/WAL from EEI in the observed quantum electronic phenomena. In the previous mesoscopic studies, this separation was done by applying a moderate magnetic field to suppress WL/WAL effect while enhancing EEI at the same time. In other words, quantum interference contributions of EEI can be isolated from those of WL/WAL under a magnetic field. Specifically, pretending that there is no WL/WAL, one first uses the EEI model with a model parameter $\tilde{F_\sigma}$ to fit the field-heat/cool $R(T)$ curves under a magnetic field [90, 92, 93] or to fit the high-field MR curve [91, 94]. If the best-fit model $\tilde{F_\sigma}$ is a constant above a certain field, then it indicates that the effect of WL/WAL has been fully suppressed, and the value of the extracted $\tilde{F_\sigma}$ is correct [92]. One can then combine the EEI model and the WL/WAL model to fit the zero-field $R(T)$, the low-field $R(T)$, and low-field MR to determine L_ϕ/L_ϕ^*, which separates WL from WAL. In this chapter, we used a similar strategy to analyze the combined EEI and WL/WAL effects of the Si_3N_4:Pt nano metal: (1) We obtained the non-saturating field-heat/cool $R(T)$ data to ascertain the existence of EEI, (2) we then used Eq. (3.11) with a reduced number of parameters that admit only 3D EEI to fit the MR data in Fig. 3.4; (3) we obtain additional information from the direct observation of $T_{\max}$ and $T_{\rm sat}$, which helps determine τ_{so} and D within a scaling factor a from inelastic scattering, and (4) we used Eq. (3.10) to fit the field-cool/heat $R(T)$ curves in Fig. 3.3a to provide another self-consistency check. Therefore, it is possible to obtain a unique set of σ_o, l, D, a, and $\tilde{F_\sigma}$ to fully explain our data.

However, the study of nano metals differs from the past mesoscopic studies in several important aspects. In past studies, the material in question was always a uniformly conducting metal. Therefore, its conductivity σ_o can be directly obtained from the four-point measurements, and from σ_o and the knowledge of carrier density and Fermi velocity, one can estimate diffusivity D without doing any QCC or MR experiment. Such direct determina-

tion of σ_o is not possible in nanometallic Si_3N_4:Pt, because like amorphous Si, its conducting fraction is much smaller than 100%. (The conduction fraction of Si_3N_4:Pt can be estimated from the nominal film conductivity of $\sim 5 \times 10^{-5}$ $(\Omega\cdot\text{cm})^{-1}$ and the extracted $\sigma_o \sim 4000$ $(\Omega\cdot\text{cm})^{-1}$, which gives a ratio of $\sim 10^{-8}$, very close to the one in amorphous Si.) Without knowing σ_o and m^* (which may be affected by the possible electron-phonon interaction) and any of its other electron characteristics, it is impossible to independently estimate nano-material's diffusivity D without engaging a full study of QCC and MR, as outlined in the last section. On the other hand, nano metals do offer some advantages. Principally, it is relatively easy to reach resistance saturation, because the nano scale transport length may be approached by diffusion distance at a relatively higher temperature above 0K. Taking advantage of of this unique feature of nano materials, one can determine D in a direct way. The temperature below T_{sat} is new regime where WL/WAL is saturated but EEI is not: The non-saturating Zeeman splitting in EEI continues to strengthen toward 0K. This feature can again be utilized to separate the EEI contribution from the WL/WAL contribution. In the following, we will further explore various aspects that differentiate nano metals from conventional metals to understand the reasons (presumably in terms of σ_o, l, D, a, $\tilde{F_\sigma}$) why enhanced quantum interference may be observed in nano metals.

(i) As discussed in the diffusion theory of Eq. (1.4)-(1.9), a small l and/or a large τ that result in a very small $\sqrt{D} \sim l/\sqrt{\tau}$ is fundamental to observing a strong QCC in 3D. A small D is a natural prerequisite for studying QCC in nano material—a large D would have resulted in the saturation of diffusion length at a temperature too high to maintain coherence for electrons. That is, if T_{sat} approaches or even exceeds T_{min}, there is very little QCC or nothing there, between T_{sat} and T_{min}, to study. The data in Table 3.2 support the above observation. According to Table 3.2, with l almost fixed at 0.3 nm, for all three Si_3N_4:Pt, the lower the metal composition, the longer the τ. This leads to a smaller D and a stronger QCC indeed, as evident in Fig. 3.1a: The $f_{\text{Pt}} = 5\%$ sample has the largest relative resistance change, ~5 times that of $f_{\text{Pt}} = 10\%$. Since the absolute $\Delta\sigma$ is larger by ~4 times after considering the factor

that σ_o of $f_{\rm Pt} = 5\%$ is smaller by 25%, this is in agreement with the diffusion theory.

(ii) Comparing QCC of Si_3N_4:Pt in this chapter to that of amorphous Si in Chapter 2, we found: (a) While MR in amorphous Si is only 5% at 0.02K, 18T (Fig. 2.8b), it is over 120% in 95%$SiN_{4/3}$:5%Pt film at the same temperature and field (Fig. 3.4c); (b) while QCC of amorphous Si is 0.5% from 1K to saturation (Fig. 2.7), it is over 2% in 95%$SiN_{4/3}$:5%Pt with a similar $T_{\rm sat}$. This enhancement can be mostly explained in a similar way: While l is similar in both nano metals, $\tau > 50$ fs resulting in $D < 10^{-6}$ m^2/s in the 95%$SiN_{4/3}$:5%Pt sample, $\tau < 10$ fs and $D \sim 1.5\times10^{-6}$ m^2/s in amorphous Si. (The difference in the values of $\tilde{F_\sigma}$ is only secondary.)

(iii) Comparing 93%$SiN_{4/3}$:7%Pt film to amorphous Si, we note that they have a similar $D \sim 1.4 \times 10^{-6}$ m^2/s. Indeed, their QCC is also similar, in the order of 0.5% from 1K to $T_{\rm sat}$. However, their MR at 0.02K, being 60% for 93%$SiN_{4/3}$:7%Pt (Fig. 3.3b) vs. 5% for amorphous Si (Fig. 2.8b), is again vastly different. Other than l, τ, D and $\tilde{F_\sigma}$, according to Eq. (3.11), EEI-MR in both systems is also related to the temperature factor $T^{*1/2}$ in front of g_3. While T^* equals nominal temperature before the crossover at $T_{\rm max}$, $T^* = T_{\rm max}$ at $T \le T_{\rm max}$ in Si_3N_4:Pt where spin-orbit interaction intervenes. In contrast, it is $T^* = T_{\rm sat}$ at $T \le T_{\rm sat}$ in amorphous Si where there is no spin-orbit interaction. (The lower left inset of Fig. 3.4a provides an independent self-consistency check for this picture for Si_3N_4:Pt, while the lower left inset of Fig. 2.6 provides a self-consistency check for this picture for amorphous Si.) Since $T_{\rm max}$ is higher than $T_{\rm sat}$ by about one order of magnitude, the $T^{*1/2}$ gives an additional factor of 3. Combined with the ratio of their $\tilde{F_\sigma}$, which is ~ 4, it results in a ratio of 12, which explains their MR ratio.

(iv) We next compare Si_3N_4:Pt with mesoscopic 3D systems tested at similar temperature and/or magnetic field in the literature. Because of the difficult of fabricating metal samples microscopically homogeneous, limited number of studies of 3D metals have been carried out [4] and most research was focused on doped semiconductors. Rosen-

baum et al. found $\Delta\sigma/\sigma_o$ of Si:P decreases by 1% when temperature decreases from 1K to 0.03K [80, 81], a percentage comparable with our results in Fig. 3.2. They also measured MR of several materials. (a) Ge:Sb at 0.02K and 2.5 T has an MR of 18% (MR at the same temperature/field is 40%, 22%, and 9% when $f_{\rm Pt} = 5$, 7, and 10%, respectively, in our Si_3N_4:Pt); (b) Si:P at 0.03K and 1 T has MR = 6% (MR at 0.02K, 1 T is 25%, 13%, and 5% when $f_{\rm Pt} = 5$, 7, and 10%, respectively, in our Si_3N_4:Pt); and (c) Si:As:B at 0.05K and 4T has MR = 13% (MR at 0.02K and 4T of 59%, 29%, and 12% when $f_{\rm Pt} = 5$, 7, and 10%, respectively, in our Si_3N_4:Pt). Another study by Dai, Zhang, and Sarachik found $\Delta\sigma/\sigma_o$ of 10% in Si:B from 1K to 0.05K [95], and its MR is 40% at 0.1K and 9 T [91] compared with our result of 9% in 93%$SiN_{4/3}$:7%Pt film at 0.2K and 9 T. Overall, these values of $\Delta\sigma/\sigma_o$ are very comparable. However, since σ_o of > 4000 $(\Omega\cdot\text{cm})^{-1}$ in nanometallic Si_3N_4:Pt is one to two orders larger than the conductivity (of the order of $10 - 100$ $(\Omega\cdot\text{cm})^{-1}$) of these previous studies, the magnitude of $\Delta\sigma$ is much larger in Si_3N_4:Pt. The enhancement of $\Delta\sigma$ by $10 - 100\times$ is remarkable especially when considering the tiny conduction fraction estimated in (i), at it may be, at least partially, attributed to the much smaller l in amorphous Si_3N_4:Pt. Quantum electronic interference differs from the standard diffusion theory in that its wavelength distance that matters. This is reflected in Eq. (1.7) for 3D QCC, reproduced below.

$$\Delta\sigma^T/\sigma \propto -\int_{\tau}^{\tau_\phi} \frac{l\lambda_F^2}{(4\pi Dt)^{d/2}W^{3-d}}\frac{dt}{\tau} \propto \begin{cases} -\dfrac{\lambda_F^2}{l^2}(1-\sqrt{\dfrac{\tau}{\tau_\phi}}) & d=3 \\ -\dfrac{\lambda_F^2}{lW}\ln\dfrac{\tau_\phi}{\tau} & d=2 \\ -\dfrac{\lambda_F^2}{W^2}(\sqrt{\dfrac{\tau_\phi}{\tau}}-1) & d=1 \end{cases} \tag{3.16}$$

Whereas in conventional metals studied for weak localization, $l \gg \lambda$, in our materials, they are quite close to each other. Therefore, unlike in conventional metals where QCC is a weak perturbation, in nano metals it can be a strong perturbation, allowing them to take more advantage of return probability in diffusion.

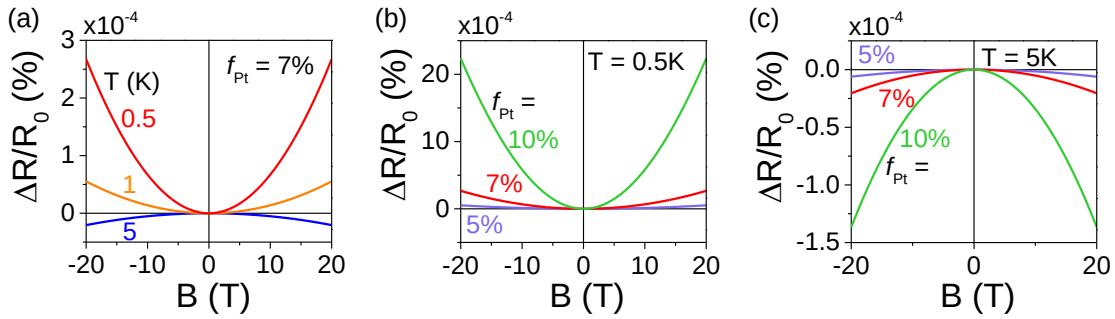

Figure 3.5: MR from WL predicted by Eq. (1.26) using parameters in Table 3.2 at various temperatures (a), and for different compositions (b-c). All of the predicted MR curves, in the unit of $10^{-4}\%$ are weaker than the experimental data in Fig. 3.4.

(v) The small D, however, is against a stronger WL-MR as it decreases the ratio of L_ϕ^2/L_B^2 as in Eq. (1.26). Applying the relevant parameters in Table 3.2, we compute WL-MR at various temperatures for different Pt compositions as shown in Fig. 3.5. As expected, it results in negative MR from WL when $T > T_{\max}$ and positive MR from WAL when $T < T_{\max}$. In both cases, however, its magnitude is of the order of 0.0001% compared with the one of at least 10% from EEI in Fig. 3.4.

From the above discussions, we can see that there may be three ways to enhance $\Delta\sigma$ in 3D conduction, and nano metals may be able to take advantage of them despite the fact that they only have a tiny conducting fraction out of the entire sample. One is small l and large τ, namely small diffusivity, which may be realized highly disordered nano metals. This will lead to the enhanced $\Delta\sigma$ and QCC of the 3D EEI and WL/WAL-origin and EEI-MR. The second one is to achieve diffusion saturation, which may be easily realized in nano metals. This will lead to separation of the EEI-MR and WL/WAL-MR, for the latter is saturated below T_{sat} but the former is not. The third one is to introduce a cutoff of τ_T by τ_{so} at $T_{\max}$, by doping, which may be realized easily in amorphous nano materials. Such dopants will impart a "contrast" agent that flips the sign of QCC and prevents the diffusion length of electrons in the triplet state from further increasing, making EEI-MR even stronger. These strategies of combining size effect and material design, to reduce D by disorder while keeping noticeable strength of SOI to freeze in a short diffusion at a relatively high temperature,

can be generalized to enhance quantum interference phenomena and differentiate EEI and WL/WAL in other nano metarials.

3.4.2. The Influence of Metal Composition on Coherent Electron Properties and QCC in Nanometallic Films

Table 3.2 clearly shows how electron doping from Pt atoms affects the coherent electron properties in nanometallic Si_3N_4:Pt films. These effects and their influence on QCC are as follows.

(i) As more Pt atoms are added to the Si_3N_4 matrix, electron density n increases, which also increases k_F since $n \sim k_F^3$.

(ii) With more doped electrons, the Coulombic repulsion from trapped charges is more fully screened. This unblocks more conduction paths and delocalizes more electrons, which enhances diffusivity D. This has an effect on τ, making it shorter in Pt-rich samples, indicating a faster v_F. It further decreases the strength of electron-electron interaction $\tilde{F}_\sigma$. As found in the last section, a larger D and smaller $\tilde{F}_\sigma$ lead to weaker QCC signal in nano metals.

(iii) As long as f_{Pt} is small, we do not expect the material structure of Si_3N_4:Pt to change much with different f_{Pt}. This is perhaps why the mean free path l for electron diffusion does not much change much either in Table 3.2. It remains close to the atomic spacing 2—4 Åin this highly disordered materials. Nevertheless, just as in amorphous Si, l is long enough to satisfy $k_F l \sim 3 > 1$, to ensure electrons have wave-like properties.

(iv) Similar to amorphous Si, D is at least one order of magnitude smaller than the conventional value found in disordered metals. According to the relation, $m^* = \hbar/2D$ [43], a small D implies a large effective mass. As we have discussed in Chapter 2, the heavy m^* comes from strong electron-phonon interaction ϕ_{ep} near local soft-spots that form virtual bound states with itinerant electrons. As more Pt dopants increase

diffusivity and reduce the random fields, the effective mass is reduced. Conversely, when a critical lower-bound f_{Pt} is approached, the electron concentration will drop along with diffusivity, and the localization length and the effective mass will rise. Eventually, m^* becomes infinite and the electron ceases to diffuse at all.

(v) From $\sigma_D = ne^2\tau/m^* \sim (m^* v_F)^3 l/v_F m^* \sim m^{*2} D^2/l$ and $m^* \sim 1/D$, σ_D is proportional to $1/l$, which is fixed around minimum conductivity $\sigma_{\mathrm{min}} \sim 4000$ $(\Omega\mathrm{cm})^{-1}$ determined by the invariant l as f_{Pt} varies.

(vi) In Table 3.2, τ_{so} decreases with more Pt atoms, as expected. The leads to an increase of T_{max} with f_{Pt} in (Table 3.1.) But τ also decreases with Pt doping, at a faster rate than τ_{so} does. This leads to smaller MR in Pt-rich Si_3N_4:Pt that may be explained in terms of the jumps in the random walk before dephasing, as follows. A small τ_{so} from strong spin-orbit interaction caps the increasing τ_ϕ early-on at T_{max}, before $\sqrt{D\tau_\phi}$ fully saturates by the thickness at T_{sat}, which is lower than T_{max}. This keeps τ_ϕ/τ smaller (i.e., fewer jumps), thus enhancing the magnitude of 3D QCC and MR. Conversely, a decreases in τ has the opposite effect, which is why MR decreases in Pt-rich samples.

(vii) While the crossover between WL and WAL under magnetic field has been widely reported in disordered metals and recently in topological insulators [96, 97], it is rarely seen in the temperature space as in Fig. 3.1 (Bergmann did predict this trend in 2D [2] in the 1980s.) In these 2D systems, the typical values of $L_{so} = \sqrt{D\tau_{so}}$ are $\sim$ 100 nm [98], which must exceed the film thickness. For $D = 1$ cm^2/s, this length gives $\tau_{so} > 10$ ps [2, 34]. In comparison, we found much shorter $\tau_{so} \sim 0.3$ ps (Table 3.2). Since the magnitude of τ_{so} sets the scale of τ_i for the crossover, one possible explanation for the absence of such transition in mesoscopic samples is that they will require a wider temperature range (over one order of magnitude according to Bergmann) to reverse the slope of QCC. As a result, the crossover is not as sharp in the temperature domain in the conventional study, thus could not be seen.

(viii) The increase of a with f_{Pt} suggests less frequent inelastic scattering. Therefore, on balance, more effective screening has a positive effect on reducing inelastic scattering, making the electron quasiparticle longer lived. While we found $a << 1$ in all three compositions, typical values of inelastic life time are found to be $10 - 100$ ps at 1K [2, 34], which suggests $a = 10$ as $\hbar/k_B = 7.64$ ps. Such short and frequent inelastic scattering are only possible in nano material where disorder can be heavily increased by the random potential.

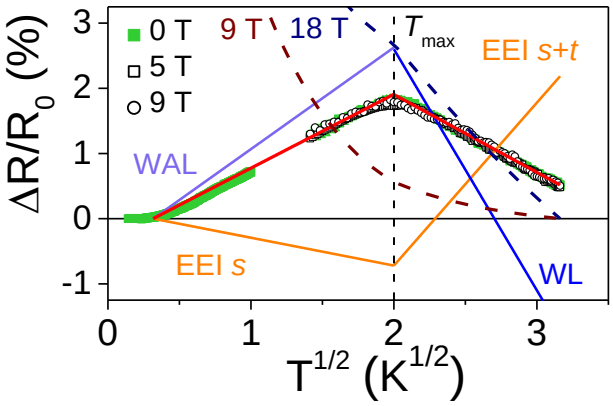

Figure 3.6: Relative resistance change of $f_{\mathrm{Pt}} = 7\%$ sample due to separate WL/WAL (blue/purple) contribution and EEI (orange) contribution at above and below $T_{\max}$. Only spin-0 singlet state (s) contributes to EEI-induced QCC while triplet state (t) below $T_{\max}$ has fixed diffusion time of τ_{so}, thus no further contribution to EEI-QCC (it does not cause WAL). Data in Fig. 3.1a are shown as 0 T (green) in agreement with the net effect indicated by red lines. Hollow symbols: relative resistance change from field-heat data at 5 T and 9 T, both from Fig. 3.3a, but after subtraction of Zeeman contribution, to emphasize agreement with 0 T data (red line). Zeeman contribution, as another part of EEI and mainly contributes to MR, is separately shown as dashed curves at 9 T and 18 T.

(ix) Since WL/WAL QCC all inversely scale with $\tau_i^{1/2}$, a very short τ_i leads to the enhancement of WL/WAL, which overwhelms EEI even in a 3D system. With the parameters in Table 3.2, we verified this by calculating the WL/WAL term and EEI term in S_1 and S_2 given by Eq. (3.6)-(3.7). These results are plotted as component $R - T^{1/2}$ curves shown in Fig. 3.6. It is found that above and below $T_{\max}$, EEI-induced QCC (orange lines) always have the opposite sign to that of WL/WAL-induced QCC (blue

and purple lines). Since the WL term dominates the entire temperature range at zero field, it is consistent with the extracted $a < 1$, which implies τ_i is shorter than the lifetime of electron quasiparticles. In Fig. 3.6, we also show the field-cool data of 5 T and 9 T, both from Fig. 3.3a, but only after their Zeeman splitting contributions have been subtracted. The fact that such data collapse into the zero-field curve (black) illustrates that the non-linearity seen in Fig. 3.3a is entirely due to the Zeeman splitting. To further demonstrate the relative weight of Zeeman splitting, we also included in Fig. 3.6 its effect at 9 T and 18 T. It is clear that it becomes increasingly important at lower temperature, but near $T_{\max}$, it is relatively unimportant at low field, which explains the inset of Fig. 3.3a.

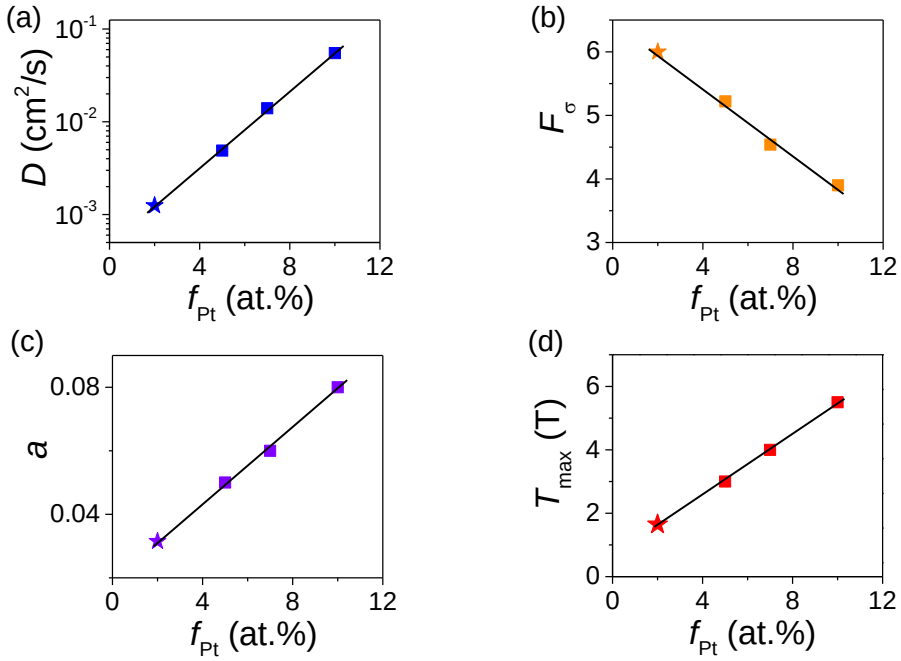

Figure 3.7: Metal composition $f_{\rm Pt}$ dependence of (a) D, (b) $\tilde{F}_\sigma$, (c) a, and (d) $T_{\max}$ plotted based on Table 3.1 and Table 3.2. Their values at $f_{\rm Pt} = 2\%$ are estimated by linear extrapolation shown as "stars" in (a)-(d).

Given the above information, we expect to see even larger WL/WAL QCC and EEI QCC/MR when $f_{\rm Pt}$ further decreases. The material parameters at lower $f_{\rm Pt}$ can be estimated by extrapolating the data in Table 3.2. This is done in Fig. 3.7, which shows a very signif-

icant change in the values of all the parameters. At $f_{\rm Pt} = 2\%$, the lowest metal composition in which nanometallicity was found [13], the predicted QCC and MR in comparison with $f_{\rm Pt} = 5\%$ samples are summarized as follows. (i) According to Eq. (3.6), $S_1 \propto (4/3 - 3\tilde{F_\sigma}/2 + 2.176/a^{1/2})/\sqrt{D}$, which gives an enhancement ratio of $130.0/46.2 = 2.81$ from $f_{\rm Pt} = 5\%$ to $f_{\rm Pt} = 2\%$ samples. (ii) According to Eq. (3.7), $S_2 \propto (4/3 - 1.088/a^{1/2})/\sqrt{D}$, which gives an enhancement ratio of $135.7/50.5 = 2.7$ from $f_{\rm Pt} = 5\%$ to $f_{\rm Pt} = 2\%$ samples. (iii) According to Eq. (3.11), MR $\propto \tilde{F_\sigma} T^{*1/2}/\sqrt{D}$ where $T^* = T$ and $T^* = T_{\rm max}$ above and below $T_{\rm max}$, which gives an enhancement ratio of 2.27 and 1.69 above and below $T_{\rm max}$. Therefore, in 98%$SiN_{4/3}$:2%Pt film, we expect to see a QCC that equals 5.7% from $T_{\rm min}$ to $T_{\rm max}$ and 7.1% from 1K to $T_{\rm sat}$. The MR enhancement is most dramatic, we expect MR of 1.1% at 6K, 9T and 203% at 0.02K, 18 T, over 2× the original resistance! The above estimations are lower bounds since σ_o, $T_{\rm max}$ and $T_{\rm sat}$ are all expected to decrease in $f_{\rm Pt} = 2\%$ sample, which makes the quantum effects even bigger.

3.5. Conclusions

1 Nanometallic Si_3N_4:Pt contains a self-similar 3D-conducting network in which weak localization and weak anti-localization coexist with electron-electron interaction in 3D, and it is the former two that dominate the QCC at zero field.

2 Pt dopants introduces strong spin-orbit interaction that fixes the phase relaxation of triplet states at τ_{so}, enables WAL and modifies EEI. This reverses the sign of the $R - T$ slope, forms a resistance maximum and enhances EEI at lower temperatures.

3 Mean free path, number of jumps in the random walk, and inelastic life time are heavily reduced by orders of magnitude in disordered nano metals, which leads to $10 - 100\times$ enhancement of $\Delta\sigma$ induced by WL and EEI effect. This lesson can be generalized to study other quantum phenomena in nano material.

4 4 Our results are in agreement with theoretical predictions once WL/WAL and EEI effects are fully accounted for. They reveal a diffusivity as low as 0.001 cm^2/s for

coherent electrons, which decreases with decreasing metal composition. This implies that coherent electrons in amorphous Si_3N_4:Pt have an effective mass over $100m_e$.

5 The large effective mass is likely to result from strong electron-phonon interaction. Such interaction is ubiquitous in nano amorphous materials, and it has previously found evidence in the effective mass of amorphous Si and in pressure-triggered insulator to metal transition of both amorphous Si and amorphous Si_3N_4:Pt.

CHAPTER 4 : Quantum Interference and Aharonov-Bohm Oscillation in Pressure-/Voltage-Metallized HfO_2 and Al_2O_3 Films

4.1. Introduction

In the previous two chapters, we have observed 3D quantum interference phenomena of coherent electrons at the nanoscale, within a volume of $(10\ \text{nm})^3$. In amorphous Si (Chapter 2), they are dominated by electron-electron interaction (EEI). In amorphous nanometallic Si_3N_4:Pt (Chapter 3), they involve both EEI and weak localization (WL) and weak anti-localization (WAL). In both cases, EEI is prominent because interaction between electrons is greatly enhanced in 3D for diffusing electrons: In a 3D network, two colliding electrons have to random walk together for a long time before they can find a way out. One may anticipate, however, that in a 1D system, the EEI may be much weaker because of the relative ease for electrons to diffuse away, but the WL and WAL are reinforced because self-crossing in random walk is much more common in lower dimensions, and it is the interference of conjugate waves on self-crossing loops that gives rise to the WL and WAL effect. These considerations suggest 1D systems may provide a better platform for manifesting the WL and WAL phenomena at the nanoscale.

Conventional 1D experiments were performed using a 3D bar with a lateral dimension much shorter than the diffusion length [99]. As a result, an electron will bounce back and forth from the wall many times before completing a diffusion distance along the length direction. In such quasi-1D experiment, although WL/WAL may be enhanced, magnetoresistance (MR) is thought to not exist: Within a dephasing distance, a random-walking electron can typically trace out multiple sets of loops that will not receive any significant net magnetic flux because of self-cancellation in loops of different orientations. (The loop orientation is defined by the right-handed rule. Two connected loops of opposite circulating directions, like the ones in "8", will receive fluxes of opposite signs from a uniform field.) However, the lack of MR may be overcome if the 1D cross section is thinner than the random walk

segment distance, l, and if only one self-intersecting loop exists, because such loop should support WL/WAL-induced MR oscillation of the Aharonov-Bohm nature [43, 39]. In the past, the Aharonov-Bohm oscillation has been seen in MR in multiply connected structures, such as hollow cylinders [36, 40, 45], nanotubes [46, 47], and lithographically defined circuit loops [100, 39], but never in a truly 1D system.

Truly 1D systems may be realized in filamentary ReRAMs that are thought to conduct along very thin and very few 1D filaments [57, 58]. Such nano filaments have been detected by transmission electron microscopy [59, 60, 61, 101]. The filaments are statistically very sparse; most likely there is only one filament per ReRAM cell according to the fracture test described in [102, 103]. If so, the transport data of filamentary ReRAM should be cleaner and hopefully easier to interpret. ReRAMs made of amorphous HfO_2 and Al_2O_3 thin films are known to be filamentary [104, 105]. In the course of this thesis research, we confirmed that amorphous HfO_2 and Al_2O_3 thin films are indeed filamentary ReRAM [103, 106, 107]. But we also discovered that a modest hydrostatic pressure can cause them to undergo an insulator to metal transition. (See Appendix C and [87].) This feature is totally unexpected since the typical virgin resistance of amorphous HfO_2 and Al_2O_3 thin films exceeded 10 GΩ, and they are known as two of the very best insulating dielectrics in industry. Moreover, having been extensively studied in the ReRAM literature [104, 105], their initial breakdown from the virgin insulator state has always been triggered by an electrical voltage in the past, and it is the electric-field-motivated ion (oxygen vacancy) migration that is thought to be needed for filament formation and breakage, which is also the putative mechanism for resistance switching. Our finding of pressure-triggered insulator transition clearly refuted the electric ion mechanism [56]. Yet it makes sense because pressure-triggered insulator to metal transitions have been ubiquitously observed in amorphous nano metals, including Si (Appendix A and Chapter 2) and Si_3N_4:Pt [15], and they are evidence of strong localized electron-phonon interaction that finds further support in Chapter 2 and 3 in the unexpected large effective mass of electrons.

Therefore, motivated by the above considerations, we will study ReRAMs made of amorphous HfO_2 and Al_2O_3 in this chapter, where 1D transport and Aharonov-Bohm oscillation may be realized. We will take advantage of both hydrostatic pressure and voltage to produce a family of filamentary nano metals for comparative QCC and MR studies. We will find that they all exhibit resistance minimum that signals coherent electron transport at low temperatures, where they also exhibit unique (a) QCC with the temperature dependence characteristic of 1D systems, and (b) robust Aharonov-Bohm oscillations under a strong magnetic field indicative of a nanosized single loop. Further refinement of the technique allowed the production of new random electron systems of slightly higher dimensions than 1D (i.e., $(1 + \epsilon)$ D material, see Appendix D), and hybrid 1D+3D systems some with a stronger random field and even spin-orbit interaction due to voltage-induced cation reduction. These novel nanoscale materials hosting myriad quantum interference phenomena will be analyzed by extending the existing theory of QCC and MR.

4.2. Experimental Procedures

Filamentary ReRAM made of metal/insulator/metal (MIM) structures of Ti/HfO_x/Pt, and Ti/AlO_x/Pt were fabricated on a substrate of thermal-oxide-coated 100 p-type silicon single crystal. A 15 nm Ti was first e-beam evaporated to form bottom electrode. A 10 nm switching layer was next deposited by atomic layer deposition (ALD) at 250°C using (a) tetrakis(dimethylamino)hafnium (HFDMA) precursor and H_2O for HfO_2 and (b) trimethylaluminum (TMA) precursor and H_2O for Al_2O_3. Finally, a 40 nm thick Pt top electrode was deposited by RF sputtering through a shadow mask that defined cells of 250 μm in radius. The pressure induced insulator-to-metal transition (i.e., "metallization") was conducted at room temperature in a hydrostatic pressure vessel using pressure P_H from 100 MPa to 350 MPa. (Because metallization is statistical in nature, caused by the removal of trapped charge at negative-U centers where strong electron-phonon interactions are destabilized by the pressure, films metallized under the same pressure can have different resistance. See metallization statistics in Appendix B.) Electrical transport measurements were performed

in PPMS at Penn's Shared Experimental Facilities and in SCM1/SCM2 at National High Magnetic Field Laboratory as described in Chapter 2.

4.3. Results

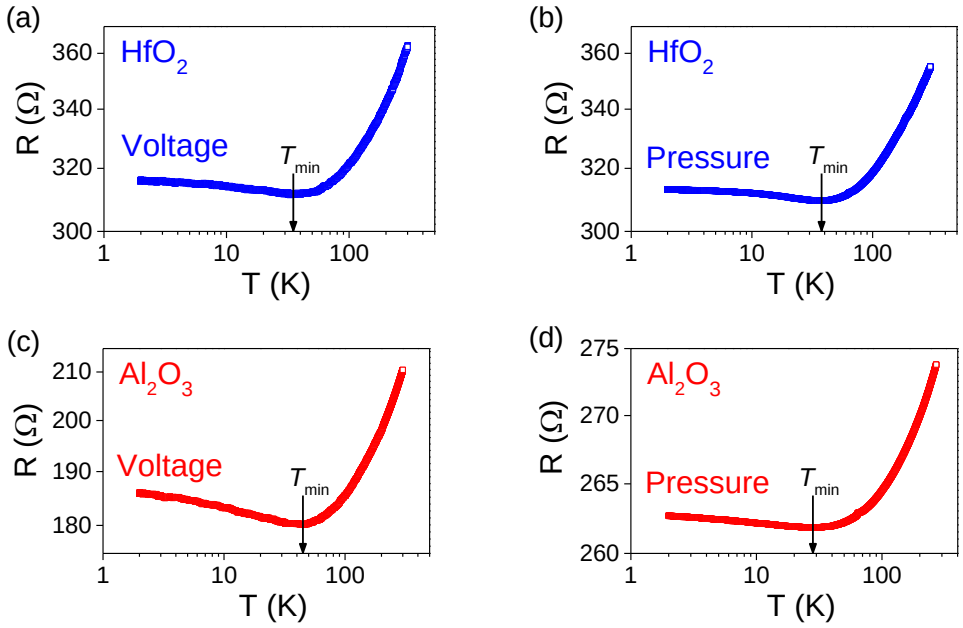

Figure 4.1: Resistance (R)-temperature (T) dependence of voltage- and pressure-metallized HfO_2 (a-b) and Al_2O_3 (c-d). They all exhibit resistance minimum at $T_{\min}$ around 30—40K marked by the arrows, in reminiscence of amorphous Si, nanometallic Si_3N_4:Pt, and mesoscopic disordered metals. A voltage of 6 V without current compliance was used to metallized (a) and (c), and a hydraulic pressure of 350 MPa was applied to obtain the metallic states in (b) and (d).

Resistance measurement of the pressure- and voltage-metallized HfO_2 and Al_2O_3 provided the $R(T)$ curves in Fig. 4.1 that all exhibit resistance minimum at $T_{\min} \sim 30$—40K similar to that in amorphous Si (Chapter 2), nanometallic Si_3N_4:Pt (Chapter 3), and mesoscopic disordered metals [70]. Since there is no magnetic impurity in HfO_2 and Al_2O_3, the resistance minimum is not likely to be due the Kondo effect [32], and must signal QCC due to the quantum interference of coherent electrons at lower temperatures. Beyond this common feature, however, it turns out that there are significant differences in the transport properties of pressure-metallized and voltage-metallized samples[1]; HfO_2 and Al_2O_3 are also

[1]As demonstrated in Chapter 2, pressure- and voltage-induced metallic states of amorphous Si exhibit

qualitatively different to some extent. Therefore, we will present their transport data, taken at temperatures down to 0.02K and under a magnetic field up to 18 T, in separate sections below.

4.3.1. Quantum Phenomena in Pressure-Metallized HfO_2 and Al_2O_3

4.3.1.1. QCC without a Magnetic Field

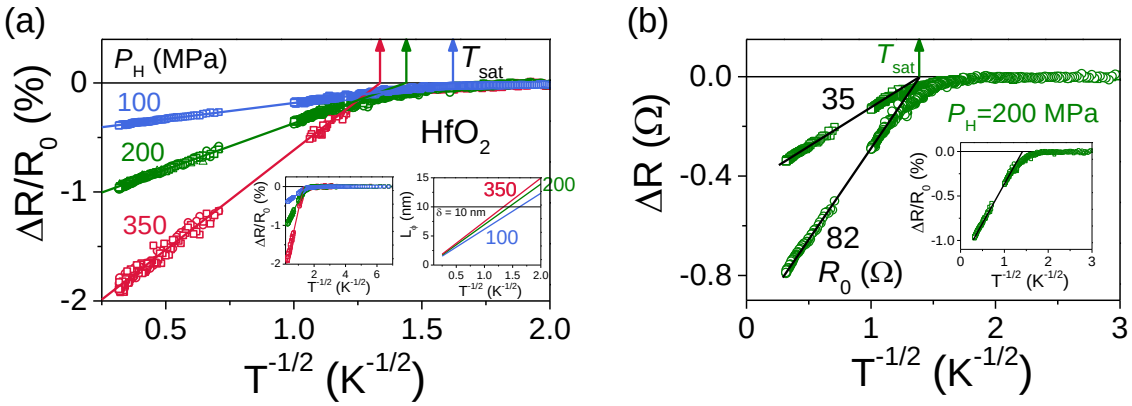

Figure 4.2: (a) Relative resistance change normalized by 0K resistance R_0 against $T^{-1/2}$, for HfO_2 films "metallized" by various hydraulic pressure P_H. Before reaching saturation at $T_{\rm sat}$, it follows linear relation consistent with quantum corrections to 1D conductivity/resistivity. Left inset: resistance change remains flat over extended low temperature range down to 0.02K. Right inset: the extracted L_ϕ for different P_H varies with $T^{-1/2}$. (b) Resistance change relative to 0K resistance R_0 as labeled against $T^{-1/2}$ for 200 MPa-formed HfO_2 films in two metallic states. Note that the two data lines intersect at $T_{\rm sat}$. Inset: Different states are self-similar in that their relative resistance—after being normalized by R_0—overlap with each other. Film thickness $\delta = 10$ nm.

The one-dimensional conduction feature of pressure-metallized HfO_2 films is first manifest in the linear relation between the relative resistance change and $T^{-1/2}$ shown in Fig. 4.2a. The dependence is consistent with the predictions of Eq. (1.14) and Eq. (1.35) of 1D QCC due to either EEI or WL.[2] The resistance change is self-similar, as illustrated in Fig. 4.2b, in that different metallic states of different reference resistance-differences (R_0) metalized under

identical 3D QCC and MR. Therefore, dimensionality matters.

[2]In WL, this temperature dependence is originated from $\tau_i \propto T^{-p}$. Our plot in Fig. 4.2 is consistent with $p = 1$. But if the data are plotted against $T^{-1/3}$, they will also appear as straight lines, which would be consistent with $p = 2/3$. This is a point made in previous two chapters: It is impossible to ascertain the value of p given the small resistance change and the limited temperature range available for our study. So we will simply take $p = 1$ and do not further differentiate it from other possibilities.

the same pressure exhibit the same relative resistance change once the resistance change is normalized by R_0 in the inset of Fig. 4.2b. This feature is the basis that allows us to remove the parasitic resistance by the subtraction method described in the Appendix C and [54]. The universal feature of different states suggests that their coherent electrons must have the same diffusion characteristics. This is confirmed by the same saturation temperature $T_{\rm sat}$, reached when their diffusion length of $\sqrt{D\tau_\phi}$ (same for 3D and 1D) reaches the film thickness (Fig. 4.2b), beyond which there is no further increase of QCC.

Normalized relative resistance change of films metallized by different pressures, however, fall on different lines in Fig. 4.2a. These lines also reach a saturation temperature $T_{\rm sat}$, when they intersect the abscissa, beyond which complete saturation of QCC is further confirmed over an extended low-temperature range in the left inset of Fig.4.2a. Setting $\sqrt{D\tau_\phi} = 10$ nm, at the film thickness at $T_{\rm sat}$ and letting $\tau_\phi = a\hbar/k_BT$ (which allows us to interrogate kinetics without differentiating the WL and EEI mechanisms at this stage), we obtain $aD = 4.98$, 6.34, and 7.32×10^{-6} m^2/s for $P_H = 100$, 200, and 350 MPa, respectively. These values are listed in Table 4.1 for ease of later comparison. Since $L_\phi = \sqrt{D\tau_\phi} = \sqrt{aD\hbar/k_BT}$, we can also calculate L_ϕ as a function of temperature, which is shown in the right inset of Fig. 4.2a. Their values are slightly increased, but not by much, in films metalized by a higher pressure.

Since the 1D QCC $\Delta\sigma$ has the unit of Ω·m as shown in Eq. (1.14), we divide it by the area A of the wire cross-section to correlate it with the observable $\Delta R/R_0$

$$\frac{\Delta R}{R_0} = \frac{e^2}{\pi\hbar}\frac{1}{A\sigma_o}L_\phi^{1/2} = \frac{e^2}{\pi\hbar}\frac{1}{A\sigma_o}\sqrt{\frac{\hbar aD}{k_B}}T^{-1/2} \tag{4.1}$$

Interpreting Fig. 4.2a using the above equation, one might contemplate that the different slopes S, which differ by a factor of ∼5, could suggest a widely different A as a result of different metallizing pressure. (In Table 4.1, $\sqrt{aD}$ only differs by 20% so it cannot account for the slope difference.) While this is not impossible, a 5× change in cross section seems extreme. In the following, we will instead seek to interpret the data in an alternative way

by assuming the conduction paths formed under different pressure have slightly different dimensionality, $d = 1 + \epsilon$. We will see that a slight increase in dimensionality alone is enough to cause a large decrease in the slope.

This alternative approach is motivated by the realization that increased dimensionality will lower the probability of self-crossing in random walk, thus reduce the QCC. Although the QCC literature has only predictions for 1D, 2D and 3D, the QCC of $d = 1 + \epsilon$ transport can be easily predicted by evaluating the back-diffusion probability following Altshuler and Aronov [4]. As shown in Appendix D, the slope S in the $R-T^{-1/2}$ dependence now acquires an additional factor of $(\tau_\phi/\tau)^{-\epsilon/2}$ to become

$$S = \frac{e^2}{\pi\hbar}\frac{1}{A\sigma_o}\sqrt{\frac{\hbar a D}{k_B}}(\frac{\tau_\phi}{\tau})^{-\epsilon/2} \tag{4.2}$$

where τ is the electron momentum relaxation time given by $\tau = l^2/D$ in 1D. Applying $\tau_\phi = a\hbar/k_B$, we get the ratio $\tau_\phi/\tau = \frac{aD\hbar}{k_B T}/l^2 = (L_\phi/l)^2$. For a mean free path of ~ 0.3 nm (this number will be justified later), we can approximate $\tau_\phi/\tau \approx 400$ over the range of $L_\phi \sim 2 - 10$ nm (inset of Fig. 4.2a). Assuming $\epsilon = 0$ for the highest $P_H = 350$ MPa and constant $A\sigma_o = 3.17 \times 10^{-11}$ Ω·m for all P_H, we obtain $\epsilon = 0.20$ for $P_H = 200$ MPa and 0.47 for 100 MPa. These estimates will not differ too much even if we allow small variations in $A\sigma_o$ and $\sqrt{aD}$—which could vary by up to 20% according to the variation in T_{sat}—because the 5× change in the slope will overwhelm these small variations. The model finding that a higher pressure causes the transport pathway to become more 1D is plausible because as a higher pressure better clears the random field of trapped charge, a filament that can support larger conductivity is more likely to form. As a result, the other branched conducting paths away from the main filament become mostly remnants carrying less and less current and contributing to less and less conductivity; this amounts to a decrease in dimensionality.

Finally, using the assumption of the atomic "wire" size of the filament as 0.3 nm, which gives $A \approx 10^{-19}$ m^2, we estimate conductivity σ_o to be about 3.17×10^8 $(\Omega\cdot\text{m})^{-1} = 3.17\times10^6$

$(\Omega\cdot\text{cm})^{-1}$. This value is comparable with $\sigma \sim 10^6$ $(\Omega\cdot\text{cm})^{-1}$ in good metals [108]. This value seems reasonable from the following estimate. The pressure-metallized device has a resistance R as low as $\sim 50\ \Omega$, yet it has only one filament with an atomically thin cross section, so a rough estimation assuming the same A gives $\sigma = \delta/AR_0 = 10^7$ $(\Omega\cdot\text{cm})^{-1}$. The parameters of pressure-metallized HfO_2 extracted above for different P_H are listed in Table 4.1 for comparison.

Table 4.1: Extracted properties of coherent electrons in the metallic states of HfO_2 obtained by various hydraulic pressure P_H.

P_H (MPa)	aD (m^2/s)	$A\sigma_o$ (Ω^{-1}m)	σ_o $(\Omega\text{cm})^{-1}$	ϵ
100	4.98×10^{-6}	3.17×10^{-11}	3.17×10^6	0.47
200	6.34×10^{-6}	3.17×10^{-11}	3.17×10^6	0.20
350	7.32×10^{-6}	3.17×10^{-11}	3.17×10^6	0

Similar data of QCC are shown in Fig. 4.3a for pressure-metallized Al_2O_3 from 10K to 2K. Here, the measurement temperature was not low enough, so there is no resistance saturation in these data. However, since different metallic states metallized under the same pressure are self-similar, as shown in Fig. 4.3b, they should share the same diffusivity, and they should intersect at T_{sat}, beyond which there is no QCC. That is, the intercept lies on the abscissa. Using such intercepts, we have determined their T_{sat} in Fig. 4.3a, and calculated aD for these 10 nm films as listed in Table 4.2. Like before, we can next calculate the dephasing length, L_ϕ, as a function of temperature and metallizing pressure. This is shown in the inset of Fig. 4.3a. Like in the case of HfO_2, the normalized relative resistance change shown in Fig. 4.3b have a smaller slope when the metallizing pressure is lower. This can again be interpreted as resulting from a larger dimensionality, $d = 1 + \epsilon$. Setting $d = 1$ for the 350 MPa data, and assuming constant $A\sigma_o$ for differently pressure-metallized samples, we obtained ϵ as listed in Table 4.2. Finally, for wires of an atomic size of 0.3 nm, which gives $A \approx 10^{-19}$ m^2, we estimate conductivity σ_o to be about 5.89×10^8 $(\Omega\cdot\text{m})^{-1} = 5.89\times10^6$ $(\Omega\cdot\text{cm})^{-1}$. These extracted material parameters are listed in Table 4.2 for pressure-metalized Al_2O_3 to be compared with their counterparts in HfO_2 in Table 4.1.

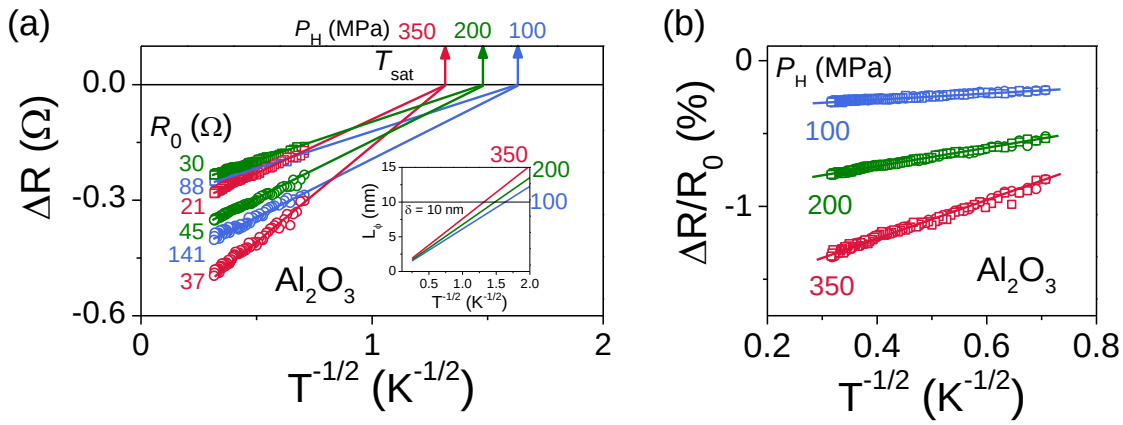

Figure 4.3: (a) Resistance change relative to 0K resistance R_0 against $T^{-1/2}$, for Al_2O_3 films "metallized" by various hydraulic pressure P_H. Common intercept of lines of different metallic states metallized by the same pressure corresponds to $T_{\rm sat}$. Inset: Calculated dephasing length L_ϕ as function of temperature. Film thickness $\delta = 10$ nm. (b) Different metallic states pressurized under the same pressure are self-similar in that their relative resistance—after being normalized by R_0—overlap with each other.

Table 4.2: Extracted properties of coherent electrons in the metallic states of Al_2O_3 obtained by various hydraulic pressure P_H.

P_H (MPa)	aD (m^2/s)	$A\sigma_o$ ($\Omega^{-1}m$)	σ_o $(\Omega cm)^{-1}$	ϵ
100	4.92×10^{-6}	5.89×10^{-11}	5.89×10^{6}	0.51
200	5.98×10^{-6}	5.89×10^{-11}	5.89×10^{6}	0.17
350	7.56×10^{-6}	5.89×10^{-11}	5.89×10^{6}	0

4.3.1.2. MR and Aharonov-Bohm Oscillation

We next investigate the MR of pressure-metallized HfO_2 films to probe the geometry of the conduction paths and the predominant interference mechanism of coherent electrons. Figure 4.4 shows two sets of Aharonov-Bohm oscillations of magnetoresistance, taken at 0.02 K, for two films metallized under different pressures. They have almost the ideal shape expected from the theory of Altshuler, Aronov, and Spivak (AAS) for a single thin loop [36], with almost identical period in magnetic field. Since different loops, if they are present, will produce oscillations that have (a) different periods—reflecting their different loop area, and (b) different phases—because the electrons in the two loops have different phases,

cancellation among them will cause a rapid loss of the oscillation amplitude. Therefore, the appearance of one very "clean" oscillation in Fig. 4.4 provides very strong evidence that only one dominant loop exists in these films. Single-period oscillations have been observed before using multiply connected metal cylinders, but they have a period of the order of tens of G [36, 40, 45].) In comparison, the period of 14 T is orders of magnitude larger. This indicates that the loops in our samples are very small.

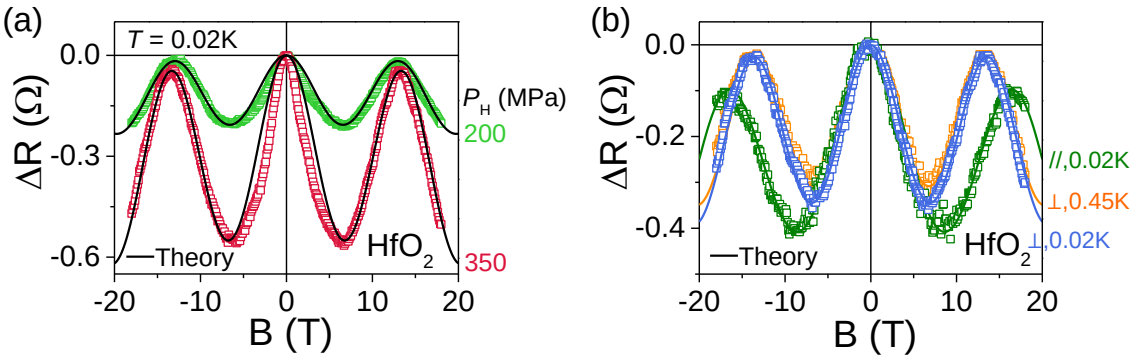

Figure 4.4: Aharonov-Bohm oscillations of pressured-metallized HfO_2 films with 1D conducting nanofilaments, consistent with the AAS theory. (a) Magnetoresistance oscillates with magnetic field that is perpendicular to the film plane at 0.02K. Nearly identical period seen for states metallized by different pressures, suggesting similar loop radius of ~ 7 nm. Preliminary fitting assuming a slight misorientation of field is shown as solid curves. Fitting parameters: $L_\phi = 10$ nm, $W = 0.1$ nm, and $\theta = 3°$ for both curves, $r = 7$ nm for $P_H = 350$ MPa, $r = 7.1$ nm for $P_H = 200$ MPa. (b) Subtracted oscillations for two field orientations. //: field parallel to the film plane; $\perp$: field perpendicular to the film plane. Data taken at 0.02K and 0.45K have identical period indicating same loop radius and nearly the same orientation, and their similar amplitude is consistent with $T_{\rm sat}$ lying above both measurement temperatures. Solid curves: predictions of the theory in Eq. (1.31). Fitting parameters: $L_\phi = 10$ nm, $W = 0.1$ nm, $r = 7$ nm and $\theta = 3°$ for two "$\perp$" curves; $L_\phi = 10$ nm, $W = 0.1$ nm, $r = 6.25$ nm and $\theta = 9.5°$ for the "//" curve.

Because the data in Fig. 4.4 were collected at a temperature below $T_{\rm sat} \sim 0.5$K, the diffusion distance should have been fully capped by the sample thickness. So the actual diffusivity in different samples does not matter; what matters is the effective dephasing length, L_ϕ, which is the sample thickness itself. Moreover, the two curves in Fig. 4.4a have almost identical periods, differing by less than 1.5%, which is much less than their aD difference of 15% in Table 4.1. Therefore, one can regard the two samples as self-similar, despite the fact

that they were metallized by different pressures. We thus apply the subtraction method to the two sets of magnetoresistance data, and plotted the subtracted data in Fig. 4.4b, in two orientations of field, blue for field perpendicular to the film surface, and green for field perpendicular to the film. We next obtained a very satisfactory fit (solid curve) for the blue-colored data using Eq. (1.31) assuming a very thin wire thickness W of 0.1 nm, a loop radius of $r = 7.0$ nm, a L_ϕ of 10 nm, and a misorientation between the loop normal and the field direction of $\theta \sim 3^\circ$. The other set of green-colored data can also be satisfactorily fit using a similar $r = 6.25$ nm but a different $\theta \sim 9.5^\circ$. These misorientations are needed in order to account for the small loss of oscillation amplitude seen in Fig. 4.4b. The above orientations suggest the loop is closer to lying parallel to the film surface than normal to the film surface.

Following the same procedure, we obtained from the same set of samples subtracted oscillation curves at 0.45K, which is shown as the orange-colored data in Fig. 4.4b. Here, the field is normal to the film surface, just like the case of the blue-colored data taken at 0.02K. From the fact that the two sets of data almost coincide, it is clear that their diffusion lengths are the same. This is possible only if diffusion is close to saturation in both films, at both temperatures. The same magnetic period indicates the same loop radius, and the very similar extent of decay indicates the same misorientation. Numerical fitting confirmed the above, with satisfactory fitting obtained by using the same parameters as the ones used for the blue-colored data (0.02K) except for a slightly decreased L_ϕ, which is reasonable in view of the higher temperature in the orange-colored data (0.45K). At 2K or higher temperature, however, the oscillation disappears due to the rapid decay of L_ϕ—indeed, we were not able to observe oscillation in the PPMS measurements.

In all the curves in Fig. 4.4, the oscillations always start with a negative MR at small field. This is consistent with the absence of WAL and EEI in pressure-metallized HfO_2, which would have given a positive MR. According to the theory, positive WAL MR is more prominent at small field, and positive EEI MR is more prominent at high field and lower

temperature. Such WAL/WL competition resulting in a phase change of π in the oscillation was seen in cylindrical samples from (WL) Li [45] to (WAL) Mg, Cd, and Pb [40], or at least a ripple at small field (seen in cylindrical samples of Li [109].) Likewise, dominance of EEI MR at high fields and low temperatures, where the effect of Zeeman splitting has survived beyond the diffusion saturation and greatly exceeded k_BT, was seen in Chapter 2 and 3 at a similar temperature of 0.02K. Yet there is no evidence of any of the above in Fig. 4.4. In view of this, we can safely conclude that in these 1D pressure-metallized HfO_2 samples, there is only WL and no WAL or EEI.

4.3.2. Quantum Phenomena in Voltage-Metallized HfO_2 and Al_2O_3

4.3.2.1. QCC without a Magnetic Field

Having unraveled the 1D WL effects in pressure-metallized HfO_2 and Al_2O_3, we next present the QCC and MR of their counterparts—films metallized by an electrical voltage with and without current compliance (Details of the voltage-triggered transitions in these materials can be found in our papers [103, 106, 107]). As already seen in pressure-metallized samples, statistics is an inherent feature of metallization. This is especially severe in voltage metallization because in this process a large current is passed through the sample. This is so even when a current compliance is imposed, because the amount of the current passed through before reaching the set compliance is still indeterminate and the current may overshoot during the resistance switching process [110]. In addition, there is no control for the paths of the current: It may pass through the film uniformly, or along myriad paths. In fact, the dielectric breakdown process is an instability, and it is fundamentally the same instability as seen in lightening and other related phenomena, simulated by the Lichtenberg figure [111]. Therefore, under the same voltage there are infinite variants in the product, and even when a compliance is set in addition to the fixed voltage, fewer but still infinite variants are expected. As a result, unlike pressure-metallized films, voltage-metallized HfO_2 and Al_2O_3 films generally lack self-similarity. Because of this, they no longer exhibit a universal behavior for normalized relative resistance changes. Nevertheless, it is advisable to use

the subtraction method to remove the parasitic resistance of the electrodes and the load, because the resistance change of the parasitic resistance, which can be quite large, may easily overwhelm the relatively small resistance change (in response to a temperature or magnetic perturbation) in the 10 nm films of metallized HfO_2 and Al_2O_3. This necessitates the following approach that utilizes the subtraction method but in an alternative way.

Table 4.3: Ordered array of voltage-metallized HfO_2 devices, and the slope characteristics of their difference QCC. The six ordered $R^{(p)}$ values of p-th devices are indicated in the first row and the same set and expressed as $R^{(q)}$ values of q-th devices are indicated in the first column. The character of the QCC of resistance difference evaluated for the pair of the p-th and q-th devices is given in the (p, q) entry: The existence of WL is indicated by a positive slope "+" in the difference QCC, that of WAL by a negative slope "−". They are strongly correlated with $R^{(p)}$ of the p-th device, or $R^{(q)}$ of q-th device, but not with the difference $R^{(p)} - R^{(q)} = R_0$ of the (p, q) pair. The systematic trend of these characters in the table indicate that spin-orbit interaction and WAL are associated with "stronger" filaments with lower device resistance obtained by more aggressive voltage-metallization, likely associated with a larger current during the "voltage-forming" process. Numbers listed in entries are used to label data curves/lines in Fig. 4.5.

$R^{(q)}$ (Ω) \ $R^{(p)}$ (Ω)	$66^{(1)}$	$91^{(2)}$	$137^{(3)}$	$186^{(4)}$	$281^{(5)}$	$313^{(6)}$
$66^{(1)}$	0	− (2,1)	− (3,1)	− (4,1)	+, − (5,1)	+
$91^{(2)}$		0	− (3,2)	+, − (4,2)	+ (5,2)	+ (6,2)
$137^{(3)}$			0	+, − (4,3)	+ (5,3)	+ (6,3)
$186^{(4)}$				0	+ (5,4)	+ (6,4)
$281^{(5)}$					0	+ (6,5)
$313^{(6)}$						0

In the modified approach, we first rank the device $R^{(p)}$ of a library of voltage-metallized samples, say six HfO_2 cells metallized by the same voltage $\sim$ 6 V without current compliance, and list them in the first row; and again, the same ordered set, denoted as $R^{(q)}$, in the first column, in Table 4.3. We then measured the QCC of these devices, and subtract them in all the pair arrangements displayed in Table 4.3. With this procedure of subtraction, the parasitic components are removed from all the pair QCC, so we can next study the QCC differences of all possible (p, q) pairs in the matrix, and the character of each (p, q) entry. These characters are expressed using a short-hand notation of "+" and

"−", which indicates WL and WAL, respectively. Specifically, "+"/"−" corresponds to the positive/negative slope in the plots of Fig. 4.5, which displays the difference QCC along several "diagonals", starting with (a): (p, q) = (6,5), (5,4), (4,3), (3,2), and (2,1), followed by (b): (p, q) = (6,4), (5,3), (4,2), and (3,1), etc., in Fig. 4.5a-d, in the above sequence. (Obviously, the difference QCC of the pair $p = q$ is zero, and the difference QCC of (q, p) is just the negative of that of (p, q), thus can be omitted.) In the figure, these data are plotted against $T^{-1/2}$ to indicate that they are consistent (or not inconsistent) with the scaling law of 1D conduction.

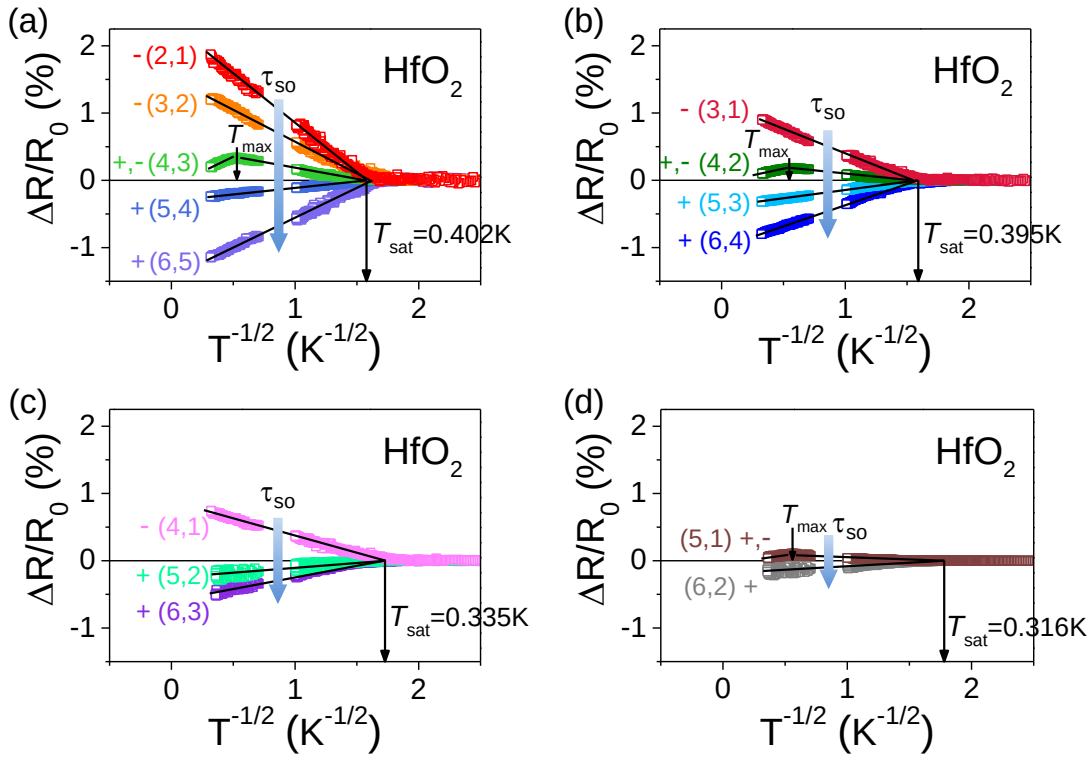

Figure 4.5: Relative resistance change normalized by 0K resistance R_0 against $T^{-1/2}$ for dissimilar voltage-metallized HfO_2 cells (a) (6,5)—(2,1), (b) (6,4)—(3,1), (c) (6,3)—(4,1), and (d) (6,2)—(5,1) in the diagonal direction of Table 4.3. Curve labeling is the same as that in Table 4.3 entry. Resistance is saturated around the same T_{sat} as marked. The decrease of τ_{so} enhances WAL along the arrow directions while both $1/\tau_{so}$ and aD slightly decreases from (a), to (b), to (c), and to (d). (See text.)

This approach of ordered pairs is motivated by our hypothesis that a smaller device resistance $R^{(p)}$—which includes the film resistance in addition to the same parasitic resistance

that is identical for all the devices—is associated with more aggressive metallization caused by passing a higher (integrated) current under the same voltage. Indeed, we find there is a systematic trend exhibited by QCC differences of the ordered pairs and it supports the above hypothesis. Specifically, the lower the device/film resistance, the more WAL and less WL contribution the film contains, whereas the higher-resistance devices/films contain only the WL contribution. In interpreting these data, we will tentatively assign the source of the WAL contribution to spin-orbit interaction associated with reduced cations: Unlike fully oxidized Hf^{4+} and Al^{3+} in pristine HfO_2 and Al_2O_3, these reduced cations have outer shell electrons that may be subject to strong spin-orbit interactions, especially in Hf because of the higher atomic number. These electrons can influence QCC through either conduction themselves or scattering conduction electrons.

Several features are next noted.

(i) All of these lines/curves break at a certain temperature ($T_{\rm sat}$) where they settle at zero, indicating saturation below this temperature.

(ii) Before final saturation at $T_{\rm sat}$, these lines/curves have slopes that are either all positive ("+"), all negative ("−"), or start with positive but change to negative ("+, −")—thus defining a $T_{\rm max}$. Since a positive slope can be attributed to WL, as we already demonstrated for pressure-metallization, we will attribute the negative slope to WAL. These sign features are noted in Table 4.3 to aid comparison.

(iii) Inspection of such features in Table 4.3 reveals that a negative slope only appears in pairs that satisfy $p + q \lesssim 6$. This suggests small $R^{(p/q)}$ devices are the source of the negative slope, or WAL. Conversely, large $R^{(p/q)}$ devices are the source of the positive slope, or WL.

(iv) The pair (4,3), which gives $p + q = 7$, is a borderline case with a $T_{\rm max}$. The other two borderline cases are (4,2) and (5,1), both giving $p + q = 6$ with smaller magnitude of the slopes and relative gradual changes in the sign of the slope. This suggests that

while the slope sign serves as a good indicator of the dominating contribution, a large WAL can mask a small WL giving a negative slope overall as in the case of (4,1), and vice versa in the case of (6,2). This is plausible: In the former case, the WL contribution should be more evident at higher temperature but at such temperature the QCC is weak anyway; in the latter case, the WAL should be more evident at lower temperature but at such temperature the QCC may have already saturated because of $T_{\rm sat}$ nearby. These situations will make it difficult to see a sign change in the slope. Another possibility is that the WL/WAL contributions of the two devices are comparable in magnitude, so after subtraction, little is left in difference QCC. This, for example, could be the case in curve/line (6,5) (WL being cancelled.) and (2,1) (WAL being cancelled.)

(v) Comparing Fig. 4.3a-d, we can see that the magnitude of the contrasting slopes and the severity of sign changes are more pronounced in Fig. 4.3a, and they decrease as it goes down to 4.3b, etc. There are two reasons for this trend. First, the $p-q$ value is smaller in Fig. 4.3a, so the difference QCC is normalized by a smaller $R^{(p)}-R^{(q)}$, which makes the relative resistance change appear larger. Second, for smaller $p-q$, the difference QCC tends to have removed the similar WL (or WAL) contributions in device (p) and device (q), thus making the contrast of WL in one device against the WAL in the other sharper.

(vi) Since all the data in Table 4.3 and Fig. 4.5 are self-consistent, we may assign the relative trend of τ_{so} in Fig. 4.5a-d to indicate the crossover from WL to WAL: An increase in τ_{so} favors WL, and vice versa.

We now attempt a more quantitative analysis, staring with estimating $T_{\rm sat}$ and $T_{\rm max}$. First, we note that within each panel of Fig. 4.5, the $T_{\rm sat}$ does not differ much. From $T_{\rm sat}$, we can calculate $aD=\delta^2 k_B T_{\rm sat}/\hbar$ as 5.26, 5.18, 4.39, and 4.13×10^{-6} m^2/s for the curve/line set (6,5)—(2,1), (6,4)—(3,1), (6,3)—(4,1), and (6,2)—(5,1), respectively. Considering the lower limit of $m^*=m_e$ corresponding to $D_{\rm max}=\hbar/2m_e=1.16\times10^{-4}$ m^2/s, the lower

bound of a is 0.043. As D decreases due to the possible large effective mass seen in Chapters 2 and 3, a should increase. Second, for the line/curves (4,3), (4,2) and (5,1) that feature transition from WL to WAL at $T_{\max}$ (resembling the same observation in 3D QCC seen in Si_3N_4:Pt in Chapter 3), we can estimate $\tau_{so}/a \sim \hbar/k_B T_{\max} = 2.04$ ps for (4,3), 2.19 ps for (4,2), and 2.39 ps for (5,1). Given the lower bound $a = 0.043$, the lower bound of $\tau_{so} \sim 50$ ps, comparable with the results in the literature [2]. Combining T_{sat} and $T_{\max}$, we can write $L_\phi^* \approx \sqrt{D\tau_{so}} = \delta\sqrt{T_{\text{sat}}/T_{\max}}$, which equals 3.27 nm for (4,3), 3.36 nm for (4,2), and 3.15 nm for (5,1). Third, by inspecting the two-slopes of (4,3), (4,2) and (5,1), we can rule out any role of EEI. This is because according to Eq. (1.14) and Eq. (1.16), the positive-slope magnitude of WL should be exactly twice the negative-slope magnitude of WAL, which is obeyed in (4,3), (4,2) and (5,1). Note that in Si_3N_4:Pt where EEI exists, the above relationship is not obeyed as we observed in Chapter 3.

Unfortunately, a further quantitative analysis of the slope is not possible. This is because the difference QCC of dissimilar devices—one with WL and the other WAL—contains different prefactors for the WL term and the WAL term. (The prefactors come from $R^{(p/q)} - R_{\text{parasitic}}$, which are different for different devices, and not knowing $R_{\text{parasitic}}$ they cannot be quantified.) Therefore, it is not prudent, for example, to assign the different slopes to small differences in dimensionality as we did for self-similar data in pressure-metallized HfO_2 and Al_2O_3; the different slope could have been caused by different $R^{(p/q)} - R_{\text{parasitic}}$.

Similar data of Al_2O_3 are analyzed in Table 4.4 and Fig. 4.6. In this case, voltage metallization was performed at ~ 6 V, but under a current compliance ~ 1 mA. The data of four devices are listed in Table 4.4 and their difference QCC are plotted in Fig. 4.6, following the same arrangement and notation as in Table 4.3 and Fig. 4.5. Compared to the HfO_2 data, the Al_2O_3 data are relatively straightforward to interpret. (a) 1D conduction is plausible since the difference QCC follows $R - T^{-1/2}$ scaling relatively well. (b) Saturation at T_{sat} is again evident, below which QCC saturates. (c) All the slopes are positive, indicating the dominance of 1D WL over WAL in all the devices. As mentioned previously, a strong

Table 4.4: Ordered array of voltage-metallized Al_2O_3 devices, and the slope characteristics of their difference QCC. This table is similar to Table 4.3 for HfO_2 cells. The four ordered $R^{(p,q)}$ values of devices are indicated in the first row and first column. The existence of WL is indicated by a positive slope "+" in difference QCC, the larger the number, the more positive the slope. Along a diagonal direction, the slope magnitude is correlated with $R^{(p)}$ of the p-th device, but not with the difference of the (p, q) pair, which is R_0. Therefore, the degree of WL is associated with stronger filaments with lower device resistance obtained by more aggressive voltage-metallization, likely associated with a larger current during the "voltage-forming" process before the current compliance is reached. Numbers in the entries are used in Fig. 4.6 to label data lines/curves.

$R^{(q)}$ (Ω) \ $R^{(p)}$ (Ω)	$75^{(1)}$	$127^{(2)}$	$175^{(3)}$	$230^{(4)}$
$75^{(1)}$	0	+++ (2,1)	+ (3,1)	+
$127^{(2)}$		0	++ (3,2)	+ (4,2)
$175^{(3)}$			0	++ (4,3)
$230^{(4)}$				0

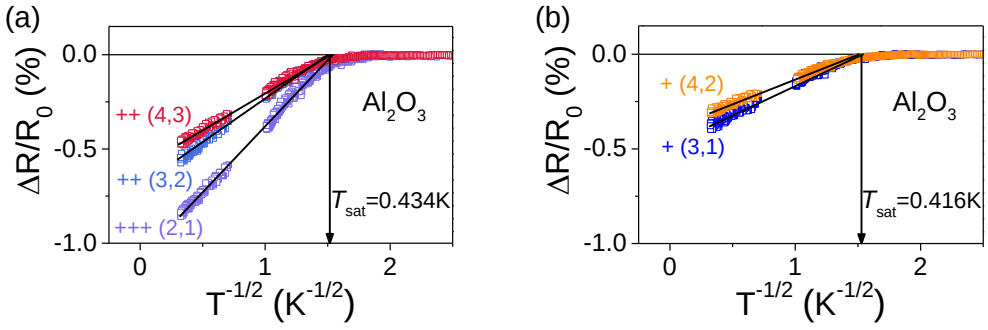

Figure 4.6: Relative resistance change normalized by 0K resistance R_0 against $T^{-1/2}$ for voltage-metallized Al_2O_3 cells (a) (4,3)—(2,1) and (b) (4,2)—(3,1), each set arranged along a diagonal direction of Table 4.4, which gives number designations for the lines/curves. Also marked are saturation temperature $T_{\rm sat}$, which are similar within each figure. Positive slope indicates dominance of WL, a higher slope likely due to stronger WL. See text.

WL can render weak WAL invisible, and likely vice versa, which could also be the case here. Another possibility is that the WAL contributions of the two devices are comparable in magnitude, so after subtraction, nothing is left in difference QCC. So the fact that only positive slopes are observed does not completely rule out the possible existence of some WAL. (d) The slope tends to be higher when the $p - q$ value along the diagonal is smaller, i.e., the slopes in Fig. 4.6a are generally larger than those in Fig. 4.6b. (The relative mag-

nitude is indicated in Table 4.4 by the number of "+" signs.) This is also observed in Fig. 4.5, and it may be because the slope is "magnified" by a small resistance difference, $R^{(p)} - R^{(q)}$, against which the resistance change is normalized. (e) Since $R^{(p)} - R^{(q)}$ is similar along the same diagonal, one can compare the magnitude of the slope to conclude that the small-resistance device is likely to be the source of the large slope, hence the source of the strongest WL. (f) Since almost the same $T_{\rm sat}$ is obtained within each group, they must have similar aD, which is 5.69 and 5.45 $\times 10^{-6}$ m^2/s in Fig. 4.6a and Fig. 4.6b, respectively. Given $D_{\rm max} = 1.16 \times 10^{-4}$ m^2/s, the lower bound of a is about 0.047 here. (g) Given the same aD in the same diagonal group as shown in Fig.4.6a, it is tantalizing to suggest that the increased slope reflects a trend toward 1D ($\epsilon \to 0$) conduction. This is plausible because within the same diagonal group, $R^{(p)} - R^{(q)}$ is relatively similar (about 50 Ω in Fig. 4.6a), so the order of the data lines/curves of very different slopes is likely to be preserved. If so, then the most 1D-like case seems to happen in the devices of the lowest $R^{(p/q)}$, and as $R^{(p/q)}$ increases, the dimensionality increases somewhat, making self-crossing during random walk less frequent, thus reducing the magnitude of QCC. However, a quantitative estimate of dimensionality similar to the one performed for pressure-metallized samples is not feasible because of the unknown nature of the weighing factor.

4.3.2.2. MR and Aharonov-Bohm oscillation

Magnetoresistance was next studied to shed further light to the WL-WAL competition in voltage-metallized samples. Special attention was also paid to any possible Aharonov-Bohm oscillation, which will give definitive evidence to the emergence of nano loops. As will become clear below, these data, along with QCC, have provide an unprecedentedly detailed view of the nanostructure of voltage-metallized HfO_2 and Al_2O_3. Referring to Table 4.3, we present the MR data of HfO_2 devices (2), (4), and (5) in Fig. 4.7. Likewise, referring to Table 4.4, we present the MR data of Al_2O_3 devices (1) and (3) in Fig. 4.8. (No subtraction was made to these data.)

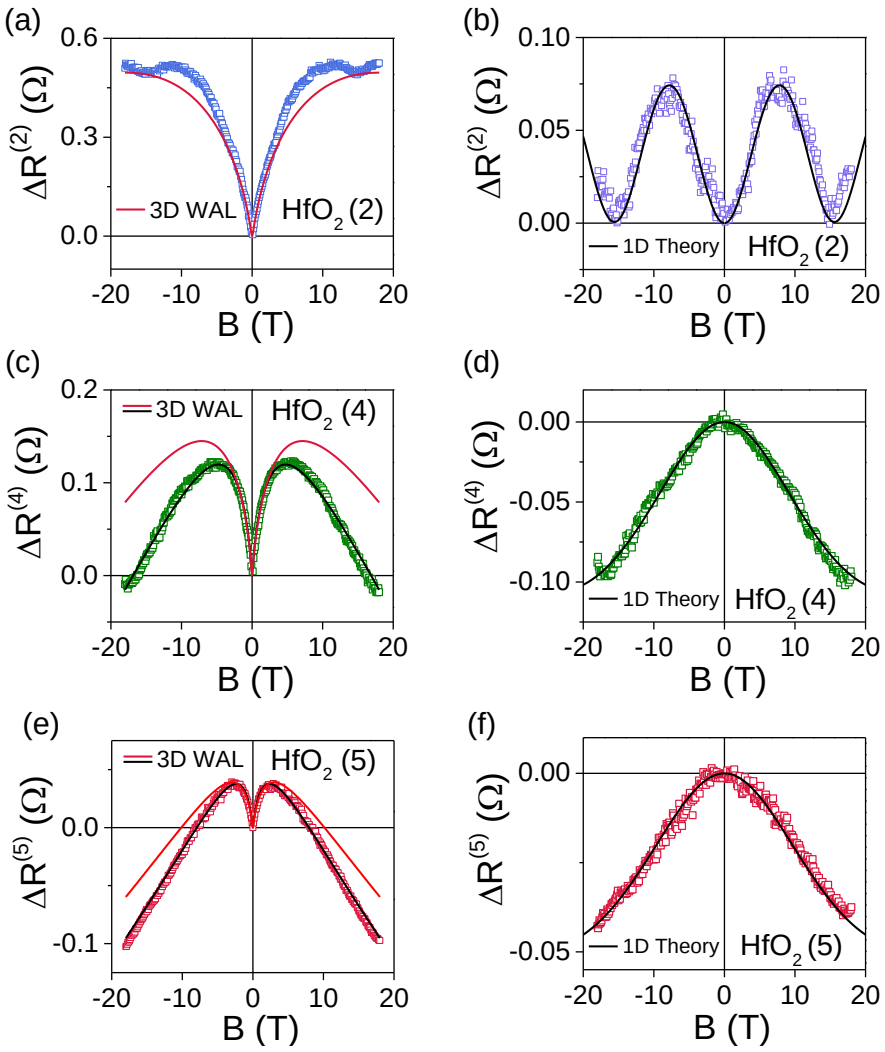

Figure 4.7: Magnetoresistance of voltage-metallized HfO_2 cells, (2), (4), and (5) in Table 4.3, shown in (a-b), (c-d), and (e-f), respectively. In (a), (c), and (e), their positive MR cusp at low field is fitted by the 3D WAL/WL theory (Eq. (1.26)) in two ways, shown as red curves and black curves, respectively. These curves indicate WAL becomes weaker in the order of (2) to (4) to (5), consistent with Table 4.3. When the red curve fitting is used, there is a remaining contribution of nature of Aharonov-Bohm oscillations, which are shown in (b), (d), and (f), and fitted by the WAL/WL theory (Eq. (1.31), black curves) for atomically thin loops, with $W = 0.1$ nm, $L_\phi = 10$ nm, radius $r \sim 6.5$ ($\theta = 2°$), 3.8, and 3.5 nm, respectively. No θ values can be obtained for the latter two oscillations that the field is not high enough to examine possible attenuations. Oscillation in (b) starts with a local minimum at small field; such positive MR indicates WAL dominance. Oscillations in (d) and (f) start with a local maximum at small field; such negative MR indicates WL dominance. These trends are consistent with the finding in Table 4.3.

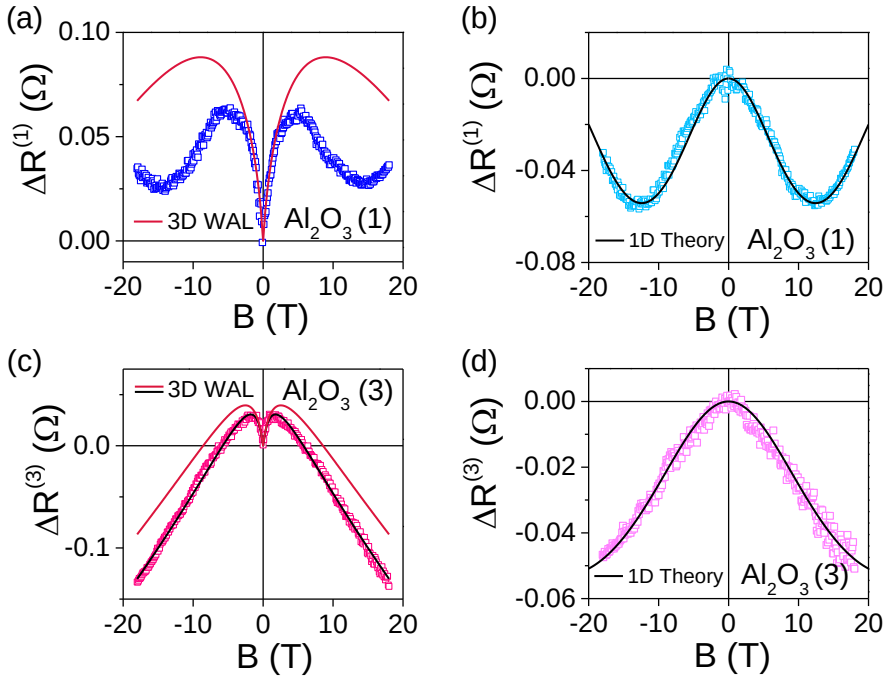

Figure 4.8: Magnetoresistance of voltage-metallized Al_2O_3 cells, (1) and (3) in Table 4.4, shown in (a-b) and (c-d), respectively. In (a) and (c), their positive MR cusp at low field is fitted by the 3D WAL/WL theory (Eq. (1.26)) in two ways, shown as red curves and black curves, respectively. These curves indicate WAL becomes weaker in the order of (1) to (3), consistent with Table 4.4. When the red curve fitting is used, there is a remaining contribution of the nature of Aharonov-Bohm oscillations, which are shown in (b) and (d), and fitted by the WAL/WL theory (Eq. (1.31), black curves) for atomically thin loops, with $W = 0.1$ nm, $L_\phi = 10$ nm, radius $r \sim 5.2$ and 3.5 nm, respectively. No θ values can be obtained for the latter two oscillations that the field is not high enough to examine possible attenuations. Oscillations in (b) and (d) both starts with a local maximum at small field; such negative MR indicates WL dominance, which is consistent with the finding in Table 4.4.

Clear evidence for oscillation is indeed found in Fig. 4.7a and Fig. 4.8a, which correspond to the sample of the lowest $R^{(p)}$ in each series. This feature indicates that a single loop exists in these samples, at least in the films that are voltage-metallized the most. However, what is also most notable is one common feature of all the data curves—not seen in the MR of pressure-metallized films, which is the appearance of a sharp cusp at small field. In fact, this feature has never been seen in the past studies of Aharonov-Bohm oscillations of WL/WAL origin: It is known both theoretically and experimentally that when WL dominates, the oscillation starts at zero field from a local maximum indicating a negative MR, and vice

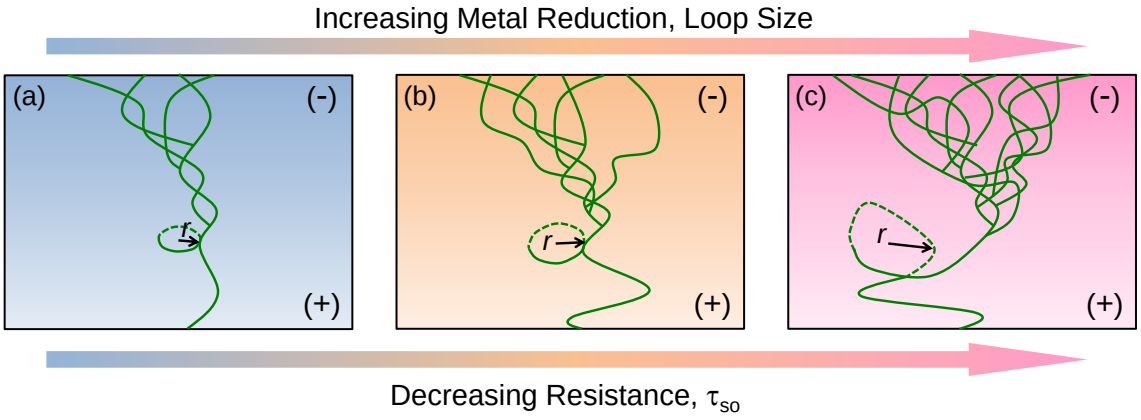

Figure 4.9: Evolution of the conducting paths during constant-voltage metallization in HfO_2 and Al_2O_3. Evolutions (a)→(c) the arrows indicating increasing total-current passed, degree of cation reduction and device conductance (i.e. decreasing device resistance). Sub-nanostructures: (i) 3D mesh at top (negative-voltage electrode) in which cation reduction also results, causing WAL (small τ_{so}), (ii) 1D filament at bottom (positive-voltage electrode) with less cation reduction but with a nanosized loop of a radius r, causing WL and Aharonov-Boham oscillation.

versa when WAL dominates [43]. The past studies of Aharonov-Bohm oscillations used a uniform material, with a known composition and nanostructure. Our voltage-metallized samples, however, may have a more complicated nanostructure. For example, they may have two sub-nanostructures that are connected in series. If so, then the overall MR is the sum of the MR of both parts. This is the picture, schematically depicted in Fig. 4.9, that we will use to interpret our data. In this picture, we envision a loop with radius of r, which gives rise to the Aharonov-Bohm oscillation that is evident in several parts of Fig. 4.7-4.8. We also envision a mesh, somewhat of a wedge shape, that may be additionally reduced to impart spin orbit interaction, hence WAL, in addition to WL. This mesh will give rise to the cusp-like MR at small field. Importantly, it must be a 3D or 2D system but not 1D system, because there is no MR in strictly 1D system or quasi-1D system in which multiple self-crossing will cause nearly complete cancellation of the MR. The loop may have either WL or WAL character; different characters will give Aharonov-Bohm oscillations of different phases.

With this picture in mind, we attempted data fitting to deconvolute the cusp from the oscillation using the theoretical predictions of 3D WAL/WL and Aharonov-Bohm oscillations. We started this exercise with the data in Fig. 4.7a and Fig. 4.8a, in which there are clear oscillations. This dictates that one must choose suitable model parameters so that the oscillation period is not significantly different from what is apparent in the un-deconvoluted data. The 3D WAL/WL contributions are shown as red curves in Fig. 4.7a and Fig. 4.8a. Next, guided by these fitting parameters, we proceeded to fit Fig. 4.7c and 4.7e, and likewise Fig. 4.8c, using new sets of reasonable fitting parameters. Here, because the oscillation is not apparent, we have two choices. We can either fit the entire curve by a single 3D WAL/WL contribution (black curves) without allowing any oscillation, or we can fit the curve by a weaker 3D WAL/WL contribution (red curves) and leave the remaining contribution to the Aharonov-Bohm oscillation, which is shown in Fig.4.7d and 4.7f, and likewise in Fig. 4.8d, all compared the theoretical predictions (black curves). Both approaches give reasonable fits, and it is difficult to distinguish the goodness of the two, given the fact that the fitting is handicapped by a residual parasitic resistance, which is unknown.

These WAL/WL curves share a common feature of a local maximum, beyond which the positive MR turns into a negative MR. This is expected because WAL does gives way to WL at higher field as known from the study of Bergmann [2]. Actually, the magnetic field at the local maximum is a good indication of the strength of WAL, which is systematically lower in the order of (a) to (b), and to (c) in Fig. 4.7. This seems reasonable because the $R^{(p)}$ of these devices, which correlates with decreased WAL as we already argued before for the QCC data, increases in the same order. Consistently, the magnitude of the WAL/WL at the maximum is smaller in the same order, reflecting a large τ_{so}. (It also confirms the picture depicted in: If WAL were not inside the nanostructures inside the film but from Pt electrode/interface, this low-field MR cusp and the field at local maximum would not likely to change in different cells.)

The deconvoluted Aharonov-Bohm oscillations, shown in Fig. 4.7b and Fig. 4.8b, are in

very good agreement with predictions of Eq. (1.31), shown as solid curves, with common W = 0.1 nm and L_ϕ =10 nm, and r = 6.5 nm and $\theta = 2^\circ$ for HfO_2, and r = 5.2 nm for Al_2O_3. These fitting parameters are quite comparable with those in pressure-metallized samples in Fig. 4.4, as are the amplitudes of the oscillation, which are not fitting parameters as they come from the value of fundamental quantum conductance. Therefore, the choices of all the fitting parameters in Fig. 4.7a-b and Fig. 4.8a-b, for 3D WAL/WL MR and the Aharonov-Bohm oscillation, seem reasonable. (They are also quite unique. For example, subtracting a WAL/WL cusp of a different strength will have resulted in oscillations with unrealistically short/long periods unreasonable for a film thickness of 10 nm.) Comparing Fig. 4.7b and Fig. 4.8b, we see the oscillations are out of phase from each other: a positive MR (indicative of WAL) in voltage-metallized HfO_2 vs. a negative MR (indicative of WL) in voltage-metallized Al_2O_3. This seems plausible since the QCC data also indicate the same, that there is more WAL in HfO_2 vs. more WL in Al_2O_3. This may reflect (a) the relative difficulty of reducing Al_2O_3, (b) the effect of the current compliance—applied to Al_2O_3 but not to HfO_2—thus limiting the degree Al reduction in Al_2O_3, , or (c) Hf being a heavier metal has stronger spin-orbit interaction. In addition, this observation is consistent with the phases of Aharonov-Bohm oscillations of pressure-metallized samples in Fig. 4.4, which all indicates negative MR, because pressure metallization is unlikely to cause cation reduction.

Lastly, in view of credible fitting of the data in Fig. 4.5a-b and Fig. 4.8a-b, we believe the "oscillatory" data of Fig. 4.7d and 4.7f, as well as the data of Fig. 4.8d, are likely to be correct. The fitting parameters of these oscillations suggest that the period increases from Fig. 4.7b, to 4.7d, to 4.7f. Although the quality of fit is not very good, possibly because of the residual parasitic resistance in these data, there is indeed some indication of an oscillation in Fig. 4.7c-d at -17 T. The best fitting parameters for Fig. 4.7d suggest a loop radius of 3.8 nm, which will see a first period at 23 T, and for Fig. 4.7f, it is 3.5 nm, which will see a first period at 27 T. Likewise, in Fig. 4.8d, we obtained a best loop radius of 3.5 nm. One important feature of these fits is that all the predicted oscillation

amplitudes in Fig. 4.7(b,d,f) and Fig. 4.6(b,d) are around 0.05 Ω. This is reassuring because the oscillation amplitude is fundamentally determined by (a) quantum conductance, which is universal, and (b) aD and diffusion length L_ϕ, which according to the earlier QCC data are very similar in all these devices. (In fact, L_ϕ is capped by the film thickness of 10 nm.) The fittings also satisfy self-consistency check: The oscillation in Fig. 4.7(d,f) starts with a local maximum unlike that in Fig. 4.7b, which is consistent with the trend of weakening WAL in the HfO_2 samples from (2) to (4) to (5). In contrast, the oscillation in Fig. 4.8d starts with a local maximum, which is the same as in Fig. 4.8b, but this is consistent with the nature of Al_2O_3 sample in which WL is stronger and WAL weakens from (1) to (3). Therefore, we may tentatively conclude that single nano loops of various sizes are likely present in these voltage-metallized HfO_2 and Al_2O_3.

4.4. Discussion

4.4.1. Atomically Thin 1D Loop in Nanoscale

The Aharonov-Bohm oscillations observed in HfO_2 and Al_2O_3 films have a period $B_0 \sim$ 13—17 T for pressure-metallized samples and $\sim$ 15—20 T for voltage-metallized samples. These large periods correspond to nanosized loops, which proved to be the smallest one ever found. To see this, one can directly estimate the loop radius r from the interference relation, $B_0 \pi r^2 = h/2e = 2.07 \times 10^{-15}$ T·m^2. For $B_0 = 15$ T, it is $r = 6.6$ nm. In the literature of Aharonov-Bohm oscillation of the WL/WAL origin, B_0 in the hollow cylinder experiment of Sharvin and Sharvin is much smaller, of the order of 10^{-3} T, which corresponds to $r = 0.8$ μm consistent with the radii of the cylinders used in the experiments [36, 40, 45]. Nanoscale oscillation has been observed, in a multi-walled carbon nanotube [46], which features a period of 9 T, corresponding to a radius $r \sim 8.6$ nm. (Recently, h/e oscillations were also reported in nano wires made of Bi_2Se_3, a topological insulator, with a feature size of several hundreds of nm [112].) In fact, since the strongest field of DC magnets in the world is currently limited to 45 T, being able to provide a period of 90 T for the Aharonov-Bohm oscillation, the smallest radius that can be measured is capped at 2.7 nm. This is

only a little smaller than the smallest loops (3.6 nm) suggested by our data.

One remarkable feature of the oscillations in this study is how little attenuation they suffer. When the magnetic field is normal to the film surface, the amplitude of the Aharonov-Bohm oscillation in HfO_2 decreases by only 5% and 1% after one period in pressure-metallized (Fig. 4.4b) and voltage-metallized films (Fig. 4.3b), respectively. This is the cleanest and least attenuated Aharonov-Bohm oscillation ever reported. In comparison, the amplitude decay is over 20% in cylindrical Mg and Li [36, 40] and over 50% in multi-walled carbon nanotubes. Such small attenuation is possible if and only if the loop is made of an atomically thin wire, i.e., $W \sim 0$ in Eq. (1.33), and if there is no misorientation between the loop normal and the field, i.e., $\theta = 0°$. It was not possible to perfectly align the loop with the field in our experiment at the SCM1 station at the National High Magnetic Field Laboratory, because there is no 3D goniometer there. Yet, despite some misorientation that must have existed, very little attenuation was seen. This implies $W \sim 0$ in our loop. Since the same fitting for different sets of W and θ is obtained if the same W^* is used in Eq. (1.34), it is W^* that sets the upper limit of W given the fact that the exact θ is not known in our analysis. The value of W^* calculated from above is 0.9 nm for the 5% attenuated oscillation and 0.6 nm for the 1% attenuated oscillation, seen respectively in pressure- and voltage-metallized HfO_2. Therefore, there are indeed very small and about the atomic scale.

4.4.2. 3D Mesh vs. 1D Filament in HfO_2 and Al_2O_3

The picture of Fig. 4.9 is proposed to account for (a) the positive MR cusp at low field (b) the Aharonov-Bohm oscillation at high fields, and (c) 1D-like QCC at low temperature including the presence of T_{max} and T_{sat}, in voltage-metallized HfO_2 and Al_2O_3 films. It contains a 3D mesh network with at lease some reduced metal ions in series with some 1D filamament(s) and a single dominant loop. (Smaller loops may also be present, but it is the largest loop that is responsible for the Aharonov-Bohm oscillation observed. The loop is also likely to be the most resistive part of the conducting path, thus more prominently featured in the resistance measurement.) The development of these nanostructures follows

the sequence of decreasing resistance: With decreasing resistance, the loop becomes more prominent (i.e., larger in radius), and the mesh more electrically reduced (i.e., the WAL cusp more pronounced). This is in concert with more total-current passage during the voltage-metallization process. Meanwhile, there is no metal ion reduction and presumably no 3D mesh in pressure-metallized samples, since in these samples only the Aharonov-Bohm oscillations were observed.

These results remind us of another set of experiments, namely the fracture tests described in [103] and Appendix B. Although both pressure and voltage can metallize films to endow comparable resistance distributions and performance to metallized devices, the statistics of the conducting paths in these metallized devices are quite different and depending on fracture tests. After severing one metallized HfO_2 or Al_2O_3 cell into two halves, we found conductive paths in only one half of the pressure-metallized sample while the other half has the same resistance as the virgin sample. In contrast, both halves of the voltage-metallized samples have resistances much lower than the virgin one, only one half is orders of magnitude less resistive than the other half. This indicates that in a voltage-metallized sample, some conductive paths do exist in both halves. Combining these statistics and the magnetoresistance data, we can associate the clean Aharonov-Bohm oscillations seen in pressure-metallized samples with the halves that have the low resistance. Moreover, it is clear that in these samples the single loop (and very likely, the filament as well) exists in such low-resistance half, while the other half has no conducting paths at all. In contrast, in voltage-metallized samples, while the single loop (and likely too, the filament) again must exist only in one half, it does contain some partially reduced 3D mesh, and the other more resistive half probably also has some 3D meshes to provide conductivity although they are yet to develop into highly conducting filaments. These assignments are made assuming the development of the mesh, the loop and electrical reduction follows the sequence depicted in Fig. 4.9, which seems to be reasonable since in metallization a lower resistance is undoubtedly associated with a later stage in the evolution.

The above picture may be used to interpret the data in Tables 4.3-4.4 and Figs. 4.5-4.8. In HfO_2, the initial filaments formed at the onset of voltage-metallization (Fig. 4.9a) may be rather weak, in that they still see relatively a strong random field and allow relatively little conductivity (hence large resistance corresponding to cells (5) and (6) in Table 3), and any loop they contain is too small to be seen (oscillation having a large period in Fig. 4.7.) They also contain relatively few reduced cations, which is why sample (5) gives a weak cusp in Fig. 4.7e and why its still strong 1D WL can overwhelm 1D WAL resulting in the "+" slopes in Fig. 4.5. As metallization continues (Fig. 4.9b-c), the 3D mesh spreads and the random field along the 1D filaments clears up, so an effectively larger loop forms, which has the overall effect of lowering the device resistance (corresponding to cells (4)-(1) in Table 4.3) and allowing a faster oscillation with more periods captured between -18 T and $+18$ T. Meanwhile, as more cations become reduced, a stronger 3D WAL cusp develops in Fig. 4.7a and the 1D WAL in the filaments now takes over leading to the "$-$" slopes in Fig. 4.5; it also imparts an opposite phase to the MR oscillation in Fig. 4.7b. This picture is also applicable to voltage metallized Al_2O_3, although cation reduction is less severe in Al_2O_3 (Al^{+3} is more difficult to reduce according to the Ellingham diagram; in addition, we used current compliance for Al_2O_3 metallization) and its spin-orbit interaction is weaker (Al's atomic number is much lower than Hf's.) This explains its weaker WAL; it may even be absent in the 1D filament as we did not observe any "$-$" slopes in Table 4.4. Neither did we see any WAL oscillation in Fig. 4.8.

This picture in Fig. 4.9 is not inconsistent with the TEM images seen in TiO_2 [59] and ZrO_2 [61] that are voltage metallized. In both cases, a cone-shaped conducting path thinning down to a filament near the positive electrode was observed. (In the so-called conducting-bridge ReRAM or CBRAM, in which electrode metal electro-migrates into the film, similar TEM images have also been observed [60].) These filaments are narrower and 1D-like near the positive-voltage electrode. A related picture of cone-shaped filaments has also been presented in several simulation models [113, 114, 115]. However, our picture differs from the past work in one important respect: All past work relied on the ionic transport mecha-

nism for filament formation and resistance switching, but this mechanism was unequivocally refuted by our pressure-metallization experiment, , which forms highly conductive samples with a single loop each. Since voltage-metallization produces a single, relatively large loop only at the end of the process, whereas pressure-metallization always produces the same sized loop regardless of pressure, it is clear that the latter method, which involves no ion diffusion and its efficacy is only dependent on reserving the electron-phonon interaction to clear the trapped charge, is much more effective/efficient. Therefore, we suggest that overcoming the electron-phonon interaction to remove the trapped charge is also the critical step in voltage-metallization, and cation reduction is just the side product that unavoidably accompanies voltage metallization that entails a large (integrated) current. If so, redox reactions and ion migration are only secondary steps of the metallization transition: Whether achieved by applying a pressure or a voltage, the transition is most critically controlled by the formation of 1D filaments with a single loop free of trapped charges. Because much voltage is used to reduce cations instead of clearing trapped charge, and cation reduction happens to more sites, voltage metallization is less efficient producing more mesh first before forming the critical loop/filament.

4.4.3. Pressure-Metallized 1D Conductors in HfO_2 and Al_2O_3

Our experiments found pressure-metallized 1D filaments/loops in HfO_2 and Al_2O_3 are excellent 1D conductors with a conductivity (10^6 $(\Omega{\cdot}\mathrm{cm})^{-1}$) comparable to that of good metal's, very robust $T_{\min}$ (30—40K), and no indication of strong localization even at the lowest temperature (0.018K). Such high conductivity is no artifact, because the device resistance is $< 100\ \Omega$, and the cross section of the conductive path is atomically thin (as indicated by our unattenuated Aharonov-Bohm oscillation), from which one also obtain a conductivity estimate of a similar magnitude. Several aspects of this observation deserve attention. First, the fact that such high quality conductive path can form is already remarkable, given how small a fraction its conductive material occupies in the sample: One atomic area is 10^{-12} of the cell area, 10^{-7} m^2). Since the pressure applied is very modest, about 10^{-3}

of the elastic modulus of HfO_2 and Al_2O_3, it stands to argue that such pressure can only minimally perturbed the sample. Yet it is able to create a continuous, highly conducting path using so low a fraction of material. (This further attests to the superior efficiency of pressure-metallization to that of voltage-metallization.) Second, it is remarkable that 1D conduction along this path shows no evidence of other influences than weak localization, which is just the quantum interference without any regard to electron spin, magnetism or orbital angular momentum. Therefore, the environment of the 1D conductive path is very "clean." (This is totally unlike the case of voltage-metallized samples.) Third, given the fact that both HfO_2 and Al_2O_3 are strong insulators, it is reasonable to visualize the 1D conductive path is bounded on both sides by two walls of very steep potential. This, combined with the knowledge that the path cross-section is of the atomic size, suggests that the path is more a true-1D conductor than a quasi-1D system.

Having argued that these are true-1D conducting paths rather than quasi-1D samples, we next compare them with what is typically expected of true-1D conductors. First, it is well known in localization theory that the 1D system (as well as 2D system) should be localized at 0K. But our 1D paths do not show indication of localization even at 0.018K; instead, their resistance has saturated by then. Second, another frequent feature of 1D systems is their tendency for Peierl distortion, which causes electron disproportionation, orbital splitting and metal-insulator transition. But our 1D paths instead support robust Aharonov-Bohm oscillation around an atomically sharp loop of a radius of 6-7 nm, a feature thus far only seen in quasi-1D systems of good metals. We believe these discrepancies may be explained by (a) our 1D conductors are truly random systems at the atomic scale, which will remove any tendency for Peierl distortion due to symmetry-dictated band-folding, and (b) our 1D conductors are truly nano systems, which allows diffusion length to cover the entire sample dimension without reaching the localization length. (Regarding (a), we should add that amorphous random systems will allow localized electron-phonon interaction to operate, causing electron trapping. However, this requires a critical voltage [107] and it likely occurs at a site adjacent but away from the 1D path.) It will be interesting to see whether these

systems offer a new platform to explore other exotic properties of 1D conduction in random environment.

4.5. Conclusions

1 Pressure-metallized HfO_2 and Al_2O_3 contain 1D conductive paths that offer metal-like conductivity. Surrounded by steep potential walls of HfO_2 and Al_2O_3, these truly 1D paths on the nanoscale do not show any evidence of localization, which is unexpected from mesoscopic or macroscopic 1D paths.

2 Pressure-metallized HfO_2 and Al_2O_3 contain self-similar 1D conduction paths with each metallized device having one atomically thin nanoscale loop. Such loops are 6-7 nm in radius, which are the smallest ones ever reported. They manifest robust, unattenuated Aharonov-Bohm oscillations with an unprecedentedly large period of 15 T.

3 Voltage-metallized HfO_2 and Al_2O_3 endure metal reduction in addition to forming smaller loops at the late stage of metallization. The reduction extends to a 3D network and is more severe as the device resistance decreases. They exhibit a positive magnetoresistance cusp at low fields that precedes loop's Aharonov-Bohm oscillation at higher fields. It also gives rise to a resistance maximum at $T_{\max}$ in QCC and a 180° phase shift in the Aharonov-Bohm oscillation.

APPENDIX A : Electrical and Mechanical Switching of Nanometallic Si ReRAM

A.1. Introduction

Nanometallicty, namely that disordered insulators become conductors when their sample size δ falls below the localization length ζ, was previously discovered in random materials with conducting component (such as $LaNiO_3$, $SrRuO_3$, Pt, and Cr) randomly dispersed into an insulating matrix (such as $LaAlO_3$, $CaZrO_3$, SiO_2, and Si_3N_4) in the atomistic level [11, 12, 13]. In addition to the size-dependent transition, when sweeping the electrical voltage, reversible change of ζ within the same film was observed from the current/resistance hysteresis between high resistance state (HRS) and low resistance state (LRS), which rendered nanometallic ReRAM as a superior candidate for next-generation non-volatile memory. Such voltage-triggered resistance switching was proven to be purely electronic [66] and explained by the injection/removal of trapped charges at a critical voltage V^*, which alters the Coulomb repulsion to itinerant electrons [14, 66]. In the proposed model of nanometallic switching [13], the electron trapping/detrapping process is rendered by strong electron-phonon interaction that converts the positive-U state of two trapped electrons into a negative-U state, stabilizing the extra electron through local bond distortion [14]. Since a mechanical stress may distort relaxed local lattice thus destabilize trapped electrons, the above physical mechanism was further validated by the HRS-to-LRS switching of metal-doped oxides/nitrides glasses triggered by moderate mechanical pressure of $20 - 350$ MPa in a wide time domain (from 10^{-13} s, the time scale of one atomic vibration for electron trapping/detrapping, to 10^3 s) [15].

In this chapter, we will explore the nanometallicity and nanometallic resistance switching in a new set of random materials free of dispersed metals: Si/Ge with and without electronegative dopants of O and N, which sets the stage of the investigations on their low-temperature quantum phenomena in Chapter 2. Made into two-terminal memory devices, the electrical and mechanical characteristics of Si ReRAM presented here were primarily

obtained from devices made of Si-Al_2O_3 (i.e., amorphous Si with atomically dispersed O from co-sputtered Al_2O_3) and nSi-Si_3N_4 (i.e., amorphous n-type Si with atomically dispersed N from co-sputtered Si_3N_4) films sandwiched between Mo and Pt electrodes, but very similar results were found in numerous combinations of semiconductors and insulating oxides/nitrides in this material universe. ReRAM devices made of SiO_x ($x \sim 2$, thickness $\sim$ 50—80 nm) has been reported by James Tour's group at Rice University [116, 117, 118], but it can only operate in vacuum ($\sim 10^{-5}$ Torr) in the unipolar mode and the resistance switching is attributed to the voltage-driven (up to 10 V) formation and modification of individual conducting paths made of silicon nanocrystals (NCs) embedded in the SiO_x matrix [119]. Amorphous Si without O sandwiched between Ag and p-Si electrodes was also made into ReRAM (or more accurately CBRAM [120]) by research team led by Wei Lu at University of Michigan [121, 122, 123], but switching in their ReRAM relies on cation migration and redox involving the active Ag electrode as the mobile species. In addition, unipolar switching of Pt/$SiO_{0.73}$ (60 nm-thick)/Pt [124] and bipolar switching of p-Si/SiO_x ($x \sim$ 1.5—1.8, thickness $\sim$ 15—120 nm)/n-Si [125, 126] were also reported. Similar to Tour's work, they both claimed ionic mechanisms related to the breakage of Si-O bonds and formation of Si rich filament.

Distinct from the above compositions that are close to SiO_2 in very thick films, our Si ReRAM are made of a large variety of Si-based random materials, only lightly doped with O or N (e.g., x of the functional SiO_x can be as low as 0.02 and the best devices have $x \sim 0.1$—0.7), in a thickness as thin as 2 nm. They all exhibit distinct uniform, electronic resistance switching. On the physics side, we will study its response to voltage/pressure stimuli in various film thickness and with different dopant compositions in a reminiscence of nanometallic ReRAM, and thus ascertain amorphous Si/Ge as a nanometallic material that exhibits (i) thickness-triggered transition from the bulking-insulating state to conducting state (with resistance falling exponentially with reduced thickness), (ii) non-volatile electrical switching at a critical voltage V^* that is constant in all devices (which also involves change of film capacitance), and (iii) HRS-to-LRS switching triggered by mechanical pres-

sure (as low as 2 MPa and as fast as 10^{-13} s). On the device side, in addition to the CMOS-compatibility and low fabrication cost apparent from its base material−Si, we will demonstrate its robust DC/AC switching down to 2×2 μm^2 in crossbar configuration and superior performance of fast switching speed (10 ns), long retention ($> 10^5$ s at 175 °C), high endurance ($> 10^5$ cycles), ultra uniformity (Weibull $k \sim 10$), and area-scalable resistance with constant switching voltage, all being superior performance over filamentary ReRAM, including any of the previous Si-based memory devices. A physical picture of electron trapping/detrapping in Si ReRAM will be given at the end of this chapter to explain all the experimental results.

A.2. Experiment

A.2.1. Sample Preparation and Characterization

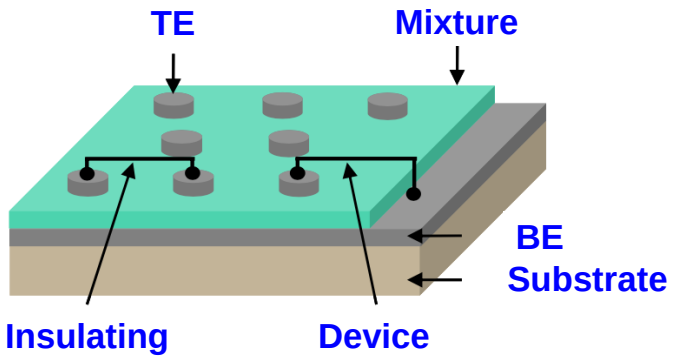

Figure A.1: Schematic configuration of the vertical BE/Mixture/TE memory cells on one chip, adapted from [11].

Amorphous thin films of Si with and without dopants were sputter deposited on a thermal-oxide-coated 100 p-type silicon single crystal with 100 nm thermal oxide. In all cases, a base pressure of 3×10^{-7} Torr was achieved before sputtering. Before deposition, the unheated substrate was first coated by a 30 nm thick Mo bottom electrode using DC sputtering (under a pressure of 7 mTorr), and the Si film was next deposited by RF sputtering without breaking the vacuum (under a pressure of 5 mTorr). Targets used were Si (bulk resistivity > 1 Ωcm), n-type Si (P-doped, bulk resistivity < 0.1 Ωcm), p-type Si (B-doped, bulk

resistivity $\sim$ 0.005-0.020 Ωcm). When desired, O/N was incorporated during Si sputtering by either injecting O_2/N_2 gas together with Ar gas into the sputtering chamber, or RF co-sputtering an oxide/nitride target chosen from Si_3N_4, AlN, SiO_2, Al_2O_3 and HfO_2. The electrical properties of films prepared by these different doping methods were similar. For example, they share the same bipolar resistance switching characteristics in appropriate thickness and O/N composition. So we mostly used Si_3N_4 for N incorporation and Al_2O_3 for O incorporation. Composition can be tuned by the flow rate of O_2/N_2 gas or by the sputtering power of the oxides/nitride target. Finally, a 40 nm thick Pt top electrode was deposited by RF sputtering (under a pressure of 7 mTorr) either through a shadow mask that defined cells of 50-250 μm in radius, or onto a lithography-defined pattern of 20 $\times$ 20 μm^2 cells followed by a lift-off process to achieve a higher cell density on one chip to be shot by electron bunch. As shown in Fig. A.1, the spacing between top Pt electrodes are typically 150 μm so they are electrically isolated from each other while single device can be accessed by probing top electrode (TE) of Pt and the common bottom electrode (BE) of Mo. Similar switching behaviors were also found in devices with switching materials of Ge, which was deposited by RF sputtering a Ge target (Sb-doped, bulk resistivity $\sim$ 5-40 Ωcm).

X-ray diffraction (XRD) patterns of Si/Ge films were measured by Rigaku GiegerFlex D/Max-B diffractometer. The patterns were compared with that of a bare single crystalline 100-Si substrate, and showed no additional peak other than the 100-Si peak of the substrate. To determine the film thickness, atomic force microscopy (AFM, Asylum MFP-3D) was used to measuring the step height created by deposition when one side was intentionally blocked. It was also used to measure the film roughness to check for any possible pin-holes and voids that may cause electrode contact. X-ray photoelectron spectroscopy (XPS) on Si films doped with O or N was collected using a RBD upgraded PHI-5000C ESCA system (Perkin Elmer) with Mg Kα radiation ($h\nu$ = 1253.6 eV). Binding energies were calibrated by referring to carbon (C 1 s = 284.6 eV). Composition of O and N in Si films was then determined using Si:2p, O:1s, and N:1s peaks by comparing them to calibrated signals from

standard SiO_2 and Si_3N_4 samples.

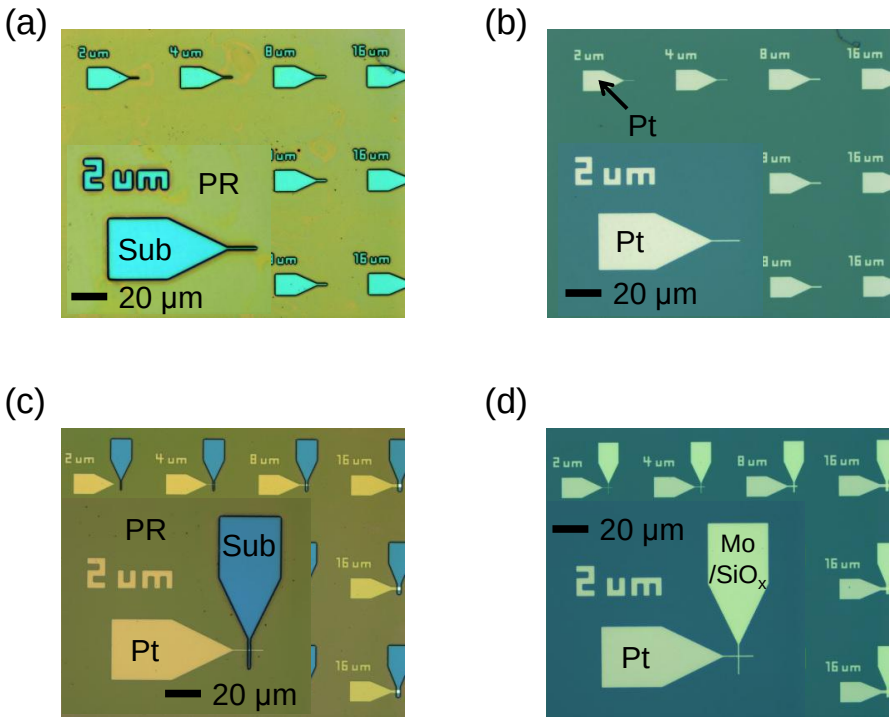

Figure A.2: Fabrication process of crossbar Si ReRAM devices. (a) Pattern photoresist (PR) exposes select regions of substrate (Sub) for bottom electrodes in various sizes. (b) Pt deposition followed by lift-off to define bottom electrodes. (c) Identical patterning of a second layer of PR aligned perpendicular to bottom Pt. (d) Switching layer (Si doped with O) and top electrode (Mo) lift-off to complete the final structure. Only small sizes are shown here (crossbar structures have sizes from 2 μm to 64 μm). High magnification pictures of the smallest device (2×2 μm^2) are shown in the insets to ensure no distortion or discontinuity is generated for each layer during the whole processes.

For the cross-bar devices, 3 nm Ti adhesion layer and 25 nm bottom electrode of Pt were deposited consecutively by ebeam-evaporator onto the patterned photoresist (double layered positive resists of LOR3A+S1813, Fig. A.2a) on silicon substrate and then lift-off to define electrode sizes of $2-64$ μm (Fig. A.2b). A second layer of identically patterned photoresist was then aligned perpendicular to the pattern of bottom Pt layer using the same mask (Fig. A.2c). Lastly, $\sim$ 5 nm amorphous Si doped with O and 30 nm Mo electrode with 10 nm Pt protection layer were sputtered consecutively and got lift-off to finalize the fabrication (Fig. A.2d).

A.2.2. Electrical Switching

To study electrical switching of Si ReRAM, current-voltage ($I-V$) and resistance-voltage ($R-V$) curves, where $R \equiv V/I$, were measured in both continuous DC and pulsed AC modes using a Keithley 237 measurement unit and an Agilent 81104A pulse generator. In a typical setting, samples were placed in a probe station (S-1160, Signatone Corporation, Gilroy, CA). In DC measurement, a continuous sweep of bias voltage supplied by a Keithley 237 was applied to the top Pt electrode while the bottom electrode was grounded. Current compliance during the negative sweep (on-switching) was applied in order to achieve intermediate states. In AC measurement, an Agilent 81104A pulse generator was used to supply a square-impulse-shaped voltage-pulse train of a constant width but an increasing height (voltage), and a Keithley 237 was used to read the device resistance at 0.2 V after each pulse (again with bottom electrode grounded).

Impedance measurements were conducted using a HP4192A impedance analyzer that superposed AC oscillation signal (oscillation level of 100 mV) with frequency of $10^2 - 10^7$ Hz (that covers the resonance frequency of most resistance states) on a DC signal to obtain the impedance spectroscopy of various resistance states at zero DC bias or the same resistance states at different DC bias from 0 V to 0.5 V. Equivalent circuit fitting was then performed to extract the intrinsic RC components of the device from its parasitic parts (here C is often treated as constant phase element−CPE in model fitting).

Uniformity and accelerated retention measurements were used to test the reliability of Si ReRAM. Cell-to-cell and cycle-to-cycle variations of Si ReRAM were obtained by collecting switching data under the same electrical sweeping conditions (either DC or AC) for 50 cells on the same device chip and for 100 DC cycling, up to 10^5 pulse switching cycles. The narrow distributions of resistance and switching voltage were shown in Weibull plots and individual DC switching curves were overlapped in the same $R-V$ plot, both demonstrating the excellent reproducibility of the resistance switching in Si ReRAM. During retention

test, the resistance values of DC- and pulse-switched resistance states (including HRS, intermediate states, and LRS) were periodically recorded at room temperature after they were kept at 175 °C for a certain time period. No degradation of resistance states was found up to 10^5 s.

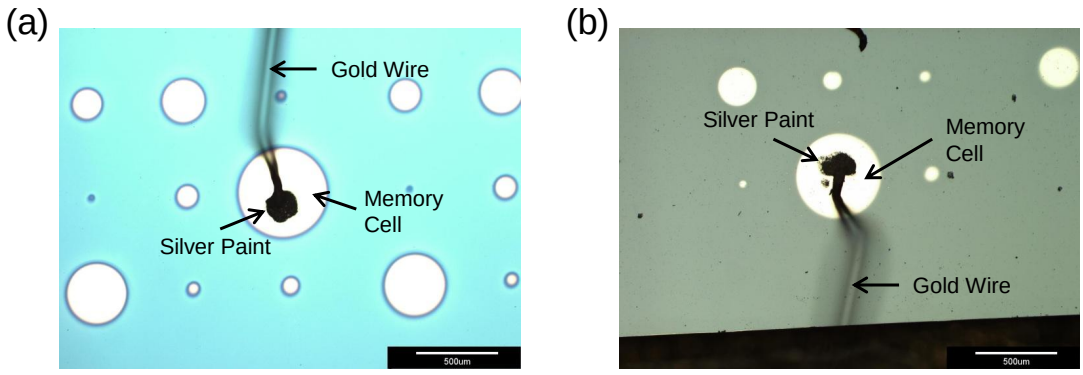

Figure A.3: Gold wires bonded to top electrode with radius of 250 μm for low temperature measurement in PPMS and later test in SCM1/2. Scale bar: 500 μm.

Low temperature switching experiment was conducted in two systems: the Lakeshore cryogenic probe station and Quantum Design PPMS. The former one, equipped with two probes that touch top and bottom electrodes, facilitates identical switching measurement in the S-1160 station at the temperature range of 77K to 400K (under 10^{-7} Torr level vacuum) by purging the sample stage with liquid nitrogen while electrically heating the stage simultaneously. In PPMS, its Ever-Cool helium cooling system allows temperate control from 2K to 300K in the vacuum of ∼5 Torr. Si ReRAM devices were mounted on a special chip holder with heat conducting vacuum grease and gold wires were bonded (dia. = 2 μm) to device electrodes and to the pins on the sample holder by silver paint (Fig. A.3). Below 10K, an appropriate current compliance was carefully chosen to prevent a sudden temperature burst due to Joule heating by the transition current.

A.2.3. Mechanical Switching

A hydraulic pressure was found to be able to on-switch HRS to LRS of Si/Ge ReRAM. Before the pressure treatment, the two-point resistance of each Si/Ge cell in an array on the same chip was read at 0.1 V or pre-switched to certain resistance state (including HRS, intermediate LRS, and LRS) using Keithley 237. Next, the chip was disconnected from the voltage source, wrapped in an aluminum foil, vacuum-sealed in an elastomer bag, and suspended in a liquid-filled pressure vessel (Autoclave Engineers, Erie, US) that was charged to a pre-set hydraulic pressure of 2—350 MPa at room temperature and held for <5 min before sample removal. The resistance of each cell was read again at 0.1 V and compared with its pre-pressure-treatment value, and switched back to HRS again by electrical voltage for the pressure-switched LRS. No difference was found between the off-switching of pressure-switched LRS and that of the voltage-switched LRS. Some higher pressure (up to 1 GPa) experiments were also similarly performed in a hydraulic pressure vessel (Dr. CHEF) at Takasago Works, Kobe Steel, at Takasago, Japan.

A magnetic pressure burst was also used to trigger HRS-to-LRS transition in Si/Ge ReRAM. In principle, a magnetic pressure may be generated by passing a burst magnetic flux between the Si/Ge-filled gap of the two electrodes, which form a metallic "container" that confines the burst magnetic field. (At high frequency, the gap resistance at the edges of the electrodes is very small so the two electrodes form a continuous circuit.) Assuming Si has a relative permeability of unity, the magnetic pressure $P_B = (B/0.501)^2$ with P_B expressed in bar (1 bar = 0.1 MPa) and B in T. The burst magnetic flux was received from an electron bunch, which is a spatially localized bundle of 20 GeV electrons generated at Stanford Linear Accelerator Center (SLAC) using the FACET facility. Each bunch contained $\sim 10^9$ electrons (>1 nC) that are narrowly collimated ($\sim$25 μm). It had a short duration, passing in $\sim$0.1 ps, which is the time for the bunch to travel 25 μm at near the speed of light, and was available on a bunch-by-bunch basis. We only allowed each cell to see one bunch during the experiment; after each shot the sample was moved to a new position before the second

shot was fired. The electron bunch hit the sample chip in the normal direction. Since the maximum magnetic field around the bunch is $\sim$ 70 T at the edge of the bunch, i.e., $\sim$ 40 μm from the flight path [67], and it decays with the radial distance r from the bunch roughly according to $1/r$, we can estimate the magnetic pressure in each cell from the cell location relative to the flight path. (To maximize the induced magnetic pressure inside the cell, we chose the cell size to be 20 μm, comparable to the bunch size.) So, the estimated maximum magnetic pressure is $\sim$1,950 MPa, and at 500 μm away it decays to $\sim$12.5 MPa. (The above estimates are lower bounds since they do not consider the pressure caused by the induced current in the electrodes.) Because of symmetry, however, there is no magnetic field at the center of the bunch. This was verified by the observation in some experiments one or two center cell that that suffered neither physical damage nor resistance change. (It also provided direct evidence that the impact damage due to momentum transfer was minimum, which is expected because the collision cross-section of a relativistic electron at 20 GeV is very small. See further discussion in [13]) The electric field is radial and follows the same radial variation as the magnetic field, but it is unimportant for this experiment as previously established in [15].

Similar to the hydraulic pressure experiment, before the magnetic-pressure treatment, cells were pre-transitioned by a voltage to certain resistance states, with their two-point resistance values recorded at 0.1 V by a Keithley 237. Their resistance was again read in the same way after the magnetic-pressure treatment and compared with the pre-treatment value. In a typical representation of the data, each cell is colored to indicate its resistance value before and after the treatment, and the colored maps are presented to aid comparison. In some experiments, the chip was covered by a photoresist, which is not a conductor and has no effect on the magnetic field. But because it can be blown away by a large magnetic field, it serves as a marker to help identify the flight path of the electron bunch. Since the cell size is about the same as the bunch size, maps that have hundreds of cells each appearing as a "dot" with changed colors provide direct evidence for the far-field effect of an electron bunch. Lastly, the magnetic-pressure-induced LRS was tested by electrical

voltage to check if it can transition back to HRS. Its subsequent electrical switching curve was compared with the curves before the shot by electron bunch.

A.3. Results

A.3.1. DC and AC Electrical Switching

A.3.1.1. Switching Characteristics of Amorphous Si/Ge

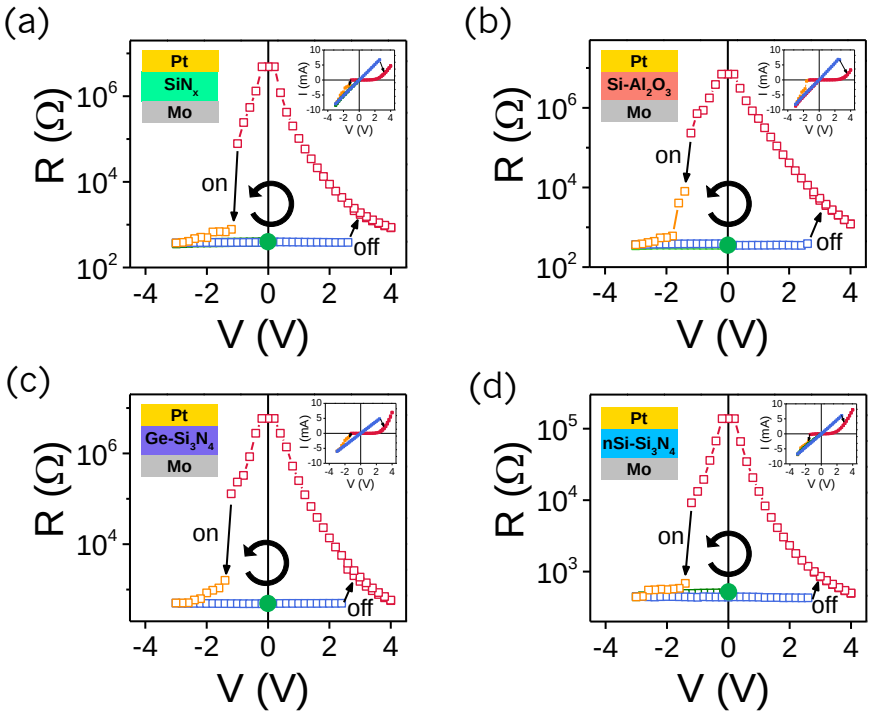

Figure A.4: Typical resistance switching with almost identical $R-V$ (and $I-V$) curves of mixture films of (a) SiN_x, (b) Si-Al_2O_3, (c) Ge-Si_3N_4, and (d) nSi-Si_3N_4. Device schematics and corresponding $I-V$ curves are shown as insets. Arrows indicate a counterclockwise switching direction. All devices have thickness $\sim$ 10 nm and size of 100 μm in radius. Each test used a virgin device never tested before, and the oversized green circle in each identifies the resistance of virgin film.

$I-V$ and $R-V$ properties of amorphous Si/Ge doped with O/N sandwiched between Mo and Pt electrodes were measured in ambient condition by sweeping quasi-DC voltage with controllable increment or decrement (each digitized value lasting for 20 ms). Here, the DC

voltage is applied to Pt electrode while Mo electrode is grounded. To set the stage for our discussion of detailed switching characteristics of Si ReRAM, we first describe typical DC resistance switching curves of four exemplary mixture films (with thickness of 10 nm and radius of 100 μm) of Si with N from N_2 gas, Si with Al_2O_3, n-type Si with Si_3N_4, and Ge with Si_3N_4 shown in Fig. A.4 ($I-V$ curves in the inset) to demonstrate their memory effects. Identical bipolar, non-volatile resistance switching was found in the hysteresis loops of all these compositions: (i) In their as-fabricated, virgin state, the mixture films start with a low initial resistance $< 500\ \Omega$ and this state is stable under a negative bias (green, overlapped by subsequent switching). (ii) Under a positive bias, it is still stable until a sudden increase of resistance around 2-3 V, which off-switches the device to high resistance state (red). Such HRS is stable after the removal of applied voltage, and under a bias between ± 1 V (it is non-linear and symmetric with respect to 0 V). (iii) A higher negative voltage over -1 V can switch HRS back to a low resistance state, whose resistance continuously decreases as the applied voltage goes more negative (orange). (iv) The LRS is linear in $R-V$ and $I-V$ (blue) and again it can be kept without voltage and when the applied voltage is less than the switching voltage (or the maximum negative voltage that on-switched the device to this state). (v) The reversible transition between the insulating HRS and conducting LRS is a genuine metal-insulator transition as revealed by the low temperature measurement. More details of the transport properties are presented in Chapter 2.

The bipolar switching between bi-stable resistance states was not only observed in the above four compositions but also extended to random materials of a semiconductor (such as Si, Ge, SiC, and mixture of two semiconductors, e.g., 50-50 alloy of Si and Ge), being doped or undoped, mixed by co-sputtering a target of insulator, being transition metal oxide (e.g., HfO_2), simple metal oxide/nitride (e.g., Al_2O_3/AlN), and semiconductor oxide/nitride (e.g., SiO_2/Si_3N_4), fabricated by co-sputtering two targets. Their characteristic $R-V$ curves, shown in Fig. A.5a-g, are indistinguishable with very similar switching voltages. In addition, O and N dopants can be introduced by reactive sputtering of Si/Ge target with O_2 and N_2 gases injected to the sputtering chamber. Their switching curves are documented in

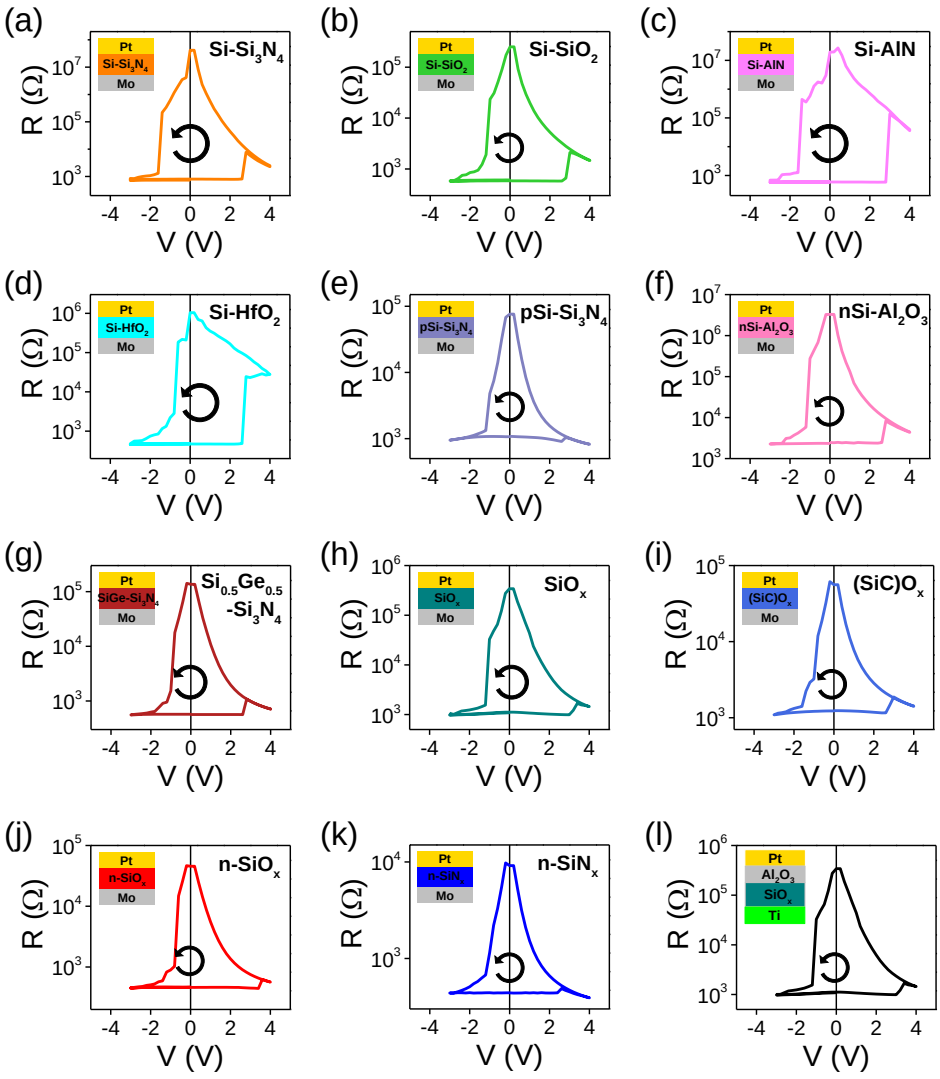

Figure A.5: Other semiconductor:insulator material systems show similar $R-V$ switching curves with almost the same switching voltage, including (a) Si-Si_3N_4, (b) Si-SiO_2, (c) Si-AlN, (d) Si-HfO_2, (e) p type Si-Si_3N_4, (f) n type Si-Al_2O_3, (g) $Si_{0.5}Ge_{0.5}$ alloy-Si_3N_4, (h) SiO_x, (i) $(SiC)O_x$, (j)n-SiO_x, (k) n-SiN_x, (l) pure Si with additional layer of Al_2O_3 that oxidized Si into SiO_x. Insets illustrate device structure with Pt as top electrode and Mo as bottom electrode in (a)-(k) and Mo is replaced by Ti in (l). Arrows indicate a counterclockwise switching direction. All devices have thickness $\sim$ 10 nm and size of 100 μm in radius.

Fig. A.4a and A.5h-k. Lastly, one can also put additional oxide layer (such as Al_2O_3) next to pure Si and/or replace Mo by Ti as electrode to obtain similar resistance switching characteristics (Fig. A.5l).

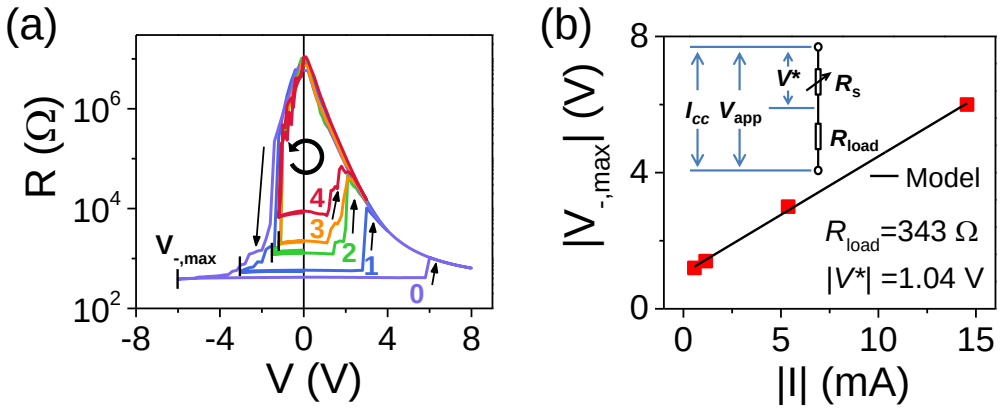

Figure A.6: Multiple LRS of Si ReRAM with radius $r = 100$ μm obtained by adjusting maximum sweeping voltage $V_{-,\max}$ during on-switching. (a) $R - V$ curves of Si-Al_2O_3 devices with various $V_{-,\max}$. The higher the $|V_{-,\max}|$, the lower the $R_{\rm LRS}$, the higher the positive off-switching voltage. Arrows indicate switching direction. (b) Linear relation between $|V_{-,\max}|$ and $|I|$ in (a) predicted by Eq. (A.1), with intercept and slope giving V^* and $R_{\rm load}$, respectively. Inset: equivalent circuit for the load-sharing DC switching model.

In addition to HRS and LRS, a multitude of intermediates states can be obtained by adjusting the maximum negative voltage ($V_{-,\max}$) that triggers the continuous on-switching in Fig. A.4 (orange). One example is demonstrated in the $R-V$ curves of Si-Al_2O_3 devices in Fig. A.6a, in which $V_{-,\max}$ marked as vertical lines progressively lowers LRS resistance (denoted as $R_{\rm LRS}$). Note that these intermediate states are off-switched back to one common HRS at different positive voltages, which is about equal to $V_{-,\max}$, i.e., as $R_{\rm LRS}$ decreases, the voltage required to switch-off LRS to HRS increases. These two features, which were also found in other nanometallic ReRAM and in many filamentary ReRAM systems, can be fully explained by a load sharing effect. As illustrated in the inset of Fig. A.6b, if we envision an equivalent circuit of a switchable resistance $R_{\rm S}$ in series with a load resistance $R_{\rm load}$ (from electrode, interface, line resistance), and let the voltage on $R_{\rm S}$ during switching

be V^*, then the applied voltage $V_{\rm app}$ is

$$V_{\rm app} = V^* + IR_{\rm load} \tag{A.1}$$

where I is the switching current of the circuit. If dividing Eq. (A.1) by current I, we get

$$R_{\rm LRS} = \frac{V^*}{I_{\rm cc}} + R_{\rm load} \tag{A.2}$$

Therefore, with fixed V^* and $R_{\rm load}$, the higher the $V_{\rm app}$, the higher the I, and thus the lower the $R_{\rm LRS}$. In addition, Eq. (A.1) implies a linear relation between $V_{\rm app}$ (or $|V_{-,\rm max}|$ for on-switching) and the corresponding current $|I|$, which is verified by the straight line of Fig. A.6b. The linear fitting of $V_{\rm app}$ vs. $|I|$ gives $|V^*| = 1.04$ V from the intercept, and $R_{\rm load} = 343\ \Omega$ from the slope. The above analysis was similarly performed for SiO_2:Pt [127] and Si_3N_4:Cr [13, 128, 129], in which $|V^*|$ values around 1 V were also obtained.

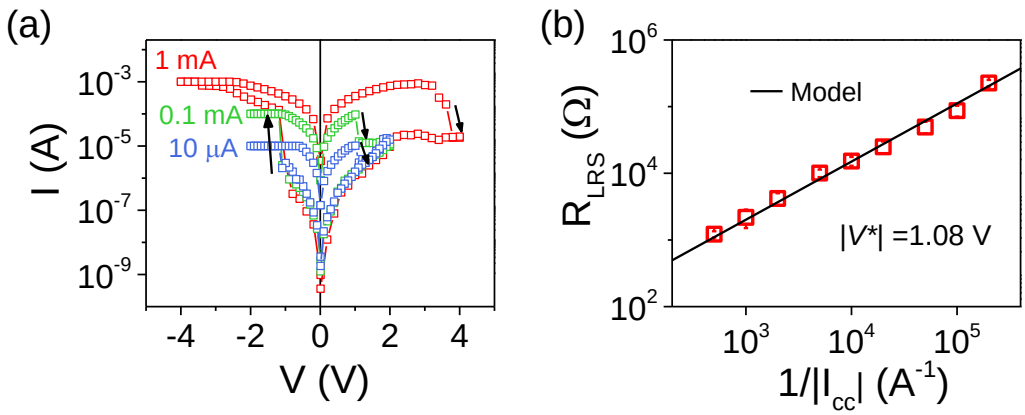

Figure A.7: Multiple LRS of Si ReRAM obtained by varying current compliance $I_{\rm cc}$ during on-switching. (a) $I-V$ curves of nSi-Si_3N_4 devices with various $I_{\rm cc}$. The higher the $|I_{cc}|$, the lower the $R_{\rm LRS}$, higher the positive off-switching voltage. Arrows indicate switching direction. (b) Linear relation between $R_{\rm LRS}$ and $1/|I_{\rm cc}|$ in (a) predicted by Eq. (A.2). Error bars are obtained from 10 tests of the same device. Devices used here are $2 \times 2\ \mu{\rm m}^2$ crossbar devices (check later sections for details).

Multiple LRS can also be obtained by setting a variable current compliance $I_{\rm cc}$ during on-switching, e.g., (Fig. A.7a for a $2 \times 2\ \mu{\rm m}^2$ Si ReRAM crossbar devices. (Check later sections

for details). Linear fitting of $R_{\rm LRS}$ vs. $1/I_{\rm cc}$ in Fig. A.7b is consistent with the prediction of Eq. (A.2), in which $V^* = 1.08$ V, almost the same as $|V^*|$ extracted in Fig. A.6b, even though the device area was reduced by almost 4 orders of magnitude.

We next describe how switching characteristics of Si ReRAM vary with device area, film thickness/composition, temperature, and switching speed. Remarkably, the critical switching voltage V^* turns out to be a constant around ± 1 V in all the devices (including nanometallic ReRAM made of electron-doped oxide/nitride glasses [12, 13]), independent of size, thickness, dopant composition, temperature, and switching rate. Therefore, switching is not controlled by the electrical field; instead, it is an energy (voltage) controlled process. Since it can be concluded from Fig. A.4-A.5 that there are no obvious difference of resistance switching among different mixture systems, we will only show the results of selected materials.

Device Size Dependence

According to Eq. (A.2) and the equivalent circuit in Fig. A.6b, when $R_{\rm S} \ll R_{\rm load}$, $R_{\rm LRS} \approx R_{\rm load}$. Since the load in these ReRAM devices is primarily due to the spreading resistance of the bottom electrode, which has a very weak, logarithmic dependence on area, $R_{\rm load}$ is insensitive to area. Therefore, $R_{\rm LRS}$ will naturally approach an area-insensitive asymptote $R_{\rm load}$ when a sufficiently large switch-on current or $|V_{-,\rm max}|$ is applied. This is often the case for resistance switching without current compliance. In comparison, since $R_{\rm S} \gg R_{\rm load}$ in the HRS, $R_{\rm HRS}$ is asymptotically $R_{\rm S}$.

This is verified in Fig. A.8 that compares $R-V$ switching curves of Si-Al_2O_3 devices with radius of 50 μm $-$ 250 μm under the same sweeping condition. It shows size-independent $R_{\rm LRS}$ (which is essentially $R_{\rm load}$), and $R_{\rm HRS}$ that is inversely proportional to device area (Fig. A.8b). Such area scalability of HRS suggests resistance switching occurs uniformly across the mixture film in Si ReRAM, which is a unique feature of nanometallic ReRAM that are discussed in [106, 103, 107]. On the other hand, switching voltage in both on-

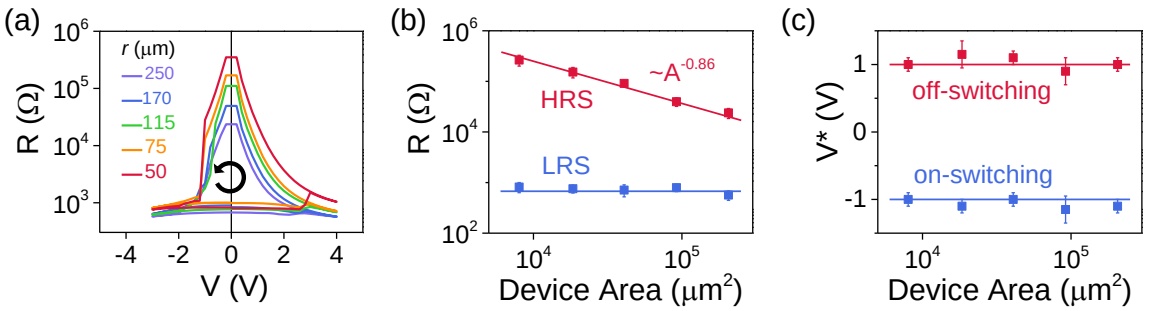

Figure A.8: Area dependence of Si-Al_2O_3 ReRAM devices (with Mo-Pt electrodes). (a) $R-V$ curves for devices with radius r from 250 μm to 50 μm under the same sweeping condition. (b) Average HRS and LRS resistance vs. device area. (c) Average critical switching voltage V^* calculated from Eq. (A.1) using size-insensitive R_{load} extracted from linear fitting. Error bars in (b) and (c) are obtained from testing 20 devices of the same size.

and off-switching is insensitive to device size (Fig. A.8c, where V^* was calculated by V_{app} and size-insensitive R_{load} using Eq. (A.1)). The above area dependence is consistent with the observations for other nanometallic ReRAM [11, 12, 13], and it will be extended to a much wider area range when we discuss small Si ReRAM devices fabricated in crossbar configuration.

Thickness and Composition Dependence

Devices made of Si-Al_2O_3 in-between Mo and Pt electrodes in the size of 100×100 μm^2 with various film thickness δ and O composition (x as in the formula SiO_x, determined by XPS measurement) are tested to determine their influence on electrical conduction and nanometallic resistance switching. For the mixture films of insulator and metal studied previously, nanometallicity occurs at a nominal metal fraction f well below the bulk percolation limit f_p [12, 13]. For Si-based nanometallic systems that are apparently free of these metal atoms, there are no such concerns about percolation or clustering of metal atoms at all. Therefore, Si ReRAM, serving as a much cleaner homogeneous system, provides a unique opportunity to demonstrate the concept of nanometallicity, i.e., how random insulators evolve into nanometals, purely tuned by localization.

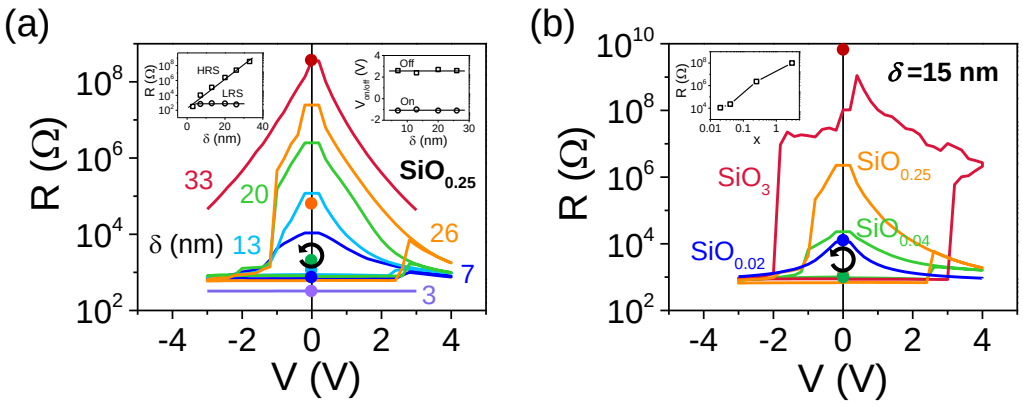

Figure A.9: $R-V$ curves of Mo/Si-Al_2O_3/Pt devices with (a) various thickness δ under fixed O composition $x_O = 0.25$. Three distinctive types of electrical conduction: insulating, switching, and conducting, occur as thickness decreases. Insets: HRS and LRS resistance vs. thickness (left) and switching voltage vs. thickness; (b) various O composition under the same thickness of 15 nm. Sufficient amount of O is necessary to render switching in SiO_x films. Inset: resistance vs. composition x_O. In both (a) and (b), O was doped into Si by co-sputtering Si and Al_2O_3 targets, which makes SiO_x compositions with $x > 2$ possible (e.g., SiO_3). First switching cycle in each curve is omitted for simplicity, and the oversized circle with corresponding color in each identifies the resistance of virgin film.

Fig. A.9a compares $R-V$ properties of $SiO_{0.25}$ films in various thickness δ (i.e., $x_O = 0.25$ is fixed). As δ changes from 33 nm to 3 nm, the device characteristics change from a non-linear insulating curve to a linear conducting behavior. More importantly, in the intermediate thickness range (7−26 nm), $SiO_{0.25}$ acquires bistable resistance states of HRS and LRS, and exhibits reversible switching between the two as described before. This is consistent with the picture of nanometallicty for other nanometallic ReRAM, random insulators are insulating because $\zeta < \delta$ (e.g., the 33 nm $SiO_{0.25}$), but become conducting when $\zeta > \delta$ (e.g., the 3 nm $SiO_{0.25}$). If ζ is tunable by electrical voltage, resistance switching occurs for $\zeta \sim \delta$. As summarized in the upper-left inset of Fig. A.9a, HRS resistance increases exponentially with thickness, following Anderson's scaling theory $R = R_0 \exp(\delta/\zeta)$. On the other hand, LRS resistance remains constant when thickness varies because it is primarily determined by spreading resistance R_{load} that is insensitive to film thickness. Such transition of electrical conduction triggered by thickness at room temperature is indeed an insulator-to-metal transition as verified by our transport study at much lower temperatures in Chapter

2. Lastly, the upper-right inset in Fig. A.9a shows constant on- and off-switching voltage, independent of thickness.

When δ is fixed at 15 nm, $R-V$ curves of the SiO_x films with different x are shown in Fig. A.9b. While $SiO_{0.04}$ and $SiO_{0.25}$ devices exhibit normal resistance switching with the same switching voltage, SiO_3 devices start with much more resistive states that can only be switched by large voltages (which is unlikely to be the same type of switching as the one of lightly-doped Si films). Their HRS resistance increases with more O, i.e., a larger x (inset of Fig. A.9b). On the other hand, SiO_x films is unable to switch when less O is introduced, as evident by the $SiO_{0.02}$ device that shows non-Ohmic resistance as voltage varies without any hysteresis (which is also named as insulating samples). Therefore, localization tuning and nanometallic resistance switching in Si ReRAM must be related to the O/N dopants. If it is due to negative-U and electron-phonon interaction (which will be proved by mechanical switching in later section), those negative-U centers must be close to Si-O or Si-N bonds that can be ultra-soft, rendering locally strong electron-phonon interaction (see more discussions at the end of this chapter).

More (δ, x) pairs in SiO_x amorphous film were tested to depict a complete mapping of electrical conduction property as shown in Fig. A.10. Four symbols in the $\delta - x$ map are used to denote four different behaviors of each (δ, x) point: filled circles are insulating films that have non-linear $R-V$ (like the 33 nm sample in Fig. A.9a and the $SiO_{0.02}$ sample in Fig. A.9b), hollow circles are conducting (or nanometallic) films that exhibit linear $R-V$ (like the 3 nm film in Fig. A.9a), hollow triangles are switchable films with hysteresis $R-V$. Similar to the $\delta-f$ maps of SiO_2:Pt [12, 14] and Si_3N_4:Cr [13, 15], we see thickness-triggered metal-to-insulator transition by traversing vertically from bottom to top in the map and composition-controlled transitions by traversing horizontally from left to right in the map (which is actually in the opposite direction of the other two systems doped with metals). Again, we have formally demonstrated such metal-insulator transitions of pure and O/N-doped Si/Ge films in Chapter 2 using transport data. Three more notes before we end this

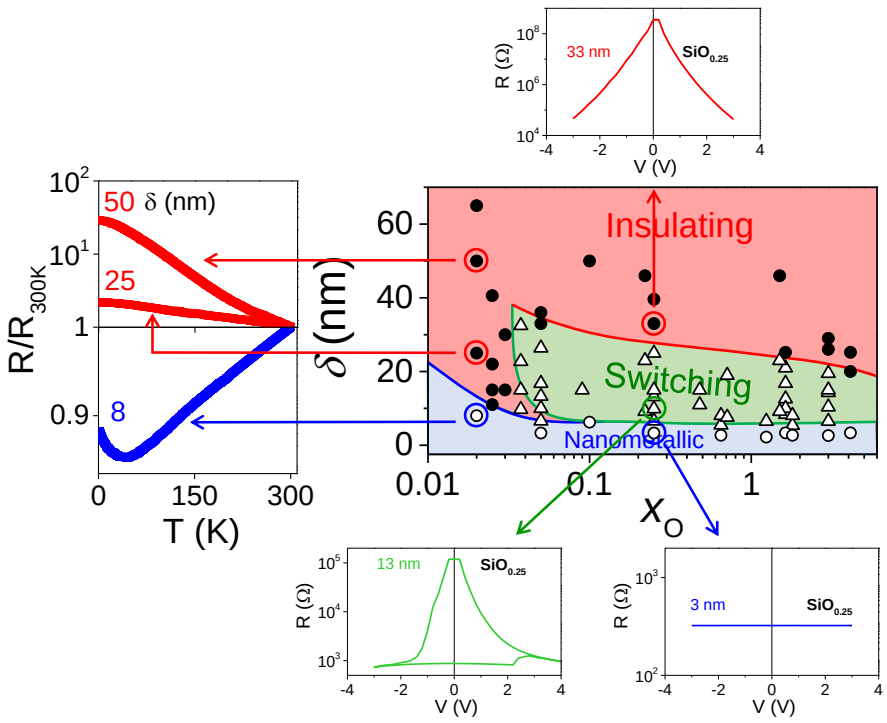

Figure A.10: $\delta - x$ map of Mo/Si-Al_2O_3/Pt ReRAM devices. O was doped into Si by co-sputtering Si and Al_2O_3 targets, which makes SiO_x compositions with $x > 2$ possible (e.g., SiO_3). Device radius: 100 μm. Corresponding $R - T$ and $R - V$ curves (at room temperature) are shown on the sides, indicated by the arrows.

subsection: (i) Regardless of the x values, the nanometallic region always appears when δ approaches 0. This means that: if δ is small enough, there is always nanometallicity. (ii) A unique feature of Si is the existence of semiconducting region for small x: pure Si film is unable to switch unless sufficient amount of O/N is added. The threshold x, below which no resistance switching occurs, is about 0.04, for Si-Al_2O_3 devices. (iii) The switching region extends to very large x over 2, in which the majority species become the oxides/nitrides. It may overlap with the cases of doping filamentary switching layer with Si [130, 131], which is not the focus of this thesis. (iv) The trend that critical thickness for NM and switching both decrease with dopant concentration in Fig. A.10 is opposite to what is seen in SiO:Pt, SiN:Cr and other NM [12, 13]. However, this makes sense because localization length decreases with O doping in Si, whereas it increases with Pt and Cr doping in SiO/N.

Temperature Dependence

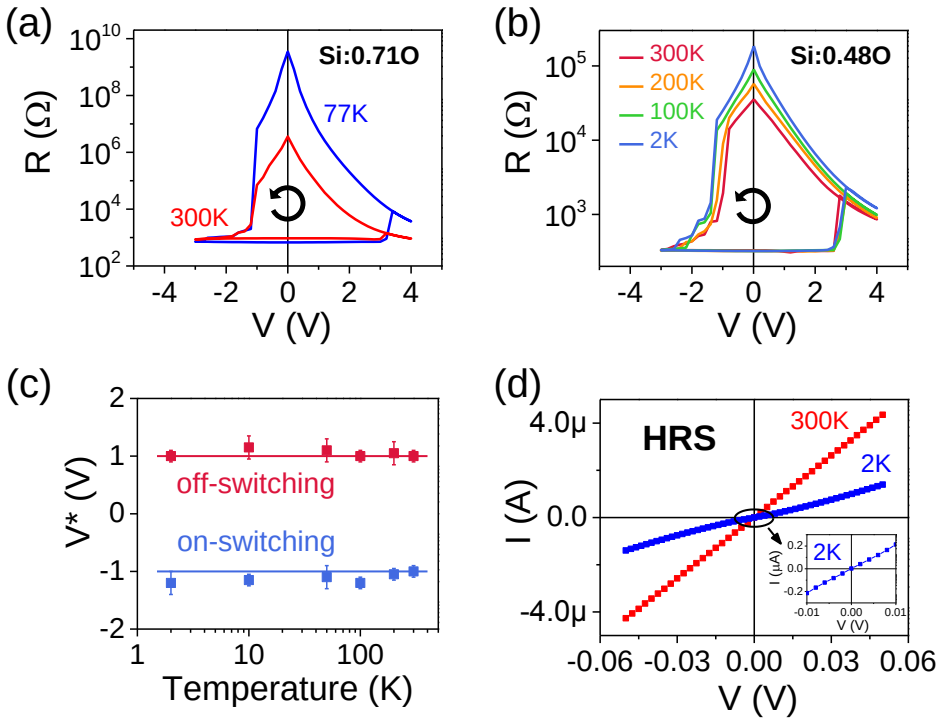

Figure A.11: Temperature dependence of switching characteristics of Mo/Si-Al_2O_3/Pt devices. (a) $R-V$ switching curves of $SiO_{0.71}$ at 300K and 77K. (b) $R-V$ switching curves of $SiO_{0.48}$ at 300K, 200K, 100K, and 2K. (c) Critical switching voltage V^* shows very weak temperature dependence. (d) HRS resistance is Ohmic at small voltages, whose range decreases at 2K (inset).

Temperature effect on resistance switching was examined for Si-Al_2O_3 devices (similar results were found in nSi-Si_3N_4 devices). Switchibility was confirmed, first at liquid N_2 temperature, i.e., 77K in cryogenic probe station (Fig. A.11a), and then at liquid He temperature−2K in PPMS (Fig. A.11b). Notably, switching voltages show a weak or no temperature dependence from 2K to 300K (Fig. A.11c): $|V^*_{\rm on}|$ slightly increases as temperature decreases while $|V^*_{\rm off}|$ is almost constant. Here, the critical voltage V^* was obtained using Eq. (A.1) assuming a temperature-independent $R_{\rm load}$. $R-V$ curves are symmetric for both LRS and HRS at all temperatures. For LRS resistance, it is Ohmic (linear $R-V$) and has weak temperature dependence. In contrast, HRS resistance increases sharply

with decreasing temperature and it is more non-linear (non-Ohmic) at lower temperatures. However, it is Ohmic at small voltage, and this linear range shrinks as temperature decreases (Fig. A.11d). These observations are also consistent with the previous results of Mo/Si_3N_4:Pt/Pt devices [13]. Besides switching, comprehensive studies of the temperature dependence of HRS and LRS resistance, e.g., the $R-T$ characteristics down to 20mK, are given in the main Chapters 2-4 for various ReRAM systems to reveal quantum phenomena related to weak localization and their conduction dimensionalities.

Switching Speed Dependence

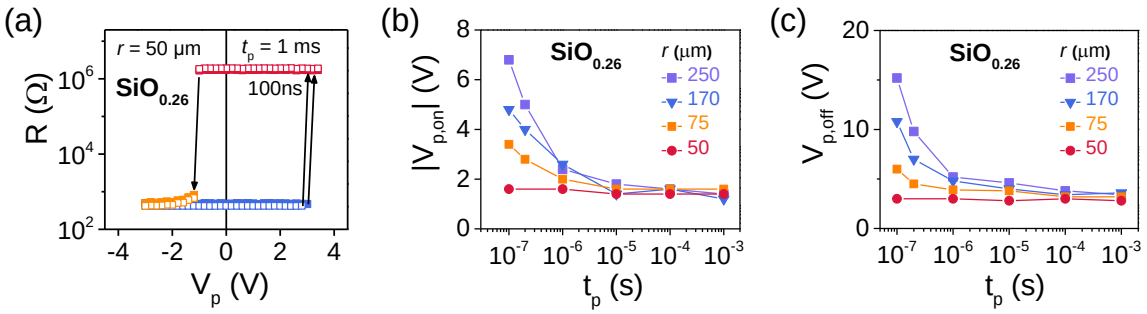

Figure A.12: Pulse switching of Mo/Si-Al_2O_3/Pt devices (δ = 11 nm, x_O = 0.25) in various sizes. (a) Typical AC switching curves of 50 μm device with independent switching voltage with respect to the change of pulse rate t_p. Dependence of $V_{p,on/off}$ on t_p for (b) on-switching and (c) off-switching, in which $V_{p,on/off}$ does not change with t_p until a sudden increase at size-dependent threshold value determined by circuit RC delay.

Lastly, resistance switching of Si ReRAM can occur much faster in AC pulse measurement. In such experiment, resistance state of Si ReRAM was read by DC voltage of 0.1 V each time after a square pulse with (width t_p and height V_p) was applied to the device. One example of such $R-V_p$ curve collected during AC switching is shown in Fig. A.12a for a 50-μm-device made of Si-Al_2O_3 switched by t_p = 1ms (hollow symbols) and 100 ns (filled symbols). Note that unlike previous switching curves, HRS resistance (red) is a constant of V_p because the reading voltage after each pulse is always 0.1 V. Collected in similar tests of more t_p values, the pulse rate dependence of switching voltage is shown in Fig. A.12b-c for various devices in different size radius r. It was found that Si ReRAM can be pulse-

switched without change of switching voltage $V_{p,on/off}$ until a threshold value limited by the circuit RC delay, which is size-dependent. In principle, ultra-fast ±1 V switching of nanometallic ReRAM can be achieved when device area is further scaled to reduce the RC delay, which was demonstrated in SiO_2:Pt devices that switches in less than 100 ps [132]. We will further discuss the limit of switching speed of Si ReRAM using the example of crossbar Si ReRAM devices later in this chapter. Also demonstrated in other nanometallic devices made of $LaAlO_3$:$LaNiO_3$ [11], SiO_2:Pt [12], and Si_3N_4:Pt [13], the independence of $V_{p,on/off}$ on t_p in small devices is a signature of electronic switching, which does not hold in filamentary ReRAM devices. An analytic model to explain the dynamic switching was given in [13] and is further developed in [106].

A.3.1.2. Device Reliability

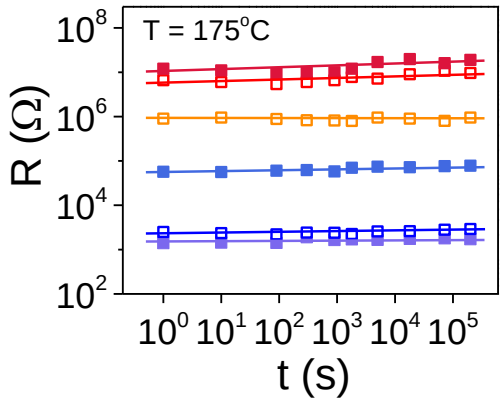

Figure A.13: Data retention of multiple resistance states in Mo/Si-Al_2O_3/Pt devices (δ = 10 nm, x_O = 0.48, size r = 50 μm) kept at 175 °C. Filled symbols: states obtained by DC voltage. Hollow symbols: states switched by 100 ns pulse.

Data retention evaluates the non-volatility of memory devices, i.e., how long it can remain in the stored states after removal of programming voltage. Si-Al_2O_3 ReRAM devices were pre-set to LRS, HRS and multiple intermediate states by DC voltage (filled symbols) and 100 ns pulse (hollow symbols), and then read by a small 0.1 V at room temperature after being kept at 175 °C for a certain time period t. Results of such accelerated retention test are shown in Fig. A.13, which clearly indicate that different resistance states of Si-Al_2O_3

devices are all stable over 10^5 s (only a slight increase of HRS resistance was found).

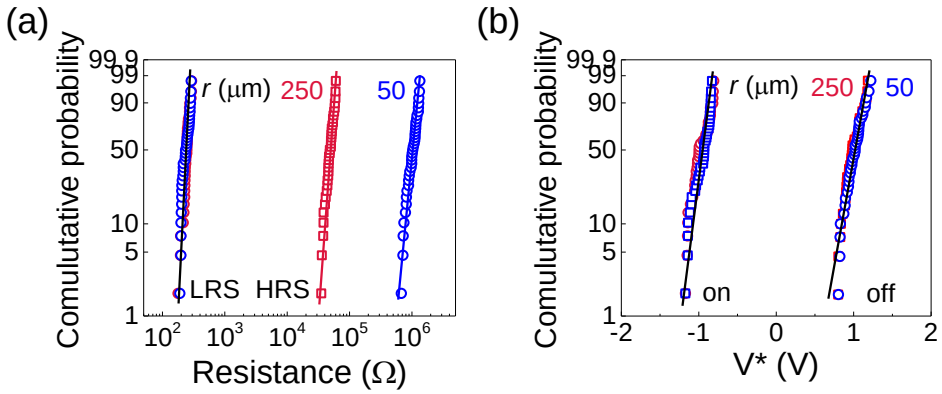

Figure A.14: Device uniformity of Mo/nSi-Si_3N_4/Pt devices ($\delta = 11$ nm, $x_O = 0.48$) in two sizes ($r = 250$ μm and $r = 50$ μm) represented in Weibull plots of (a) size-dependent HRS and size-independent LRS resistance (excluding load resistance R_{load}, (b) critical switching voltage V^*. Each distribution contains 35 devices tested under the same condition.

Cell-to-cell variation, or device uniformity of Si ReRAM was tested by switching many "identically fabricated" devices under the same sweeping condition (-3 V to 4V). The Weibull statistics of HRS and LRS resistance, and critical on- and off-switching voltage V^* for 35 nSi-Si_3N_4 devices of two sizes are shown in Fig. A.14. The narrow distributions imply resistance switching is highly reproducible in both large and small devices (they only differ in their HRS resistance as discussed early in the section of area scaling). Highly uniform switching characteristics are unique advantage of nanometallic ReRAM over filamentary ReRAM, in which large switching variations are caused by the stochastic filaments formation. From straight lines in Fig. A.14, device uniformity can be quantified by the Weibull shape parameter k is about 10 for nSi-Si_3N_4 devices (a greater k means smaller standard deviation over the mean value$-\Delta/\mu$), which is about the same as for nanometallic SiO_2:Pt and Si_3N_4:Cr devices and much greater than for filamentary ReRAM in the literature as summarized in [66].

Fatigue test over on/off switching cycles was used to evaluate cycle-to-cycle variation, or the endurance of Si ReRAM. The robust resistance switching of Si-Al_2O_3 devices over cycling

is demonstrated by the overlapping $R-V$ and $I-V$ switching curves of consecutive 50 DC cycles in Fig. A.15a. In addition, the stable HRS-to-LRS resistance window, recorded after each 10 μs pulse switching for up to 10^5 cycles, is shown in Fig. A.15b. According to the mechanical experiment switching described later in this chapter and previous studies in [13], the endurance performance can be improved if (a) mechanical contact is avoided during testing, (b) the device is isolated from ambient moisture and (c) the quality of electrodes is improved to avoid wear, decohesion or oxidation.

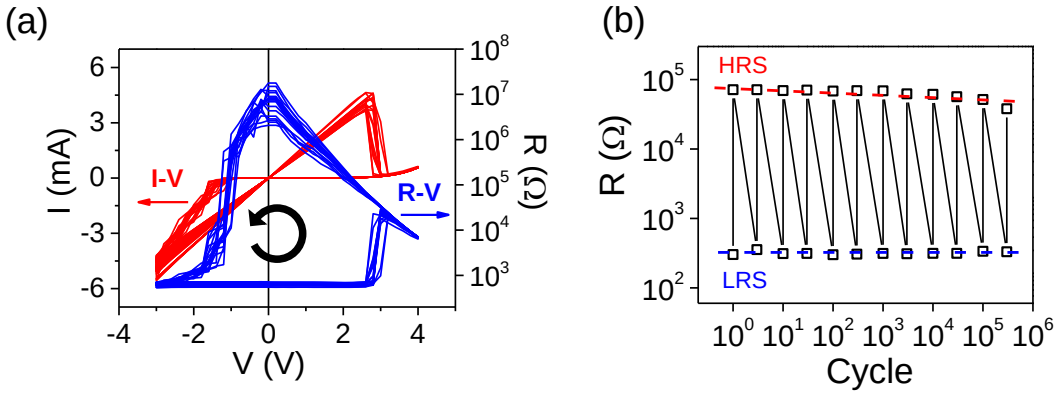

Figure A.15: Device fatigue of Mo/Si-Al_2O_3/Pt devices (δ = 10 nm, x_O = 0.48). No resistance degradation or loss of switchibility was found after (a) 50 DC switching cycles from -3 V to 4 V (r=50 μm), and (b) 10^5 AC switching cycles with pulse width of 10 μs (r=250 μm).

A.3.2. Impedance Measurement

The impedance of Si ReRAM was studied by impedance spectroscopy in the frequency domain. The generalized impedance Z, which is a frequency-dependent complex number $Z = Z_{\text{re}} + jZ_{\text{im}}$, was measured and then analyzed using the Cole-Cole plot where $-Z_{\text{im}}$ is plotted against Z_{re}. In an equivalent circuit, physical and chemical processes in thin films can be represented as a capacitor C in parallel with a resistor R. Since $Z_{\text{C}} = 1/j\omega C$ and $Z_{\text{R}} = R$, the total impedance of a parallel RC unit can be written as

$$Z = \frac{R/j\omega C}{R + 1/j\omega C} = \frac{R}{1 + j\omega RC} \tag{A.3}$$

with $Z_{\rm re} = R/(1+(\omega RC)^2)$ and $-Z_{\rm im} = \omega R^2 C/(1+(\omega RC)^2)$. Therefore,

$$(Z_{\rm re} - \frac{R}{2})^2 + (-Z_{\rm im})^2 = \frac{R^2}{4} \tag{A.4}$$

Eq. (A.4) represents a perfect semicircle with a radius of $R/2$ centered at $(R/2, 0)$. It can be verified by checking the limits of Eq. (A.3): (i) when $\omega \to 0$, $Z \approx R$, which is the rightmost point intersecting $Z_{\rm re}$ axis. (ii) when $\omega \to \infty$, $Z \approx -j/\omega C \to 0$, which crosses the (0,0) origin point. (iii) At resonance, $\omega = \omega_c = 1/RC$, $-Z_{\rm im,max}(\omega_c) = Z_{\rm re}(\omega_c) = R/2$.

The DC equivalent circuit in Fig. A.6b suggests there are at least two sets of parallel $R\|C$ units in Si ReRAM (Fig. A.16a): $R_{\rm S}//C_{\rm S}$ for the switching film that may vary between different states, and $R_{\rm load}\|C_{\rm E}$ for the load, mostly from spreading resistance and the electrode/film interface that remain constant during switching. For completeness, we also added the line resistance $R_{\rm L}$ and the inductance L that arise from the testing circuit and other non-capacitive parasitic component serially connected to the memory device, which will manifest at very high frequency.

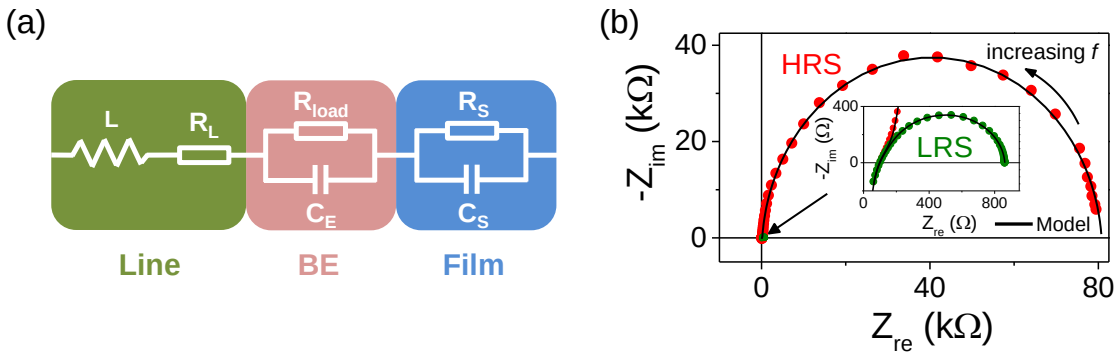

Figure A.16: (a) Equivalent circuit of Si ReRAM. (b) Cole-cole plots of HRS (red) and LRS (green, inset) of Si-Al_2O_3 devices ($\delta = 14$ nm, $x_{\rm O} = 0.25$, r=250 μm) at zero DC bias. Solid lines are fitting results by the circuit in (a).

Typical Cole-Cole plots (Nyquist plots) of Si-Al_2O_3 devices obtained by measuring device impedance under 100 mV AC oscillation from 100 Hz to 13 MHz are shown in Fig. A.16b (for HRS) and its inset (for LRS). Both curves have a shape of depressed semicircle: HRS

data falls on a large one with diameter ~ 80 kΩ and reaches a "peak" at resonance frequency ~ 1380 Hz and LRS impedance has a much smaller diameter ~ 850 Ω and higher resonance frequency ~ 220 kHz. They converge to a common part at high frequency distorted by a second semicircle (inset), which eventually becomes negative ($Z_{\text{im}} > 0$). The features of Fig. A.16b can be attributed to the circuit elements in Fig. A.16a: (i) The low-frequency semicircle that changes with resistance states comes from parallel $R_{\text{S}}C_{\text{S}}$, (ii) the common distortion is related to $R_{\text{load}}//C_{\text{E}}$ which gives a second semicircle at high frequency, (iii) the non-zero crossing of Z_{re} axis and convergence toward positive Z_{im} correspond to the resistance element $R_L + L$ in series with the above two distinct RC elements.

In order to fit the semicircles in Fig. A.16b and all the other Cole-Cole plots of Si ReRAM, the two capacitors C_{S} and C_{E} are replaced by constant phase elements (CPE) [133, 134] in our model fitting. CPE accounts for the frequency dispersion of a linear capacitance (which should be independent of frequency) with impedance given by

$$Z_{\text{CPE}} = \frac{1}{(j\omega)^n Q} \tag{A.5}$$

where $n \leq 1$ is an ideality factor ($n = 1$ for the capacitor, $n = 0$ for resistor, and $n = -1$ for inductor) and Q is the admittance (reciprocal impedance) at $\omega = 1$ rad/s. Based on Eq. (A.5) and the equivalent circuit in Fig. A.16a, impedance spectra of Si ReRAM can be fitted by

$$Z = j\omega L + R_L + \frac{R_{\text{load}}}{1 + (j\omega)^{n_E} Q_E} + \frac{R_{\text{S}}}{1 + (j\omega)^{n_S} Q_S} \tag{A.6}$$

Obviously any spectrum can be fitted by sufficiently large number of CPEs, but in order to inform meaningful physics of the system, n should be as close to 1 as possible. As suggested by Hsu and Mansfeld [135], for CPE in parallel with R, Q can be converted into C by $Q(\omega_m)^{n-1}$, when ω_m is the frequency where Z_{im} reaches its maximum. Following this

conversion, it can be derived that

$$C = \frac{(QR)^{1/n}}{R} \tag{A.7}$$

Data in Fig. A.16b was fitted by Eq. (A.6) with fixed $L = 3.2$ μH, $R_L = 10$ Ω, $R_{\text{load}} = 150$ Ω, $Q_E = 1.8 \times 10^{-8}$ Fs$^{n_E-1}$, and $n_E = 0.74$ in both HRS and LRS. The fitting results are shown as solid lines, which are in excellent agreement with experimental results. Here the two sets of parameters used for HRS and LRS are: $R_{\text{S,HRS}} = 80.5$ kΩ, $Q_{\text{S,HRS}} = 2.32 \times 10^{-9}$ Fs$^{n_{\text{S,HRS}}-1}$, $n_{\text{S,HRS}} = 0.968$; $R_{\text{S,LRS}} = 701$ Ω, $Q_{\text{S,LRS}} = 1.69 \times 10^{-9}$ Fs$^{n_{\text{S,LRS}}-1}$, $n_{\text{S,LRS}} = 0.965$. Q was then converted into C using n and R according to Eq. (A.7), which gave 30% difference between the two capacitance values $C_{\text{S,HRS}} = 1.53$ nF and $C_{\text{S,LRS}} = 1.15$ nF. Given the nominal device area of 2×10^5 μm^2 and thickness of 14 nm, the dielectric constant was calculated to be around 9 in LRS and 12 in HRS, comparable with the well-known value of 11.8 for amorphous silicon.

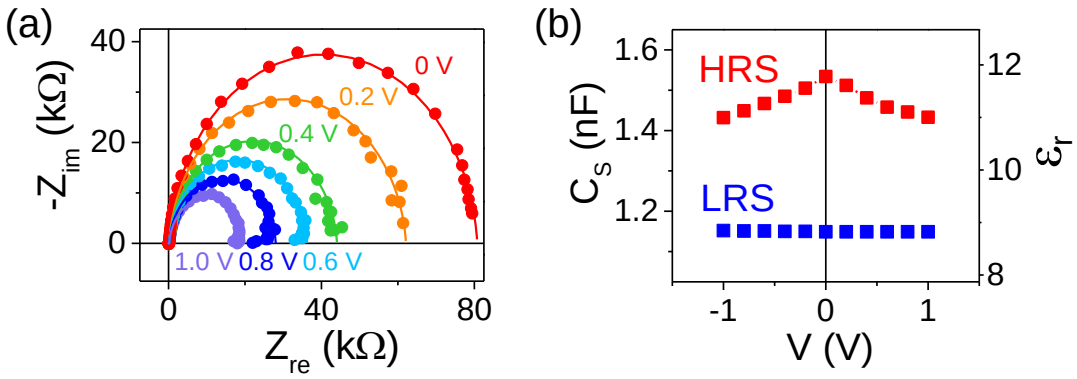

Figure A.17: (a) Cole-cole plots under 0−1 V DC bias of HRS in Si-Al_2O_3 devices ($\delta = 14$ nm, $x_{\text{O}} = 0.25$, r=250 μm). Solid lines are model fittings. (b) Extracted C_{S} from plots in (a) (and more plots not shown) vs. bias voltage V. C_{S} in HRS is higher than that in LRS, and it decreases with larger V that also lowers R. C_{S} was converted into dielectric constant ϵ_r shown on the right axis using nominal geometry. Small V was selected to prevent any switching of the device.

The $C - R$ correlation in Si ReRAM revealed by $C_{\text{S,HRS}}$ and $C_{\text{S,LRS}}$, namely a lower R corresponds to a lower C, was further confirmed by the change of C in the same state under different DC bias voltage V. As evident in $R - V$ switching curves, while LRS is Ohmic

(i.e., resistance does not change with applied voltage), HRS resistance decreases with V. Fig. A.17a shows the Cole-Cole plots of HRS under different bias from 0 V to 1 V (the results of negative bias are not shown because they behave the same). Following the same procedure in Fig. A.16b, C_S under each bias was extracted from model fitting and plotted against V in Fig. A.17b. The $C-V$ dependence within each state is consistent with $C-R$ dependence between HRS and LRS: when R deceases (either from HRS to LRS in a non-volatile way, or under higher V in a volatile way), C also decreases. But since R does not change with V in LRS, its $C-V$ is flat.

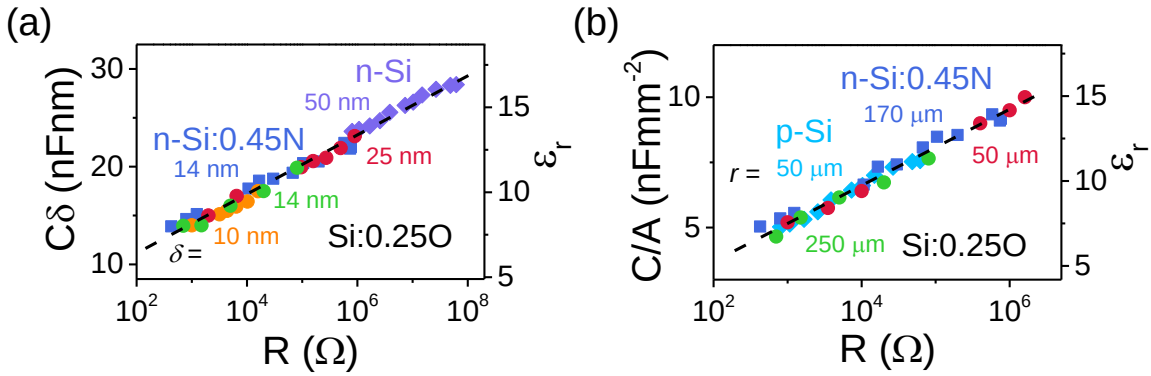

Figure A.18: Universal $C-R$ correlation in various Si ReRAM devices normalized by (a) film thickness δ^{-1} in which all devices have the same size $r = 250$ μm, and (b) device area A, in which thickness is fixed at 14 nm. The change of R was either from multiple resistance states after non-volatile switching or volatile change under DC voltage bias.

The Si-oxide/nitride mixture films studied so far are uniform dielectrics, i.e., their capacitance should obey the scaling laws of $C_S \propto$ device area A and $C_S \propto$ film thickness δ^{-1}. Therefore, the $C-R$ correlation in devices of different geometries may be normalized by dividing C by A or δ^{-1}. In other words, the $C-R$ correlation may evolve into a universal $\epsilon-R$ correlation. This is verified by Fig. A.18 in which two sets of $C\delta$ vs. R and C/A vs. R (or ϵ vs. R) data in different thickness/size follow the same dependence in a straight line on the linear-log plot. Moreover, experiment results of devices made of different compositions in Fig. A.18 all collapse into one linear curve after normalization, irrespective to the nature of their resistance changes—either from different states of the switchable O/N doped films

or under different bias of the unswitchable pure films.

The CPE element replacing C_S in the above circuit modelings was made because real materials such as amorphous Si often show frequency dispersion when probed over a wide range of frequency. On the other hand, since Q does not have the unit of capacitance, it does not have a simple physical meaning. In our data fittings, we find $0.95 < n < 1$ in all cases, which is common for dispersive systems; and n approaches 1 as the resistance increases. The capacitance obtained in this model is $Q(\omega)^{n-1}$, which does not have a fixed value and is a decreasing function of frequency, the more so the lower the resistance. Following the standard practice, we estimated C at the frequency when $Z_{re} = -Z_{im}$, since it is known that in this regime C is relatively weakly dependent on frequency, and in the limit of $n \to 1$, such C coincides with the Debye capacitance. (The above condition is akin to the resonance condition.) It is this C that is reported in Fig. A.17 and Fig. A.18, which shows higher R is associated with higher C.

The physical reason of why such C has an apparent R dependence can be understood from considering the relaxation time, or the RC constant, which is inversely proportional to the resonance frequency. Since R changes by orders of magnitude whereas the apparent C extracted above changes relatively modestly, it is clear that the RC constant is much longer in higher-resistance states than in the lower-resistance states. Therefore, in the AC domain, the higher-resistance states see more relaxation, thus seeing more capacitive components for a given frequency range (in the Cole-Cole plot) than in the lower-resistance states. This is the reason why the apparent capacitance increases with the resistance. Another way to state it is that the higher resistance state is more capacitor-like in the AC domain, allowing the current to by-pass the resistive elements more easily.

Clearly, the above picture breaks down in the DC limit. To see whether this is true, we used a standard bridge to measure the capacitance as a function of frequency. As shown in Fig. A.19, the apparent capacitance indeed increases with decreasing frequency, the more so the lower the resistance. Therefore, the apparently lower capacitance of the higher-resistance

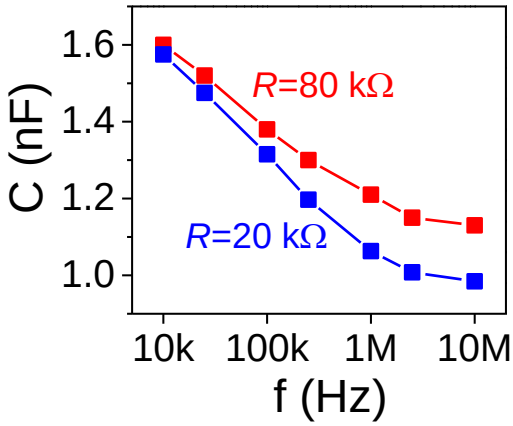

Figure A.19: Frequency dependence of capacitance in two different resistance states in the same Si film.

states is a phenomenon more prominent at higher frequency and it may disappear or even reverse in the DC limit. (We are not able to test whether it does reverse or not. Also, we are not able to perform the above measurement for the resistance states with an R less than a few kΩ, since in such states the capacitance C cannot fully shunt the R at the measuring frequency available in our instrument, thus not providing an adequate dynamic range to accurately extract the R and the C. These results are consistent with the above picture.

A.3.3. Small Si ReRAM Devices in a Crossbar Structure

In applications, standalone ReRAM devices need to be integrated into large arrays. The most straightforward realization is a 2-D crossbar structure, in which each cell is individually addressed by word and bit lines connected to the top and bottom electrodes, respectively. As described in the Experiment section (Fig. A.2), we have fabricated Si ReRAM in a crossbar structure, where the bottom electrode of 25 nm Pt intersects the switching layer of amorphous Si doped with O in the thickness of 2 nm ($x_O \sim 0.08$ according to HRS scaling in Fig. A.9) covered by 30 nm Mo top electrode with cross section area from 64 × 64 μm^2 down to 2 × 2 μm^2 (see SEM image in Fig. A.20a). As shown in Fig. A.20, the scaling law of large devices in Fig. A.8 is still obeyed in small devices down to 2 × 2 μm^2, all together over 5 orders of magnitude. Moreover, the current compliance can also work to achieve

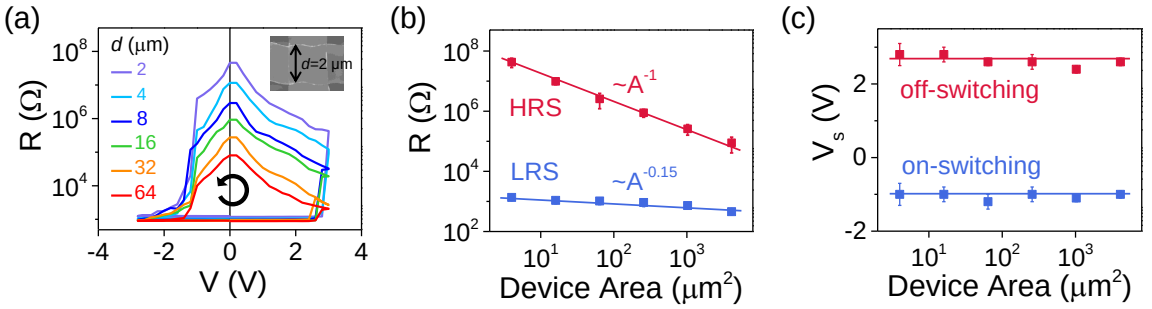

Figure A.20: Area dependence of Si ReRAM crossbar devices (with Mo-Pt electrodes). SiO_x in the thickness of 2 nm is the switching layer, with $x_O \sim 0.08$ (O was introduced by injecting O_2 gas during sputtering). (a) $R-V$ curves for devices in various sizes d as labeled. Inset: SEM image of a 2×2 μm^2 device reproduced courtesy of Shuang Wu). (b) Area-dependent HRS and area-independent LRS resistance. (c) Area-independent switching voltage V_s read from switching curves in (a). Error bars in (b) and (c) are obtained by averaging 5 devices of the same size.

multiple LRS modeled by the circuit in Fig. A.6b. The results have already been presented in Fig. A.7.

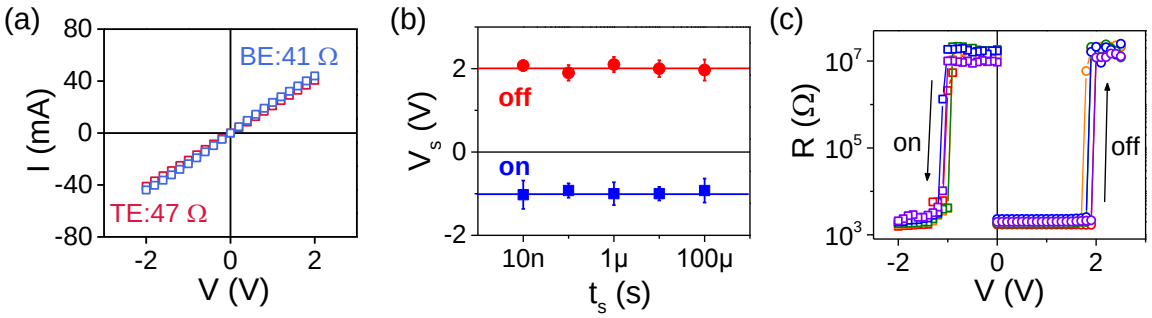

Figure A.21: (a) linear $I-V$ curve obtained by probing two tips on top electrode (TE) and bottom electrode (BE) gives a load resistance of ~ 40 Ω. (b) Switching voltage V_s is independent of pulse width t_s according to switching curves in (c), in which pulse switching in different t_s indicated by different color overlap with each other. In (b) and (c), a positive current/voltage was applied from bottom Pt to top Mo electrode.

As implied by the pulse switching experiment of large devices in early section, the switching speed of Si ReRAM is limited by the circuit RC delay in the order of μs for large devices. By down-sizing the devices to 2×2 μm^2, $C \propto A$ can be greatly reduced: According to the normalized $C-R$ correlation in Fig. A.18, Si mixture film is a uniform dielectric, and its

dielectric constant is about 7.5 in LRS. Applying a film thickness $\delta = 5$ nm for the Si-O film crossbar devices, $C = \epsilon_0 \epsilon_r A/\delta \approx 0.06$ pF. The line resistance can be estimated by probing two tips on the same electrode. As shown in Fig. A.21a, both top Mo electrodes (TE, covered by 10 nm Pt) and bottom Pt electrodes (BE) show a linear load resistance $\sim$ 40 Ω. Therefore, the *RC* time constant in the Si crossbar devices is about 20 ps (including spearding resistance $\sim$ 300 Ω). Since the electron's trapping/detrapping time can be as short as $\sim$fs, this estimation suggests that in few-micron-sized Si ReRAM devices, the *RC* threshold will not cap the switching time until the pulse width t_s is in the order of ps. It was verified in Fig. A.21b that switching voltage V_s obtained in pulse switching curves in Fig. A.21c did not change with pulse rate t_s in both on- and off-switching all the way down to 20 ns, the limit of our current measurement circuit. Furthermore, it will be shown in the later sections that when triggered by purely mechanical stimulus that is free of the circuit *RC* artifacts, HRS-to-LRS switching in Si ReRAM occurs within 0.1 ps.

A.3.4. Hydraulic Pressure Induced Switching in 10^2 s

Uniform isostatic pressure was previously used to on-switch Si_3N_4:Pt nanometallic ReRAM from HRS to LRS [13]. And the pressure-induced LRS can be switched back to HRS by electrical voltage in exactly the same way as before. Here, we present similar results for Si ReRAM devices with more statistics to delineate a more complete picture. A physical mechanism of mechanical switching of Si ReRAM will be given in the section of Discussion.

We first describe the experiment on Mo/Si-Al_2O_3/Pt devices, with film thickness of 11 nm and oxygen composition $x_O = 0.48$. Very similar results of other Si/Ge mixture films will be presented later. Before pressure treatment, Si-Al_2O_3 ReRAM cells were preconditioned to HRS (Fig. A.22a) and to LRS (Fig. A.22b) by electrical voltage. Next, the chip that contains many cells in different resistance states with various sizes was disconnected from the voltage source, wrapped in an aluminum foil, vacuum-sealed in an elastomer bag, and loaded into a cold isostatic press (CIP). Hydraulic pressure (P_H) was then applied and lasted for $\sim$ 1 minute (Fig. A.22c). After the removal of P_H, while cells in LRS were still

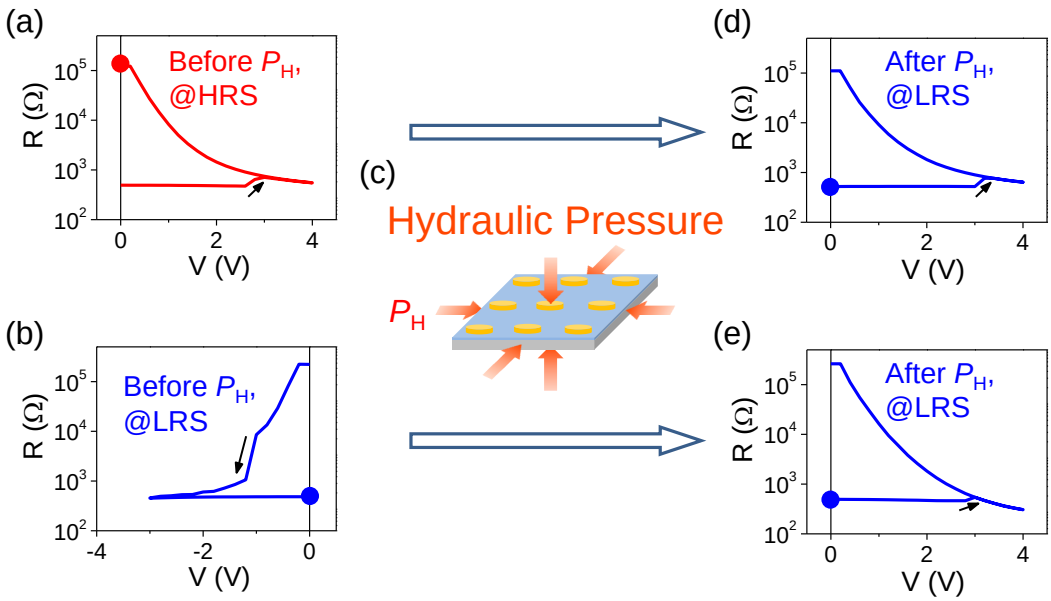

Figure A.22: Pressure effect of HRS and LRS in Mo/Si-Al_2O_3/Pt devices (δ = 10 nm, x_O = 0.48, cell radius r = 250 μm), taking two HRS/LRS memory cells as example. Before pressure treatment, Si-Al_2O_3 cells on one chip were preswitched to (a) HRS and (b) LRS by electrical voltage. (c) Disconnected from the voltage source, hydraulic pressure P_H was then applied to all the cells (gold circular pads). (d)&(e) Both resistance states were found to be LRS after pressurization, and able to switch (back) to HRS in the same way as before. Arrows indicate switching directions. Red/blue dots in the $R-V$ curves indicate the HRS/LRS states before and after pressure treatment.

in LRS and able to switch to HRS by similar positive voltage as before (Fig. A.22e), many HRS cells were switched to LRS by P_H. As shown in Fig. A.22d, the pressure-induced LRS can switch back to HRS as if it was obtained by electrical voltage, which suggests that mechanical switching caused no damage to the memory cells. It is further verified by the overlapping $R-V$ curves of pressure-switched Si-Al_2O_3 device by various P_H and of the one before pressure treatment in Fig. A.23. We have seen in Chapter 2 that mechanical switching causes a insulator-to-metal transition, and the pressure-induced metallic state shares the same quantum corrections to conductivity as that of voltage-induced LRS.

The observed P_H-induced HRS-to-LRS switching is statistical. Similar to the multiple intermediate resistance states obtained by electrical voltage in Fig. A.6-A.7, hydraulic pressure

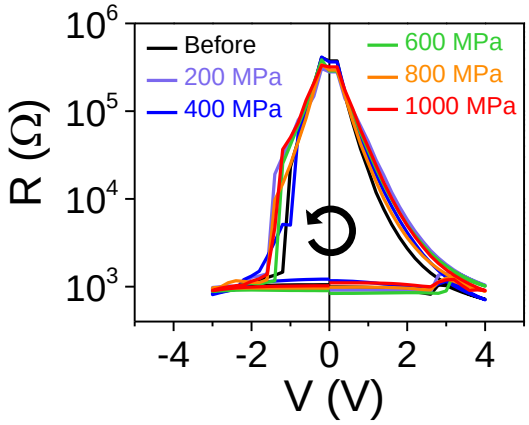

Figure A.23: Comparison between $R-V$ switching curve of Mo/Si-Al_2O_3/Pt devices (δ = 10 nm, x_O = 0.48, r = 250 μm) and their subsequent $R-V$ curves after switched by various hydraulic pressure.

was also found to lower HRS into a continuum of resistance states between HRS and LRS (indeed a insulator-to-metal spectrum). Fig. A.24a shows such distribution of resistance R collected from $\sim$ 50 cells pre-switched to HRS (marked as "before") and the distribution of those cells after pressurization by various P_H in the Weibull plots (each data point represents one memory cell that undergoes pressure treatment). As P_H increased from 2 MPa to 1 GPa, it resulted in a higher transition yield and a lower average resistance. The switching yield can be determined if we choose a threshold resistance value of 10^4 Ω for the transition (indicated by the dashed line). The result is plotted in Fig. A.24b, in which the yield increases from 1.5% in 2 MPa to 51% in 1 GPa.

The statistics in Fig. A.24a for each P_H contain $\sim$ 50 $SiO_{0.48}$ memory cells equally distributed in different sizes. (The area-scalable HRS explains the relatively wide distribution of pre-set HRS resistance before pressure treatment in hollow black symbols.) To investigate the size effect, separated resistance distributions of devices, each with different cell radii r after applying the same P_H = 350 MPa, were plotted in Fig. A.25a. A larger r not only increases switching yield but also lowers the pressurized resistance, which implies the pressure-triggered transition is uniform in Si ReRAM. As shown in Fig. A.25b, the size-proportional switching yield was similarly calculated by setting 10^4 Ω as transition

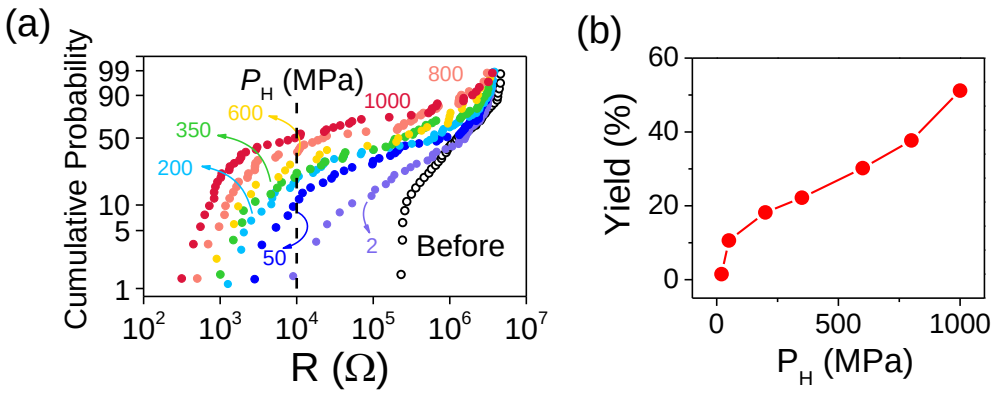

Figure A.24: P_H dependence of mechanical switching in Mo/Si-Al_2O_3/Pt devices ($\delta = 10$ nm, $x_O = 0.48$). (a) Weibull plots of resistance distribution of ~ 50 cells pre-switched in HRS before and after pressurized by various P_H. Different device sizes are contained in each P_H value. (b) Switching yield determined by a threshold resistance value of 10^4 Ω (indicated by the dashed line), increases with higher pressure.

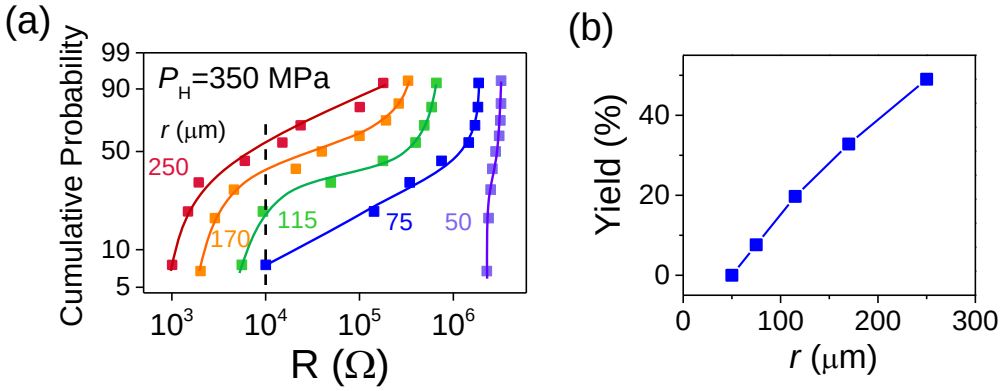

Figure A.25: Size dependence of mechanical switching in Mo/Si-Al_2O_3/Pt devices ($\delta = 10$ nm, $x_O = 0.48$). (a) Weibull plots of resistance distribution of ~ 10 cells pre-set in HRS with various device radii r after pressurized by $P_H = 350$ MPa. (b) Switching yield determined by a threshold resistance value of 10^4 Ω (indicated by the dashed line), increases with larger area. Solid lines are guide to the eyes.

threshold.

The size and pressure dependence of pressure switching of Si-Al_2O_3 devices was not only consistent with previous findings of Si_3N_4:Pt devices but also reproduced in other random mixtures of Si/Ge doped with O/N (Fig. A.26, in which the result of $SiO_{0.48}$ cells under

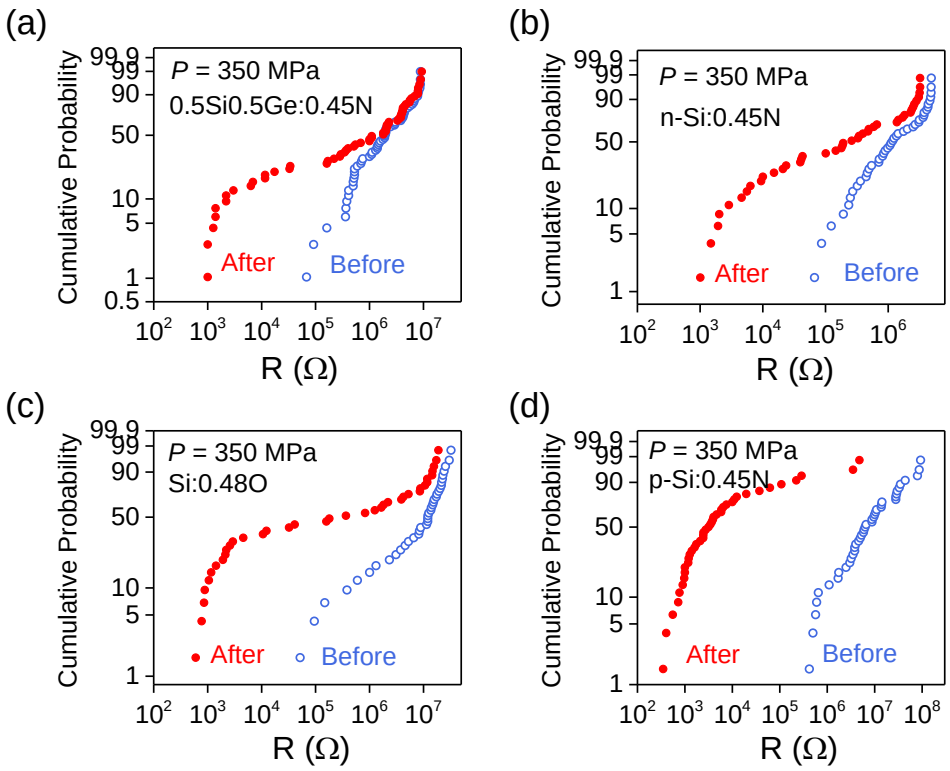

Figure A.26: HRS-to-LRS transition induced by external hydraulic pressure of 350 MPa in various O/N-doped Si/Ge films: (a) 0.5Si:0.5Ge:0.45N, (b) n-Si:0.45N, (c) Si:0.48O, (d) p-Si:0.45N. At this pressure and 50% transition yield, the relative resistance drop increases in the order of (a), (b), (c), (d).

350 MPa was duplicated for comparison). Similar to electrical switching, O/N dopants are necessary for mechanical switching observed in Si ReRAM (we did not find any pressure-induced switching of pure Si/Ge films). A switching model related to the doped O/N is proposed in the section of Discussion to account for all these observations in mechanical switching and electrical switching of Si ReRAM.

A.3.5. Magnetic Pressure Induced Switching in 10^{-13} s

Having demonstrated the mechanical switching of Si ReRAM by a static pressure, we next show its dynamic response to impulse pressure in a much faster time domain $\sim$ 0.1 ps, which will provide important evidence for the electronic nature of resistance switching in Si ReRAM. The dynamic pressure was applied in the form of Lorentz force (i.e., a magnetic

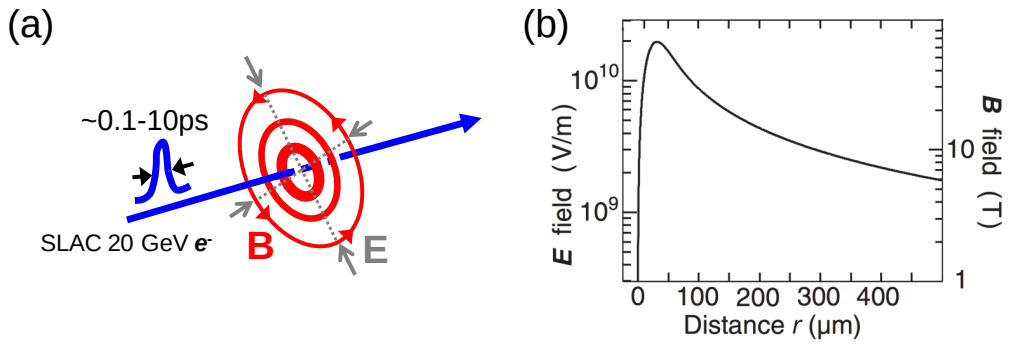

Figure A.27: (a) Schematic of a single shot of relativistic electron bunch, adapted from [15]. The E and B fields are perpendicular to the beam. (b) Plot of maximum E- and B-field amplitude vs. distance r from the beam center, adapted from [67].

pressure denoted as P_B), which is a self-force acting on any circuit loop with a circulating current. In our experiment, the "circuit loop" consists of top and bottom electrodes, and the insulator gap that can be penetrated through at high frequency [15]. Two examples of macroscopic P_B are (a) in the wall of a high-field magnet and (b) in the aircraft launch pad on USS Gerald R. Ford [136]. In our study, the ultra-fast magnetic pressure was made possible by shooting a single bunch of 10^9 20 GeV electrons at the film, just once, inside a linear accelerator (SLAC) (Fig. A.27a). As this technique has previously been used to test the switching behaviors of Si_3N_4:Pt nanometallic ReRAM devices, we will skip the detailed description of the experiment and only present the statistical results of Si ReRAM below (a detailed analysis of the electron bunch experiment was published in [15] and documented in [13]).

A large array of 20 × 20 μm^2 nSi-Si_3N_4 memory cells (δ = 11 nm, nitrogen composition $x_N = 0.45$) were pre-set to their HRS of 10^8 Ω by electrical voltage (each cell is represented by squared pixels in the dark blue color according to the resistance spectrum in Fig. A.28). The preswitched region on the chip was then shot by electron bunch only once. The bunch has a size of 20 μm × 20 μm × 20 μm and carries a pulse of circumferential magnetic field of 10^{-13} s, which is the time to travel 20 μm at ∼ the speed of light [67]. As shown in Fig. A.27b, the field peaks at 70 T at the edge of the bunch (r = 40 μm), falls off

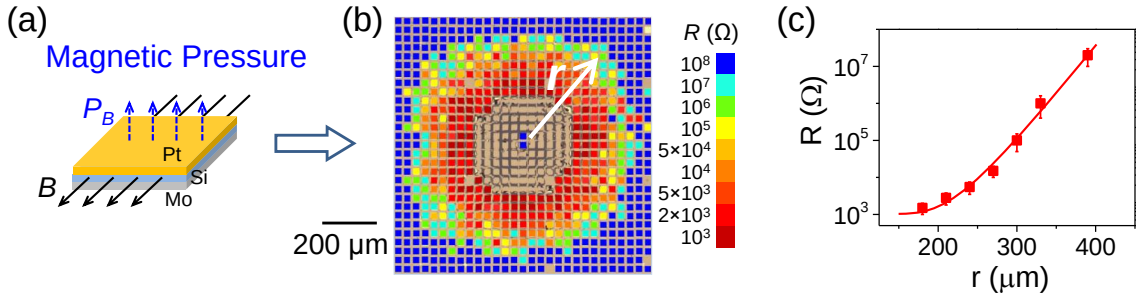

Figure A.28: (a) One electron bunch hitting $r = 0$ generates one 10^{-13} s pulse of magnetic far field ($B \sim 1/r$) and magnetic pressure $P_B \sim 1/r^2$ inside n-Si:0.45N memory cells. (Each colored "dot" is a 20×20 μm^2 cell.) (b) All pre-conditioned to HRS $\sim 10^8$ Ω (dark blue), cells close to $r = 0$ was switched to LRS with resistance indicated by colors according to spectrum on right (resistance read at 0.2 V DC). Excessive P_B generates excessive biaxial tension in top electrode (schematic on left) and ruptures it (uncolored earth-tone cells at small r), but no change in two center cells because $B = 0$ there. Lower bound estimate for P_B: $r = 40$ μm (electron bunch boundary), ~1,950 MPa; $r = 180$ μm (rupture boundary), ~96 MPa; $r = 390$ μm (transition boundary), ~21 MPa. (c) Averaging resistance obtained from (b) decreases with decreasing r that contains higher P_B, crossing many intermediate resistance states.

as $\sim 1/r$ with the radial distance r [67], and remotely delivers to a two-side-electroded film (located at r away from the flight path) a P_B that peaks at 1,950 MPa and decays with $\sim 1/r^2$ according to $P_B = (B/0.501)^2$ (see the early Experiment section for details). The above estimates are lower bounds because there is also an induced pressure due to the induced current in the electrodes, which inversely depends on the (pulse width)^2 [15]. In the schematic of Fig. A.28, the pressure is actually a body force on the electrodes. But to keep the upper electrode in balance an interface uniaxial tension of the same magnitude as P_B must be generated, which will also stretch the film as if there is a negative pressure. These forces in turn generate a biaxial tension in the top electrode, which can be ripped apart as in the earth-colored region in the center of the right panel of Fig. A.28. (According to the physical appearance after electron-bunch shot discussed in [13], rupture can be avoided by using a thicker, hence stiffer, top electrode.) Like the case of P_H, a higher transition yield (Fig. A.28b) and a lower average resistance (Fig. A.28c) were seen from more reddish squares when P_B increases with decreasing r (the two cells at $r = 0$ experienced no transition

because $P_B = 0$, by symmetry). Also similar to the distributions in Fig.A.24-A.26, many intermediate resistance states between HRS and LRS were obtained by moderate P_B from $r = 180$ μm (where P_B ~96 MPa) to $r = 390$ μm (where P_B ~21 MPa).

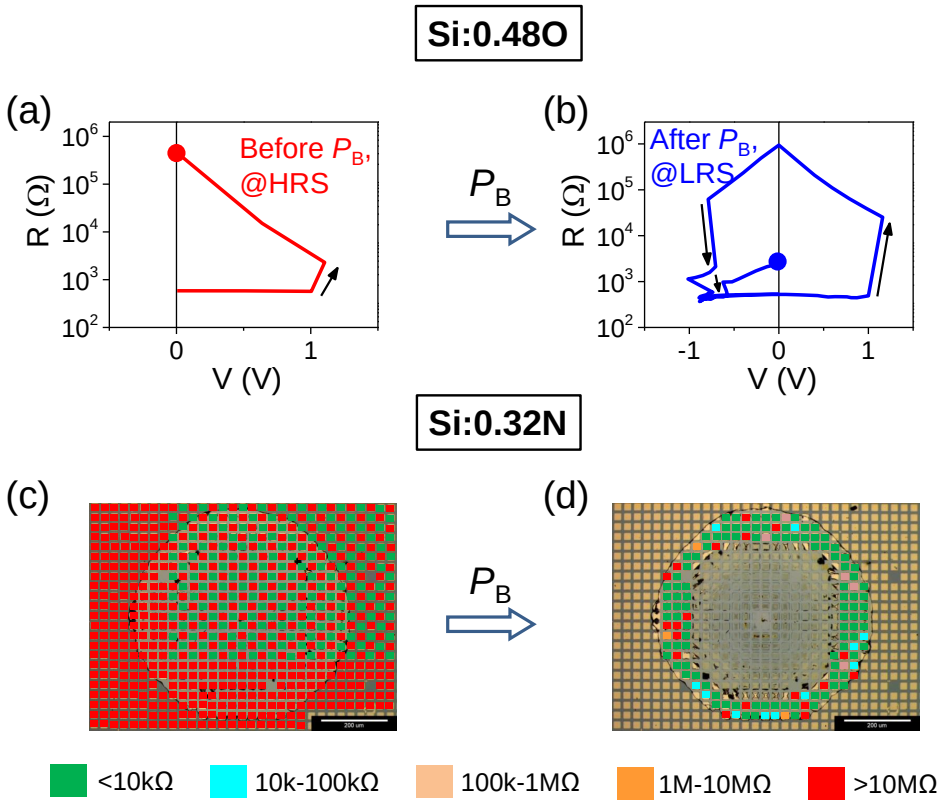

Figure A.29: HRS-to-LRS switching in O/N-doped Si films induced by magnetic pressure delivered by a SLAC 20 GeV electron bunch. (a) Switching curve that pre-set Si:0.48O to HRS $> 10^5$ Ω before exposure to electron bunch. (b) Switching curve of the same cell in (a) after one shot of an electron bunch, which switched the cell to LRS $< 10^4$ Ω. Arrows indicate switching direction. (c) Resistance map of Si:0.32N cells (shown as squares) pre-set to HRS > 10 MΩ (red dot) or LRS < 10 kΩ (green dot) before exposure to electron bunch. The sample was next coated by an insulating photoresist that does not affect magnetic field. (d) Resistance map of same region as (c) after one shot of an electron bunch at $r = 0$. While LRS cells (green) maintained their low resistance, HRS cells (red) were transitioned to either metallic state (green) or intermediate states (orange, blue; see color spectrum at bottom.) Resistance was not read in the central region (blurry grey, $r < 240$ μm) where top electrodes were completely torn off by magnetic pressure. Resistance was also not read in the outer region, $r > 300$ μm, where photoresist survived and covered the cells. Resistance read by 0.2 V DC.

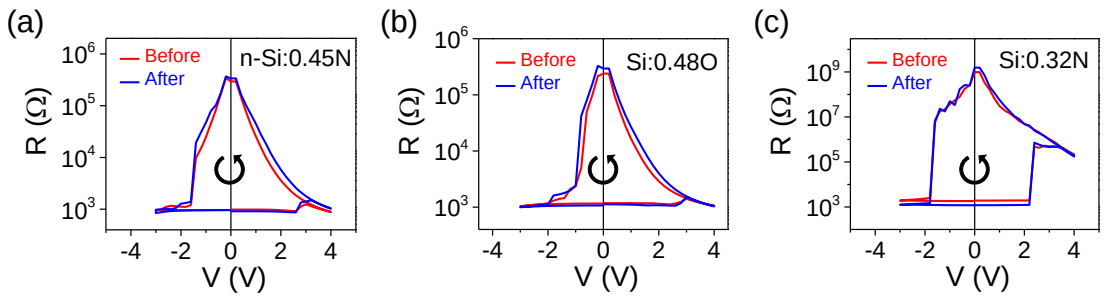

Figure A.30: Comparison between $R-V$ switching curves before (red) and after the electron bunch shot (blue) for the pressure switched (a) n-$SiN_{0.45}$, (b) $SiO_{0.48}$, and (c) $SiN_{0.32}$ memory cells. Overlapping curves imply no damage caused by the electron bunch.

As shown in Fig. A.29, similar 10^{-13} s magnetic pressure induced switching was found in undoped Si films mixed with Al_2O_3 ($x_O = 0.45$) and Si_3N_4 ($x_N = 0.32$). For the $SiO_{0.45}$ memory cell, it was pre-set to its HRS by electrical voltage (Fig. A.29a), exposed to a single shot of electron bunch, and examined by electrical voltage after the shot. It was found to be switched to LRS by the electron bunch and the resultant LRS can be switched reversibly by electrical voltage in almost the same loop (Fig. A.29a). In the early P_H experiment, it was found that hydraulic pressure can only switch HRS to LRS but not in the opposite direction. The one-way mechanical switching was confirmed for P_B by testing $SiN_{0.32}$ cells pre-switched to both HRS (red) and LRS (green) in a checkerboard pattern shown in Fig. A.29c. The chip that contains the pre-conditioned region was covered by a photoresist, which is not a conductor and has no effect on the magnetic field. But because it can be blown away by a large magnetic field, it serves as a marker to help identify the flight path of the electron bunch. As shown in the resistance map in Fig. A.29d, while HRS cells close to the damage zone were switched to LRS as expected, all LRS cells remained in their original states regardless of their distance to the center. The similarity of electrical switching between Fig. A.29a and Fig. A.29b is further verified in Fig. A.30 by the overlapping $R-V$ curves of the same cell (of various materials) before and after the mechanical switching by electron bunch. Combining it with Fig. A.23, it can be concluded that mechanical pressure, being hydraulic pressure or magnetic pressure, caused no damage

to Si ReRAM, and the pressure-induced LRS is the same as voltage-induced LRS in terms of their electrical switchibility.

A.4. Discussion

A.4.1. Switching Mechanism

Si ReRAM shares very similar electrical and mechanical switching characteristics with nanometallic ReRAM. In particular, the unique features of nanometallic switching, including the constant critical voltage in all devices and switching speed, localization-related thickness/composition parity, and pressure-induced switching in 0.1 ps, all manifested in Si ReRAM. As introduced at the beginning of this chapter, resistance switching of nanometallic ReRAM is closely related to the charge trapping/detrapping in negative-U centers facilitated by strong electron-phonon interaction. Based on the above experimental results, we next propose a physical model dedicated to the electron-phonon interaction and negative-U properties of Si ReRAM.

To summarize the results in this chapter, mechanical experiments provided definitive evidence for electron-phonon interactions in real time: As much as a $10^5\times$ drop in resistance is triggered by a very modest (positive or negative) mechanical pressure lasting from 0.1 ps to 1 minute in films that are not in contact with any electrical voltage. However, although voltage can trigger the transition in both directions, pressure can only trigger the insulator-to-metal transition. Importantly, for the transition to occur there must be Si-O/N-Si bridges−we have not seen resistance transition in films that have not incorporated some O or N. To explain these results, we will adopt the energy-configuration diagram (Fig. A.31) of Street and Mott [78]. The diagram was originally proposed for spin-paired bipolarons in highly polarizable chalcogenide glasses. In poorly polarizable Si and SiO_2, we will specialize it to some ultrasoft, thus highly polarizable Si-O/N-Si bridges.

As depicted in Fig. A.31, we now apply the idea of a localized negative-U, which we previously proposed to explain resistance-switching in other amorphous materials—metal-doped

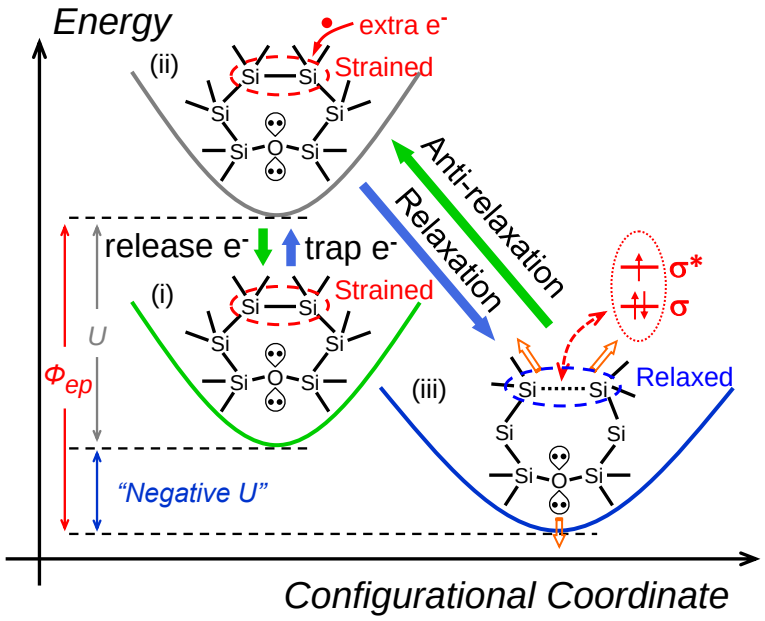

Figure A.31: Energy-configuration coordinate diagram specialized to a strained Si-Si bond next to Si-O-Si: (i) Initial stable state (strained Si-Si bond); (ii) metastable state with positive Hubbard-U (extra electron entering strained Si-Si region); (iii) stable state (Si-Si triple bond—two bonding electrons+one anti-bonding electron); (arrowed) relaxation caused by longer bond length and electron repulsion with negative U enabled by $\phi_{\rm ep}$ due to relaxation. Voltage delivers an extra electron to trapped site; opposite voltage destabilizes the trapped electron. Pressure does not deliver electron but triggers detrapping by forcing (arrowed) anti-relaxation (iii) to (ii). Stably trapped electron in (iii) exerts long-range repulsion against itinerant electrons.

oxides/nitrides[15], to one possible bond-electron evolution in amorphous Si doped with O, in which an ultrasoft Si-O bridge serves as a negative-U center where electron attachment (trapping) helps relieve a strained (Si-Si) bond nearby. Three electron states are involved in this diagram:

(i) The initial ground state (green) contains a strained Si-Si and Si-O-Si bond.

(ii) The activated metastable state prior to relaxation (grey) contains an extra electron burdened by a positive on-site Coulomb energy, i.e., Hubbard-U.

(iii) The relaxed stable state (blue) contains a Si-Si triple bond, having a longer bond length with two electrons in the bonding σ orbital and one electron in the anti-bonding

σ^* orbital, overall relaxed and stabilized by an effectively negative U.

(Other possibilities may also apply. For example, with the addition of one electron and relaxation, the strained Si-Si bond may break to form a Si dangling bond and a Si with one set of lone-pair electrons. Alternatively, the strained Si-O-Si bond may break to form a Si dangling bond and an O with one set of lone-pair electrons.) To turn the positive Hubbard-U in (ii) into the negative U in (iii) after bond severing, this Si-O neighborhood must be a "soft spot" where the newly formed bond(s) can easily lengthen or recoil from each other, and from the lone-pair electrons, thereby lowering the electron repulsion, without incurring much elastic energy. It also helps to have an initially highly strained Si-Si and Si-O bonds that arise from O incorporation. In Fig. A.31, this is represented by a large local ϕ_{ep} that overcompensates the positive U, and the amount overcompensated $\phi_{\text{ep}} - U$ is the negative U that stabilizes the trapped electron. Assuming the trapped electron can exert Coulomb blockade to itinerant electrons, we shall associate (i) to an unoccupied trapped site in the conducting state and (iii) to an occupied trapped site in the insulating state, which explains the LRS-to-HRS switching triggered by a voltage that brings in an extra electron, which becomes trapped. The reverse transition can then be explained by forcing configuration (iii) to configuration (ii), either electrically or mechanically, so that the trapped electron must leave. In this picture, there is no pressure-triggered LRS-to-HRS transition because there can be no pressure work on an undistorted configuration (i).

The picture is further consistent with the following observations. (a) While amorphous structure always contains some very soft local structures, their population is low and their distribution is statistical. This explains why very low pressure suffices in our mechanical experiments and why the transition yield is statistical, increasing with pressure in Fig. A.24 and Fig. A.28. (b) Conversion from configuration (iii) to configuration (ii) may take as short as one atomic vibration ($\sim 10^{-13}$ s). This explains why our 0.1 ps P_B experiment works (Fig. A.28 and A.29). Transitions at a much lower nominal rate should be rate-insensitive. Indeed, we were able to electrically switch the devices from 2K to 300K (Fig. A.11), and with

voltage pulses lasting from 1 ms to 10 ns (Fig. A.12), all at the same critical voltage $\sim \pm 1$ V. (d) While a voltage of ± 1 V can cause switching, the negative U in (iii) can also explain why without such voltage the insulator state is stable: We found undisturbed insulator states can remain for over 10^5 s at 175 °C (Fig. A.13) and for years at room temperature. (e) Lastly, it is conceivable that strained Si-Si bonds at low-density spots in O/N-free Si can likewise have a strongly localized ϕ_{ep}, and cause a virtual bound state on a conducting electron thereby increasing latter's effective mass (as seen in Chapter 2). But lacking the O/N heterogeneities that create further distortion to help immobilize electrons, O/N-free Si can neither trap electron nor undergo electrical/mechanical switching (Fig. A.10).

Lastly, since we observed pressure-induced resistance switching in various random materials, ultrasoft local structures with a negative U could be ubiquitous for all amorphous inorganic insulators. But these ultrasoft centers must be very scarce in population. We have shown in the main chapters that local strong electron-phonon interaction also left a mark on quantum corrections to conductivity by affecting electron's effective mass m^* and diffusivity D, so the low-temperature electrical measurement of these pressure-reponsive materials serves as an extraordinarily sensitive probe to these centers.

A.5. Conclusions

1 Nanometallicity was found in thin films of a wide variety of random mixtures of semiconductors (such as doped and undoped Si, Ge, and SiC) and oxides/nitrides (such as SiO_2, Si_3N_4, Al_2O_3, AlN, and HfO_2). When sandwiched between Mo and Pt electrodes and doped with sufficient amount of O and N (whose sources can be from the oxides and nitrides in the mixtures themselves), these Si/Ge-based random materials of appropriate thickness exhibit bipolar resistance switching phenomenon and can be made into a new kind of memory devices—Si ReRAM.

2 Si ReRAM has great potential in applications due to its CMOS-compatible materials, crossbar feasibility (down to 2×2 μm^2), area-scalable resistance, size/resistance

independent low switching voltage (± 1 V), fast switching speed (10 ns demonstrated and 1 ps theoretically possible, for crossbar devices), long retention ($> 10^5$ s at 175 °C), high endurance ($> 10^5$ cycles), ultra uniformity (Weibull $k \sim 10$).

3 Si ReRAM is nanometallic ReRAM, i.e., its resistance switching is purely electronic, volume proportional, and related to trapped charge in local negative-U centers rendered by electron-phonon interaction.

(1) The critical switching voltage of $\sim \pm 1$ V is independent of material composition, film thickness, device area, switching speed,and temperature.

(2) Its HRS, with a resistance exponentially scaled with thickness and inversely proportional to the device area, is a metastable state that can be switched to LRS by mechanical pressure that reverts bond distortion and prompts charge release in as fast as 10^{-13} s. Its LRS, whose resistance can be progressively lowered by depleting the trapped charge using large voltage or pressure, is a stable state with respect to mechanical stimuli.

(3) There is a strong correlation between film capacitance C and resistance R: the higher the R, the higher the C ($C_{\mathrm{HRS}} > C_{\mathrm{LRS}}$ and C_{HRS} decreases with ± 1 V in the $C - V$ plot).

4 The HRS of Si ReRAM is associated with trapped-electron state, and the LRS with detrapped-electron state. Trapped electrons are stabilized at negative-U centers.

5 Negative-U centers are ultrasoft Si-O/N-Si bridges. Because its surrounding is so soft, such center can capture an extra electron to form a new bond that can easily adjust in length/orientation to lower electron repulsion without incurring much elastic energy. This amounts to a large local ϕ_{ep} that stabilizes a trapped electron. The trapped electron can later be destabilized, and detrapped, when the relaxed bond is forced to return to the strained configuration.

APPENDIX B : Pressure-Induced Insulator-to-Metal Transition Provides Evidence for Negative-U Centers in Large-Gap Disordered Insulators

B.1. Introduction

Electronic centers usually repel electrons because of electron-electron interactions, among them the positive Hubbard interaction U between opposite-spin electrons in the same local state has a strong influence on electronic properties [137]. However, a negative effective U can also be realized when a strong electron-phonon interaction intervenes [78, 138, 139, 140]. Anderson illustrated how a negative U is linked to electron-phonon interaction by the following example: When a second electron is added to a bonding orbital, the bond retracts; likewise, when a second electron is added to an antibonding orbital, the bond extends [138]. Therefore, the freedom to adjust bond length thus stabilizing the bonding orbital is crucial for attracting an extra electron. Since strong electron-phonon interaction and bond distortions require a high polarizability and disorder in the solid state [141], abundant negative U centers were first seen in amorphous chalcogenides where they open up a gap of the order of U [79]. On the other hand, negative U centers play a critical role in the nanometallic switching as revealed by the mechanical switching phenonmenon and other unique properties of nanometalliac ReRAM ([15] and Appendix A). The negative-U properties stabilize the trapped electrons in nanometallic films, and get reverted to positive U under perturbative stress, which prompts charge releasing [15]. Note that all the nanometallic materials discovered so far are poorly polarizable [11, 12, 13]. Being amorphous, however, they always suffer bond-length/angle dispersions and configurational frustrations. So they invariably contain some local atomic arrangements that can relatively easily relax without straining the surrounding very much−thus without much elastic-energy penalty [142, 143]. These "soft spots" (e.g., near the strained Si-O/N-Si bridge in Si ReRAM as proposed in Chapter 2), should be highly polarizable even though the bulk material, on average, is not. So they could offer negative-U centers to host self-trapped electrons. If the amorphous structure also contains some nanoscale paths that should have been conducting were they not blocked by

these negatively charged, self-trapped electrons, then detrapping could dramatically lower its nanoscale resistance, which the basic idea of nanometallic resistance switching. Since only locally polarizable sites are required in this picture, switchable nanometallicity phenomenon was ubiquitously found in disordered perovskite [11], SiO_2:Pt [12], other dielectrics dispersed with metal [13] and Si doped by O/N (Chapter 2 and Appendix A in this thesis).

Then what bout filamentary-switching materials (e.g., HfO_x and AlO_x) that are also amorphous? Although redox reaction and ionmigration [144, 104], instead of an electronic process, are often regarded as the origin of resistance switching, there are definitely soft spots in local environment in the amorphous matrix that hosts conducting filaments. Indeed, negative-U centers have been described for crystalline insulators such as quartz [145], alumina [146] and cubic hafnia [147, 148, 149], at point defects and surfaces, and such attractive centers are thought to increase the leakage current in amorphous SiO_2/HfO_2 films causing insulation degradation [145, 148]. But direct evidence for their existence is scant because these oxides have either wide band gaps well in excess of $|U|$ or quite populous paramagnetic centers (see, e.g., EPR studies of amorphous SiO_2 [150] and HfO_2 [151, 152]) that will mask any diamagnetic signature from electron pairing at negative U centers. But the demonstration of negative-U in the amorphous counterparts of HfO_x and AlO_x might be given by similar pressure-induced resistance switching in their memristive forms as that in nanometallic ReRAM. If successful, the experiment will also suggest that Mott insulators when disordered may become Anderson insulators with strong electron-phonon interactions regulating incipient conduction paths.

In this chapter, we will report how we literally "squeezed" pristine HfO_x and AlO_x-ReRAM by both isostatic pressure in 10^2 s and dynamic pressure in 10^{-13} s to "pinch off" their negative-U centers and dramatically lowered the resistance. By studying the switching statistics and transport properties, here we will demonstrate metal-insulator transitions in HfO_x and AlO_x-ReRAM, which is one-way if triggered by pressure and two-way if controlled by voltage. Unlike nanometallic ReRAM, these transitions are localized in percolative

networks in the insulating matrix of HfO_x and AlO_x, which can be described by a binomidal statistical model proposed at the end of this chapter. Both being filamentary, the pressure-induced metallic states are proved to be identical to the voltage-switched metallic LRS that we investigated in [106, 103, 107], e.g., these states share similar temperature dependence of resistance and can both be switched to HRS by voltage in an almost identical way. Such remarkable observations are profound not only in the fact that they are totally unexpected from any ionic mechanism proposed for filamentary switching but also in their implication that Mott insulator, in which strong inter-electron repulsion prohibits electrons from moving around, becomes an Anderson insulator when randomized, and just by chance the disordered network may contain enough sites to host strongly localized electron-phonon interaction and to channel short-distance electron conduction.

B.2. Physical Picture and Material Background

Before presenting the experimental data, we first describe the motivating picture of the negative-U physics in amorphous films of HfO_x and AlO_x, which resembles the one we used for nanometallic films such as amorphous Si in Chapter 2 and amorphous Si_3N_4:Cr published in [15] although the transition only occurs in localized percolative nteworks. As depicted in Fig. B.1a, it is adapted from a simpler diagram of Street and Mott [78], who explained the energy variation of a negative-U site in terms of its configurational coordinate. The key idea is: While an extra electron usually raises the energy from A to B due to on-site Coulomb repulsion (positive U), by polarizing the neighboring environment so severely the electron may instead render a coordinate relaxation (bond contraction/extension) that lowers the overall energy to C. Since the relaxation realizes an effectively negative U, the extra electron becomes self-trapped. As mentioned in the introduction, we hypothesized that such self-trapped electrons are blocking the few conducting paths in amorphous insulators. So, clearing them ought to render the insulator conductive. Therefore, our experimental objective is to find a way to block and unblock the conducting paths by leveraging the negative U centers.

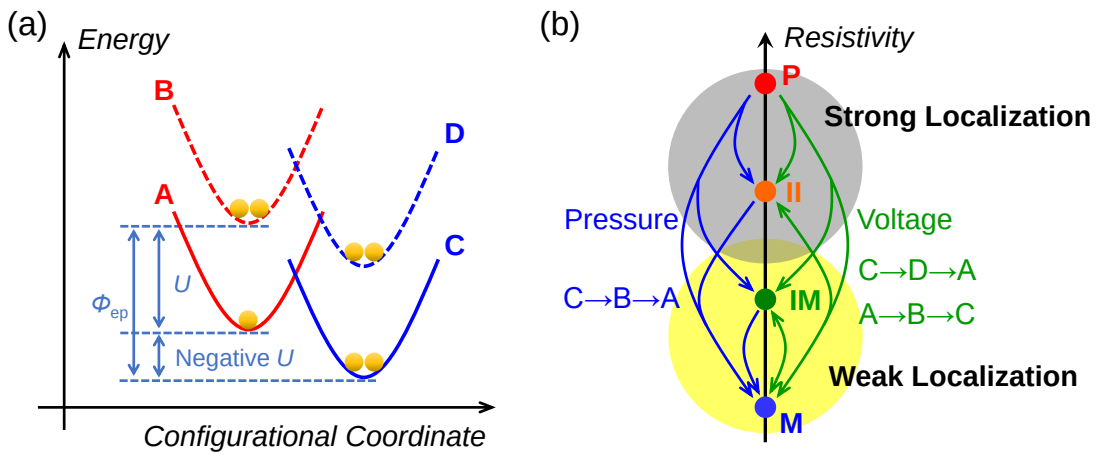

Figure B.1: Mediated by electron-phonon interaction ϕ_{ep}, negative-U state regulates charge-trapping/detrapping and enables pressure/voltage-induced metal-insulator transitions over a wide spectrum from strong to weak localization. (a) A: Empty trap-state (single-electron occupancy, conducting); B: Filled trap-state (double-electron occupancy, insulating) without relaxing configurational-coordinate, showing positive U; C: same as B but with relaxed configurational-coordinate, showing negative U; D: same as C but voltage-elevated to metastable state without relaxing configurational-coordinate. Although only one A state and one C state are shown, in amorphous materials there are a multitude of A states and C states. (b) Pressure and voltage induced transitions between pristine insulating state (P) and metallic state (M), via a intermediate continuum including intermediate metallic state (IM) and intermediate insulting state (II). For pressure transitions (one-way, shown in blue), P-to-M/IM/II, II-to-M and IM-to-M transitions in (b) correspond to reaction C→B→A in (a). For voltage transitions (two-way, shown in green), P-to-M/IM/II, II-to-M, and IM-to-M transitions in (b) correspond to C→D→A in (a); and M/IM-to-IM/II transition in (b) corresponds to A→B→C in (a). All transitions have been experimentally verified in this thesis.

Our first experiment seeks to exert a mechanical force to restore the configurational coordinate from C to B, thus destabilizes the state and prompts spontaneous electron detrapping, back to state A, thereby clearing the conducting paths. In Anderson's example, this is like compressing an antibonding orbital to make it so unstable as to release the antibonded electron. In parallel, we will also exert an electrical voltage: (i) to raise the energy from C to D without disturbing their configurational coordinates, thus prompts electron detrapping after which the one-electron state relaxes back to A; and (ii) to raise the energy of A and B while keeping their configurational coordinates the same, thus adds more driving force for B to relax to C if B already captured a second electron. Indeed, (ii) may even work for a

positive U, i.e., when the energy of A is lower than that of C, although this will result in a metastable state C. All these pressure/voltage-triggered changes should leave very prominent signatures in resistance, as depicted in Fig. B.1b by arrows that indicate transitions in the resistance spectrum: According to Fig. B.1a, they are one-way transitions for pressure, and two-way ones for voltage. As will be supported by the temperature dependence of resistance data, we identify the resistance extrema as pristine insulator (P) where strong localization [8] reigns and metal (M) where weak localization [2, 153] manifests, but we reckon that there may be other states of intermediate insulator (II) and intermediate metal (IM).

To lend support to the picture in Fig. B.1a, we will experimentally demonstrate all the transitions in Fig. B.1b. In fact, the voltage-triggered transitions have already been presented as the electrical switching data of HfO_x filamentary ReRAM in [106, 103, 107], in which electroforming transition P (virgin) to II/M (HRS/LRS) states, and RESET/SET corresponds to the reversible M/II-to-II/M transitions with many intermediate IM obtainable by current-compliance-control. In this chapter, we will provide transport results to validate the names of HRS/LRS as II/M states by demonstrating that the reversible electrical switching is indeed a metal-insulator transition and examine the intercommunity between these two types of transitions, e.g., if the pressure-induced M state can be switched by voltage, or if the voltage-switched II (HRS) state can be transitioned to M state by pressure.

Besides their robust resistance switching as in filamentary ReRAM, our experiments used HfO_x and AlO_x because they are strong and insulating materials before electroforming, with band gaps from 5.7 to 8.7 eV [154], elastic moduli from 150 to 300 GPa [155, 156] and melting points from 2,300 to 3,000K. In both bulk and nanoscale forms they are among the most reliable electrical insulators; amorphous HfO_2 films (1-2 nm) is the gate oxide in the state-of-the-art nanoelectronics capable of withstanding fields of $\sim$ 1 V/nm [157]. For such application, amorphous films are especially advantageous because they are free of field-concentrating, breakdown-initiating lattice defects. The electric forces exerted by

the breakdown field on the cations/anions are equivalent to a mechanical stress; in HfO_2 it is $\sim$ 5 GPa. So a stress less than 0.5 GPa is unlikely to cause any significant defect formation, dielectric breakdown or phase transition. To further eliminate any artifact, we used a hydraulic pressure of no higher than 350 MPa. Indeed, as described below, we observed abrupt, dramatic and robust insulator-to-metal transitions in few-nm-thick amorphous HfO_x and AlO_x films even at 2 MPa.

Atomic-layer-deposition (ALD) is a method commercially used to fabricate conformal thin film gate oxides over a large area. We used it to deposit the above materials (5-15 nm thick), embedded in a metal-insulator-metal (MIM) structure between sputtered Pt film (40 nm) as top electrode and Pt or Ti (15 nm) as bottom electrode. The structure allows us to measure DC and AC current (I)-voltage (V) responses across the MIM to obtain the V/I ratio as an indicator of resistance. The deposited Pt films have a grain size of 2 nm. Therefore, their finely spaced grain boundaries make it extremely difficult to nucleate and propagate dislocations. So they should have a tensile/compressive yield stress $\sim$1 GPa according to the Hall-Petch relation [158, 159]. This was verified in broken films: Unlike coarse-grain Pt that fails by grain tearing and thinning indicative of dislocation-mediated plasticity, our films broke in a completely brittle manner absent of any dislocation plasticity [13]. This finding ensures that a pressure <350 MPa cannot possibly cause any accidental shorting of the MIM by filling the oxide pinholes with Pt, because the pressure required to deform Pt to do so (like in an indentation test) is about three times the tensile/compression yield stress [160], thus exceeding 2 GPa. Below we will describe the Ti/HfO_x/Pt (thickness of HfO_x being 10 nm) results in details; very similar findings for Pt/HfO_x/Pt and Ti/AlO_x/Pt MIM will also be presented.

B.3. Experiment

B.3.1. Sample Preparation

Filamentary ReRAM made of metal/insulator/metal (MIM) structures of Ti/HfO_x/Pt, Pt/HfO_x/Pt, and Ti/AlO_x/Pt were fabricated on a substrate of thermal-oxide-coated 100 p-type silicon single crystal. At the beginning, 20 nm Pt or 15 nm Ti was RF-sputtered or e-beam evaporated as bottom electrode. After that, the switching layer in the thickness of 5/10/15 nm was deposited by atomic layer deposition (ALD) at 250°C using HFDMA precursor and H_2O for HfO_x or Trimethylaluminum−TMA precursor and H_2O for AlO_x. Finally, a 40 nm thick Pt top electrode was deposited by RF sputtering either through a shadow mask that defined cells of 50-250 μm in radius, or onto a lithography-defined pattern of 20 $\times$ 20 μm^2 radius cells followed by a lift-off process. The former type of cells was used for hydraulic pressure experiments and transport measurements, while the latter type was used for most magnetic pressure experiments.

B.3.2. Electrical Measurement

Electrical properties of AlO_x and HfO_x films were measured by similar methods described in Appendix A.

B.3.3. Mechanical Switching Experiment

Response of virgin state, HRS, and LRS of HfO_x- and AlO_x-ReRAM to mechanical stress was tested in the same way as described in Appendix A for Si ReRAM (see more details there).In a typical representation of the data from electron bunch experiment, each cell is colored to indicate its resistance value before and after the treatment, and the colored maps are presented to aid comparison. Since the cell size is about the same as the bunch size, maps that have hundreds of cells−each appearing as a "dot" with changed colors due to the treatment−provide direct evidence for the far-field effect of an electron bunch.

B.3.4. Low Temperature Measurement

Low temperature switching and transport properties of HfO_x and AlO_x devices were measured by Quantum Design Physical Property Measurement System (PPMS) from 300K to 2K. As fabricated, voltage-formed and pressure-formed HfO_x and AlO_x devices were mounted on sample holders and their top/bottom electrodes were similarly wire-bonded to the experiment of Si ReRAM in Appendix A. In order to study their transport properties, two-point DC resistance (V_{2pt}/I) was obtained using a Keithley 237 High Voltage Source Measure Unit to apply a constant voltage V_{2pt} of 0.01 V across the top and bottom electrodes, while measuring the current (I) passing through the films. During measurements, synchronized voltage, current, and temperature data were recorded while the heating/cooling rate was set at an appropriate value (e.g., 6K/min from 300K to 100K, 4K/min from 100K to 10K, and 0.5K/min from 10K to 2K). Electrical switching was also performed at fixed low temperatures. Below 10K, an appropriate current compliance was carefully chosen to prevent a sudden temperature burst due to Joule heating by the transition current.

B.4. Results

B.4.1. Hydraulic-Pressure-Induced Transition in a Wide Insulator-Metal Spectrum

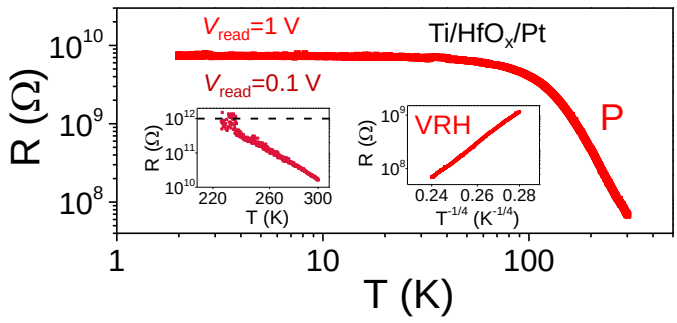

Figure B.2: As-fabricated (pristine) Ti/HfO_x/Pt MIM resistance (R) read by voltage V_{read} = 1 V vs. temperature (T). Flat top is elastic tunneling limit. Left inset: Resistance read at 0.1 V curve is much higher, reaching instrument's limit (dashed line). Right inset: variable range hopping plot, $\log R \sim T^{-1/4}$.

The x-ray amorphous virgin films were all extremely insulating. For example, at ambient temperature a 172 μm radius Ti/HfO$_x$/Pt MIM has a resistance > 10 GΩ read at 0.1 V (left inset, Fig. B.2). As temperature is lowered, the resistance soon reached instrument's sensing limit (0.1 pA) as indicated by the dashed line. So a higher reading voltage of 1 V was used to capture more features of the pristine state: The resistance rises with decreasing temperature T, having the behavior of variable-range-hopping (right inset) [161], but below $\sim$160K elastic tunneling across the MIM caps the low-temperature resistance. For such as fabricated film−the P state in Fig. B.1b−the Ohmic range is rather small before the resistance rapidly decreases with voltage, but the film does not suffer breakdown at least up to $\pm$6 V when the $I-V$ and $R-V$ curves remain fully reversible (as evident from the electroforming behavior over 7 V for HfO$_x$ ReRAM in [106, 103, 107]).

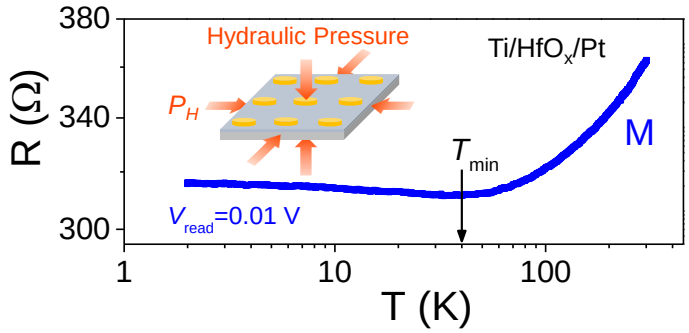

Figure B.3: Post-pressurization (350 MPa) $R-T$ curve read at 0.01 V has low resistance, which is voltage-independent with a shallow minimum at $T_{\min} \sim 40$ K—a common feature of disordered electron systems. Inset: schematic of applying hydraulic pressure to a MIM array of many pristine cells.

A pressure treatment at ambient temperature was provided to pristine MIM arrays vacuum-sealed in an elastomer bag and suspended in a liquid-filled pressure vessel, which was charged and held at the set pressure for < 5 min before sample removal (see inset of Fig. B.3). As shown in Fig. B.3, the brief treatment triggered a $10^8\times$ drop in resistance (from 10^{10} Ω to $\sim 10^2$ Ω) in this MIM, which acquired a totally different $R-T$ dependence in 100-300K indicating a metal state (M). A shallow resistance minimum at $T_{\min} \sim 40$K also emerged at low temperature, which is a common feature of metal/bad-metal with impurities/disorders

[70, 64] and a signature of weak (electron) localization [3]. (Hf^{4+} has no magnetic moment, and our sample contains too few magnetic impurities, if any, to cause the Kondo effect [32].) A detailed model fitting of resistance minimum in HfO_x and AlO_x films and their other quantum phenomena is provided in Chapter 4. The pressure-induced insulator-to-metal transition conforms to our expectation in Fig. B.1. Pressure causes the C-to-B configuration/energy change, followed by the spontaneous B-to-A conversion, thus dumping the trapped electron, removing the Coulomb barriers and clearing the conduction paths.

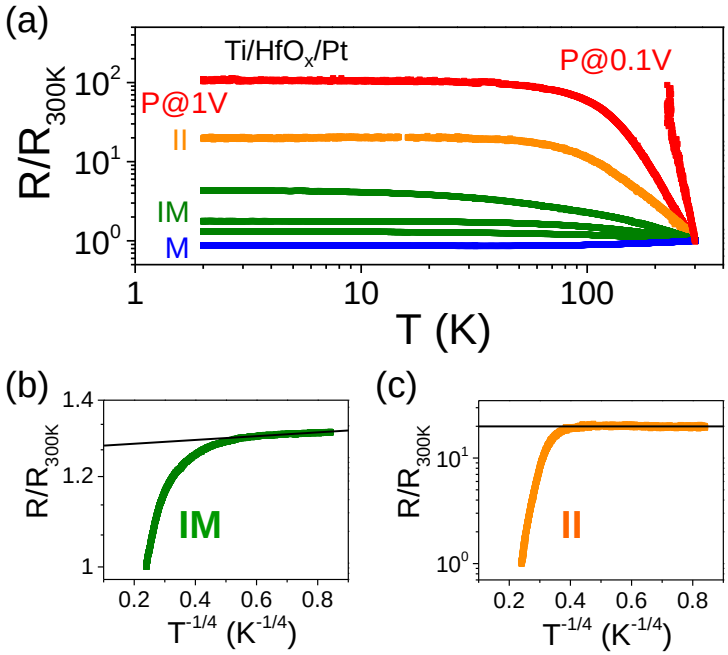

Figure B.4: (a) Normalized by their 300K resistance, various post-pressurization $R-T$ curves demonstrate intermediate states obtainable from pristine Ti/HfO_x/Pt MIM. (Cell size: 172 μm; pressure: 350 MPa). One M with $R_{300K} = 162\ \Omega$; three IM with $R_{300K} = 505\ \Omega$, 672 Ω, and 865 Ω; one II with $R_{300K} = 25$ kΩ, all the above read at 0.01 V; one P with $R_{300K} = 10$ GΩ read at 0.1 V and 68 MΩ read at 1 V. IM and II are distinguished by setting $R/R_{300K} < 10$ for IM (as commonly so designated for dirty metals) and $\log R \sim T^{-1/4}$ plot in (b)-(c) (applicable over wide resistance range for II).

We also verified that the pressure treatment resulted in a continuum of intermediate states with different resistance values corresponding to the multiple blue arrows emanating from P in Fig. B.1b. These states have distinctly different $R-T$ curves in Fig. B.4a, in which resistance R is normalized by their room temperature value R_{300K}. Here we distinguish II

and IM states by the magnitude of $R/R_{300\mathrm{K}}$ ratio: M has a ratio less than 10, which is the criteria commonly used to assign a bad metal instead of an insulator. In addition, as shown in Fig. B.4b-c, while II follows the $T^{-1/4}$ law of Mott for variable range hopping over a relatively large resistance range before complete saturation in the tunneling regime at low temperature, the resistance of IM continues a gradual rise at the lowest temperature and the magnitude of change is just too small to invoke the notion of hopping.

B.4.2. Statistics of the Pressure-Induced Transition

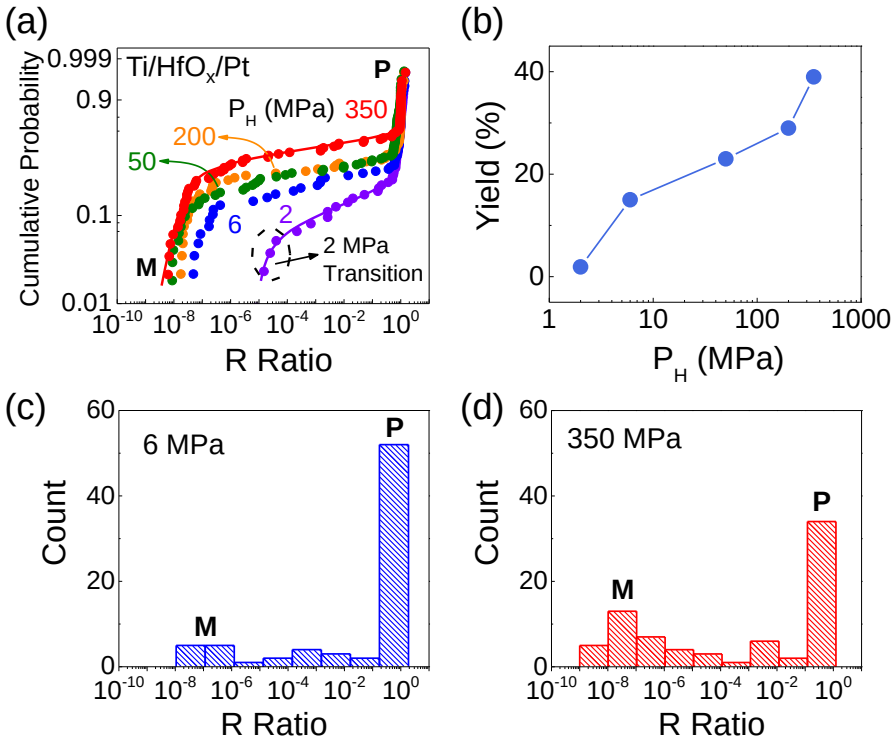

Figure B.5: Pressure effect on the statistics of pressure-induced insulator-to-metal transition. (a) Weibull plots, which shows cumulative transition probability p in $\ln[\ln[1/(1-p)]]$ scale vs. resistance ratio (post-pressurization to initial) showing higher p and lower resistance at higher pressure P_H, with 2 MPa transition circled. Each curve contains 60-80 points, each as one pristine cell (10 nm thick), equally distributed between 5 cell sizes A (with radius r). (b) Transition yield vs. P_H obtained by setting threshold R ratio of 10^{-5} in (a). (c)-(d) Sigmoidal plot signifies a bimodal resistance distribution with two modes at two ends of P (R ratio = 1) and M states (R ratio $\sim 10^{-8}$). Resistance read at 0.2 V.

The P−II−IM−M continuum resulting from the pressure-triggered transition of the pristine

P state suggests a statistical phenomenon. This is evident from Fig. B.5a, which displays the Weibull plots of cumulative probability of the post-treatment resistance or the resistance ratio comparing pre- and post-treatment. These probability plots having a sigmoidal shape correspond to the somewhat bimodal resistance distributions in Fig. B.5c-d. It clearly shows a wide distribution of the ratio, from 1 (a remaining P state) to 10^{-8} (an M state). As highlighted in Fig. B.5a, pressure as low as 2 MPa, which is the accuracy of our pressure reading, can already trigger transitions in some MIM! But a higher pressure does give a higher transition yield and lowers the resistance; e.g., the transition yield, for cumulative probability at ratio $< 10^{-5}$, increases with pressure (Fig. B.5b).

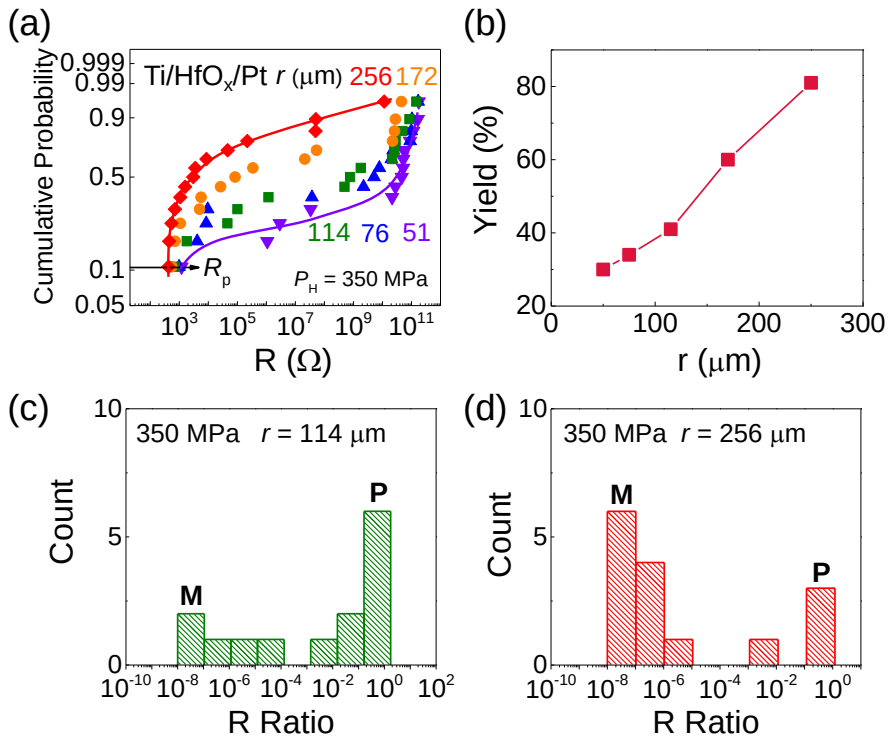

Figure B.6: Size effect on the statistics of pressure-induced insulator-to-metal transition. (a) Weibull plots, which shows cumulative transition probability p in $\ln[\ln[1/(1-p)]]$ scale vs. resistance pressurized by $P_H = 350$ MPa (initial R is size-dependent, close to the largest value after pressure) showing higher p at larger device radius r with similar lowest R_p. Each curve contains 12-16 points, each as one pristine cell (10 nm thick). (b) Transition yield vs. r obtained by setting threshold R ratio of 10^{-5} in (a). (c)-(d) Sigmoidal plot signifies a bimodal resistance distribution with two modes at two ends of P (R ratio = 1) and M states (R ratio $\sim 10^{-8}$).

Likewise, the cumulative probability increases in larger MIMs (Fig. B.6) while the lowest resistance (R_p) after pressurization of each curve is close to each other, indicative of the statistical nature in percolative networks (see more details in the Discussion). Similar transitions probabilities were found in other MIMs shown in Fig. B.7a, with a higher yield in HfO_x than in AlO_x perhaps because HfO_x is not as stiff as AlO_x. Lastly, we reason that an increased oxide thickness, unlike an increased oxide area, should decrease rather than increase the yield because of the decreased probability for percolation in a longer network. Indeed, the average relative yield to reach R ratio $< 10^{-5}$ at 200 MPa in five sizes of Ti/HfO_x/Pt MIM in Fig. B.7b was 30% for 5 nm thickness, 25% for 10 nm, and 17% for 15 nm.

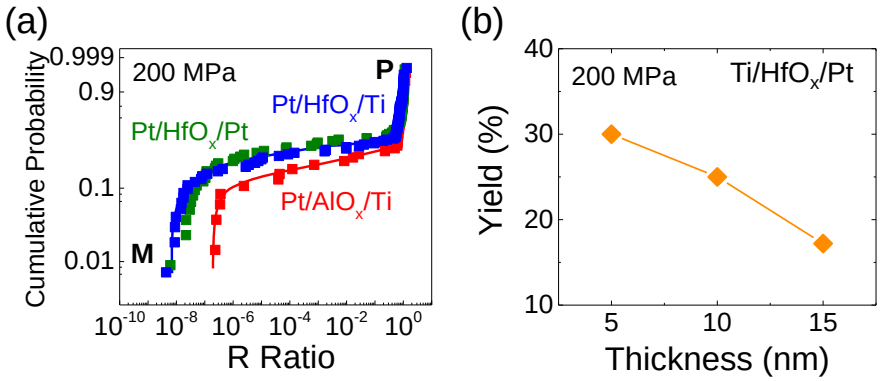

Figure B.7: (a) Weibull plots showing similar transition curves for different MIM configurations, all from pristine state under 200 MPa. Different electrode configurations for HfO_x have the same p, which is higher than for AlO_x. (b) Transition yield under 200 MPa of Ti/HfO_x/Pt MIM in different thickenss. Defined as the accumulative probability of R ratio $< 10^{-5}$ in their P-to-M transition Weibull plots.

Similar to the case of nanometallic ReRAM, pressure transitions are one-way transitions. As depicted in Fig. B.1b, pressure cannot induce any metal-to-insulator transition but voltage can. In fact, all the voltage-induced transitions has already been verified in [106, 103, 107], in which we used negative forming for the P-to-M transition, positive forming for the P-to-II transition, RESET/SET for the reversible M/II-to-II/M with many intermediate IM achievable by controlling current compliance. Here we only examine if the pressure-induced M state can be switched by voltage and compare it with the switching of voltage-formed M.

As shown in Fig. B.8, we used a positive voltage of about 1 V (in our convention, a positive voltage forces current to flow from the top electrode to the bottom electrode) to convert M−obtained from a previous pressure treatment−to II, then used a negative voltage of about −1 V to convert II to M (curve 1 and 3, at 300K and 2K, respectively). We also used a voltage to convert P to M (forming curve not shown), and next, M-to-II (curve 2 and 4, at 300K and 2K, respectively). In this way, we verified all the green arrows in Fig. B.1b. From these results, we conclude that the irreversibility of pressure transition is intrinsic as expected from Fig. B.1, and not because the MIM cell was damaged by the pressure treatment.

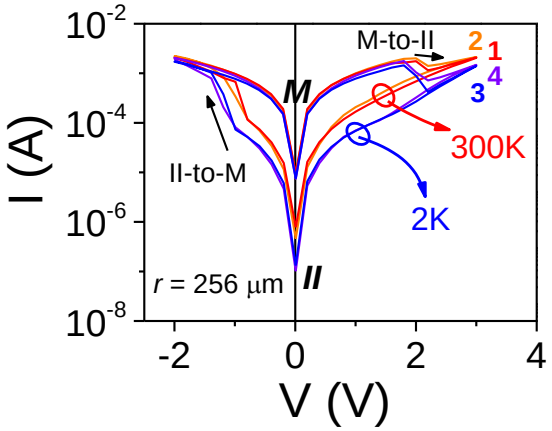

Figure B.8: Voltage-induced two-way transition between II state and M state in HfO_x. Bipolar current-voltage (I-V) M-II-M transition loops of either pressure-initiated M (loop 1, 3) or voltage-initiated M (loop 2, 4), initiation starting with two pristine MIMs of same cell radius (256 μm). As marked by circles, resistance values of II differ in loops at 300K (loop 1, 2) and 2K (loop 3, 4), in contrast to similar resistance of M in all loops. Arrows indicate switching directions of M-to-II (+ bias) and II-to-M (− bias).

Note that, once again, we cannot convert M, IM, or II into P. So, once the P state has transitioned to a lower resistance state, it cannot be recovered. This is not unreasonable because statistically it is very unlikely to reestablish (by electron trapping) same blocking at all the critical points−any failure to do so at just one critical point is likely to lower the network resistance by a large amount, hence the impossibility of returning to the P state.

We next compare the two M states obtained by pressure and voltage treatment, respectively.

First, we verified their resistances are similar and insensitive to their respective cell area (see[106, 103, 107] and Fig. B.6), implicating the same type of metallic network states in both.

Second, we compared their subsequent voltage-induced two-way transitions and found them essentially indistinguishable (Fig. B.8), not only at 300K but also at 2K. Note in particular that the transition voltage is insensitive to temperature (just like the characteristic switching voltage of nanometallic ReRAM), which is consistent with the picture in Fig. B.1a where the transition criterion is based on energy only.

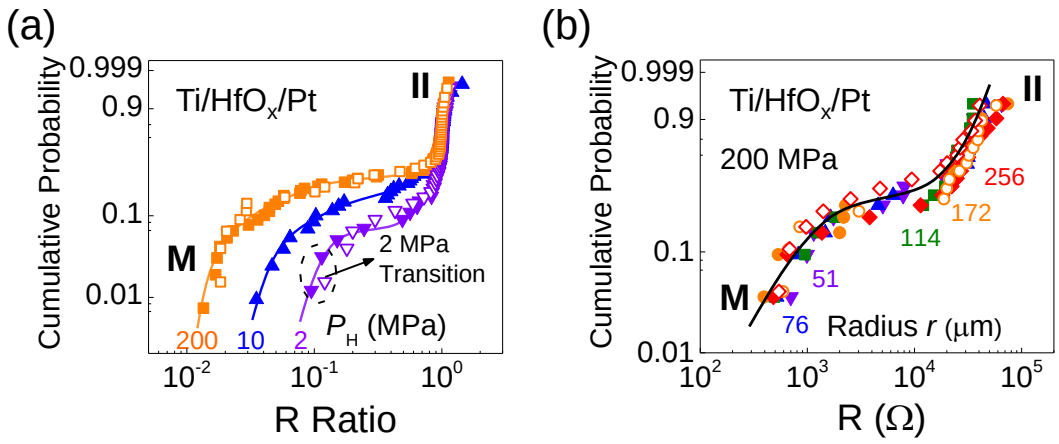

Figure B.9: Weibull plots for pressure-induced II-to-M transition of pressure-initiated (hollow symbols) and voltage-initiated (solid symbols) cells: A pressure/voltage was used to initiate transition from P to M, then a voltage was used to transition M to II, followed by pressurization at P_H. They both share similar p, bimodal resistance distribution, and the follow characteristics: (a) Higher P_H induced lower resistance and more transitions. (b) No area dependence of the Weibull statistics.

Third, when the two II states obtained from these two M states were subject to a pressure treatment, they exhibited the same transition statistics in Fig. B.9 (hollow vs. solid), again leaving a continuum of intermediate states and again with a pressure-dependent transition yield (Fig. B.9a). However, their transition statistics are insensitive to the cell area (Fig. B.9b) unlike the case in Fig. B.6. This is a general observation: The area dependence only appears in the first transition from the P state and not in the subsequent pressure-induced transitions. This can be understood in the context of the network picture as follows.

A comparable resistance of M or II implies the same (or comparable) number of unblocked critical points. Any subsequent transition is thus mostly likely to involve the same set of critical points; a voltage-induced M-to-II transition re-blocks some of these points, and a voltage- or pressure-induced II-to-M transition unblocks some of these points. Inasmuch there is no longer a need to involve new points−the random statistics of finding them is the origin of the area dependence−there is no longer an area dependence. In this way, all the transitions depicted in Fig. B.1b have been verified, and all the data displayed in Fig. B.5-B.9 including their statistics can be rationalized.

Lastly, as a disordered metallic state, $R-T$ dependence of voltage-induced M state share the same feature of resistance minimum at similar $T_{\min}$ with that of the pressure-induced M in Fig. B.3. In fact, as summarized in Fig. B.10, there is a rich variety of transitions between II and M triggered by either voltage or pressure and all M/II states have very similar trends in their $R-T$ curves.

The above findings also apply to other MIMs having a different electrode configuration (Pt/Pt vs. Ti/Pt) or a different oxide type (AlO_x vs. HfO_x) as shown in Fig. B.11. Specifically, under electrical voltage, similar electroforming (P-to-M, Fig. B.11a) and bipolar switching (Fig. B.11c, between II and M) were also found in material stacks of Pt/HfO_x/Pt and Ti/AlO_x/Pt. And they also exhibit pressure-induced P-to-M (Fig. B.11b) and II-to-M (Fig. B.11d) transitions with similar bimodal-shaped Weibull distribution over a wide spectrum. Lastly, metallic conduction featuring resistance minimum was found in both pressure- and voltage-formed M states of AlO_x devices (Fig. B.11e). Since they all provide the same findings, electrode-induced redox reactions (Ti is a reducing agent but Pt is not) and bulk polarizability (HfO_2's dielectric constant is 4× that of Al_2O_3) cannot be a major factor in these transitions. These transitions leave very similar states in Fig. B.10, with very similar resistances as well as their temperature dependence. In all cases, the metallic and weak-localization features of the M state and the insulating feature of the II state are clearly manifest.

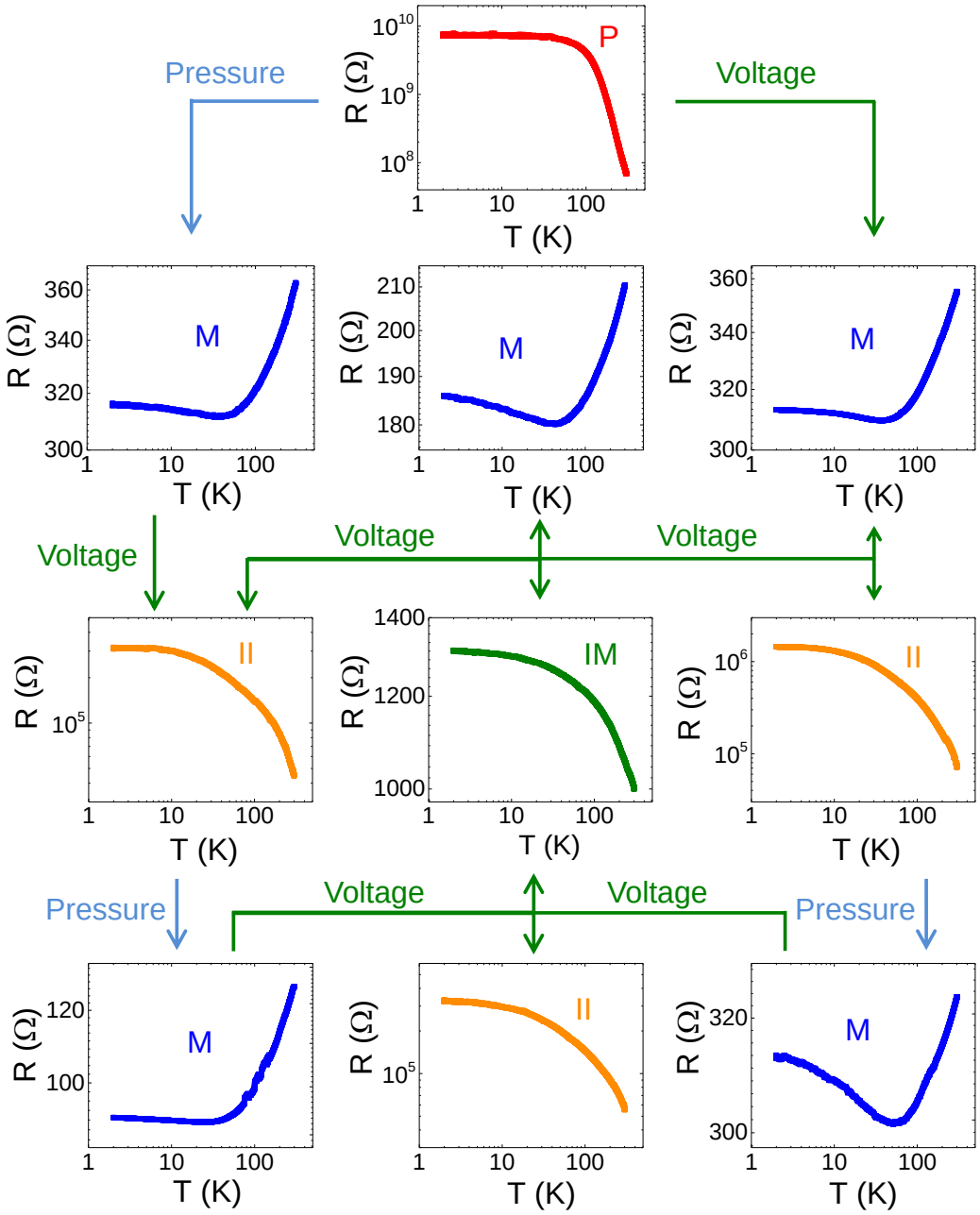

Figure B.10: Summary of $R - T$ curves in different states, starting from pristine state P through various possible pressure/voltage treatments. Blue arrows indicate pressure-induced one-way insulator-to-metal transitions from P/II to M (the IM-to-M one not shown). Green arrows indicate voltage-induced one-way transition to M or two-way transitions between M/IM and IM/II. All P/II curves feature variable-range-hopping at high temperature and elastic tunneling at low temperature; all M curves feature resistance minimum at some $T_{\min}$. Resistance values read at 0.01 V except for P, read at 1 V.

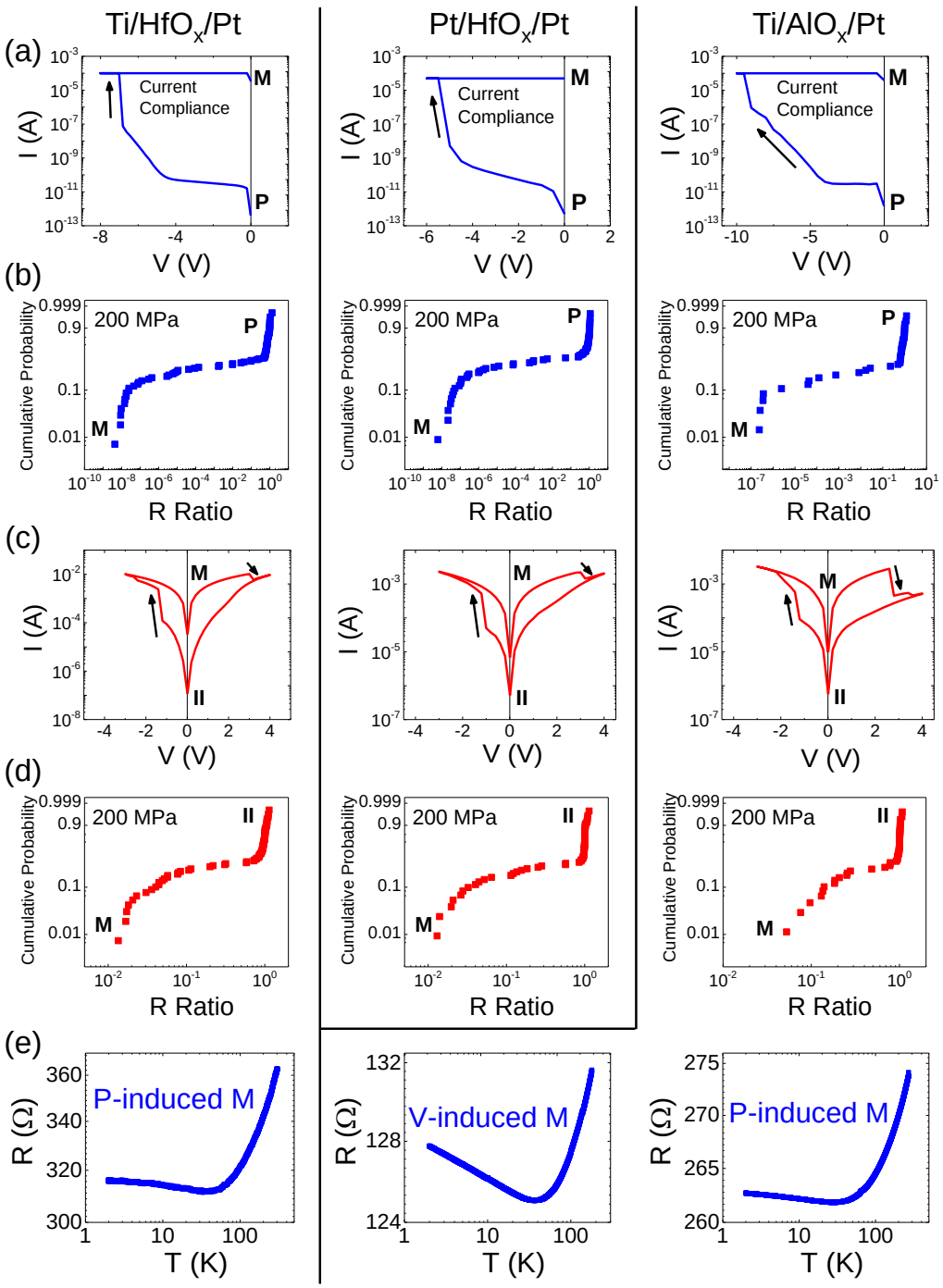

Figure B.11: Data summary of Ti/HfO$_x$/Pt, Pt/HfO$_x$/Pt and Ti/AlO$_x$/Pt MIM. (IM state omitted for brevity.) In all of the materials: their pristine state P can be (a) voltage- or (b) pressure-transitioned to metallic state (M), then (c) voltage-transitioned to intermediate insulating state (II), which can again be (d) pressure-transitioned to M state. (e) Their voltage (V)- and pressure (P)-induced M states are disordered metallic states that feature a resistance minimum in the $R-T$ curves.

B.4.3. Magnetic-Pressure-Induced Transition in 10^{-13} s

Physically, the conversion from configuration C to configuration B in Fig. B.1a may take as short as the period of one atomic vibration, ~0.1 ps, which sets the upper limit for the speed of the insulator-to-metal transition. We have previously seen how an ultrafast, sub-picosecond pressure impulse can be provided by a Lorentz switch that harnesses the magnetic transient of an ultrarelativistic electron bunch to mechanically induce an insulator to metal transition by locally reversing a negative U in Si ReRAM (Appendix A) and Si_3N_4:Pt nanometallic ReRAM. Here, we verify that this switch also works for Ti/HfO_x/Pt filamentary ReRAM, giving the same results except its transition here is network-percolative.

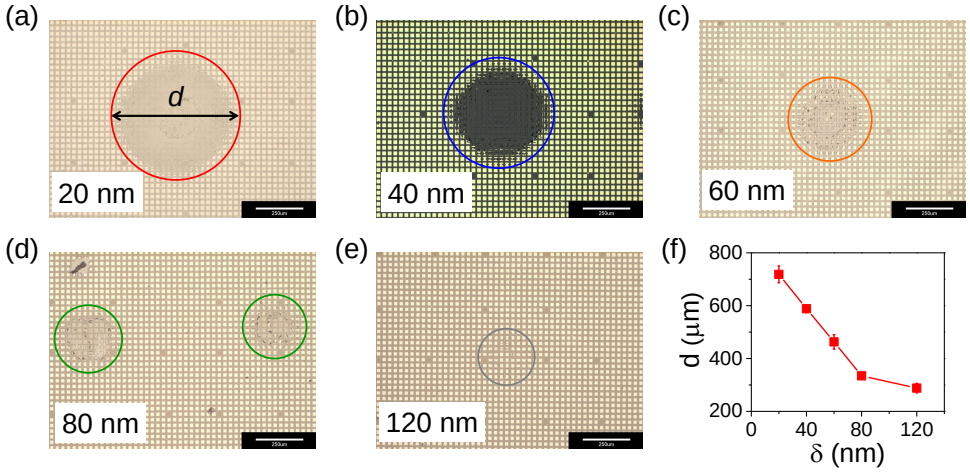

Figure B.12: Thickness effect of top Pt electrode on the damage (peeled-off) zone by electron bunch. (a)-(e): Images of the damage zones, defined as regions in which top electrodes have disappeared after one single shot of electron bunch, in arrays of Ti/HfO_x/Pt cells with Pt electrode having thickness δ of (a) 20 nm, (b) 40 nm, (c) 60 nm, (d) 80 nm, and (e) 120 nm where no cell completely lost the electrode. Gold-color squares are undamaged Pt electrodes, while the earth-color regions are the damage zones. Circles outline damage regions with visible deformation, which shrink as Pt electrode becomes thicker as shown in (f). All scale bars on bottom right in (a-e) are the same, being 250 μm.

Briefly, the experiment was performed inside a linear accelerator (SLAC) that shot, just once, a single bunch of 10^9 20 GeV electrons at the film. The bunch has a size of 20 μm×20 μm×20 μm and carries with it a 10^{-13} s pulse of circumferential magnetic field, the pulse time being the time to travel 20 μm at the speed of light. The field peaks at 70 T at the

edge of the bunch (r=40 μm) [67], falls off as $\sim 1/r$ with the radial distance r, and remotely delivers to a two-side-electroded film (located at r away from the flight path) a magnetic pressure P_B that peaks at 1,950 MPa and decays roughly with $\sim 1/r^2$. (There is also an induced pressure due to the induced current in the electrodes, which inversely depends on the (pulse width)^2). As explained in Chapter 2, the pressure generates a uniaxial tension to stretch the oxide film. It also generates a biaxial tension in the top electrode, which can be ripped apart if the electrode is thin, but not if the electrode is thick. (The stiffness increase with the third power of the thickness.) This is evident in Fig. B.12 in which the damage zone caused by the electron bunch shrinks as the electrode thickness increases (see more details of physical appearance after electron bunch in [13]). This feature makes it easy to identify where the flight path hit the MIM array, and since the electron bunch is only as big as an MIM cell, $\sim$ 20 by 20 μm^2, each of them appearing as a "dot" in Fig. B.13-B.14, all the pressure impulses seen by the cell are entirely remote and magnetic in origin, and they radially decay from the center (where electron bunch hit) that is indicated by a radial arrow. Per reversible transition II-M curve in Fig. B.8 and in [106, 103, 107], we often also preset some MIM cells to II (or HRS) and M (or LRS) states prior to the experiment to study various transition possibilities. In the following, we describe three key observations of these 0.1 ps pressure-impulse-transition experiments.

(a) One-way transitions: In an MIM array that contains either P states (red) or voltage-preset II (yellow) and M states (medium blue) shown on the left of Fig. B.13, we found after one single shot of an electron bunch, resistances of cells within an area from the flight path were lowered to mostly that of M states, shown on the right maps which contains numerous blue dots. Next we examine the three exemplary cells initially in P, II and M states in each array, marked by the white circles and located on a circle of $r \sim 300$ μm from the center, thus having seen the same magnetic pressure. While the M cell remained as M (but one cell's resistance decreased from 200 Ω to 100 Ω on the top plot), both P and II cells had transitioned to the M state. This confirms that the magnetic pressure is effective to induce all the one-way transitions depicted in Fig. B.1b despite its subpicosecond duration. The

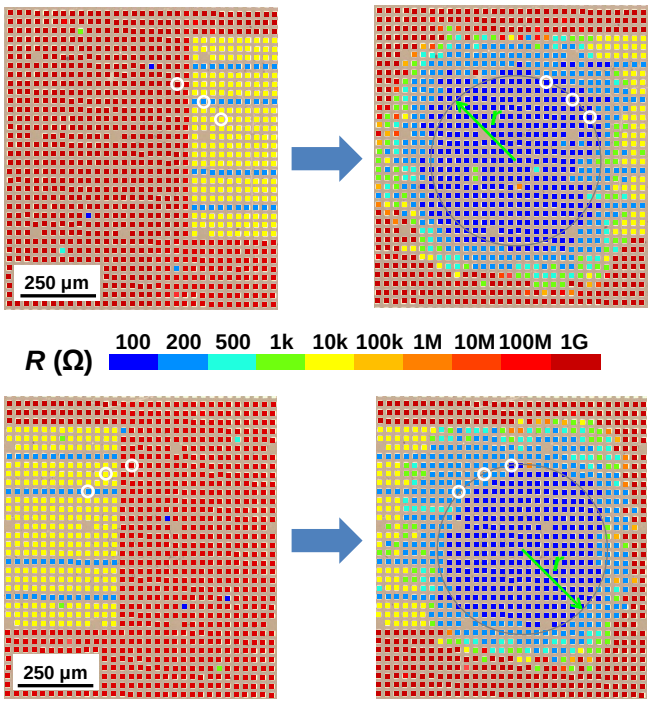

Figure B.13: Impulse-magnetic-pressure-induced insulator-to-metal transitions in HfO_x with thick Pt electrodes that all remained in contact with the film after shot by electron bunch. The subpicosecond transitions were simultaneously induced by one 10^{-13} s impulse of magnetic pressure represented in two colored resistance maps before and after shot by electron bunch, in which each colored "dot" represents one cell. Left: Most Ti/HfO_x/Pt MIM cells left in pristine P states (red), some voltage-preset to II (yellow) and M (medium blue). Right: After electron bunch (of a size of 20 μm) hit center ($r = 0$) of the two arrays once, cell resistances are re-measured and cells are colored per color spectrum in the middle. As exemplified by the three cells marked by white circles in each array at same distance ($r = 300$ μm) from center, P and II are transitioned to M state, and M state of 200 Ω lowers resistance to 100 Ω (top map) or stays at 200 Ω (bottom map).

critical pressure can be estimated by the edge of the "blue circle", which extends to ∼300 μm, where the primary magnetic pressure is about 10 MPa.

(b) Percolative transition: Fig. B.14 shows another MIM array that has thinner top electrodes, which were peeled off by the magnetic pressure when the cells are located too close to the center. A few cells, however, still had some remnants of the top electrodes, and two such cells are marked by white circles with $r = 240$ μm. Although they have about the same

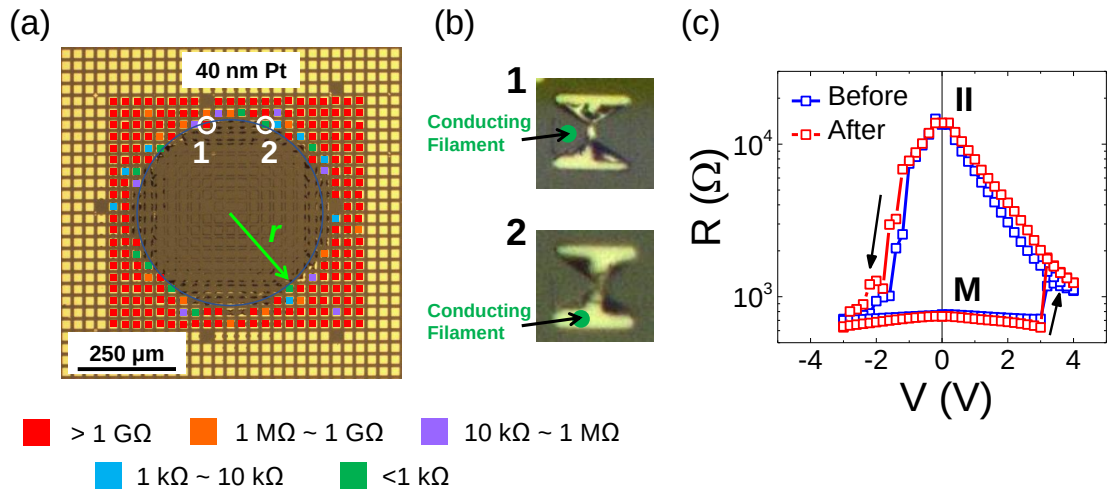

Figure B.14: Impulse-magnetic-pressure-induced insulator-to-metal transition in HfO_x with thin Pt electrodes. Colored resistance map in (a) records post-shot resistance values of Ti/HfO_x/Pt MIM cells, originally in P state (red). Most Pt top electrodes (thickness: 40 nm) were blown off by a single shot of electron bunch making cell resistance unreadable. Cells further away at $r = 250$ μm having part of electrodes remaining are readable, but their resistances vary by many orders of magnitude. Cell 1 (red, > 1 GΩ) and 2 (green, < 1 kΩ), marked by white circles, have vastly different resistances from those of most other cells (in blue, having resistance of 1 kΩ ~ 10 kΩ) at same radial distance. Such feature is a consequence of having top electrode in contact with only a portion of a cell (visualized by green dots) that has undergone percolative transition. (c) The impulse-magnetic-pressure transitioned M states can be voltage-transitioned to II following blue transition $R - V$ curve (marked after), which appears the same as red curve before, even though it only had partially left top electrode.

radial distance from the center, hence the same magnetic pressure ($P_B \sim 50$ MPa), they have very different resistances (2 GΩ vs. 300 Ω). Comparable tests that used MIM arrays of thicker electrodes found that, at this radial distance, all the cells should have transitioned to the M state, so the highly resistive cell in this set seems to be an anomaly. However, such anomaly is consistent with the picture of percolative network because if a cell had lost the part of the top electrode that was in contact with the percolative part of the network (the green dots in Fig. B.14b, e.g., the conducting filaments in Chapter 4 and [106, 103, 107]), then the remaining part of the top electrode would not be able to communicate with the bottom electrode, hence such cell will read a very high resistance. A check of other cells with similar top-electrode remnants confirmed this picture: Their resistances are either that

of the M state, or very much higher. For the 9 cells at $r = 250$ μm with electrode remnants in Fig. B.14, 5 of them have resistance $\sim$300 Ω, and the other 4 cells have resistance $\sim$2 GΩ. This finding is similar to the previous fracture test of HfO_x ReRAM in [103], in which we intentionally severed the cells to study the resistance statistics of the two severed halves and only one half was found to inherit the conducting filament(s) with similar resistance (we will compare the results of these two tests in the Discussion shortly).

(c) Cell reversibility: To again check whether the magnetic-pressure-transitioned M states were damaged or not, we applied an electrical voltage to see if they could be transitioned to II, and indeed they could, with a voltage transition curves that appear normal (red curve in Fig. B.14c). This similarity reconfirms the picture of percolative, localized conduction in pressurized HfO_x in (b): even though the cell only had a partial electrode left, it exhibited almost identical switching curves because the remaining electrode is in contact with the same percolative network (or conducting filaments). This not only rules out any permanent damage caused by electron bunch but also establishes the equivalency between the pressure-transitioned state and the voltage-transitioned state. Thus, there is no difference between the two pressure experiments, one by a static hydraulic pressure and the other a dynamic 0.1 ps magnetic pressure: They both reverse the sign of negative U in the same way.

B.5. Discussion

B.5.1. Network-Percolative Transition in Comparison with Nanometallic Transition

We have demonstrated in [106, 103, 107] that resistance switching in HfO_x ReRAM is localized in area-insensitive nanofilaments formed by electrical voltage, in contrast to the uniform switching of nanometallic ReRAM that is area-scalable. In terms of the circuit model, the single-filament switching picture was supported by the size-independent circuit elements of the filaments, such as internal load, and the dynamic filament capacitance. More straightforward evidence came from the fracture test of a LRS cell preswitched by voltage, in which only one of the two severed halves inherit the voltage-formed filament(s)

and had similar resistance as before while the other half is much more resistive.

Regarding the pressure-induced insulator-to-metal transition observed in this chapter, an interesting question to ask is: Does pressure also form single-filament(s) in HfO_x and AlO_x? Below we discuss their network-percolative feature of the pressure-induced transition in a comparison with pressure-induced transitions in nanometallic ReRAM and its counterpart triggered by voltage.

(i) The first evidence of the localized transition comes from the electron bunch experiment of HfO_x films with thin electrodes. As presented in the Results section, the magnetic impulse pressure not only triggered an insulator-to-metal transition in HfO_x cells but also teared off the top electrodes close to the shot center of electron bunch. Therefore, this experiment is equivalent a combined test of pressurization followed by fracture of the HfO_x cells. Fig. B.14 shows that two cells located at the same r that underwent similar pressure by electron bunch have vastly different resistance. This observation is reminiscence of the result of the voltage-induced transition in [103]. Regardless of origins of the stimuli (electrical or mechanical), they clearly indicate the existence of localized conducting paths: the cell is conducting if its partial electrode happens to be in contact with such percolative network. Further evidence that supports this picture comes from the switching curves in Fig. B.14c and in [103]: the subsequent electrical switching is almost identical to the one before the fracture by mechanical/magnetic pressure even though it has reduced area of top electrode.

(ii) Also demonstrated in the fracture test of voltage-induced LRS in [103], the severed half that does not contain conducting filament is not as resistive as the pristine sample before any voltage/pressure treatment [103]. We argued that it was due to partially developed filaments generated during electroforming by voltage, which were by complete filaments in parallel before fracture. In the electron bunch experiment, however, we found the pressure-transitioned metallic HfO_x cells with partial electrodes are either as conducting as 300 Ω or as insulating as its pristine form of 2 GΩ without any intermediate value (Fig. B.14). To reproduce this observation, we similarly fractured the HfO_x and AlO_x cells in the metallic

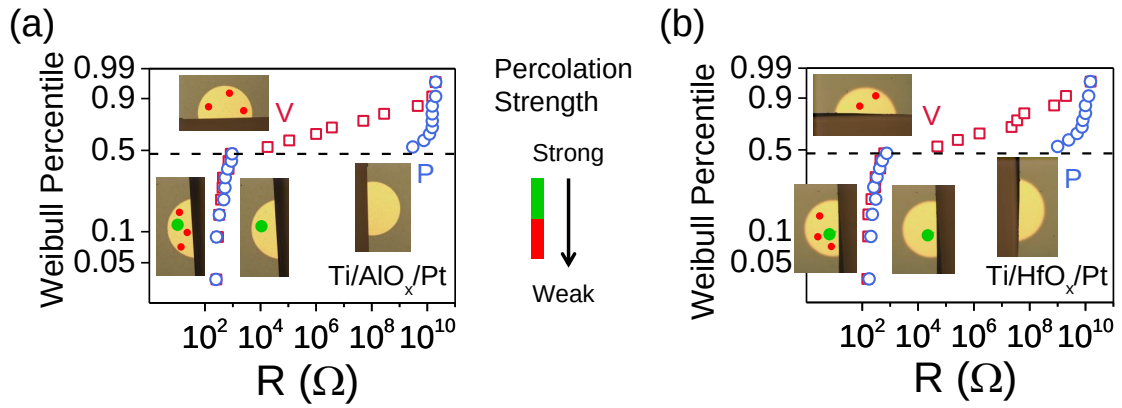

Figure B.15: Comparison between the resistance distributions of conducting/insulating halves severed from AlO_x (a) and HfO_x (b) cells in metallic states induced by voltage (V, red) and pressure (P, blue). The spreading distribution implies the coexistence of strongly (green dots) and weakly percolating networks (red dos) in the voltage-formed cells.

states induced by hydraulic pressure of 300 MPa and studied the resistance distribution of the two severed pieces as shown in Fig. B.15. Consistent with the localized transition induced by electrical voltage and magnetic pressure, the two severed pieces again have vastly different resistance for both AlO_x (a) and HfO_x (b) cells. More interestingly, the more resistive halves fractured from cells formed by pressure (P, blue circles) have resistance distributed only at two extrema in contrast to the wide resistance distribution between the two modes of the same cell group obtained by voltage (V, red squares). If we envision percolation networks with different strength (middle spectrum) in these severed pieces, the results indicate that while both voltage and pressure induce strongly percolating path(s) inherited by the conducting halves (green dots in lower left schematic), electrical voltage also forms less strong paths in the other halves (red dots in upper left schematic) but pressure cannot not (right schematic). In other words, pressure induces cleaner insulator-to-metal transitions with singularly percolative network. Among all the similarities mentioned earlier, this is the only difference between the transitions by these two means.

B.5.2. Statistical Switching Model of the Perssure-induced Percolative Conduction

The next question is, why is the pressure-induced transition localized in HfO_x and AlO_x films? One possibility is that the pristine P state already has a filamentary conductive network that is nevertheless blocked at N critical points, and as the pressure treatment clears n such points (e.g., by reverting the sign of negative-U), the network finally becomes sufficiently conducting with its resistance R mostly reflecting the local resistances around the few cleared-and-critical points in a way that is akin to resistance percolation.

To quantify this model, we start with the relevant experimental result of the pressurized resistance of the metallic states in different sizes. Fig. B.6 shows their lowest resistances (R_p) after a given pressure fall within a factor of 3-4 from each other despite their area varies as much as 25 times. This is different from the pressure-induced transitions in nanometallic films, which reached resistance values inversely proportional to device area A after pressure treatment (e.g., Fig. A.25 for amorphous Si doped with O in Appendix A) and can be rationalized as follows. Apparently the probability $p(n)$ of clearing n critical point out of the total N points that block the conduction follows a binomial distribution $B(N, q)$ with q as the probability to clear a single critical point. For $N \gg n$ and $q \ll 1$, $B(N, q)$ converges towards the Poisson distribution with mean value of $\lambda = Nq$. Therefore, $p(n)$ can be written as,

$$p(n) = \frac{(Nq)^n e^{-Nq}}{n!} \tag{B.1}$$

For a given probability and pressure, $(Nq)^n e^{-Nq} \propto n!$. Taking logarithm on both sides and applying Sterling formula, $n\ln(Nq) - Nq \propto n\ln(n) - n$, which implies $n \propto Nq$. To infer on the area dependence of pressurized resistance, we need to know, (i) how n affects the total network resistance R and (ii) how N varies with area A.

We determine these relations by fitting the cumulative probabilities in the Weibull plots in Fig.B.5a and Fig.B.6a. From a binomial distribution, its cumulative probability function

(CDF) $F_b(n)$, the probability of $k \leq n$, is given by

$$F_b(n) = \sum_{k=0}^{k=n} \binom{N}{k} p^k (1-p)^{N-k} \tag{B.2}$$

We denote the percolative network resistance as $R_k(k)$, which is in parallel with the resistance of insulating matrix R_m/A, and the total is in series with spreading resistance R_{E}. Then the total resistance R_{tot} measured in experiment is,

$$R_{\mathrm{tot}}(k) = R_{\mathrm{E}} + \frac{R_k(k) R_m/A}{R_k(k) + R_m/A} \tag{B.3}$$

From Eq. (B.3), it can be seen that $\lim_{k\to\infty} R_{\mathrm{tot}}(k) = R_{\mathrm{E}}$ and $\lim_{k\to 0} R_{\mathrm{tot}}(k) = R_m/A$. The cumulative distribution function of R_{tot} is

$$F(R_{\mathrm{tot}}) = p(R_{\mathrm{tot}} \leq R_{\mathrm{tot,n}}) = p(k \geq n) = 1 - p(k \leq n) = 1 - F_b(n) \tag{B.4}$$

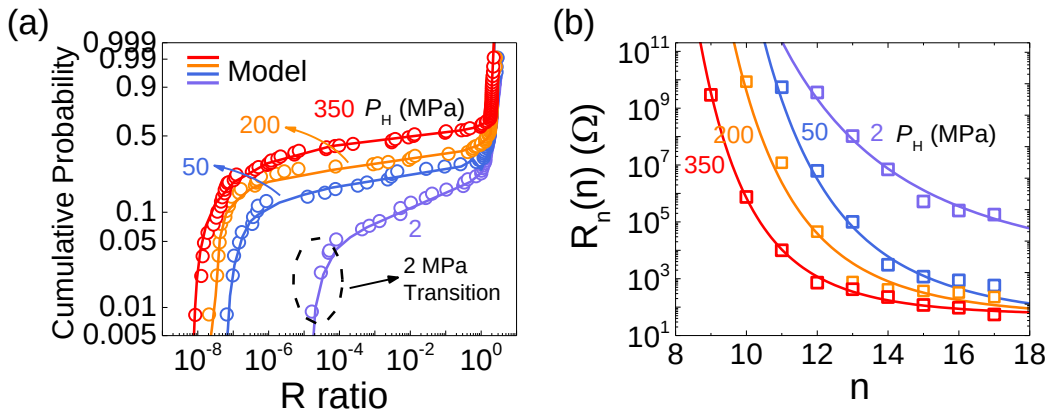

Figure B.16: (a) Modeling fitting of the pressure-dependent transition statistics previously shown in Fig.B.5a using Eq. (B.2)-(B.4) and $R_n(n) = R_0 \exp(a/n^b)$ in (b) with fixed $q = 0.1$ and $N = 100$, and R_0, a, and b as free parameters.

Using Eq. (B.2)-(B.4), the fitting results of the distribution data under different pressure P_H are shown as solid lines in Fig. B.16a. Here, we set $q = 0.1$ and $N = 100$ as fixed parameter for different P_H and extract the pressure-dependent relation $R_n(n)$ as shown in Fig. B.16b.

$R_n(n)$ is in a nonlinear form of $R_n(n) = R_0 \exp(a/n^b)$, in which both a and b increase with higher P_H. In addition, Eq. (B.2)-(B.4) with $R_n(n)$ extracted at certain $P_H = 350$ MPa was used to fit area-dependent data in Fig. B.17a, with Nq as a free parameter. The fitting results suggest $Nq \propto \ln(A)$ as shown in Fig. B.17b. Now the weak area dependence of R_p, the lowest resistance after pressurization, has a more intuitive interpretation. Considering Eq. (B.1), result in Fig. B.17b suggests that $n \propto Nq \propto \ln(A)$. If we write R_p in a simple form of $R_p \propto 1/n$ (as if there are n parallel conducting paths), then $R_p \propto 1/\ln(A)$, which is consistent with the experimental data shown in the inset of Fig. B.17a.

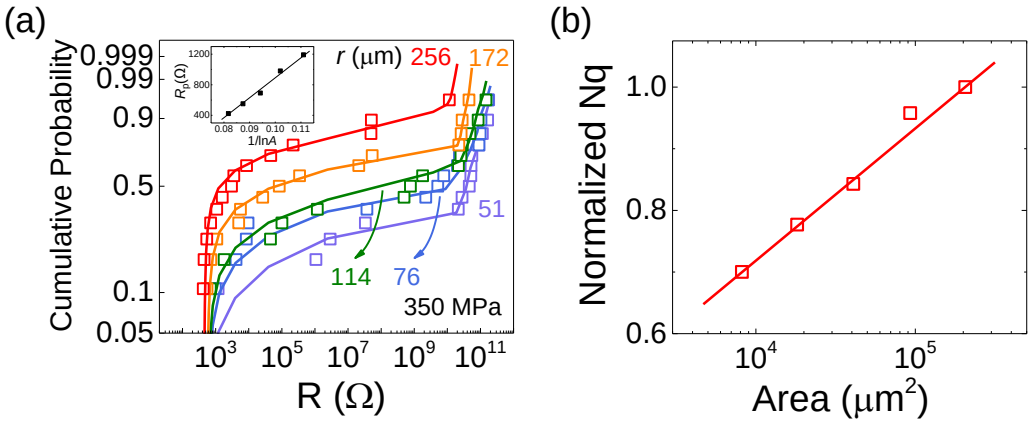

Figure B.17: (a) Modeling fitting of the size-dependent transition statistics under 350 MPa previously shown in Fig.B.6a using Eq. (B.2)-(B.4) and $R_n(n) = R_0 \exp(a/n^b)$ determined by previous fitting in Fig. B.16b. Nq are free parameters for different sizes and it scales with $\ln(A)$ as shown in (b). Inset in (a): the minimum pressurized resistance is proportional to $1/\ln(A)$.

Previously, irreversible initial voltage transition from the pristine state and subsequent reversible voltage transition between two resistance states were observed in amorphous HfO_2, Al_2O_3, and many other oxides but interpreted entirely differently emphasizing oxygen ion migration that causes a "soft" dielectric breakdown along a filament and subsequent electrical reconnection of the filament, possibly involving local Joule heating. Although this statistical model deos not rely on any physical mechanism of clearing the critical points that block the pathway, such consensus mechanism obviously cannot explain pressure-induced insulator-to-metal transitions in which neither voltage nor heat was involved.

B.6. Conclusions

1 Pressure-induced insulator-to-metal transition, which involves as dramatic as 10^9-fold drop of resistance, was found in nanofilms of amorphous HfO_2 and Al_2O_3 in both pristine form and voltage-conditioned form of ReRAM.

2 The above transition only requires a hydraulic pressure as low as 2 MPa and/or a pressure impulse as fast as 10^{-13}s. It provides evidence for the existence of negative-U centers in wide band-gap and low polarizability materials that have not been thought of as natural hosts of strong electron-phonon interactions.

3 The pressure-induced one-way transition in HfO_2 and Al_2O_3 occurs only within localized percolation networks, in contrast to the uniform transition in nanometallic films triggered by the same stimuli.

4 During a rich variety of transitions, the pressure-induced metallic state is the same as voltage-induced metallic state as in filamentary ReRAM devices: they have similar temperature dependence of resistance, and can both be switched back to insulator state by electrical voltage and exhibit almost the same statistics when transitioned to metallic states again by pressure. Such similarity challenges the widely reported ionic switching mechanism in filamentary ReRAM.

5 The results strongly suggest that Mott insulators, once disordered, become Anderson insulators, and within the latter, there is a possible crossover from strong localization to weak localization as the sample size is reduced to the nanoscale where a short conducting length of the order of 10 nm becomes important.

APPENDIX C : Probing Material Conductivity in Two-terminal Devices by Resistance Difference

An electronic device always contains a functional *material* component and a parasitic component, which includes device terminals, interfaces between the functional component and the terminals, leakage pathways and serial loads. So the device response inevitably includes the parasitic response, which may mask the response of the device material. While the four-terminal method can isolate the material response [162], it is impossible to implement in two-terminal devices, such as diodes (rectifier and light-emitting types) [163], solar cells [164] and non-volatile memories(phase change (PCRAM)[165] or resistance (RRAM) types [166, 103].) Probing these memories are especially challenging, for they are made of three-film stacks with the device-material sandwiched between a top electrode and a bottom electrode, all three films having a huge ratio ($10^2 - 10^4$) of the lateral dimension to the thickness. Yet it is the resistance of the device material that dictates the device behavior, measured by passing a test current between electrodes.

This appendix presents a method to separate the material resistance from the electrode/interface/load resistance for a library of devices that comprise a *self-similar* device material and the same terminals/interfaces, configured in an identical manner. Here, self-similarity refers to similar voltage responses to the stimuli (current (I), temperature (T), magnetic field (B), etc.), which differ by at most a multiplication factor. Self-similarity is manifest if the device material in different devices exhibits the same fractional change of resistance or conductivity ($\Delta R/R = -\Delta\sigma/\sigma$) in response to the stimulus. Such property is not uncommon, for it is often rooted in material physics. For example, the material resistivity/conductivity may vary with temperature in a power law, T^p, with an exponent p [3], or its magnetoresistance may obey a power law such as B^2 or $B^{1/2}$ [94].

The method will determine whether a self-similar material can maintain self-similar responses in known devices. It can also uncover hitherto unknown self-similar material re-

sponses in new devices. For example, when a voltage switches a RRAM [15], the resistance of its device material switches between a high resistance state (HRS) and a low resistance state (LRS), often with additional intermediate states between the two [127, 129, 106]. It may turn out that RRAM of different intermediate states form a self-similar library. It may even be conceivable to generate such library from only one parent device−later set into many different intermediate states. If the material is uniform, then one can also build a library of devices with different material thickness.

To extract self-similar $\Delta\sigma/\sigma = -\Delta R/R$, we will analyze, for each device pair (p, q) in the library, the device-resistance difference, $R^{(p)} - R^{(q)}$. Obviously, $R^{(p)} - R^{(q)}$ no longer contains parasitic resistance and equals the material-resistance difference. Therefore, the library of $R^{(p)} - R^{(q)}$ is like a library of material resistances, unencumbered by the parasitic resistance. Since the material response is self-similar, we can simply analyze the relative response of $R^{(p)} - R^{(q)}$ to the perturbation, i.e., $-\Delta R/R = -(\Delta R^{(p)} - \Delta R^{(q)})/(R^{(p)} - R^{(q)})$, to obtain material's relative response, $\Delta\sigma/\sigma = -\Delta R/R$. Of course, to verify self-similarity in the library, we must check whether all the device pairs indeed share the same $(\Delta R^{(p)} - \Delta R^{(q)})/(R^{(p)} - R^{(q)})$ value. If they do not, then the material in some, if not all, devices in the library must have behaved dissimilarly. This idea is illustrated in Fig. C.1, in which the (p-th) device voltage $V^{(p)}$ is conceptually separated into a material (film) component $V_{\mathrm{F}}^{(p)}$ and a common parasitic (electrode) component V_{E}, which is identical in device (p) and (q).

We use a multiplication factor ϕ, which does not change with I, to relate self-similar $I - V$ (current-voltage) curves, $V_{\mathrm{F}}(I, \phi) = (1/\phi)V_{\mathrm{F}}^{*}(I)$ with reference to the intrinsic film voltage of a reference film, V_{F}^{*}. This reference device need not actually exist in the library; even if it does, its choice need not be unique. Writing the device response as

$$V(I, \phi) = V_{\mathrm{F}}(I, \phi) + V_{\mathrm{E}}(I) = \frac{1}{\phi}V_{\mathrm{F}}^{*}(I) + V_{\mathrm{E}}(I) \tag{C.1}$$

we see the following "difference voltage" of pair (p, q) no longer includes V_{E} albeit it involves

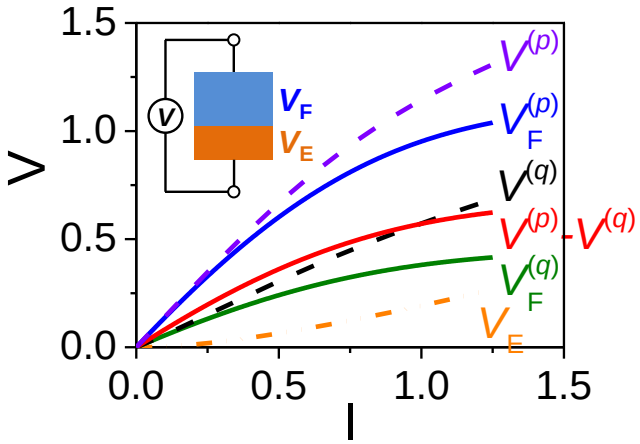

Figure C.1: Schematic $I-V$ curves of a pair of two-terminal devices, p and q, each separated into two parts (inset), self-similar device material (film) carrying voltage $V_{\rm F}$, and identical parasitic component (e.g., electrode) carrying $V_{\rm E}$, for total $V^{(p/q)} = V_{\rm F}^{(p/q)} + V_{\rm E}$. Shapes of $V^{(p)}$ and $V^{(q)}$ are different. Shapes of $V^{(p)} - V^{(q)}$, $V_{\rm F}^{(p)}$ and $V_{\rm F}^{(q)}$ are identical within a multiplication factor.

a new multiplication factor of $1/\phi^{(p)} - 1/\phi^{(q)}$,

$$V^{(p)}(I,\phi^{(p)}) - V^{(q)}(I,\phi^{(q)}) = (\frac{1}{\phi^{(p)}} - \frac{1}{\phi^{(q)}})V_{\rm F}^{*}(I) \tag{C.2}$$

Next, we call any perturbation other than current a "field", J, which may be a temperature change (T) or a magnetic field (B). Including both I and J while still assuming self-similarity, we generalize Eq. (C.1-C.2) to write

$$V(I,J,\phi) = \frac{1}{\phi}V_{\rm F}^{*}(I,J) + V_{\rm E}(I,J) \tag{C.3}$$

$$V^{(p)}(I,J,\phi^{(p)}) - V^{(q)}(I,J,\phi^{(q)}) = (\frac{1}{\phi^{(p)}} - \frac{1}{\phi^{(q)}})V_{\rm F}^{*}(I,J) \tag{C.4}$$

For applications such as resistance memory, it is also convenient to recast the above results into resistance, defined as $R = V/I$. With the additional definitions $R_{\rm E}(I,J) = V_{\rm E}(I,J)/I$,

$R_{\rm F}(I,J,\phi) = V_{\rm F}(I,J,\phi)/I$, and $R^*_{\rm F}(I,J) = V^*_{\rm F}(I,J)/I$, Eq. (C.3) becomes

$$R(I,J,\phi) = \frac{1}{\phi} R^*_{\rm F}(I,J) + R_{\rm E}(I,J) \tag{C.5}$$

We now contemplate changing the current and field from (I_0, J_0) to (I, J). The perturbation causes a resistance variation $\Delta R^{(p)}$ for any device p. For self-similar devices, $\phi^{(p)}$ is independent of (I, J). Then with the following definitions along with Eq. (C.5)

$$\Delta R^{(p)}(I,J,\phi^{(p)}) = R^{(p)}(I,J,\phi^{(p)}) - R^{(p)}(I_0,J_0,\phi^{(p)}) \tag{C.6}$$

$$\Delta R_{\rm E}(I,J) = R_{\rm E}(I,J) - R_{\rm E}(I_0,J_0) \tag{C.7}$$

$$\Delta R^*_{\rm F}(I,J) = R^*_{\rm F}(I,J) - R^*_{\rm F}(I_0,J_0) \tag{C.8}$$

$$\begin{aligned} \Delta R^{(p)}_{\rm F}(I,J,\phi^{(p)}) &= R^{(p)}_{\rm F}(I,J,\phi^{(p)}) - R^{(p)}_{\rm F}(I_0,J_0,\phi^{(p)}) \\ &= \frac{1}{\phi^{(p)}} \Delta R^*_{\rm F}(I,J) \end{aligned} \tag{C.9}$$

we get

$$\Delta R^{(p)}(I,J,\phi^{(p)}) = \frac{1}{\phi^{(p)}} \Delta R^*_{\rm F}(I,J) + \Delta R_{\rm E}(I,J) \tag{C.10}$$

Applying this to any device pair (p, q), we obtain the following equality

$$\frac{\Delta R^{(p)}(I,J,\phi^{(p)}) - \Delta R^{(q)}(I,J,\phi^{(q)})}{R^{(p)}(I,J,\phi^{(p)}) - R^{(q)}(I,J,\phi^{(q)})} = \frac{\Delta R^*_{\rm F}(I,J)}{R^*_{\rm F}(I,J)} \tag{C.11}$$

Unlike Eq. (C.1-C.10), the right-hand side of this exact result does not contain ϕ. It represents an intrinsic property of the device material, and is obtainable from the left-hand side that involves measured device-resistances only.

This intrinsic property can be alternatively represented in terms of conductivity σ. To do this, we write $R^*_{\rm F}$ as $G/\sigma^*_{\rm F}$, where G is a geometric constant (e.g., the ratio of thickness to

area in the case of a film), and $\sigma_{\rm F}^*$ is the intrinsic conductivity of the reference film. With this definition, Eq. (C.11) reduces to

$$\frac{\Delta R^{(p)}(I,J,\phi^{(p)}) - \Delta R^{(q)}(I,J,\phi^{(q)})}{R^{(p)}(I,J,\phi^{(p)}) - R^{(q)}(I,J,\phi^{(q)})}$$

$$= -\frac{\sigma_{\rm F}^*(I,J) - \sigma_{\rm F}^*(I_0,J_0)}{\sigma_{\rm F}^*(I_0,J_0)} \equiv -\frac{\Delta\sigma_{\rm F}^*}{\sigma_{\rm F}^*(I_0,J_0)} \equiv -x(I,J) \tag{C.12}$$

In the above, the response is expressed as a dimensionless quantity $x(I,J)$, such that $x(I_0,J_0) = 0$ before perturbation and $\sigma_{\rm F}^*(I,J) \equiv [1 + x(I,J)]\sigma_{\rm F}^*(I_0,J_0)$ after perturbation. This establishes the "resistance-difference" method, which is exact. In practice, if $\Delta R^{(p)} << R^{(p)}$ for all p, then replacing $R^{(p)}$ and $R^{(q)}$ in the denominator on the left hand side of Eq. (C.12) by their values at (I_0,J_0) in data analysis will also suffice. The intrinsic property can also be obtained from a device quartet (r,s,t,v) constructed from the library: First combine the (r,s) pair to make another "p", and likewise combine the (t,v) pair to make another "q"; next use the new pair (p,q) and Eq. (C.11-C.12) to obtain $\Delta R_{\rm F}^*/R_{\rm F}^*$ and $\Delta\sigma_{\rm F}^*/\sigma_{\rm F}^*$. The procedure can also cancel $R_{\rm E}$ and eliminate ϕ, and it can be further generalized: For a library containing N self-similar devices, there are altogether $\binom{N}{2} + \binom{N}{4} + \ldots + \binom{N}{N-2n}$ sets of resistance-difference to consider. The maximum $2n$ is either $N-1$ or N.

We next address the issue of accuracy according to our experience in these ReRAM. One most remarkable feature of the resistance-difference method is that the data quality depends only on the signal-to-noise ratio in $R_{\rm E}(I,J)$ or $V_{\rm E}(I,J)$ but not on the relative magnitude of $\Delta R(I,J)$, or $x(I,J)$: As long as $R_{\rm E}(I,J)$ is the same for all devices in the library, it can be removed by computing the resistance-difference, and high-fidelity data of $\Delta R(I,J)$ can be obtained. Because of this, we have determined $\Delta\sigma_{\rm F}^*/\sigma_{\rm F}^*$ as small as 0.1% in Mo/Si:0.45N/Pt RRAM and other related RRAM [54], which follows a (T,B) dependence in excellent agreement with the theoretical prediction of disordered electron physics [3]. Therefore, our analysis should be especially valuable for RRAM that have $R_{\rm F}$ of the same

order of magnitude as, or even smaller than, $R_{\rm F}$ [167].

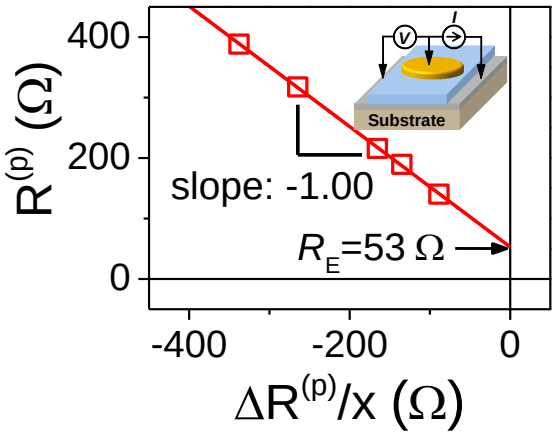

Figure C.2: LRS resistance $R^{(p)}$ at (18 T, 300mK) against $\Delta R^{(p)}/x$ in different $Mo/SiN_{4/3}$:0.07Pt/Pt devices follow straight line with slope of negative unity, consistent with Eq. C.14 when $\Delta R_{\rm E}(I,B)$ is small. Intercept of 53 Ω is $R_{\rm E}$. Inset: Schematic of three-point measurement configuration for two-terminal device, with patterned top electrode (yellow) and continuous bottom electrode (gray).

Besides the exact solution for $\Delta R^*_{\rm F}/R^*_{\rm F}$ and $\Delta\sigma^*_{\rm F}/\sigma^*_{\rm F}$, an approximate solution for $R_{\rm E}$ is also available when $\Delta R_{\rm E}$ is small. From Eq. (C.10) and Eq. (C.12), we have

$$\Delta R^{(p)}(I,J,\phi^{(p)}) = -\frac{1}{\phi^{(p)}}\frac{x(I,J)}{1+x(I,J)}\frac{G}{\sigma^*_{\rm F}(I_0,J_0)}$$

$$+\Delta R_{\rm E}(I,J) \tag{C.13}$$

Combining Eq. (C.5) and Eq. (C.13) to eliminate $(1/\phi^{(p)})G$, we obtain

$$R^{(p)}(I,J,\phi^{(p)}) = -\frac{\Delta R^{(p)}(I,J,\phi^{(p)}) - \Delta R_{\rm E}(I,J)}{x(I,J)}$$

$$+R_{\rm E}(I,J) \tag{C.14}$$

Since $x(I,J)$ is known from Eq. (C.12), we can plot $R^{(p)}$ against $\Delta R^{(p)}/x$ in the library, using those from devices of different ϕ but under the same (I,J) to determine $R_{\rm E}(I,J)$ from the intercept−if $\Delta R_{\rm E}(I,J) << \Delta R^{(p)}(I,J,\phi^{(p)})$ for all p. This is illustrated in Fig. C.2 using

the magnetoresistance data for several LRS devices in one library of Mo/$SiN_{4/3}$:0.07Pt/Pt RRAM collected at 18 T and 300mK (not-shown data at other fields following very similar trends.) In accordance with Eq. (C.14), all the data follow a straight line with a slope of negative unity.

Obviously, the above procedure works best with a larger x, which may be realized under a strong field, e.g., a strong magnetic field. As shown below, once $R_{\rm E}(I, J >> 1)$ is obtained, the following procedure can be used to determine $R_{\rm E}(I, J)$ for all J. First, we measure $R^{(p)}(I, J, \phi^{(p)})$ for $J >> 1$ to realize a large x, which allows us to use Eq. (C.14) to find $R_{\rm E}(I, J >> 1)$. After subtracting $R_{\rm E}(I, J)$ from $R^{(p)}(I, J, \phi^{(p)})$, we obtain $R_{\rm F}^{(p)}(I, J, \phi^{(p)})$ for all the devices in the $J >> 1$ limit. Next, we recall that $R_{\rm F}^{(p)}(I, J, \phi^{(p)})$ is proportional to $1/\phi^{(p)}$. Therefore, referring to any device in the library as the reference state with ϕ^*, we can express the resistance of other devices as $R_{\rm F}^{(p)}(I, J, \phi^{(p)}) = R_{\rm F}(I, J, \phi^*)(\phi^*/\phi^{(p)})$. From this, we obtain $\phi^*/\phi^{(p)}$ for all the devices, still under the same (I, J) in the $J >> 1$ limit. Third, for any other J that may not satisfy $J >> 1$, thus may not have a large x, we still have the following relation because $\phi^{(p)}$ is not changed by J

$$R^{(p)}(I, J, \phi^{(p)}) = R_{\rm F}^*(I, J)(\phi^*/\phi^{(p)}) + R_{\rm E}(I, J) \tag{C.15}$$

Here $R_{\rm F}^* = R_{\rm F}(I, J, \phi^*)$ denotes the reference film resistance. Fourth, plotting the measured device resistance $R^{(p)}(I, J, \phi^{(p)})$ against $\phi^*/\phi^{(p)}$, which we already obtained for all the devices from the $J >> 1$ data, we should obtain a straight line from which the intercept gives $R_{\rm E}(I, J)$. Fifth, having determined $R_{\rm E}(I, J)$ for all J, we can subtract it from the device resistance $R^{(p)}(I, J, \phi^{(p)})$ to finally have $R_{\rm F}^{(p)}(I, J, \phi^{(p)})$ for all J, for all the devices. The problem of film resistance of the two-terminal devices is now completely solved. If spreading resistance provides too large a $\Delta R_{\rm E}(I, J)$ thus rendering Eq. (C.14) useless, it can be removed by using the three-point method in the inset of Fig. C.2. The remaining $R_{\rm E}$ contains only the top-electrode resistance and is more likely to give a smaller $\Delta R_{\rm E}$. The method is advantageous in magnetic measurement because current spreading in the

large-area bottom electrode may entail a large magnetoresistance.

APPENDIX D : QCC in $d = 1 + \epsilon$ Systems

We start with the path crossing probability $\mathscr{P}$ calculated by Eq. (1.5) in Chapter 1,

$$\mathscr{P} = \int_{\tau}^{\tau_\phi} P(0,t) l^d \frac{dt}{\tau} = \int_{\tau}^{\tau_\phi} \frac{l^d}{(4\pi D t)^{d/2}} \frac{dt}{\tau} = \frac{l^d}{\tau} \frac{1}{(4\pi D)^{d/2}} \int_{\tau}^{\tau_\phi} t^{-d/2} dt \tag{D.1}$$

Replacing d by $d = 1 + \epsilon$ where $0 \leq \epsilon < 1$, we obtain

$$\mathscr{P} = \frac{l^{1+\epsilon}}{\tau} \frac{1}{(4\pi D)^{1/2+\epsilon/2}} \frac{2}{1-\epsilon} \left(\tau_\phi^{1/2-\epsilon/2} - \tau^{1/2-\epsilon/2} \right) \tag{D.2}$$

$$\mathscr{P} = \frac{2}{(1-\epsilon)(4\pi)^{1/2+\epsilon/2}} \frac{l^{1+\epsilon} \tau^{1/2-\epsilon/2}}{D^{1/2+\epsilon/2} \tau} \left[\left(\frac{\tau_\phi}{\tau} \right)^{1/2-\epsilon/2} - 1 \right] \tag{D.3}$$

$$\mathscr{P} = \frac{2}{(1-\epsilon)(4\pi)^{1/2+\epsilon/2}} \frac{l^{1+\epsilon}}{(D\tau)^{(1+\epsilon)/2}} \left[\left(\frac{\tau_\phi}{\tau} \right)^{1/2} \left(\frac{\tau_\phi}{\tau} \right)^{-\epsilon/2} - 1 \right] \tag{D.4}$$

Since $l = (D\tau)^{1/2}$, we have

$$\mathscr{P} \propto \sqrt{\frac{\tau_\phi}{\tau}} \left(\frac{\tau_\phi}{\tau} \right)^{-\epsilon/2} - 1 \tag{D.5}$$

proportional to the number of jumps τ_ϕ/τ in the $(1+\epsilon)$ D random walk before dephasing. Since $\tau_\phi/\tau \gg 1$, a non-zero ϵ in the range of $(0,1)$ weakens the temperature dependence in $d = 1 + \epsilon$ systems by a factor of $(\tau_\phi/\tau)^{-\epsilon/2}$, in comparison with Eq. (1.5).

Similarly,

$$\frac{\Delta\sigma_{1+\epsilon}^T}{\sigma} \propto - \int_{\tau}^{\tau_\phi} \frac{l \lambda_F^2}{(4\pi D t)^{(1+\epsilon)/2} W^{2-\epsilon}} \frac{dt}{\tau} \propto - \frac{\lambda_F^2}{W^{(2-\epsilon)} l^\epsilon} \left[\sqrt{\frac{\tau_\phi}{\tau}} \left(\frac{\tau_\phi}{\tau} \right)^{-\epsilon/2} - 1 \right] \tag{D.6}$$

and

$$\Delta\sigma_{1+\epsilon}^T \propto - \left[\sqrt{\frac{\tau_\phi}{\tau}} \left(\frac{\tau_\phi}{\tau} \right)^{-\epsilon/2} - 1 \right] \tag{D.7}$$

which implies an additional factor of $(\tau_\phi/\tau)^{-\epsilon/2}$ for the slope of QCC against $T^{-p/2}$, which comes from $\tau_\phi \propto T^{-p}$ for a small ϵ, and non-linear dependence of QCC against $T^{-p/2}$ since

this factor itself contains temperature dependence from $\tau_\phi \propto T^{-p}$.

Bibliography

[1] P. W. Anderson, E. Abrahams, and T. V. Ramakrishnan. *Phys. Rev. Lett*, 43:718, 1979.

[2] G. Bergmann. *Phys. Rep.*, 107:1, 1984.

[3] P. A. Lee and T. V. Ramakrishnan. *Rev. Mod. Phys*, 57:287, 1985.

[4] B. L. Altshuler, A. G. Aronov, M. E. Gershenson, and Y. V. Sharvin. *Sov. Sci. Rev. Sect. A: Phys. Rev.*, 9:223, 1987.

[5] M. H. Cohen, H. Fritzsche, and S. R. Ovshinsky. *Phys. Rev. Lett.*, 22:1065, 1969.

[6] N. F. Mott and E. A. Davies. chapter 2, page 49. Oxford, New York, second edition, 1979.

[7] N. F. Mott and E. A. Davies. Oxford, New York, second edition, 1979.

[8] P. W. Anderson. *Phys. Rev.*, 109:1492, 1958.

[9] S. John. *Phys. Rev. Lett.*, 58:2486, 1987.

[10] D. S. Wiersma, P. Bartolini, A. Lagendijk, and R. Righini. *Nature*, 390:671, 1997.

[11] Y. D. Wang. *Alloy perovskite oxide thin film as resistance switching non-volatile memory.* Ph.D. thesis, University of Pennsylvania, 2008.

[12] A. B. Chen. *Size-dependent metal-insulator transition in platinum-dispersed silicon dioxide thin film: A candidate for future non-volatile memory.* Ph.D. thesis, University of Pennsylvania, 2011.

[13] X. Yang. *Resistance switching devices based on amorphous insulator-metal thin films.* Ph.D. thesis, University of Pennsylvania, 2014.

[14] A. B. Chen, S. G. Kim, Y. Wang, W. S. Tung, and I. W. Chen. *Nature Nanotech.*, 6:237, 2011.

[15] X. Yang, I. Tudosa, B. J. Choi, A. B. Chen, and I. W. Chen. *Nano Lett.*, 14:5058, 2014.

[16] E. Abrahams, P. W. Anderson, D. C. Licciardello, and T. V. Ramakrishnan. *Phys. Rev. Lett.*, 42:673, 1979.

[17] N. F. Mott. chapter 1, pages 26–27. Taylor & Francis, London, second edition, 1990.

[18] Charles Kittel. chapter 6, pages 148–149. John Wiley & Sons, New York, seventh edition, 1996.

[19] I. L. Aleiner, B. L. Altshuler, and M. E. Gershenson. *Waves in Random Media*, 9:201, 1999.

[20] B. L. Altshuler and A. G. Aronov. *Solid State Commun.*, 39:115, 1979.

[21] B. L. Altshuler and A. G. Aronov. *Zh. Eksp. Teor. Fiz.*, 77:2028, 1979.

[22] A. F. Ioffe and A. R. Regel. *Prog. Semicond*, 4:237, 1960.

[23] L. P. Gorkov, A. I. Larkin, and D. E. Khmelnitzkii. *JETP Lett.*, 30:228, 1979.

[24] S. Hikami, A. I. Larkin, and Y. Nagaoka. *Prog. Theor. Phys.*, 63:707, 1980.

[25] A. Kawabata. *J. Phys. Soc. Jpn.*, 49:628, 1980.

[26] H. Fukuyama and K. Hoshino. *J. Phys. Soc. Jpn.*, 50:2131, 1981.

[27] D. V. Baxter, R. Richter, M. L. Trudeau, R. W. Cochrane, and J. O. Strom-Olsen. *Journal de Physique*, 50:1673, 1989.

[28] D. J. Thouless. *Phys. Rev. Lett.*, 39:1167, 1977.

[29] B. L. Altshuler, A. G. Aronov, D. E. Khmel'Nitzkii, and A. I. Larkin. pages 130–237. Mir Publisher, Moscow, 1980.

[30] P. W. Anderson, E. Abrahams, and T. V. Ramakrishnan. *Phys. Rev. Lett.*, 43:718, 1979.

[31] B. L. Altshuler, A. G. Aronov, and P. A. Lee. *Phys. Rev. Lett.*, 44:1288, 1980.

[32] J. Kondo. *Progress of theoretical physics*, 32:37, 1964.

[33] G. J. Dolan and D. Osheroff. *Phys. Rev. Lett.*, 43:721, 1979.

[34] J. J. Lin and J. P. Bird. *J. Phys. Condens. Matter*, 14:R501, 2002.

[35] G. Bergmann. *Phys. Rev. Lett.*, 48:1046, 1982.

[36] B. L. Altshuler, A. G. Aronov, and B. Z. Spivak. *JETP Lett. Pis'ma Zh. Eksp. Teor. Fiz.*, 33:94, 1981.

[37] Y. Aharonov and D. Bohm. *Phys. Rev.*, 115:485, 1959.

[38] J. Bardeen, L. N. Cooper, and J. R. Schrieffer. *Phys. Rev.*, 108:1175, 1957.

[39] S. Washburn and R. A. Webb. *Adv. Phys.*, 35:375, 1986.

[40] D. U. Sharvin and Y. U. V. Sharvin. *JETP Lett. Pis'ma Zh. Eksp. Teor. Fiz.*, 34:272, 1981.

[41] B. L. Altshuler, D. E. Khmel'Nitzkii, A. I. Larkin, and P. A. Lee. *Phys. Rev. B*, 22:5142, 1980.

[42] B. L. Altshuler and A. G. Aronov. *JETP Lett.*, 33:449, 1981.

[43] A. G. Aronov and Y. V. Sharvin. *Rev. Mod. Phys.*, 59:755, 1987.

[44] Y. V. Sharvin. *Physica B+C*, 126:1, 1984.

[45] B. L. Altshuler, A. G. Aronov, B. Z. Spivak, D. U. Sharvin, and Y. U. V. Sharvin. *JETP Lett. Pis'ma Zh. Eksp. Teor. Fiz.*, 35:588, 1982.

[46] A. Bachtold, C. Strunk, J. P. Salvetat, J. M. Bonard, L. Forro, T. Nussbaumer, and C. Schonenberger. *Nature*, 397:673, 1999.

[47] H. R. Shea, R. Martel, and Ph. Avouris. *Phys. Rev. Lett.*, 84:4441, 1999.

[48] G. Zala, B. N. Narozhny, and I. L. Aleiner. *Phys. Rev. B*, 64:214204, 2001.

[49] B. L. Altshuler and A. G. Aronov. chapter 1, page 11. North-Holland, Amsterdam, first edition, 1985.

[50] J. C. Ousset, S. Askenazy, H. Rakoto, and J. M. Broto. *Journal de Physique*, 46:2145, 1985.

[51] J. Zhang and R. M. White. *J. Appl. Lett.*, 83:6512, 1998.

[52] M. Sharma, S. X. Wang, and J. H. Nickel. *Phys. Rev. Lett.*, 82:616, 1999.

[53] J. Park, A. N. Pasupathy, J. I. Goldsmith, and C. Chang. *Nature*, 417:722, 2002.

[54] Y. Lu and I. W. Chen. *Appl. Phys. Lett.*, 111:083501, 2017.

[55] M. E. Gershenson, Y. B. Khavin, A. G. Mikhalchuk, H. M. Bozler, and A. L. Bogdanov. *Phys. Rev. Lett.*, 79:725, 1997.

[56] R. Waser and M. Aono. *Nature Mater.*, 6:833, 2007.

[57] R. Waser, R. Dittman, G. Staikov, and K. Szot. *Adv. Mater.*, 21:2632, 2009.

[58] J. J. Yang, D. B. Strukov, and D. R. Stewart. *Nature Nanotech.*, 8:13, 2013.

[59] D. H. Kwon, K. M. Kim, J. H. Jang, M. H. Lee, G. H. Kim, X. S. Li, G. S. Park, B. Lee, S. Han, M. Kim, and C. S. Hwang. *Nature Nanotech.*, 5:148, 2010.

[60] Y. Yang, P. Gao, S. Gaba, T. Chang, X. Pan, and W. Lu. *Nat. Commun.*, 3:732, 2012.

[61] J. Y. Chen, C. L. Hsin, C. W. Huang, C. H. Chiu, Y. T. Huang, S. J. Lin, W. W. Wu, and L. J. Chen. *Nano Lett.*, 13:3671, 2013.

[62] B. L. Altshuler and A. G. Aronov. volume 10, chapter 1, pages 1–154. Elsevier, New York, 1 edition, 1985.

[63] N. F. Mott. Taylor & Francis, London, second edition, 1990.

[64] Ping Sheng. chapter 10, pages 281–296. Springer, New York, second edition, 2006.

[65] R. A. Street. Cambridge University Press, 2005.

[66] B. J. Choi, A. B. Chen, X. Yang, and I. W. Chen. *Adv. Mater.*, 23:3847, 2011.

[67] S. J. Gamble, M. H. Burkhardt, A. Kashuba, R. Allenspach, S. S. Parkin, H. C. Siegmann, and J. Stohr. *Phys. Rev. Lett.*, 102:217201, 2009.

[68] A. S. Rodin and M. M. Fogler. *Phys. Rev. B*, 84:125447, 2011.

[69] K. Bodurtha and J. Kakalios. *J. Appl. Phys.*, 118:215103, 2015.

[70] M. A. Howson and B. L. Gallagher. *Phys. Rep.*, 170:265, 1988.

[71] M. L. Roukes, M. R. Freeman, R. S. Germain, R. C. Richardson, and M. B. Ketchen. *Phys. Rev. Lett.*, 55:422, 1985.

[72] R. P. Peters and G. Bergmann. *J. Phys. Soc. Jpn.*, 54:3478, 1985.

[73] D. S. Golubev and A. D. Zaikin. *Phys. Rev. Lett.*, 81:1074, 1998.

[74] F. Pierre, A. B. Gougam, A. Anthore, H. Pothier, D. Esteve, and N. O. Birge. *Phys. Rev. B*, 68:085413, 2003.

[75] J. J. Lin and J. P. Bird. *J. Phys. Condens. Matter*, 14:R501, 2002.

[76] W. E. Spear and P. G. Le Comber. *Solid State Commun*, 17:1975, 1975.

[77] J. T. Devreese. volume 14. VCH Publishers, New York, 1996.

[78] R. A. Street and N. F. Mott. *Phys. Rev. Lett.*, 35:1293, 1975.

[79] S. C. Agarwal. *Phys. Rev. B*, 7:685, 1973.

[80] M. A. Paalanen, T. F. Rosenbaum, G. A. Thomas, and R. N. Bhatt. *Phys. Rev. Lett.*, 48:1284, 1982.

[81] T. F. Rosenbaum, R. F. Milligan, M. A. Paalanen, G. A. Thomas, R. N. Bhatt, and W. Lin. *Phys. Rev. B*, 27:7509, 1983.

[82] P. Dai, Y. Zhang, and M. P. Sarachik. *Phys. Rev. Lett.*, 66:1914, 1991.

[83] T. Egami, K. Maeda, and V. Vitek. *Philos. Mag. A*, 41:883, 1980.

[84] T. Egami. *Prog. Mater. Sci.*, 56:637, 2011.

[85] M. L. Manning and A. J. Liu. *Phys. Rev. Lett.*, 107:108302, 2011.

[86] I. W. Chen and Y. Lu. U.S. Patent No. 14/507,977, 7 April 2016.

[87] Y. Lu and I. W. Chen. Pressure-induced insulator-to-metal transition provides evidence for negative-u centers in large-gap disordered insulators. e-print arXiv: 1703.02003, 2017.

[88] W. J. Skocpol, L. D. Jackel, E. L. Hu, R. E. Howard, and L. A. Fetter. *Phys. Rev. Lett.*, 49:951, 1982.

[89] J. Wang, A. M. DaSilva, C. Z. Chang, K. He, J. K. Jain, N. Samarth, X. C. Ma, Q. K. Xue, and M. H. Chen. *Phys. Rev. B*, 83:245438, 2011.

[90] B. Jouault, B. Jabakhanji, N. Camara, W. Desrat, C. Consejo, and J. Camassel. *Phys. Rev. B*, 83:195417, 2011.

[91] P. Dai, Y. Zhang, and M. P. Sarachik. *Phys. Rev. B*, 46:6724, 1992.

[92] Y. Takagaki, B. Jenichen, U. Jahn, M. Ramsteiner, and K. J. Friedland. *Phys. Rev. B*, 85:115314, 2012.

[93] N. P. Breznay, H. Volker, A. Palevski, R. Mazzarello, A. Kapitulnik, and M. Wuttig. *Phys. Rev. B*, 86:205302, 2012.

[94] T. F. Rosenbaum, R. F. Milligan, G. A. Thomas, P. A. Lee, T. V. Ramakrishnan, R. N. Bhatt, K. DeConde, H. Hess, and T. Perry. *Phys. Rev. Lett.*, 47:1758, 1981.

[95] P. Dai, Y. Zhang, and M. P. Sarachik. *Phys. Rev. B*, 45:3984, 1992.

[96] H. Z. Lu, J. Shi, and S. Q. Shen. *Phys. Rev. Lett.*, 107:076801, 2011.

[97] M. Liu et al. *Phys. Rev. Lett.*, 108:036805, 2012.

[98] H. Wang et al. *Sci. Rep.*, 4:5817, 2014.

[99] J. C. Licini, G. J. Dolan, and D. J. Bishop. *Phys. Rev. Lett.*, 54:1585, 1985.

[100] R. A. Webb, S. Washburn, C. P. Umbach, and R. B. Laibowitz. *Phys. Rev. Lett.*, 54:2696, 1985.

[101] M. H. Jang, R. Agarwal, P. Nukala, D. Choi, A. C. Johnson, I. W. Chen, and R. Agarwal. *Nano Lett.*, 16:2139, 2016.

[102] J. J. Yang, M. D. Pickett, X. Li, D. A. Ohlberg, D. R. Stewart, and R. S. Williams. *Nature Nanotech.*, 3:429, 2008.

[103] Y. Lu, J. H. Lee, X. Yang, and I. W. Chen. *Nanoscale*, 8:18113, 2016.

[104] H. S. Wong, H. Y. Lee, S. Yu, Y. S. Chen, Y. Wu, P. S. Chen, B. Lee, F. T. Chen, and M. J. Tsai. *Proceedings of the IEEE*, 100:1951, 2012.

[105] K. M. Kim, D. S. Jeong, and C. S. Hwang. *Nanotechnology*, 22:254002, 2011.

[106] Y. Lu, J. H. Lee, and I. W. Chen. *ACS nano*, 9:7649, 2015.

[107] Y. Lu, J. H. Lee, and I. W. Chen. *Nanoscale*, 9:12690, 2017.

[108] Wikipedia page `https://en.wikipedia.org/wiki/Electrical_resistivity_and_conductivity#Metals`.

[109] G. J. Dolan, J. C. Licini, and D. J. Bishop. *Phys. Rev. Lett.*, 56:1493, 1986.

[110] S. Yu, X. Guan, and H. S. P. Wong. *IEEE IEDM Digest*, pages 26–1, 2012.

[111] Wikipedia page `https://en.wikipedia.org/wiki/Diffusion-limited_aggregation`.

[112] S. Cho et al. *Nat. Commun.*, 6:7634, 2015.

[113] U. Russo, D. Ielmini, C. Cagli, and A. L. Lacaita. *IEEE Trans. Electron Devices*, 56:193, 2009.

[114] K. M. Kim and C. S. Hwang. *Appl. Phys. Lett.*, 94:122109, 2009.

[115] P. Huang, X. Y. Liu, B. Chen, H. T. Li, Y. J. Wang, Y. X. Deng, K. L. Wei, L. Zeng, B. Gao, G. Du, and X. Zhang. *IEEE Trans. Electron Devices*, 60:4090, 2013.

[116] J. Yao, Z. Sun, L. Zhong, D. Natelson, and J. M. Tour. *Nano Letters*, 10:4105, 2010.

[117] J. Yao et al. *Nat. Commun.*, 3:1101, 2012.

[118] G. Wang, A. R. O. Raji, J. H. Lee, and J. M. Tour. *ACS nano*, 8:1410, 2014.

[119] J. Yao, L. Zhong, D. Natelson, and J. M. Tour. *Sci. Rep.*, 2:242, 2012.

[120] Y. Yang and W. Lu. *Nanoscale*, 5:10076, 2013.

[121] S. H. Jo and W. Lu. *Nano Lett.*, 8:392, 2008.

[122] S. H. Jo, K. H. Kim, and W. Lu. *Nano Lett.*, 9:870, 2009.

[123] S. H. Jo, K. H. Kim, and W. Lu. *Nano Lett.*, 9:496, 2009.

[124] Y. Wang, X. Qian, K. Chen, Z. Fang, W. Li, and J. Xu. *Appl. Phys. Lett.*, 102:042103, 2013.

[125] A. Mehonic, S. Cueff, M. Wojdak, S. Hudziak, O. Jambois, C. Labbe, B. Garrido, R. Rizk, and A. J. Kenyon. *J. Appl. Phys.*, 111:074507, 2012.

[126] A. Mehonic, S. Cueff, M. Wojdak, S. Hudziak, C. Labbe, R. Rizk, and A. J. Kenyon. *Nanotechnology*, 23:455201, 2012.

[127] A. B. Chen, B. J. Choi, X. Yang, and I. W. Chen. *Adv. Funct. Mater.*, 22:546, 2012.

[128] X. Yang and I. W. Chen. *Sci. Rep.*, 2:744, 2012.

[129] X. Yang, A. B. Chen, B. J. Choi, and I. W. Chen. *Appl. Phys. Lett.*, 102:043502, 2013.

[130] S. Kim, S. Choi, J. Lee, and W. Lu. *ACS nano*, 8:10262, 2014.

[131] Y. Y. Chen et al. *IEEE VLSI-Technology Digest*, pages 1–2, 2014.

[132] B. J. Choi, A. C. Torrezan, K. J. Norris, F. Miao, J. P. Strachan, M. X. Zhang, D. A. Ohlberg, N. P. Kobayashi, J. J. Yang, and R. S. Williams. *Nano Lett.*, 13:3213, 2013.

[133] Ian D. Raistrick, Donald R. Franceschetti, and J. Ross Macdonald. chapter 2, pages 37–41. Wiley-Interscience, Hoboken, New Jersey, second edition, 2005.

[134] J. B. Jorcin, M. E. Orazem, N. Pebere, and B. Tribollet. *Electrochimica Acta*, 51:1473, 2006.

[135] C. H. Hsu and F. Mansfeld. *Corrosion*, 57:747, 2001.

[136] New US Navy Aircraft Carrier Will Launch Fighters Using Electromagnetic Force. `http://nationalinterest.org/blog/the-buzz/new-us-navy-aircraft-carrier-will-launch-fighters-using-16624`.

[137] J. Hubbard. *Proceedings of the Royal Society of London. Series A. Mathematical and Physical Sciences*, 276:238, 1963.

[138] P. W. Anderson. *Phys. Rev. Lett.*, 34:953, 1975.

[139] M. Kastner, D. Adler, , and H. Fritzsche. *Phys. Rev. Lett.*, 37:1504, 1976.

[140] G. D. Watkins and J. O. R. Troxell. *Phys. Rev. Lett.*, 44:593, 1980.

[141] S. R. Elliott. Longman, New York, 1983.

[142] T. Egami. *Prog. Mater. Sci.*, 56:637, 2011.

[143] S. S. Schoenholz, E. D. Cubuk, E. Kaxiras, and A. J. Liu. *Prog. Mater. Sci.*, 114:263, 2017.

[144] L. Goux, P. Czarnecki, Y. Y. Chen, L. Pantisano, X. Wang, R. Degraeve, B. Govoreanu, M. Jurczak, D. J. Wouters, and L. Altimime. *Appl. Phys. Lett.*, 97:243509, 2010.

[145] B. Moyzhes, T. H. Geballe, S. Jeong, D. Gitlin, and J. Karp. *J. Appl. Phys.*, 97:074104, 2005.

[146] K. H. Lee and J. H. Crawford Jr. *Phys. Rev. B*, 15:4065, 1977.

[147] A. S. Foster, F. L. Gejo, A. L. Shluger, and R. M. Nieminen. *Phys. Rev. B*, 65:174117, 2002.

[148] C. Shen, M. F. Li, H. Y. Yu, X. P. Wang, Y. C. Yeo, D. S. H. Chan, and D. L. Kwong. *Appl. Phys. Lett.*, 86:093510, 2005.

[149] J. X. Zheng, G. Ceder, T. Maxisch, W. K. Chim, and W. K. Choi. *Phys. Rev. B*, 75:104112, 2007.

[150] E. H. Poindexter and W. L. Warren. *J. Electrochem. Soc.*, 142:2508, 1995.

[151] S. Wright and R. C. Barklie. *J. Appl. Phys.*, 106:3917, 2009.

[152] R. Gillen, J. Robertson, and S. J. Clark. *Appl. Phys. Lett.*, 101:102904, 2012.

[153] D. M. Basko, I. L. Aleiner, and B. L. Altshuler. *Ann. Phys.*, 321:1126, 2006.

[154] G. D. Wilk, R. M. Wallace, and J. M. Anthony. *J. Appl. Phys.*, 89:5243, 2001.

[155] J. B. Wachtman Jr, W. E. Tefft, D. G. Lam Jr, and C. S. Apstein. *Phys. Rev.*, 122:1754, 1961.

[156] R. Thielsch, A. Gatto, and N. Kaiser. *Appl. Opt.*, 41:3211, 2002.

[157] A. I. Kingon, J. P. Maria, and S. K. Streiffer. *Nature*, 406:1032, 2000.

[158] T. G. Nieh and J. Wadsworth. *Scripta Metall. Mater.*, 25:955, 1991.

[159] N. Hansen. *Scripta Mater.*, 51:801, 2004.

[160] A. L. Romasco, L. H. Friedman, L. Fang, R. A. Meirom, T. E. Clark, R. G. Polcawich, J. S. Pulskamp, M. Dubey, and C. L. Muhlstein. *Thin Solid Films*, 518:3866, 2010.

[161] N. F. Mott and E. A. Davies. chapter 2, pages 32–37. Oxford, New York, second edition, 1979.

[162] F. M. Smits. *Bell System Technical Journal*, 37:711, 1958.

[163] I. Schnitzer, E. Yablonovitch, C. Caneau, T. J. Gmitter, and A. Scherer. *Appl. Phys. Lett.*, 63:2174, 1993.

[164] A. Ortiz-Conde, F. J. G. Sanchez, and J. Muci. *Sol. Energ. Mat. Sol. Cells*, 90:352, 2006.

[165] D. Roy, M. A. in't Zandt, and R. A. Wolters. *IEEE Electron Device Lett.*, 31:1293, 2010.

[166] D. S. Jeong, R. Thomas, R. S. Katiyar, J. F. Scott, H. Kohlstedt, A. Petraru, and C. S. Hwang. *Rep. Prog. Phys.*, 75:076502, 2012.

[167] X. Yang, Y. Lu, J. Lee, and I. W. Chen. *Appl. Phys. Lett.*, 108:013506, 2016.